

*NEW YORK CITY DEPARTMENT OF ENVIRONMENTAL PROTECTION
BUREAU OF WATER SUPPLY*

**Multi-Tiered Water Quality Modeling Program
Annual Status Report**

This status report describes work completed by NYCDEP's Multi-Tiered Water Quality Modeling Program during October 2010 – September 2011.

October 31, 2011

Prepared in accordance with Section 5.2 of the July 2007 United States Environmental Protection Agency Filtration Avoidance Determination

Prepared by: Don Pierson, PhD, WWQSR, Water Quality Modeling
Elliot Schneiderman, PhD, WWQSR, Water Quality Modeling
Mark Zion, WWQSR, Water Quality Modeling
David Lounsbury, WWQSR, Water Quality Modeling
Donald Kent, WWQSR, Water Quality Modeling
Adao H. Matonse, City University of New York, Institute for Sustainable Cities
Soni Pradhanang, City University of New York, Institute for Sustainable Cities
Rajith Mukundan, City University of New York, Institute for Sustainable Cities
Yongtai Huang, City University of New York, Institute for Sustainable Cities
Nihar Samal, City University of New York, Institute for Sustainable Cities
Aavudai Anandhi, Kansas State University

Table of Contents

1. Introduction.....	1
2. Use of Models for Support of Operational Decisions	2
3. Use of Modeling System to Evaluate Watershed Management Programs	9
4. Climate Change Integrated Modeling Project	12
5. Model Development	53
6. Model Data Acquisition and Organization.....	82
7. Modeling Program Collaboration	85
8. Modeling Program Scientific Papers and Presentations.....	90
9. References	100
Appendix A:	A-1

1. Introduction

This status report describes work completed for DEP's Multi-Tiered Water Quality Modeling Program during October 2010 – September 2011. The report presents progress on activities discussed in Section 2.4.2 of the New York City's Long-Term Watershed Program (DEP, 2006a). The following activities are reported herein:

- Application of DEP's reservoir, watershed and system models to inform operational decisions during the reporting period (Section 2);
- Application of DEP's watershed and reservoir models to evaluate watershed management programs (Section 3);
- Progress on the Climate Change Integrated Modeling Project including studies related to: strategies to improve and refine future climate scenarios; understanding potential changes in sediment sources under future climate change; regime shifts in hydrologic streamflow statistics, changes in stream ecological indicators under potential climate change; effects of climate change on reservoir thermal structure; and assessment of climate change related vulnerability and risk management on the water system operations (Section 4);
- Studies related to model development including: development of empirical rating curves for turbidity load estimation in Esopus Creek; studies on sediment fingerprinting; calibration of the SWAT-WB watershed model; modeling studies on relation of channel processes to phosphorus export; development of regression models for individual reservoir inflow for EOH reservoirs; and further calibration of 1D reservoir models (Section 5);
- Model data acquisition, development and organization (Section 6);
- Collaboration of the modeling section with other projects and organizations including cooperative arrangements, contracts and proposals. (Section 7); and
- Summary of scientific journal papers and presentations at scientific conferences that the modeling section has given over the last year (Section 8).

2. Use of Models for Support of Operational Decisions

During the period from October 2010 – September 2011 there were a number of major storm events that led to turbidity related issues for the Ashokan Reservoir. Figure 2.1 shows the time series of flows, based on provisional data collected by USGS for the Esopus Creek at Coldbrook, the major tributary input to the Ashokan Reservoir. The water year was characterized by five major events: a large rain event in early October 2010, another large rain event at the beginning of December 2010, the spring snowmelt event in March 2011, Hurricane Irene at the end of August 2011 and the remnants of Tropical Storm Lee in early September 2011. During and for a period after these events, the Water Quality Modeling Section performed a number of model simulations to better guide the operations of the Catskill System to ensure the delivery of high quality water while minimizing the use of alum. This section describes a few examples of these model simulations.

Simulation Descriptions

Three types of models - reservoir, watershed, and system - were used for the simulations during the reporting period. For all of the simulations, LinkRes and its component model 2D reservoir model CEQUAL W2 (DEP 2004, Cole and Buchak 1995) were used to simulate turbidity values within the reservoir and aqueduct withdrawals. The model has been set up and tested for the Ashokan West Basin, the Ashokan East Basin and the Kensico Reservoir. In addition a number of simulations utilized the OASIS system model (HydroLogics, Inc., 2007; Gannett Flemming and Hazen and Sawyer, 2007) as set up for the New York City supply to simulate aqueduct flows.

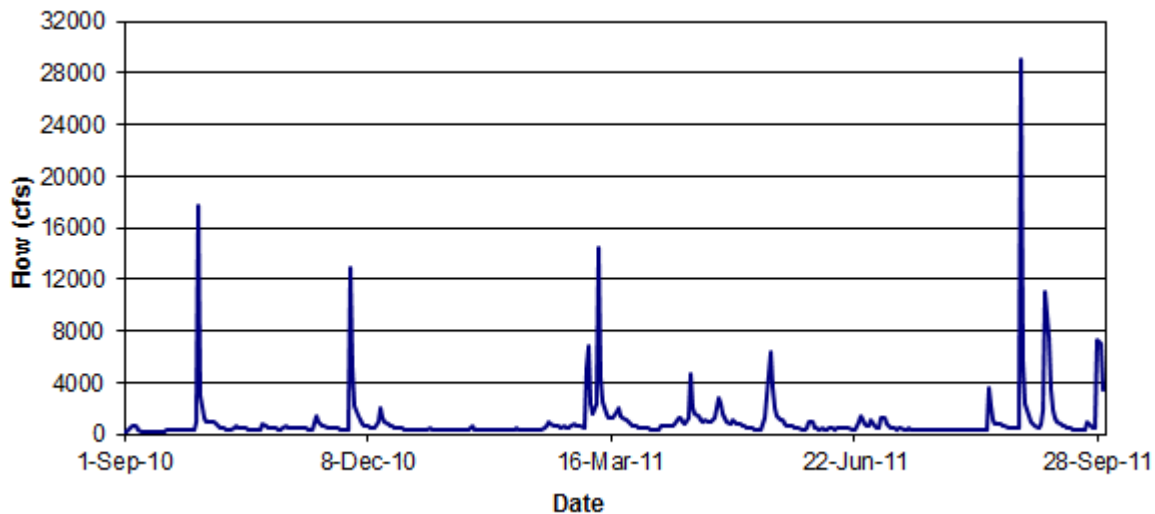


Figure 2.1. Provisional streamflow time series as measured at USGS gage #01365000, Esopus Creek at Coldbrook for September 1, 2010 – September 30, 2011.

During the October 2010 – September 2011 reporting period, 23 separate modeling analyses were performed. The dates and the reservoirs included in each analysis are listed in Table 2.1. For each of the simulations, a number of scenarios of different Catskill and Delaware system turbidity and flow inputs were modeled to predict their effects on Kensico effluent turbidity levels. In general, model runs were used to guide reservoir operations so that simulated turbidity levels at both the CATLEFF and DEL18 effluents would not exceed safe turbidity levels. Model results helped determine Catskill and Delaware Aqueduct flow rates that would allow DEP to continue to deliver Catskill water into Kensico Reservoir, while at the same time allowing an acceptably small increase in turbidity at the effluents.

A “positional analysis” strategy was followed for these model runs. Under this strategy, the initial conditions of the reservoir are used as the starting point for the model simulations. Then the model is run for a forecast period which ranges from 1 to 6 months into the future, depending on the simulation goals. For the forecast period, inputs of meteorology and aqueduct water temperature are based on each year in the historical record (1948-2004 for Ashokan model runs and 1987-2004 for Kensico model runs), while initial conditions are set to most recently measured values based on a combination of limnological survey data and in-lake automated buoy measurements. For simulations of Kensico Reservoir, flows and derived turbidity loads are set at fixed values associated with the forecast conditions. With this method, each year represents a separate realization (or trace) of the simulated model outcome and variability in the traces will result from year-to-year changes in weather conditions only. For Ashokan and combined Ashokan-Kensico simulations, the input flow and turbidity load to Ashokan Reservoir is based on the historical record and a series of different fixed operational strategies are employed. In these cases, each trace represents a simulated outcome that incorporates both climatic and flow variability in the historical record, when comparing the outcomes of different operational strategies. In both cases, the complete set of positional analysis traces, taken in total, can then be used to develop a statistical probability of potential simulated reservoir storage levels and effluent turbidity.

The example model runs described in this section relate to decisions made for inflows to the Kensico Reservoir. The major focus of these simulations is to help determine the ratios of Catskill versus Delaware inputs to the Reservoir, given turbidity levels in each system, to ensure that effluent turbidity will not exceed the 5 NTU regulatory limit.

Table 2.1. List of modeling analyses performed during the reporting period including the reservoirs simulated in each analysis.

Turbidity Modeling Runs October 2010-September 2011			
Date	Ashokan West	Ashokan East	Kensico
10/01/2010			X
10/04/2010			X
10/06/2010			X
10/15/2010			X
10/19/2010	X		
11/03/2010			X
12/03/2010			X
12/06/2010	X		
12/09/2010	X	X	
12/15/2010			X
12/23/2010	X	X	
01/03/2011			X
01/12/2011	X	X	X
01/18/2011	X	X	X
01/21/2011			X
01/27/2011	X	X	X
02/17/2011			X
08/30/2011			X
08/31/2011			X
09/02/2011			X
09/07/2011			X
09/23/2011			X
09/30/2011			X

Example Simulations

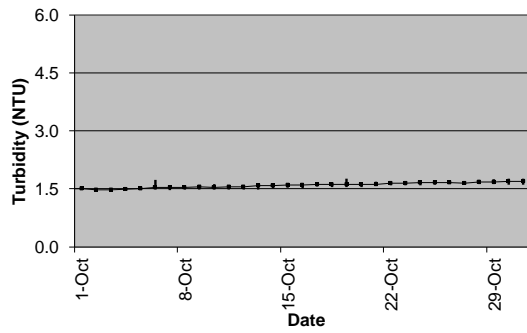
Simulations October 4, 2010

This first example set of simulations was initiated after the effects of a large storm at the beginning of October filled the Ashokan Reservoir and elevated turbidity in the entire reservoir. It was expected that Ashokan effluent turbidity levels would go above 10 NTU and that stop shutters would be required to reduce the Ashokan diversion to the Catskill Aqueduct to below 300 MGD in order to maintain acceptable water quality at Kensico Reservoir.

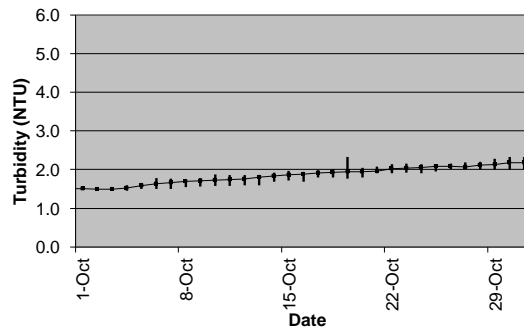
To help determine the necessity for stop shutter installation and to ascertain a recommended flow level, sensitivity simulations for Kensico Reservoir were performed. The positional analysis framework was used with meteorological forcings and aqueduct input water temperatures for the years 1987-2004 (18 traces) to represent historical variability in the model forcings. The simulations were run for a 30 day forecast period from October 1 – October 31. Initial conditions in the reservoir were based on robotic monitoring information collected on October 1, which indicated isothermal conditions with a water temperature of 18°C and turbidity of 1.5 NTU throughout water column. Aqueduct flow outputs from Kensico were set to 400 MGD and 800 MGD via Catskill and Delaware aqueducts, respectively. For all runs the input turbidity from the Delaware Aqueduct was set to 1.5 NTU based on conditions at the time. To test various inflow and turbidity input combinations from Catskill Aqueduct to Kensico Reservoir, flows were set to 50, 150, 250 MGD and input turbidities were set to 20 and 40 NTU. Delaware Aqueduct inflows were set to balance the Catskill Aqueduct flows so total inflow of the two aqueducts equaled 1200 MGD. Each of the simulations assumes that these inputs and outputs are constant for the 30 day forecast period.

Figure 2.2 shows the results for the scenarios. These runs indicated that if Catskill influent turbidity was above 20 NTU flow rate should be reduced to 150 MGD. If Catskill influent turbidity rises to about 40 NTU for an extended period, then flow should be reduced to about 50 MGD.

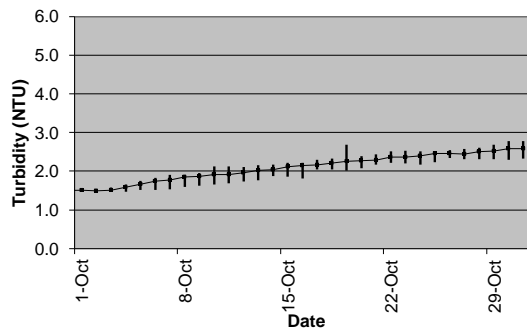
(a) Catskill inflow 50 MGD, 20 NTU:



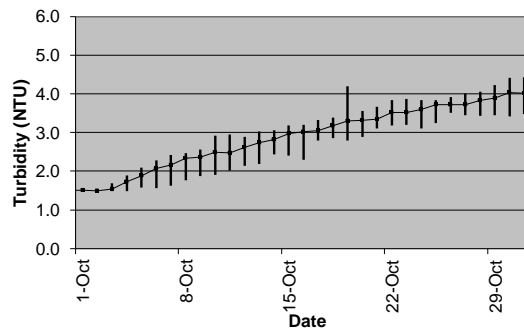
(b) Catskill inflow 50 MGD, 40 NTU:



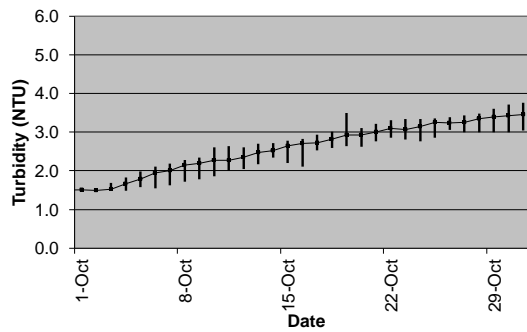
(c) Catskill inflow 150 MGD, 20 NTU:



(d) Catskill inflow 150 MGD, 40 NTU:



(e) Catskill inflow 250 MGD, 20 NTU:



(f) Catskill inflow 250 MGD, 40 NTU:

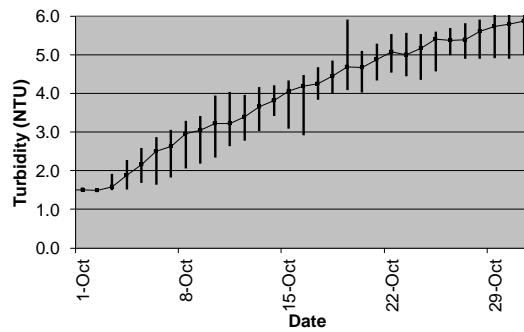
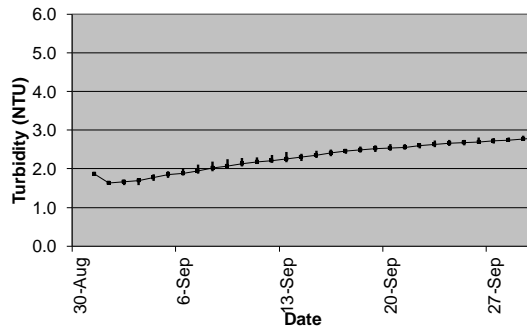
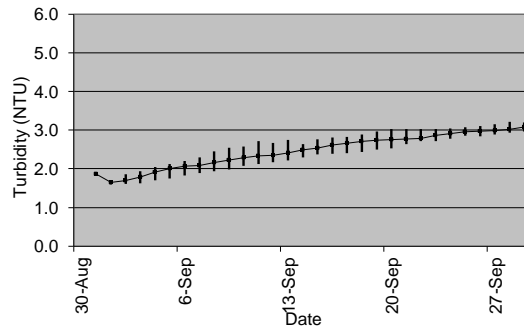


Figure 2.2. Results of CEQUAL-W2 simulations from October 4, 2010 for effluent turbidity from Kensico Reservoir with Catskill Aqueduct inflow of 50, 150 and 250 MGD and influent Catskill turbidity of 20 and 40 NTU. Vertical bars show the range of variability associated with the 18 positional analysis traces.

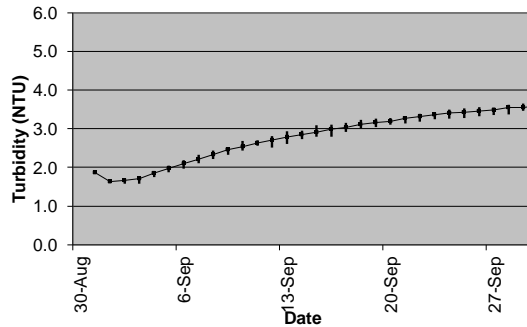
(a) Delaware inflow 800 MGD, 4 NTU:



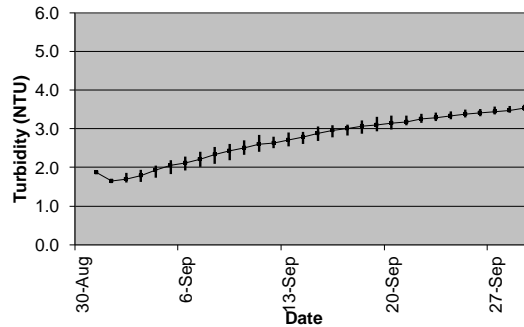
(b) Delaware inflow 500 MGD, 4 NTU:



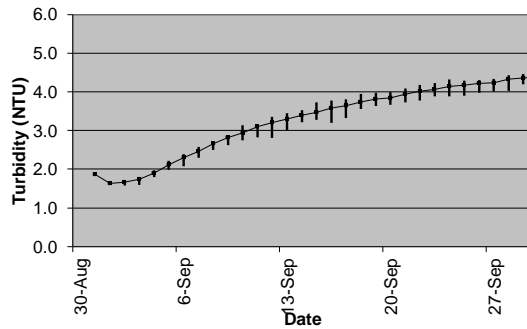
(c) Delaware inflow 800 MGD, 6 NTU:



(d) Delaware inflow 500 MGD, 6 NTU:



(e) Delaware inflow 800 MGD, 8 NTU:



(f) Delaware inflow 500 MGD, 8 NTU:

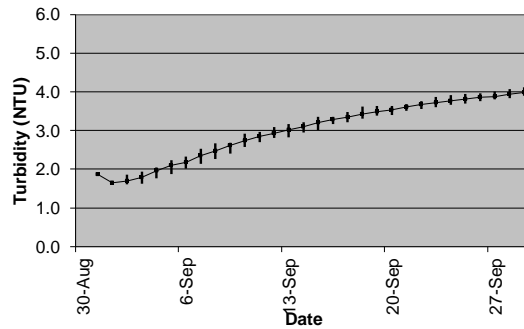


Figure 2.3. Results of CEQUAL-W2 simulations from September 2, 2010 for effluent turbidity from Kensico Reservoir with Delaware Aqueduct inflow of 800 and 500 MGD and influent Delaware turbidity of 4,6 and 8 NTU. Vertical bars show the range of variability associated with the 18 positional analysis traces.

Simulations September 2, 2011

Hurricane Irene occurred at the end of August 2011, and resulted in record flows at many stream gages throughout the watershed. This event greatly affected turbidity in all the WOH reservoirs including the Rondout Reservoir. Under most storm event conditions, the Rondout Reservoir turbidity remains low and this source of low turbidity water can be used to reduce the risk of high turbidity at Kensico Reservoir. At the time of these simulations, however, turbidity in Rondout Reservoir diversion was about 15 NTU and profiles from a Rondout limnological survey indicated a plume of high turbidity in the upper layers of the reservoir near the intake and a plume of about 100 NTU in the upstream area of the reservoir. Meanwhile, Ashokan Reservoir diversion turbidity was about 100 NTU. Alum was used to reduce turbidity in the Catskill Aqueduct influent to Kensico Reservoir. Under these conditions the treated Catskill effluent was of lower turbidity than the untreated Delaware System water.

A set of Kensico Reservoir sensitivity simulations were run to provide refined guidance for the levels of turbidity from the Delaware Aqueduct that could be tolerated as inputs to Kensico Reservoir with varying inflow rates from the Catskill and Delaware Aqueducts. As with the previous example, the positional analysis framework was used with meteorological forcings and aqueduct input water temperatures for the years 1987-2004 (18 traces) to represent historical variability in the model forcings. The simulations were run for a 30 day forecast period from August 31 – September 30. Initial conditions in the reservoir were based on limnological survey measurements collected on August 31, 2011. Aqueduct flow outputs from Kensico were set to 350 MGD and 750 MGD via Catskill and Delaware aqueducts, respectively. For all runs the input turbidity from the Catskill Aqueduct was assumed to be 100 NTU which when treated with alum is assumed to be reduced by 95% to yield an effective input of 5 NTU. (Later runs during this event use data from the limnological surveys to better ascertain the correct effective turbidity to use for alum treated Catskill influent.) To test various inflow and turbidity combinations input from the Delaware Aqueduct to Kensico Reservoir, flows were set to 800, 700, 500 MGD and input turbidities were set between 2.5 and 8 NTU. Catskill Aqueduct inflows were set to balance the Delaware Aqueduct flows so total inflow of the two aqueducts equaled 1100 MGD. Each of the simulations assumes that these inputs and outputs are constant for the 30 day forecast period.

Figure 2.3 illustrates the results for the scenarios. At Delaware influent turbidity less than 6 NTU (figure 2.3a-b), simulated Kensico effluent is improved by increasing Delaware Aqueduct inflow. At Delaware influent turbidity greater than 6 NTU (figure 2.3e-f) simulated Kensico effluent is improved by increasing Catskill Aqueduct inflow. At Delaware influent turbidity equal to 6 NTU (figure 2.3c-d) simulated Kensico effluent turbidity is insensitive to varying Delaware and Catskill inflow rates.

Conclusions

The set of events during October 2010 – September 2011 represented a combination of many extreme events, some of which created record streamflows. The modeling activities performed during this period were used to inform operational decisions and, in turn, helped to minimize alum use while maintaining high quality source water during these turbidity events.

3. Use of Modeling System to Evaluate Watershed Management Programs

As part of the 2011 FAD evaluation process (DEP 2011), the effects of non-point source management, point source upgrades, and land use change on eutrophication in the Cannonsville and Pepacton Reservoirs were evaluated using DEP’s Eutrophication Modeling System (Figure 3.1). Output from the GWLF watershed model provided loading estimates to evaluate watershed programs implemented as part of the MOA. Four watershed management programs were evaluated: Watershed Agricultural Program; Urban Stormwater Retrofit Program; Septic Rehabilitation and Replacement Program and WWTP Upgrade Program. In addition, a significant decline in agricultural land use and agricultural activity that occurred from the early 1990s to the late 2000s independent of deliberate watershed management was evaluated.

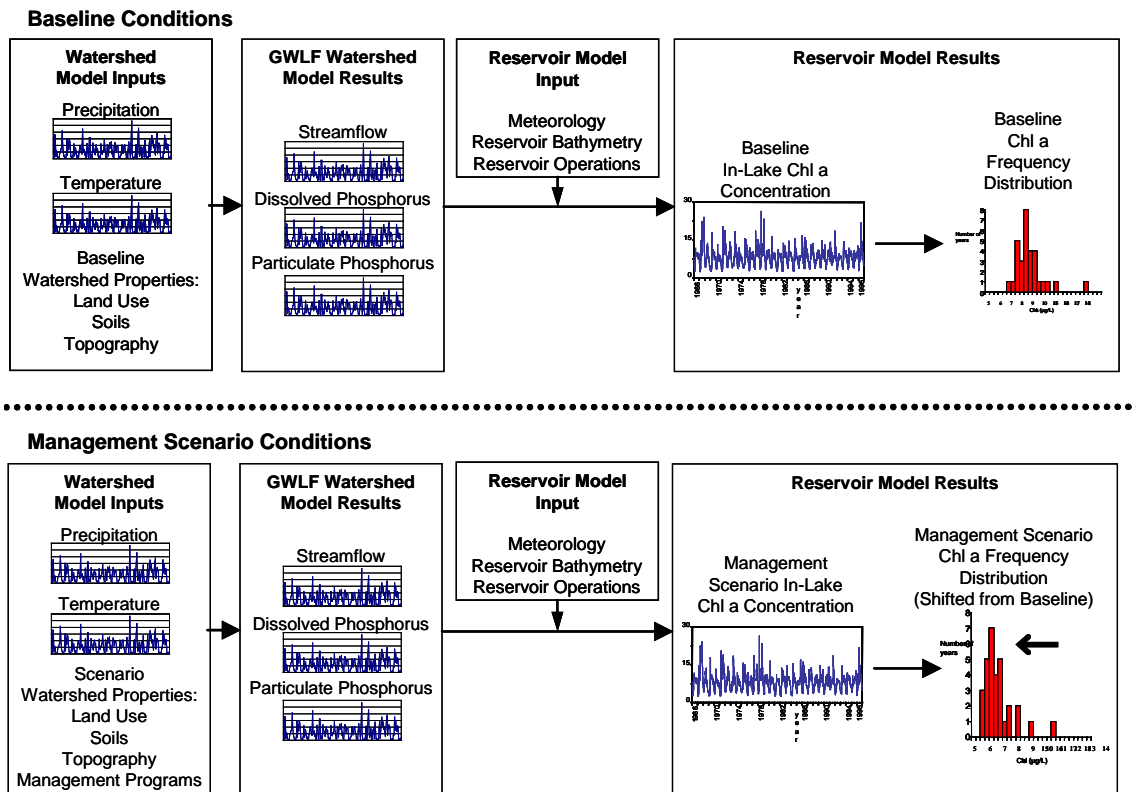


Figure 3.1. DEP’s Eutrophication Modeling System.

Calibrated and validated GWLF models for Cannonsville and Pepacton were used to estimate nutrient loads for a series of scenarios, each of which represents a combination of land use, non-point source management and point source conditions. A *BASELINE* scenario represents conditions existing in the 1990s prior to implementation of FAD programs. Two FAD evaluation scenarios represent conditions of the early 2000s (*FADPERIOD1*) and late 2000s (*FADPERIOD2*), before and during which substantial implementation of FAD programs occurred. Nutrient reduction factors due to watershed management programs based BMP nutrient removal and implementation data were applied to represent watershed management effects in each *FADPERIOD* scenario.

Changes in nutrient loading due to the combined effects of land use change and FAD programs were examined by comparing the *FADPERIOD* scenarios to the *BASELINE*. There was a ~49% reduction in dissolved P (P) loads from Cannonsville watershed from the *BASELINE* to *FADPERIOD1* and an additional ~7% reduction from *FADPERIOD1* to *FADPERIOD2*. For Pepacton watershed dissolved P export was reduced by ~23% from *BASELINE* to *FADPERIOD1* and an additional ~3% from *FADPERIOD1* to *FADPERIOD2*. The large reductions seen between the *BASELINE* and *FADPERIOD1* correspond to a combination of high rates of new program implementation and substantial reduction in agricultural activity during that period. Continued but slower declines in P loads from *FADPERIOD1* to *FADPERIOD2* occurred as FAD programs became more focused on maintenance and improvement than on new program development, and the reduction in agricultural activity continued.

The relative effects of land use change vs. watershed management on load reductions were examined by comparison of the *BASELINE* to *FADPERIOD2*. Land use change (decline in agriculture) and watershed management both produced substantial reductions in P loading. Loading reductions due to land use change alone were ~18% for dissolved P in Cannonsville, and ~10% for dissolved P in Pepacton. The combination of land use change and watershed management produced reductions of ~55% for dissolved P in Cannonsville, and ~26% for dissolved P in Pepacton. WWTP upgrades and the implementation of agricultural BMPs by the Watershed Agricultural Program provided most of the loading reductions, with minor reductions from septic system remediation and urban stormwater management.

The effects of land use change, non-point BMPs, and point source management on the trophic status of the Cannonsville and Pepacton Reservoirs were evaluated by driving reservoir water quality models with the different nutrient loading scenarios simulated using GWLF. Simulated loading reductions due to combined land use change and watershed management between *BASELINE* and *FADPERIOD1* resulted in a ~34% reduction in the May – October epilimnetic chlorophyll concentrations, and a ~30% reduction in the May – October epilimnetic total P concentrations in Cannonsville Reservoir. For Pepacton Reservoir the same reductions in concentration were ~15% and ~9% for chlorophyll and Total P respectively. As was the case for the input loads simulated with GWLF, reductions in reservoir concentrations during *FADPERIOD2* were lower. Between *FADPERIOD1* and *FADPERIOD2* there was a further reduction of ~5% in May – Oct epilimnetic chlorophyll concentrations and a ~3% further reduction in May – Oct epilimnetic total P concentrations. For Pepacton Reservoir the additional reductions in concentration simulated as occurring between *FADPERIOD1* and *FADPERIOD2* were ~3% and ~2% for chlorophyll and total P.

Landuse and FAD program specific effects on reservoir trophic status were examined by comparison of *BASELINE* with *FADPERIOD2*. For Cannonsville Reservoir, lower watershed loads due to land use change only (decline in farming) resulted in reductions of ~9% for in-lake growing season chlorophyll *a* and ~8% for total P. Greater reductions were predicted when the FAD programs were considered in addition to land use change (~39% for chlorophyll *a* and ~32% for total P). The response of Pepacton Reservoir (which exhibited less eutrophication under *BASELINE* conditions) was similar, but the magnitudes of the reductions were less, suggesting that reservoirs with higher eutrophic condition tend to benefit proportionately more from watershed load reductions.

Examination of daily, as well as long term mean reservoir chlorophyll levels, suggests that the occurrence of extreme “bloom-like” epilimnetic chlorophyll concentrations are also affected by differing nutrient loading scenarios, and that the implementation of watershed management programs had an even greater impact on reducing the frequency of extreme epilimnetic chlorophyll concentrations than in reducing long term mean concentrations.

4. Climate Change Integrated Modeling Project

4.1. Project Overview

DEP has undertaken a long-term effort to evaluate the effects of future climate change on the quantity and quality of water in the NYC water supply, and to also evaluate how such effects could influence the use and operation of the water supply. This project designated the “Climate Change Integrated Modeling Project for Water Quantity and Quality” (CCIMP), was an outgrowth of the DEP climate change task force. Project planning took place during 2006-2007. A series of meetings which included members of the DEP Bureau of Water Supply Water Quality Modeling Program, the Strategic Services Unit, the Bureau of Environmental Planning and Assessment, and the Columbia University Center for Climate Systems Research were used to develop an overall project strategy and plan (Major et al. 2007), which was evaluated by a leading group of climate change, and water science experts. The work specified by this plan became an integral part of the task to “Quantify the Potential Climate Change Impacts on NYC Water Systems” in the DEP Climate Change Program Assessment and Action Plan (DEP 2008a).

An overview of the CCIMP is presented in the 2007 Modeling Program status report (DEP 2007), and subsequent results were presented in the 2008-2010 Modeling Program status reports (DEP 2008b; 2009; 2010). The project continues, and during the last year we have developed an improved and expanded series of future climate scenarios that are used to drive watershed and reservoir model simulations; have made new simulations and analyses that examine the potential effects of climate change on watershed erosion, streamflow and ecological indices related to streamflow; and have made a series of simulations that examined potential future changes in the thermal structure of the reservoirs. DEP is also a participating utility in a number of climate change related projects (See Section 4.7) and during 2011 contributed significantly to WRF project 4262 which has the goal of identifying vulnerabilities and risks in the operation of the NYC water supply system, and which will also try to identify adaptation strategies to mitigate the potential risks. In this section of the report we briefly describe these CCIMP research activities that were accomplished during 2010.

4.2. Refining Climate Change Scenarios

Previous model simulations used to evaluate future climate impacts on the NYC water supply (DEP 2008b, 2009, 2010) have been made using three to four GCM models that were downscaled using a single monthly additive or multiplicative change factor (CF), an approach that is widely used for climate impact analysis (e.g. Hay et al 2000 Anandhi et al. 2011), During the past year we have created a number of additional scenarios (Table 4.1) using all available daily data from the World Climate Research Program Coupled Model Intercomparison Project 3 (CMIP3) climate data archive (http://www-pcmdi.llnl.gov/ipcc/about_ipcc.php). Furthermore, when creating the expanded set of scenarios, two different variant of change factor methodology (CFM) were used: the original version based on single monthly CF; and a new version (described below) using 25 additive CFs for each month. Below the 25 bin CFM methodology is described and the characteristics of the derived scenarios are discussed.

In an earlier study by Anandhi et al. (2011) for the region, several types of CFMs categorized by temporal scale, temporal resolution, mathematical formulation, or number of change factors analyzed. Based on the results from this study, DEP decided to employ a method using 25 change factors applied additively for each month when creating scenarios based on GCM runs in Table 1. In this method, separate cumulative distribution functions (CDFs) of the simulated baseline (*GCMb*) and future (*GCMf*) climates are estimated for each month. Each CDF is divided into 25 equal parts (bins) with each bin having 4 percentile (=100/25) as its resolution. The mean monthly values of *GCMb* and *GCMf* climates are estimated for each bin using equations 4.1 and 4.2.

$$\overline{GCMb_n} = \sum_{i=1}^{Nb} GCMb_{i,n} / Nb \quad (4.1)$$

$$\overline{GCMf_n} = \sum_{i=1}^{Nf} GCMf_{i,n} / Nf \quad (4.2)$$

where *Nb* and *Nf* represent the number of days in a month during the baseline and future time periods, and *n* equals the change factor bin (1 to 25).

For each climate variable (i.e. precipitation air temperature etc.) the 25 additive change factors (*CF_{add,n,j}*) are calculated for each month (*j*) by taking the arithmetic difference between the corresponding bins (*n*) derived from a current climate simulation and those derived from a future climate scenario taken at the same GCM grid location (equation 4.3). The resulting CFs are then added to the corresponding bins associated with a given month in the time series of local historical data (*LOB_{n,j}*) to obtain future scaled climate scenarios (*LSf_{add,n,j}*) (equation 4.4).

$$CF_{add,n,j} = \overline{GCMf_{n,j}} - \overline{GCMb_{n,j}} \quad (4.3)$$

$$LSf_{add,n,j} = LOB_{n,j} + CF_{add,n,j} \quad (4.4)$$

where $LSf_{add,n,j}$ is a daily value of the locally downscaled daily data series that has a parameter magnitude in bin n and occurs in month j ; $LOB_{n,j}$ is a daily observed historical data value occurring in bin n associated with month j ; $CF_{add,n,j}$ is an additive CF associated with bin n in month j .

Thus, for each month, 25 CFs are calculated for each meteorological variable of interest for the future scenarios (A1B, A2, B1), time periods (2045-2065, 2081-2100) and GCMs (listed in Table 4.1). Future scenarios are created by adding CFs to the historical daily time series. These CFs are dependent on the month (j) and the magnitude (n) of the daily observed value during that month.

As a first step in the use of these scenarios we evaluated the monthly climatology of the scenarios of precipitation, air temperature and streamflow. Data are plotted in figures 4.1-4.4. The precipitation scenarios are also analyzed using an index of the intensity of the wet day (IWD). IWD is calculated using pooled monthly data for a given scenario so that for example, January values of IWD are calculated using the combined data from 20 January months. IWD for any month is calculated by summing the rainfall on all days that exceed a specific threshold of 1mm (Benestad, 2010) and divided that by the total number of days exceeding the same threshold condition

Boxplots of the monthly scenarios of precipitation and temperatures for each of the six watersheds were obtained by applying the 25 CFs to the observed data for the combination of GCMs, scenarios and time periods (figures 4.1 and 4.2). Most scenarios show an increase in precipitation for all the 12 months, with the variability in the predicted precipitation between GCM scenarios being ~10mm/month (figure 4.1). Very few scenarios showed a decrease in mean monthly precipitation (mostly in B1 and A2 scenarios). All the derived temperature scenarios consistently show an increase in temperature of 2 to 4° C in the study region (figure 4.2). The variability in the predicted temperature among GCMs is ~2 to 6°/month.

In general the IWD (figure 4.3) is highest for the Ashokan, Neversink and Rondout watersheds (range 8 to 13mm), followed by the Pepacton and Schoharie watersheds (range 7 to 11 mm) and with the Cannonsville watershed having the lowest IWD (range 6 to 8mm). Compared to values calculated using historical data, most future scenarios predict an increase in IWD during January, February, April, May, August, October and November months and a decrease in IWD during the rest of the year.

Table 4.1. GCM scenarios downloaded from the Lawrence Livermore National Laboratory's Program for Coupled Model Diagnosis and Inter-comparison (PCMDI) data archive. Numbers identify the different realizations of each GCM scenario that were obtained

GCM Acronym	Daily Precipitation				Daily Average Air Temperature			
	20C3M	A1B	A2	B1	20C3M	A1B	A2	B1
1 BCCR	1	1*	1	1	1	1	1	1
2 CCSM3	1,3,5,6,7,8,9	3,5,6,7,8	1,3,5	6,7,8	1,3,5,6,7,8,9	3,5,6	1,3,5	6,7,8
3 CGCM3.1(T47)	1,2,3,4,5	1,2,3	1,2,3	1,2,3	1,2,3,4,5	1,2,3	1,2,3	1,2,3
4 CGCM3.1(T63)	1	1		1	1	1		1
5 CNRM-CM3	1	1	1	1	1	1	1	1
6 CSIRO-Mk3.0	1,2,3	1	1	1	1,2,3	1	1	1
7 CSIRO-Mk3.5	1	1			1,2,3	1		
8 ECHAM5/MPI-OM	1,4	4	1	1	1,4	4	1	1
9 ECHO-G	1,2,3	1,2,3	1,2,3	1,2,3	1,2,3	1,2,3	1,2,3	1,2,3
10 FGOALS-g1.0	1,2,3	1,2,3		1,2,3	1,2,3	1		1,3
11 GFDL-CM2.0	1	1	1	1	1	1	1	1
12 GFDL-CM2.1	2				2			
13 GISS-AOM	1	1		1**	1	1		1
14 GISS-ER	1	1	1	1	1	1	1	1
15 INGV-SXG	1	1	1		1	1	1	
16 INM-CM3.0	1	1	1	1	-			
17 IPSL-CM4	1,2	1	1	1	1,2	1	1	1
18 MIROC3.2-hires	1	1		1	1	1		1
19 MIROC3.- medres	1,2	1,2	1,2	1,2	1,2,3	1,2,3	1,2,3	1,2,3
20 MRI-CGCM2.3.2	1,2,3,4,5	1,2,3,4,5	1,2,3,4,5	1,2,3,4,5	1,2,3,4,5	1,2,3,4,5	1,2,3,4,5	1,2,3,4,5
Total no. scenarios	43	34	25	30	44	30	25	29

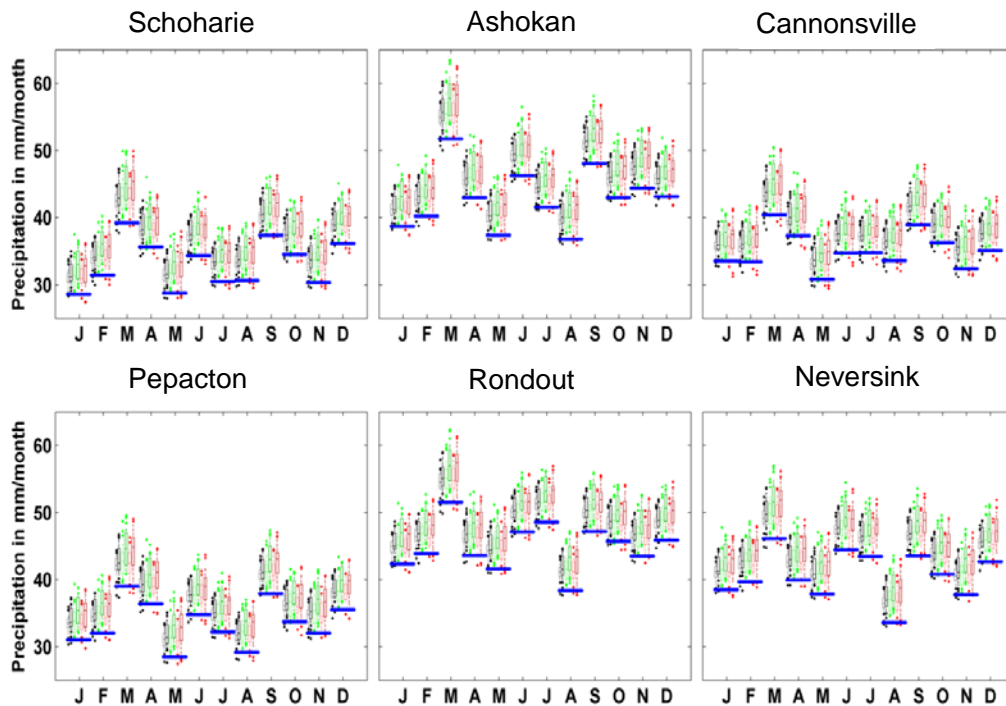


Figure 4.1. Boxplot of mean monthly precipitation input to each reservoir watershed obtained by applying the 25 bin CFs from GCMs listed in table 4.1 for combinations of scenarios B1 (black), A1B (green), and A2 (red), and for the time period 2046-2065 (light shade), 2081-2100 (dark shade). The whiskers in the boxplot extend from the 10 to 90th percentile values. The outliers of the 10-90 percentile range are shown as dots in the figures. The blue bar is the median of historical observations.

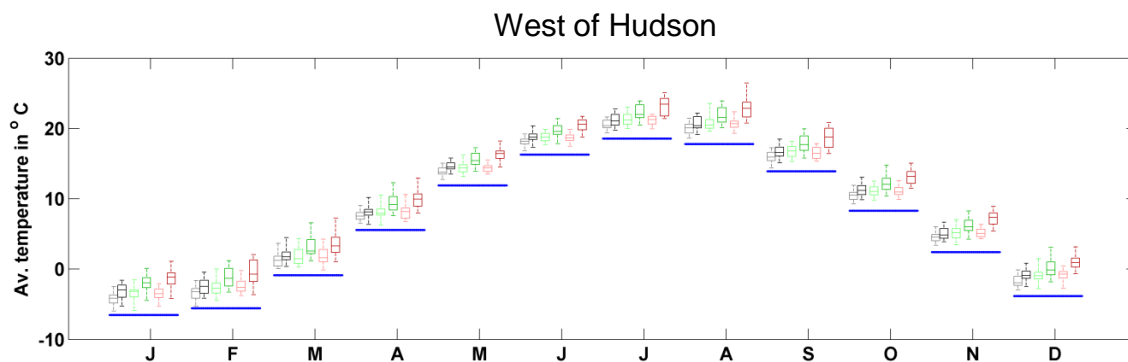


Figure 4.2. Boxplot of mean monthly average temperature over the entire WOH region obtained by applying the 25 bin CFM to the GCM scenarios listed in table 4.1. The blue bar is the median of historical observations.

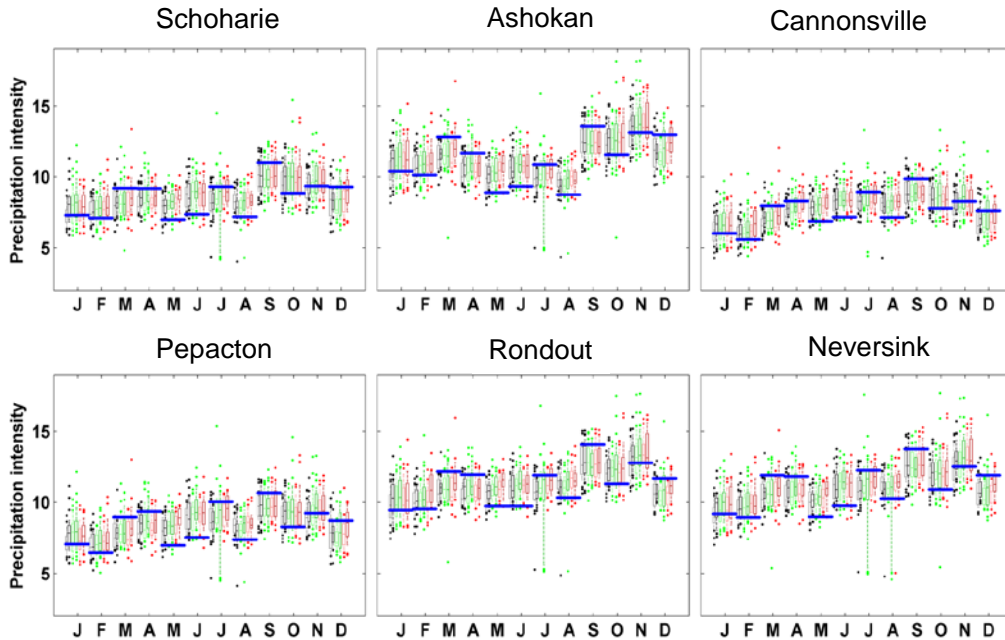


Figure 4.3. Boxplot of mean monthly intensity of wet days (IWD) obtained by applying the 25 bin CFM to the GCM scenarios listed in table 4.1. The blue bar is the median of historical observations.

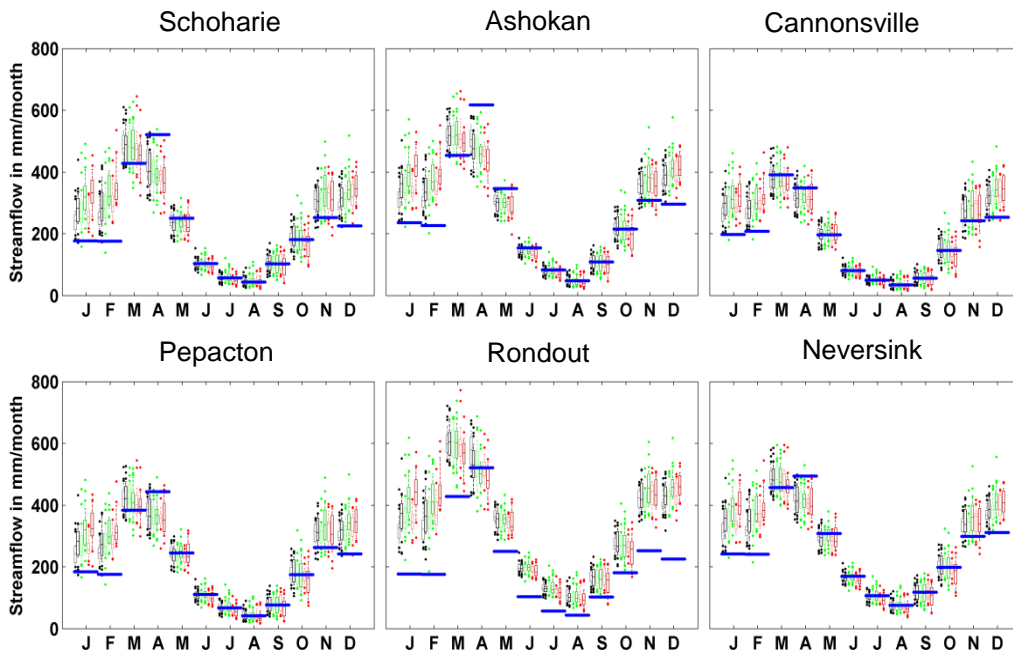


Figure 4.4. Boxplot of mean monthly streamflow simulated using the GWLF model and input data of air temperature and precipitation derived by applying the 25 bin CFM to the GCM scenarios listed in table 4.1. The blue bar is the median of historical observations.

A preliminary evaluation of variations in streamflow that could be expected to occur under the expanded set of climate scenarios was also made. Scenarios of daily streamflow were simulated using Generalized Watershed Loading Function - Variable Source Area (GWLF –VSA) watershed model. More details of the model may be found in Haith et al. (1992), Schneiderman et al. (2002), Matonse et al. (2011) and Zion et al. (2011). The scenarios of precipitation and temperatures created using the GCM data in table 4.1 and CFM described by equations 4.1-4.4 were input to the calibration GWLF model to create scenarios of streamflow for the six West of Hudson reservoir watersheds, three scenarios, two time periods.

For most scenarios the late fall to winter period (November - March) had higher streamflow compared to the streamflow simulated using the observed historical precipitation and air temperature data, while April showed reduction in streamflow (figure 4.4). For the remainder of the year there was no clear future trend. Approximately 50 percent of the GCMs showed an increase and the rest showed a decrease compared to simulation based on contemporary conditions. Similar results were observed in Zion et al. (2011).

4.3. Modeling Sediment Source Areas and Future Climate Impact on Erosion and Sediment Yield in Cannonsville Watershed

Introduction

Recent studies have focused on the potential effects of climate change on water resources including water quality, hydrology, water demand, and socio-economic changes (Aber et al., 1995; Christensen et al., 2004; Parry et al., 2004; Bates et al., 2008). However, little research has been undertaken on the potential impact of climate change on sediment loads of streams and rivers (IPCC, 2007a). Quantifying spatial and temporal patterns in sediment loads under present and future conditions will be valuable in both understanding and predicting sediment transport processes as well as watershed-scale management of sediment for maintaining high water quality.

In this section we apply the Soil Water Assessment Tool-Water Balance (SWAT-WB) model (White et al., 2011) to simulate sediment transport and quantify the potential impact of climate change on soil erosion and sediment yield in the Cannonsville watershed. The watershed drains into the Cannonsville Reservoir, one of the drinking water supply reservoirs for New York City (NYC). An examination of historical data and results of model simulations for this region have both shown an increasing trend in precipitation and streamflow over the past fifty years (Burns et al., 2007; Zion et al., 2011). Our goal in this study is to examine how changes in precipitation and streamflow translate into changes in soil erosion and sediment transport in the Cannonsville watershed using a physically based semi-distributed model. Our study assumes stationary land use/cover for the study region. The specific objectives of this study are:

- (1) To identify the major sediment source areas within the Cannonsville watershed; and
- (2) To quantify the impact of future climate on long-term sediment loads at the watershed outlet

Methods

SWAT-water balance model

The SWAT-WB is a modified version of the SWAT-2005 model (Neitsch et al., 2005). The original SWAT model uses Hydrologic Response Units (HRU) to define the scale at which precipitation is partitioned into runoff and infiltration. Each HRU is defined based on land use and soil, while the runoff curve number method is used to partition precipitation into runoff and infiltration. In SWAT-WB each HRU is defined based on land use and topographic location which defines soil moisture pattern, and the partitioning of precipitation into runoff and infiltration is calculated based on daily soil water balance for the HRU. The modified version (SWAT-WB) has been found to perform well in simulating streamflow and sediment yield in watersheds where saturation excess runoff process is the dominant runoff generation mechanism (Easton et al., 2010a; White et al., 2011).

Sediment transport in SWAT

The SWAT model simulates soil erosion and sediment export from hillslopes as well as in-stream channel processes (Nietsch et al., 2005). Erosion caused by rainfall and runoff is calculated with the Modified Universal Soil Loss Equation (MUSLE) as:

$$sed = 11.8 \cdot (Q_{surf} \cdot q_{peak} \cdot area_{hru})^{0.56} \cdot K \cdot C \cdot P \cdot LS \cdot CFRG \quad (4.5)$$

where sed is the sediment exported from a HRU to the channel on a given day (metric tons), Q_{surf} is the surface runoff volume (mm ha^{-1}), q_{peak} is the peak surface runoff rate ($\text{m}^3 \text{s}^{-1}$), $area_{hru}$ is the area of the HRU (ha), K is the USLE soil erodibility factor ($\text{T h MJ}^{-1} \text{mm}^{-1}$), C is the USLE cover and management factor (dimensionless), P is the USLE support practice factor (dimensionless), LS is the USLE topographic factor (dimensionless) and $CFRG$ is the coarse fragment factor (dimensionless). The use of a runoff term in the equation avoids the use of a sediment delivery ratio. Deposition and degradation are the dominant channel processes influencing sediment yield at the basin outlet. These channel processes are determined by the upland sediment loads and also the transport capacity of the channel network. The transport capacity of the channel segment is determined by the simplified Bagnold's equation (Bagnold, 1977):

$$T_{ch} = a \cdot v^b \quad (4.6)$$

where T_{ch} (T m^{-3}) is the transport capacity of a channel segment, a and b are user defined coefficients, and v (m s^{-1}) is the peak channel velocity. Parameters related to channel cover and channel erodibility that have a linear influence on channel contribution of sediment can be adjusted in SWAT.

SWAT model calibration

The model was calibrated for streamflow and sediment yield at the watershed outlet for the 1991-1995 water years and validated for the 2000-2002 water years. Measured daily streamflow data was obtained from the USGS gauging station (#01423000) located at the watershed outlet near Walton. Daily time series of total suspended solids (TSS) collected near the Walton stream monitoring station using a sampling protocol that allowed accurate estimation of both baseflow and storm event sediment loads (Longabucco and Rafferty, 1998). The calibrated streamflow and sediment models were used to simulate a historical baseline scenario (1965-2008) of sediment yield using measured meteorological forcing.

Future climate scenarios

The potential effect of climate change on soil erosion and sediment yield was evaluated using scenarios derived from a suite of nine Global Climate Model (GCMs) that represent a range of future climate conditions, for the 2081-2100 future period. In this study, the A1B scenario from the Special Report on Emission Scenarios (SRES) in the IPCC Fourth Assessment Report (AR4) was used. Climate scenarios were downscaled using change factor methodology described in

Anandhi et al., (2011). Monthly change factors (CFs) were calculated from the difference between baseline (20C3M) and future GCM simulations. These monthly CFs were used to adjust the same local meteorological data used for the baseline simulation to represent the future climate conditions associated with a given GCM. Use of long term observed data in generating future climate scenarios ensured that the scenarios were representative of the observed climate patterns in the region.

Results and Discussion

Model calibration for hydrology and sediment

Both hydrology and sediment calibration used the goal of maximizing the coefficient of determination (R^2), maximizing Nash-Sutcliffe efficiency (NSE) (Nash and Sutcliffe, 1970), and minimizing percent bias. In addition, hydrology calibration was optimized so that the runoff and baseflow components of streamflow were simulated reasonably well compared to values derived from measured data using standard baseflow separation techniques (Arnold and Allen, 1999). The calibrated model simulated streamflow reasonably well as evident from the monthly statistics for the calibration ($R^2 = 0.76$ and NSE= 0.76) and validation period ($R^2 = 0.71$ and NSE= 0.68). The calibrated model simulated monthly suspended sediment load at the watershed outlet with acceptable model performance ($R^2 = 0.62$ and NSE= 0.61 during calibration and $R^2 = 0.70$ and NSE= 0.70 during validation).

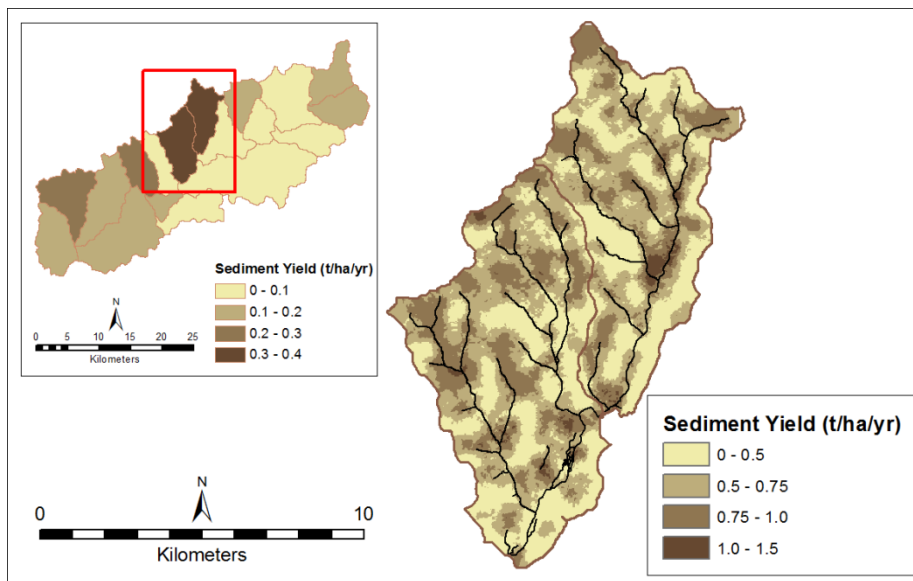


Figure 4.5. Map showing spatial variability in average annual sediment export from sub-basins (inset) and HRUs expressed as sediment yield to stream channels from the dominant sediment generating region

Spatial variability in sediment source areas

Figure 4.5 shows the spatial variability in sediment generating areas across the watershed. The model computes the sediment generated from each HRU and thereby enabling identification of the actual location of erosion within a sub-basin. The high sediment generating areas would be a combination of relatively high surface runoff and erosive land cover (e.g. agricultural field). The HRU maps of the highest sediment generating sub-basins were visualized to locate the sites of maximum erosion.

Model evaluation of future climate impact on soil erosion and sediment yield

Simulated future changes in watershed water balance that may influence soil erosion and sediment yield are presented in figure 4.6. Our analysis of future climate impact on sediment included changes in basin wide average annual sediment export from HRUs as well as changes in average annual sediment yield (sediment exiting the watershed outlet). Future sediment export from HRUs based on the wide range of future climate conditions represented by the GCMs showed wide variability. The ensemble mean showed a net increase in future sediment export by 49% from average historical values indicating the possibility of higher rates of soil erosion in the future (2081-2100). In comparison, the sediment yield from the watershed outlet showed only a 3.9 % increase in the ensemble mean compared to average historical values.

Analysis of seasonal changes in basin wide sediment export from HRUs showed increases in the winter and in the early spring and decreases in the summer and in early fall season (figure 4.7). The increase was much higher in magnitude compared to the decrease. This increase is due to the combined effect of increase in precipitation and also the decrease in precipitation falling as snow. The SWAT model predicts less erosion in the presence of snow. A comparison of the cumulative annual proportion of precipitation received as snow predicted by the model between the historical and future scenarios showed a sharp decline by 46% in the ensemble mean with a range of 38-62% decline predicted by the nine GCMs (figure 4.6, panel 1). Decrease in erosion during summer and early fall period is related to the changes in antecedent soil water content during rainfall events under future conditions. Although an increase in summer rainfall was predicted by the GCMs (figure 4.6, panel 2) increases in evapotranspiration (figure 4.6, panel 4) cause reduction in soil water content which result in increased saturation deficit. This means that more rainfall is required to bring the soil to saturation and generate equal amount of runoff as the current conditions. The importance of antecedent soil moisture on erosion from saturation excess dominated landscapes has been previously reported (Fitzjohn et al., 1998). Analysis of one of the HRUs under agricultural land use revealed an increase in crop biomass productivity during the months July and August by 19% and 29% respectively suggesting an earlier onset of growing season due to warmer climate. Such phenological changes are expected to affect the amount and timing of residue going back to the soil and thus soil erosion. These results are consistent with the finding of Nunes et al (2011) using a SWAT model application for climate change assessment of soil erosion in two Mediterranean watersheds.

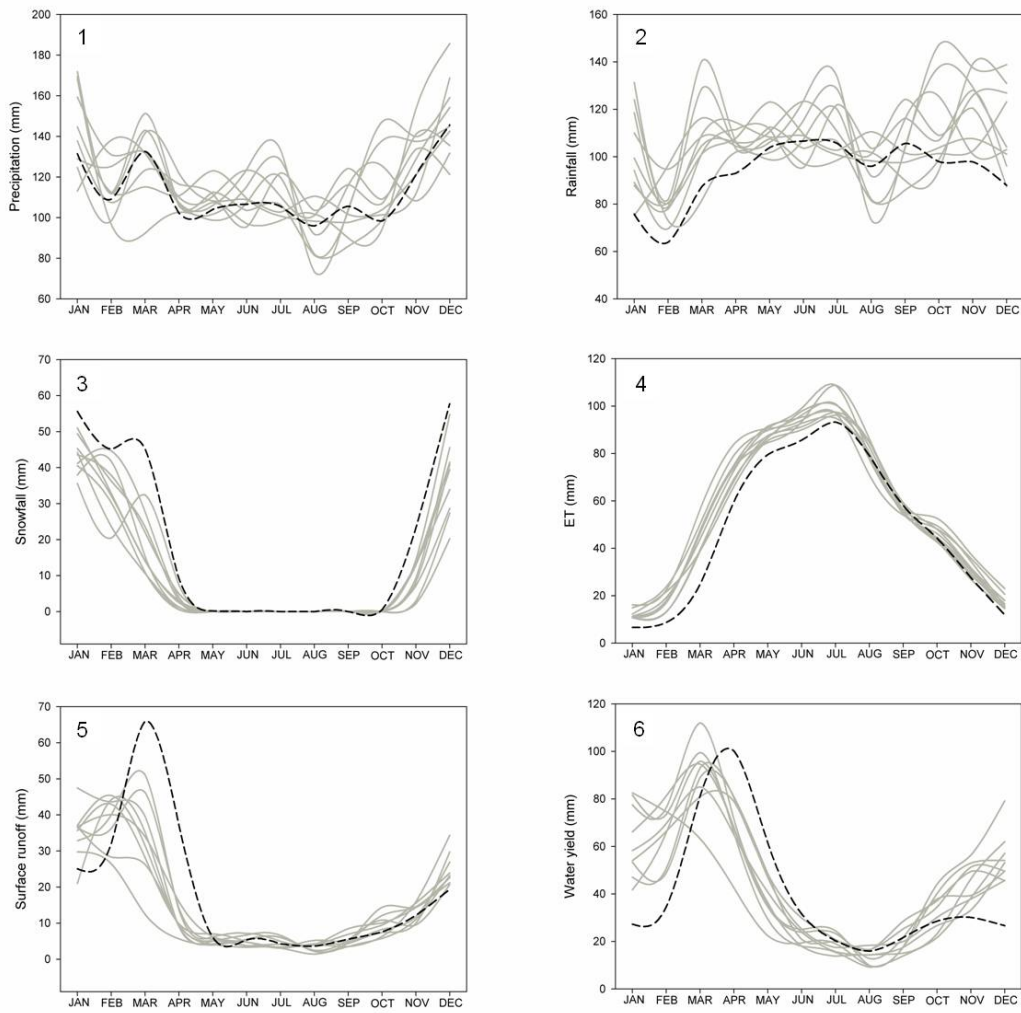


Figure 4.6. Monthly simulated components of the watershed water balance, Historical (1965-2008) in dark dotted lines versus Future (2081-2100) in gray lines.

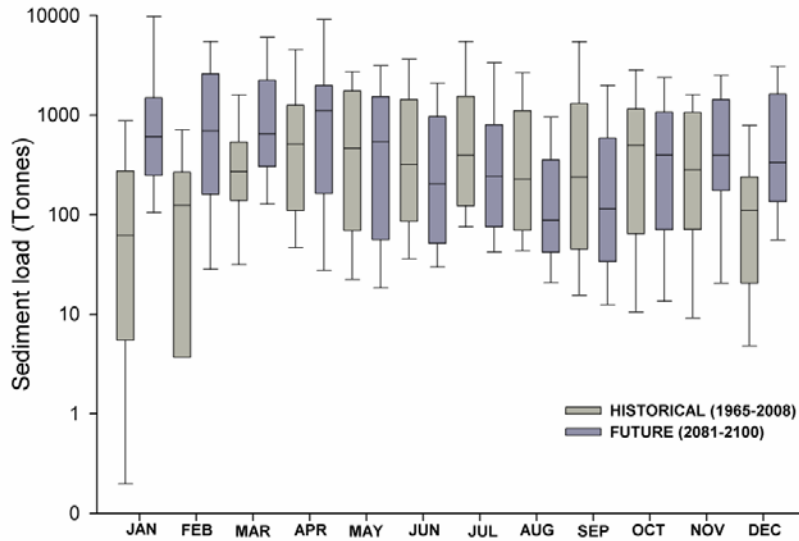


Figure 4.7. Boxplot of average monthly basin wide sediment export from HRUs expressed as sediment load to stream channels. Boxes represent the 25th and the 75th percentile and whiskers represent the 5th and 95th percentile values.

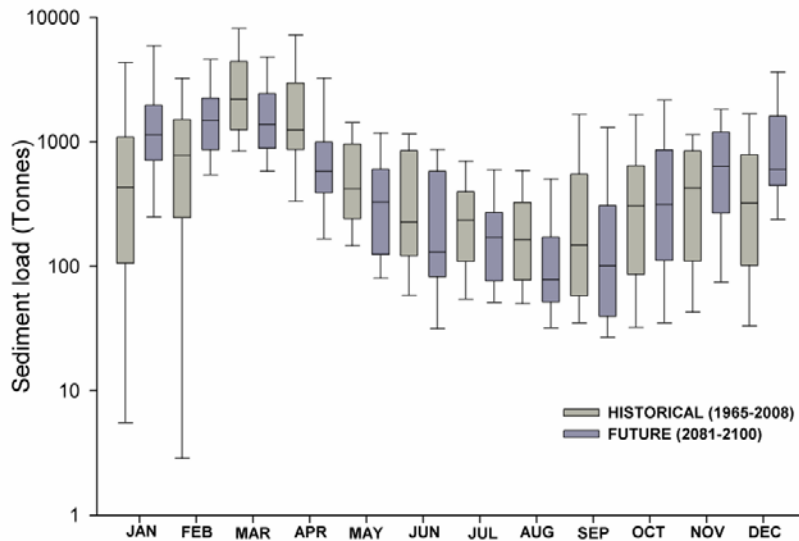


Figure 4.8. Boxplot of average monthly sediment yield from watershed outlet. Boxes represent the 25th and the 75th percentile and whiskers represent the 5th and 95th percentile values

Future trends in sediment yield at the watershed outlet followed the soil erosion trends for most months except for March and April (figure 4.8). These two months transported the maximum amount of sediment through the watershed outlet as seen in the historical scenario. Decline in sediment yield in these months during future periods explains to a certain extent the relatively small increase in average annual sediment yield at the watershed outlet. The decrease in sediment yield is related to the decrease in basin wide surface runoff and streamflow during this period. The decrease in April streamflow results from early snowmelt being observed in the region (Burns et al., 2007; Zion et al., 2011; Matonse et. al., 2011). Although summer precipitation appeared to increase in the future scenarios, a decrease in water yield resulting from an increase in saturation deficit predicted by the model coupled with a decrease in erosion resulted in less sediment yield at the watershed outlet in the summer.

Summary and Conclusions

A physically based watershed model was used to identify the location of major sediment generating areas in a NYC water supply watershed. To evaluate the effect of future climate on soil erosion and sediment yield, the model output was compared using historical (1965-2008) and future (2081-2100) climate scenarios. The predictions presented here should be viewed as qualitative trends, rather than as absolute numerical predictions, given the uncertainty in future climate predictions, particularly since potential changes in extreme events are not completely captured by GCMs and the downscaling method used in this study. Results indicate a sharp increase in the annual rates of soil erosion although a similar result in sediment yield at the watershed outlet was not evident. Analysis of seasonal changes in basin wide soil erosion and sediment export from HRUs showed an increase in the winter and in the early spring and a decrease in the summer and early fall seasons. Future simulated sediment yield at the watershed outlet followed the soil erosion results for most months except for March and April. Future climate related changes in soil erosion and sediment yield were more significant in the winter due to a shift in the timing of snowmelt and also due to a decrease in the proportion of precipitation received as snow. Although an increase in future summer precipitation was predicted, soil erosion and sediment yield appeared to decrease owing to an increase in soil moisture deficit and a decrease in water yield due to increased evapotranspiration.

4.4. Regime Shift Detection in Streamflow and selected NYC Water Supply Indicators

Introduction

Analysis of abrupt shifts in both historical and current streamflow, reservoir status, and system performance is an important component of water supply system operational support and planning. An increasingly useful statistical method for evaluating abrupt shifts is regime analysis. One method of regime analysis entails applying a moving window to data and statistically analyzing changing in the windows properties as time progresses, whereby statistical discontinuities represent regime shifts. By adjusting the size of the moving window patterns of historical trends at differing time scales can be detected and potentially inform future trends. In this preliminary study a single 7-year window regime analysis is presented. For the NYC water supply the importance of regime shift analysis of regional hydrology is associated with the possibility of early shift detection and the subsequent use of the information gained in the analysis to improve operation and management of the water supply.

Complex systems including financial markets, ecosystem and climate are susceptible to a sudden shift from one regime (or state) to a contrasting dynamical regime. Examples in global finance include the occurrence of systematic market crashes, in medicine asthma attacks or epileptic seizures, in the Earth System this may include abrupt shifts in ocean circulation or climate, regime shifts in rangelands, fish or wildlife populations (Scheffer et al. 2009). Regime shift involves the notion of multiple stable states in a system and a fast reorganization (or transition) from one state to another (Rodionov, 2006; Rodionov and Overland, 2005).

There is a diversity of regime shift studies in the literature. Scheffer et al. (2009) discussed the use of catastrophe theory as a conceptual framework for understanding gradual and abrupt behavior in both, terrestrial and aquatic ecosystems. Lockwood and Lockwood (2008) applied a catastrophe theory and self-organized method to describe and explain the pattern and process of grasshopper population outbreaks in the western United States (Washington-Allen et al., 2010). Garmestani et al. (2009) evaluate evidence of discontinuous distributions within complex systems to study the occurrence of emergent properties, including resilience. They analyzed the regime shift study in the context of the panarchy theory which indicates that complex systems exhibit multiple dynamic regimes nested within larger systems, each of which operate at unique spatial scales. The authors used analysis of discontinuities to reveal panarchy and interpret patterns in ecological as well as urban and social systems to further explain how resilience is generated. Allen and Holling (2010) describe the concept of novelty within complex systems that emphasizes changes in key drivers and self-organizing interactions to maintain, establish, or re-establish resilience. They hypothesize that novelty will most likely be expressed near shifts or breaks in scale where large fluctuations in resource variability increase the success of random events to affect system reorganization. Ernstson et al. (2010) discusses the issue of urban resilience as a particular case of the resilience of human-dominated ecosystems in a world of uncertainty. He proposes a transition in city planning to account for aspects of global multidimensionality of contemporary urbanization and increasing uncertainty due to climate change, migration of people, and changes in the capacity of ecosystems to generate goods and services. The goal of the new approach as he describes is to 'enable cities to navigate change, build capacity to withstand shocks, and locate sources of experimentation and innovation in face

of uncertainty’. Rodionov and Overland (2005) applied a sequential t-test analysis of regime shift (STARS) method to detect shifts in the Bering Sea ecosystem at their earlier stage. This approach has the ability to process data in real time making it possible to early detect emerging regime shifts as new data become available.

The following section presents initial results of an ongoing study of regime shift detection on NYC water supply region and system. The study is based on various historical data analysis to learn more about long term patterns, variability and other characteristics in regional climate, hydrologic data and reservoir system indicators and how these can relate and accounted for in the NYC water supply management process. The results here presented cover both streamflows and selected reservoir system indicators.

Regime shift detection methodology

Various methods have been applied in the literature to address regime shift detection of mean, variance, frequency structure, or a system shift. Methods applied to detect a shift in mean (which is the focus of this initial study) include a sequential t-test analysis regime shift (STARS) by Rodionov (2004), Bayesian analysis (Perreaut et al., 2000), Mann-Whitney U-test (Mauget, 2003), Wilcoxon rank sum (Ducre-Robitaille et al., 2003), and a two-phase regression model (Lund and Reeves, 2002), just to refer to few examples. Some of the techniques can only detect a single change-point, others can be applied for multiple shifts and some are sensitive to the presence of trends in the data set.

The present study is based on applying the STARS methodology (Radionov, 2004) with pre-whitening (Radionov 2006). This methodology is based on a sequential algorithm and the Student’s t-test. Three parameters are required when applying this method; (i) a significance level for the t-test, (ii) a cut-off length for the regime, and (iii) the Huber’s weight which sets the weight to be assigned to outliers in the variable time series.

Pre-whitening is a procedure used to eliminate serial correlation and to reduce the impact of red noise in time series. Red noise is characterized by observations remaining relatively long intervals above or below the overall variable mean value. Red noise is often modeled by the first order autoregressive (AR1) model. It occurs when the autoregressive parameter ρ is positive and must be <1 . Because red noise can be misinterpreted as climatic regime it needs to be removed from time series prior to regime shift detection. The removal of red noise using pre-whitening consists of using the first order difference

$$(X_t - \rho X_{t-1}) \tag{4.7}$$

instead of the variable X_t , where X_t is the variable at time t and X_{t-1} is the variable at a previous time step in the time series.

Results

Figures 4.9 and 4.10 show the results of regime shift detection for the mean on Schoharie Creek at Prattsville, NY streamflow (figure 4.9) and on selected reservoir indicators (figure 4.10).

For the regime shift detection analysis we applied the methodology by Radionov (2006, 2004) based on a sequential Student's t-test with pre-whitening. The level of significance for the t-test was set to 0.1, the cutoff length for the regime was set to 7 years and the Huber parameter which controls the weights assigned to outliers was set to 2. In order to estimate the parameter ρ a subsample technique associated with the Inverse Proportionality with 4 corrections (IP4) was applied. IP4 has shown to work well with relatively small (<10) subsample sizes. In this study a subsample size of 4 was selected. Estimating ρ based on sampling is preferred than using the entire time series when the data has both regime shift and red noise (Rodionov, 2006).

Streamflow records from four USGS gauges covering the period from 1929 to 2010 were analyzed for the presence of regime shift on an annual and seasonal basis. In figure 4.9, a summer period includes June, July and August (JJA), while a winter period expands through December, January to February (DJF).

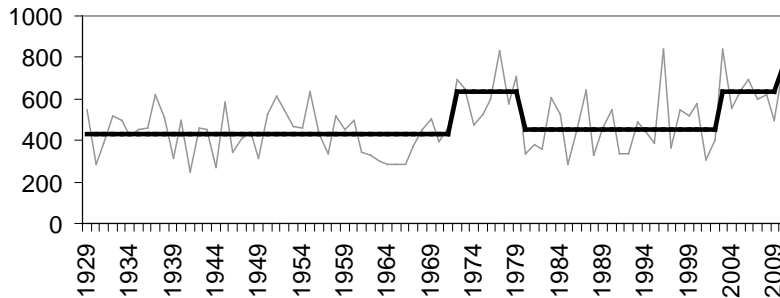
The results from figure 4.9 indicate that:

1. There are multiple regime shifts for the mean annual streamflow including increased flows during the 1970s and in recent years since 2000.
2. At a 0.1 confidence level there is a seasonal behavior in regime shift occurrence in Schoharie Creek at Prattsville streamflow. For the winter period multiple shifts are present including a shift to a drier period around early 60's followed by a wetter period in earlier 1970s and another wet period in early 2000s.
3. For the summer period only one up-shift to a wetter regime is observed during the early 2000s.

Figure 4.10 shows results of regime shift detection for three reservoir system indicators: (i) the Julian Day the reservoir storage is above 90% of its capacity (JDRSANC), (ii) the volume of spill before March 1st (VSBM1), and (iii) the number of drought days per year (NDDPY). Using a similar methodology and parameters as with the streamflow the top graph in figure 4.10a shows three dry regimes in the 1940s, 1960s and 1980s for the JDRSANC (reservoir storage reaches 90% later in the year). For the VSBM1 (figure 4.10b) one regime of high spills before March 1 is observed in the mid-1970s but the regime following the shift has returned to slightly higher spills than during the earlier starting regime. The only period with a different regime detected by the NDDPY analysis is the 1960s drought.

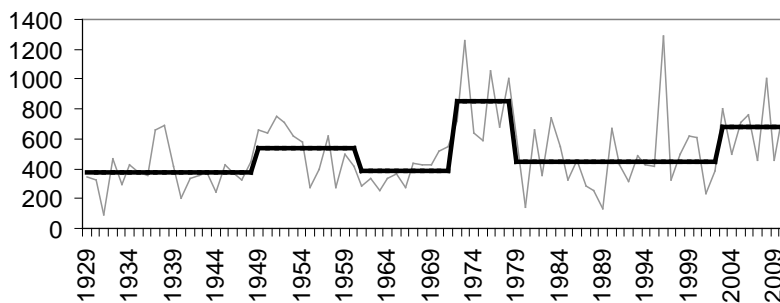
(a)

Shifts in the mean **Annual flow** USGS-1350000, 1929-2010
Probability = 0.1, cutoff length = 7, Huber parameter = 2
AR(1) = 0.00 (IPN4), subsample size = 4
Shift detection: After prewhitening, Plot: Original data



(b)

Shifts in the mean **Winter flow** USGS-1350000, 1929-2010
Probability = 0.1, cutoff length = 7, Huber parameter = 2
AR(1) = 0.00 (IPN4), subsample size = 4
Shift detection: After prewhitening, Plot: Original data



(c)

Shifts in the mean **Summer flow** USGS-1350000, 1929-2010
Probability = 0.1, cutoff length = 7, Huber parameter = 2
AR(1) = 0.00 (IPN4), subsample size = 4
Shift detection: After prewhitening, Plot: Original data

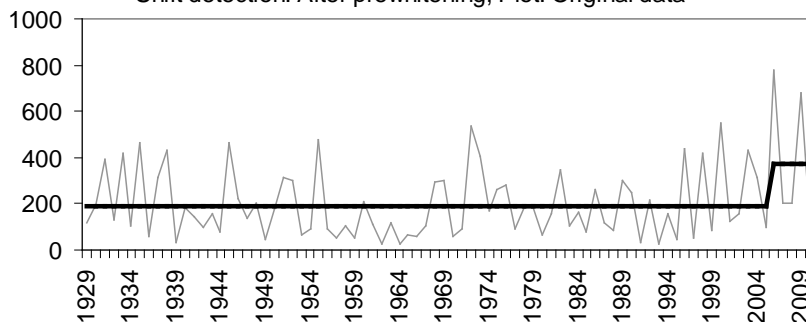
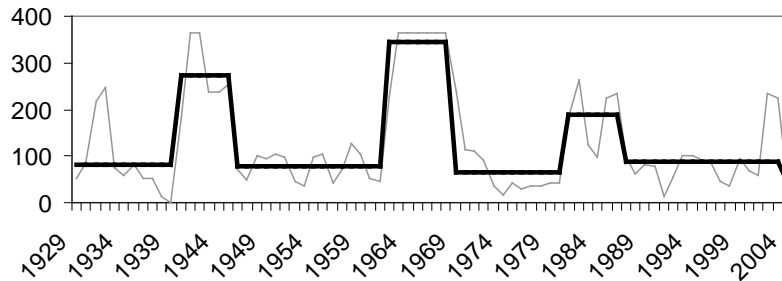


Figure 4.9. Regime shift detection for Schoharie Creek at Prattsville, NY (USGS gauge 1350000). From top down the figures show the (a) mean annual, (b) winter (December, January, February) and (c) summer (June, July, August) flows.

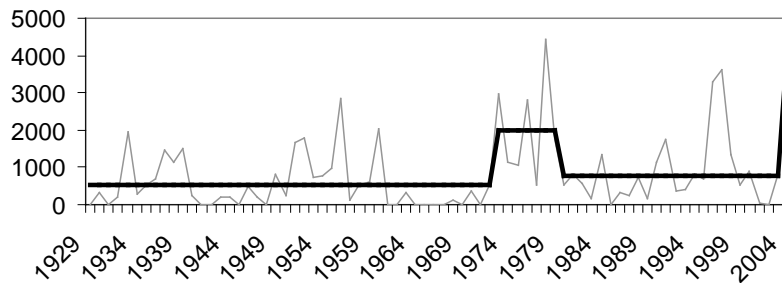
(a)

Shifts in the mean **JDay Sto > 90% Capacity**, 1929-2004
Probability = 0.1, cutoff length = 7, Huber parameter = 2
AR(1) = 0.49 (IPN4), subsample size = 4
Shift detection: After prewhitening, Plot: Original data



(b)

Shifts in the mean for **Vol Spill before Mar 1st**, 1929-2004
Probability = 0.1, cutoff length = 7, Huber parameter = 2
AR(1) = 0.00 (IPN4), subsample size = 4
Shift detection: After prewhitening, Plot: Original data



(c)

Shifts in the mean for **Number of Drought Days**, 1929-2004
Probability = 0.1, cutoff length = 7, Huber parameter = 2
AR(1) = 0.49 (IPN4), subsample size = 4
Shift detection: After prewhitening, Plot: Original data

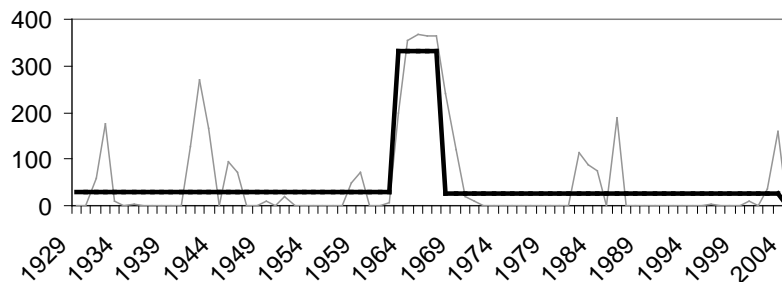


Figure 4.10. Regime shift detection for (a) the Julian Day the reservoir storage is above 90% of its capacity (JDRSANC), (b) the volume of spill before March 1st (VSBM1), and (c) the number of drought days per year (NDDPY).

During the most recent years in the early 2000s results in reservoir system indicators indicate emerging shifts i.e. the right end of the regime line either points upwards or downwards. This is consistent with increased flow regime in regional streamflow as indicated in figure 4.9, following the early 2000s. Since streamflow time series end in 2010 and for reservoir indicators in 2004 more years of analysis are necessary to see how the emerging shifts will sustain. Reservoirs filling later and increased number of drought days in figure 4.10 are consistent with the historical drought in the mid-1960s.

Conclusions

A regime shift detection methodology with sequential analysis and pre-whitening by Rodionov (2006) was applied to the annual and seasonal Schoharie Creek at Prattsville streamflow and for three New York City reservoir system indicators. Based on data from 1929 to 2010, historical streamflow in the region exhibit multiple regime shifts with more shifts occurring during winter (DJF) than during summer (JJA). This is not new; Matonse et al. (2011) have found that regional changes in climate are most likely to have a greater effect on winter hydrology rather than summer hydrology in the study region. Also, regime shift detection for selected reservoir indicators shows at least one regime change and an emerging shift (in the early 2000s) during the analysis period. The results are consistent with the mid 1960s drought period and higher streamflow in the early 2000s. These results are part of an ongoing study that will help to better understand the relationship between regional climate and water supply. Of importance is the potential of using regime adjusted rules and forecast to improve water supply management and reservoir system reliability. However, for such an adjustment option to be possible further investigation is needed that addresses the issue of earlier regime shift detection and the relationship between trends, regime shift and climate change.

4.5. Streamflow responses and ecological implication of climate change

Introduction

Streamflow and its components represent a good proxy of the combined impact of climate change because of the spatially integrated hydrologic response that they provide. Small perturbations in precipitation frequency and/or quantity can impact mean annual streamflow (Risbey and Entekhabi, 1996). An examination of historical data and results of model simulations in the northeastern US have shown an increasing trend in precipitation and streamflow during the last fifty years (Burns et al., 2007; Zion et al., 2011). Changes in precipitation levels and even temporal shifts in the water balance are expected to bring changes in hydrologic regimes, which will affect stream habitat, ecosystem diversity, and water resource management (Gibson et al., 2005; Pradhanang et al., 2011) and is deemed important for New York City water supply watersheds. The characteristics related to amount and variability of discharge are considered to be the most fundamental variables defining the stream ecosystem (Bunn and Arthington, 2002; Poff and Ward, 1990) and the alteration of flow regimes is identified as a potentially serious threat to the ecological sustainability of rivers (Richter et al., 1996). Ecologists have consistently identified flow magnitude, duration, frequency, timing, and rate of change (Poff and Ward, 1990; Poff et al., 1997) as the most influential responses to consider in ecological studies. The goals of this study are:

1. To examine how changes in precipitation and air temperature translate into changes in streamflow responses in the Cannonsville Reservoir Watershed (CRW) using a physically based semi-distributed SWAT-WB model (Easton et al., 2010b; White et al., 2011).
2. To analyze baseline and future streamflow scenarios using the Indicators of Hydrologic Alterations (IHA) tool (Richter et al., 1996) to gain an overall indication of the extent of hydrological change from reference conditions.

The potential effect of climate change on streamflow was assessed using scenarios derived from a suite of nine Global Climate Model (GCMs) that represent a range of future (2081-2100) climate conditions (Table 4.2) for A1B scenario (representing rapid economic growth with balanced emphasis on all energy sources) (IPCC, 2007b). Climate scenarios were downscaled using change factor methodology described in (Anandhi et al., 2011).

Table 4.2. Global Climate Models (GCMs) used in this study

<i>GCM ID*</i>	<i>Acronym used</i>
CGCM3.1(T47)	CC4
CGCM3.1 (T63)	CC6
CSIRO-MK 3.0	CS0
GISS-AOM	GAO
GFDL-CM 2.0	GF0
IPSL-CM4	IPS
MIROC3.2 (HIRES)	MIH
ECHAM5/MPI-OM	MPI
MRI-CGCM 2.3.2	MRI

Methods

Hydrologic Assessment

The general approach for hydrologic assessment consisted of defining a series of 33 hydrologic attributes that characterize intra-annual variability in streamflow conditions and then analyzing these variations as a foundation to compare baseline streamflow versus the impact of climate change on streamflow. The hydrologic attributes are based upon five characteristics of hydrologic regimes, known as Indicators of Hydrologic Alterations (IHA). Details on IHA tool can be obtained from IHA Manual (Richter et al., 1996). A summary of the parameters, and their characteristics, used in the IHA is provided in table 4.3. The IHA analysis statistically characterizes inter-annual variation in flow regimes and, because the methodology uses median daily streamflow rates, it is suitable for detecting the hydrological characteristics relevant to sustaining aquatic ecosystems. Eighteen of the 33 IHA parameters (Groups 2, 3 and 4 in table 4.3) focus on the magnitude, duration, timing and frequency of extreme events, whereas the other fifteen parameters (Groups 1 and 5 in table 4.3) are measures of the median of the magnitude of flows or the rate of change of water conditions. The steps used in hydrologic assessment are as follows:

1. The streamflow time series for baseline simulation (1964-2008) and nine climate change scenarios were defined. During the data set up, baseline simulation is treated as pre-impact scenario and each climate change scenario as post-impact scenarios.
2. The values for ecologically relevant 33 parameters (table 4.3) for each year in each time series were calculated.
3. Inter-annual statistics such as measures of central tendency and dispersion were calculated for each time series for 33 parameters.
4. The median and coefficient of variations for each parameter was then compared between simulated streamflow and streamflow as a result of climate change

Changes in daily streamflow metrics were analyzed to identify changes in dynamics of streamflow in the CRW between the baseline simulation period and the various climate change scenarios (table 4.2). When examining the hydrologic effects of climate change scenarios, the change in the hydrologic responses were calculated relative to the results from the calibrated baseline simulation, rather than the historic observations.

Table 4.3. Indicators of Hydrologic Assessment (Richter et al., 1996)

IHA group	Hydrologic parameters	Ecosystem Influences
Magnitude of monthly water conditions	Median value for each calendar year (12 parameters)	<ol style="list-style-type: none"> 1. Availability of habitat for aquatic organisms 2. Availability of soil moisture for plants 3. Availability of water 4. Reliability of water supplies for wildlife 5. Effects of water temperature and dissolved oxygen
Magnitude and duration of annual extreme water conditions (median daily flow)	<ol style="list-style-type: none"> 1. Annual 1-day minima 2. Annual 3-day minima 3. Annual 7-day minima 4. Annual 30-day minima 5. Annual 90-day minima 6. Annual 1-day maxima 7. Annual 1-day maxima 8. Annual 1-day maxima 9. Annual 1-day maxima 10. Annual 1-day maxima 11. Number of zero flow days 12. 7-day minima/median for year 	<ol style="list-style-type: none"> 1. Balance of competitive and stress tolerant organisms 2. Creation of sites for plant colonization 3. Structure of river channel morphology and physical habitat conditions 4. Soil moisture stress in plants 5. Dehydration of wildlife 6. Duration of stressful conditions 7. Distribution of plant communities
Timing of annual extreme of high and low pulses	<ol style="list-style-type: none"> 1. Julian date of each annual 1-day maxima 2. Julian date of each annual 1-day minima 	<ol style="list-style-type: none"> 1. Predictability and avoidability of stress for organisms 2. Spawning cues for migratory fish
Frequency and duration of high and low pulses	<ol style="list-style-type: none"> 1. Number of low pulses within each year 2. Median duration of low pulses each year 3. Number of high pulses within each year 4. Median duration of high pulses each year 	<ol style="list-style-type: none"> 1. Frequency and magnitude of soil moisture stress for plants 2. Availability of floodplain habitat for aquatic organisms 3. Effects of bedload transport and channel sediment distribution, and duration of substrate disturbance
Rate and frequency of water condition changes	<ol style="list-style-type: none"> 1. Medians of all positive difference between consecutive daily values 2. Medians of all negative difference between consecutive daily values 3. Number of hydrologic reversals 	<ol style="list-style-type: none"> 1. Drought stress on plants 2. Desiccation stress on low-mobility stream-edge organisms

Results and Discussions

Hydrologic Assessment of Indicators

We used median as an estimate of central tendency and the variance as an estimate of dispersion. For each 33 hydrologic parameters the differences between the baseline and climate change ensemble scenario is expressed as both a magnitude of difference and a deviation percentage (table 4.4).

Magnitude of the monthly median of daily flows

The hydrologic assessment showed increase in median monthly streamflow for winter months (figure 4.11). The highest increase in median daily flow was observed for during January (379%) month. Such large increase in winter flow can affect not only habitat suitable for winter flora and fauna, but can increase stream bank erosion and mass flux of pollutants due to high flow. The streamflow decreased from April through September. The reduced flow during April and summer months can have adverse impacts on fish habitats and spawning. A study specific to the Catskill Mountain region of NYS (Burns et al., 2007) reported that there was notable shift in peak snowmelt from early April at the beginning of the historic record to late March by the end of the record and an increase in runoff from June to October. Annual mean streamflow increased for all the climate change scenarios. (Gan, 1998), in a study of the Canadian Prairies, found that over the last 40-50 years many stream and river gauging stations observed an increase in streamflow during March, attributed to earlier snowmelt, followed by reduced flow in May and June.

Magnitude and duration of extreme annual conditions

The percent change values are less for the annual maximum daily streamflow compared to the annual minimum and median daily streamflow for non-winter months similar to the observations made by McCabe and Wolock (2002) for the conterminous United States. Our study indicates that streamflow will become much more extreme with increases in both consecutive 7-day low flow (124% increase from baseline) (figure 4.12a) and in 7-day high flow (3.5% increase from baseline) (figure 4.12b) under different climate scenarios. The magnitude of increase however is higher for annual daily minimum flow. A study in Monroe County, NY (Coon, 2005) assessing trends from 1965 to 2005 noted an increase in temperature, precipitation, and 7-day low-flows in rural streams, consistent with trends observed elsewhere in the U.S. Because the amount of water available in a river system defines the suitability of a habitat to aquatic organisms, flow alteration, especially at low flows, create unfavorable conditions for native species (Poff et al., 1997). Lower summer flows can lead to increase in water temperatures and reduced dissolved oxygen. Lower flows also indicate a reduced wetted perimeter, which would decrease habitat availability and impact lateral exchanges between the riparian zone and the stream.

Table 4.4. Results of indicators of hydrologic alteration analysis for stream at Walton, NY

	Medians			Dispersion		
	Streamflow ^a (m ³ /s)			Baseline Condition (1964- 2008)	Ensemble scenario (2081- 2100)	Deviation/ Magnitude%
	Baseline Condition (1964-2008)	Ensemble scenario (2081- 2100)	Deviation ^b / Magnitude%			
<i>Parameter Group #1: Monthly magnitude</i>						
January	4.07	19.50	15.40/379.0	2.10	1.02	-1.08/ -51.4
February	4.99	22.20	17.20/ 344.0	2.44	0.81	-1.63/ -66.9
March	25.5	31.60	6.10/ 23.9	0.98	0.47	-0.51/ -52.0
April	40.80	24.70	-16.10/ -39.5	0.40	0.52	0.12/ 29.2
May	19.90	12.90	-7.03/ -35.3	0.47	0.67	0.20/ 41.5
June	9.69	8.06	-1.63/ -16.8	0.81	1.01	0.20/ 24.6
July	7.00	6.58	-0.42/ -6.0	0.84	0.83	-0.01/ -1.20
August	4.71	4.44	-0.27/ -5.8	0.68	0.65	-0.03/ -5.00
September	4.61	4.11	-0.50/ -10.9	0.88	0.91	0.02/ 2.80
October	7.12	7.59	0.47/ 6.6	1.63	1.74	0.11/ 6.80
November	12.5	20.20	7.68/ 61.2	0.99	0.98	-0.02/ -1.50
December	8.73	19.20	10.50/ 120.0	0.82	0.82	0.00/ -0.20
Group averages			68.4%			-6.11%
<i>Parameter Group #2: Magnitude and duration of annual extremes</i>						
1-day minimum	0.21	0.50	0.29/ 140.0	2.81	1.38	-1.43/ -50.8
3-day minimum	0.27	0.65	0.38/ 144.0	2.55	1.27	-1.28/ -50.4
7-day minimum	0.47	1.04	0.58/ 124.0	2.16	0.89	-1.27/ -58.9
30-day minimum	2.44	2.73	0.29/ 12.0	0.95	0.70	-0.24/ -25.5
90-day minimum	5.20	5.11	-0.09/ -1.8	0.46	0.49	0.03/ 6.0
1-day maximum	130.00	137.40	7.40/ 5.7	0.59	0.57	-0.10/ -2.30
3-day maximum	98.30	105.00	6.57/ 6.7	0.54	0.49	-0.05/ -9.30
7-day maximum	80.20	82.40	2.17/ 2.7	0.54	0.39	-0.15/ -28.0
30-day maximum	51.70	53.50	1.80/ 3.5	0.49	0.37	-0.12/ -24.0
90-day maximum	36.50	35.30	-1.14/ -3.1	0.30	0.35	0.50/ 17.0
Base flow index	0.02	0.07	0.05/ 222.0	2.41	0.80	-1.61/ -66.7
Group averages			54.6%			-24.4%
<i>Parameter Group #3: Timing of annual extremes</i>						
Date of minimum	50.00	253.50	202.50/397.0	0.14	0.11	-0.03/ -23.6
Date of maximum	84.00	79.80	-4.22/ -5.0	0.14	0.19	0.04/ 29.2
Group averages			196%			2.80%
<i>Parameter Group #4: Frequency and duration of high and low pulses</i>						
Low pulse count	11.00	9.11	-1.89/ -17.2	0.55	0.56	0.02/ 3.30
Low pulse	5.00	4.67	-0.33/ -6.7	0.60	0.68	0.08/ 13.9
High pulse count	12.00	14.20	2.22/ 18.5	0.42	0.44	0.027/ 5.1
High pulse	4.00	3.94	-0.66/ -1.4	0.50	0.58	0.08/ 16.9
Group averages			-1.70%			9.80%
<i>Parameter Group #5: Rate and frequency of change in conditions</i>						
Rise rate	2.16	2.33	0.17/ 8.1	0.61	0.42	-0.19/ -31.5
Fall rate	-1.12	-1.37	-0.25/ 22.5	-0.28	-0.35	-0.07/ 24.3
Number of	116.00	126.20	10.22/ 8.8	0.15	0.11	-0.04/ -24.5
Group averages			13.1%			10.6%

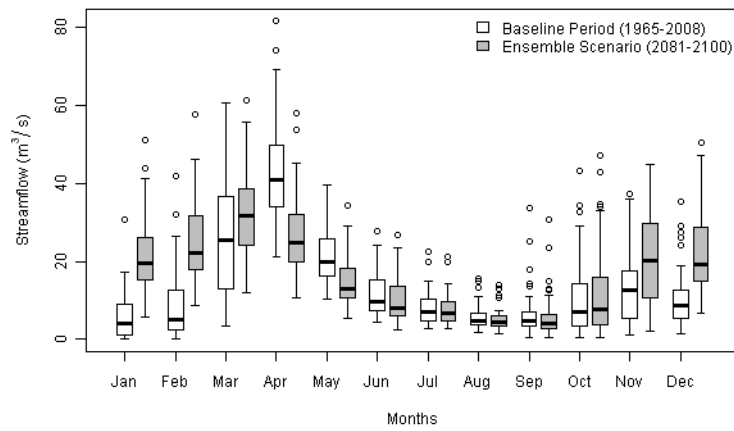


Figure 4.11. Boxplot of median daily streamflow by month. White boxes show baseline, grey boxes show climate change ensemble.

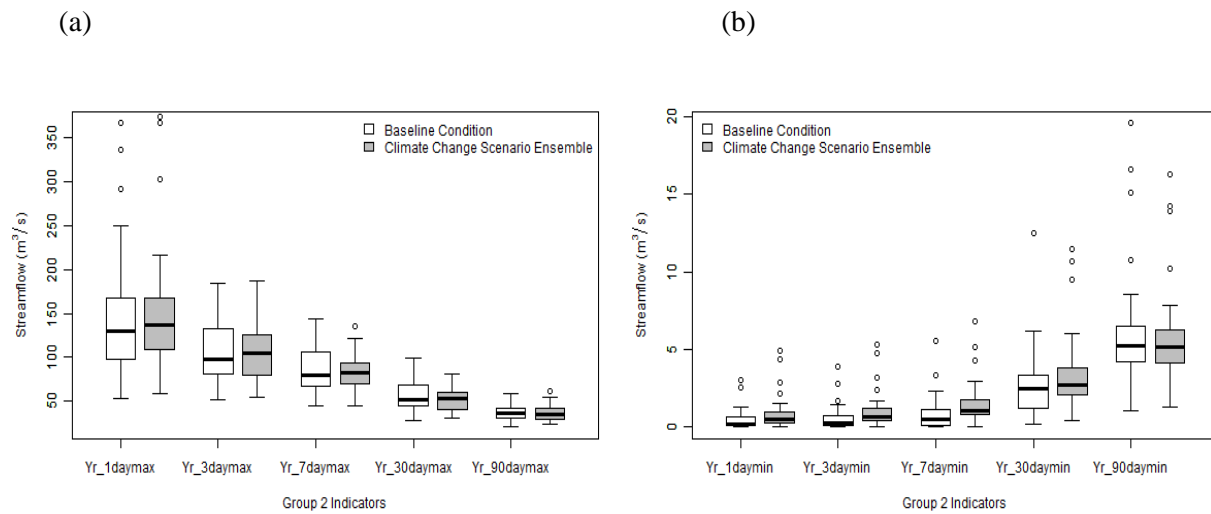


Figure 4.12. Boxplots of magnitude and duration of extreme annual conditions: (a) annual 1, 3, 7, 30 and 90 day minimum streamflow and (b) annual 1, 3, 7, 30 and 90 day maximum streamflow. White boxes show baseline, grey boxes show climate change ensemble.

Timing of the annual extreme conditions

The timing of the maximum 1-day flow shifted back from March 25 to March 19 (by approximately 6-days), while there was a forward shift in the timing of minimum flow as it shifted from early February to late October (figure 4.13a). This degree of shift would likely adversely affect the fall spawners such as brook trout due to reduced habitat availability resulting from extended low flow conditions. A shift in the timing of peak flow can alter the retention time of organic matter (Mulholland et al., 1997), disrupt the recruitment of riparian species that rely on appropriately-timed high flows to disperse seeds on the flood plain (Auble et al., 1994; Rood et al., 1995), and impact the survival of certain fish species whose larval emergence is timed to avoid high spring flows (Hauer et al., 1997).

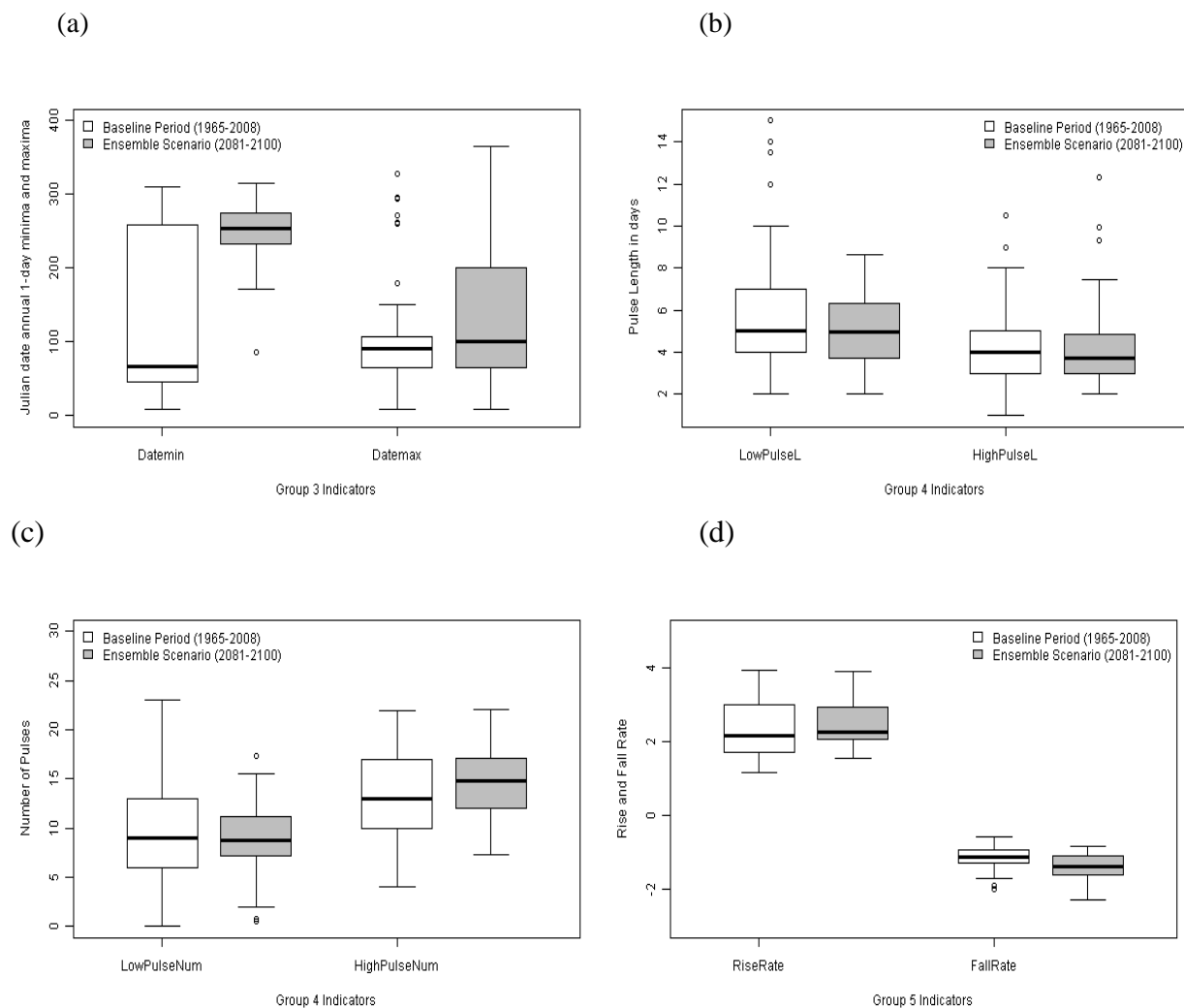


Figure 4.13. Boxplots of (a) Julian day annual 1-day minima and maxima showing timing of the annual extreme conditions; (b) Length of pulses in days showing rate and frequency of change in conditions; (c) number of flow pulses within each year; and (d) rate of hydrograph fall and rise for each year. White boxes show baseline, grey boxes show climate change ensemble.

Frequency, Rate and frequency of change in conditions

The pulsing behavior of the stream at the USGS gauge in Walton NY shows a reduced (17.2%) number of low pulse events but increase of 18.5% in high pulse events compared to the baseline scenario (figure 4.13b,c,d). Changes in flow pulses will lead to changes in channel geometry depending on the channel substrate. Increase in high flow pulses also lead to shift towards weedy invertebrate species and loss of species with poor re-colonization ability. Our results showed an increase in both rise and fall rate of the hydrograph (e.g., steeper rising and receding limbs) resulting in increase in number of reversals.

Table 4.4 shows the temporal variability in streamflow for baseline and climate change scenarios. The variability has been reduced for the summer monthly median flows, the 90-day minimum and maximum flow, the timing of annual highs, the frequency and duration of low pulses, and the duration of high pulses. Temporal variance increased for April through June and during fall months, specifically the 90-days minimum and maximum, timing of annual extremes and hydrograph rise rate. These results of IHA analysis for Walton, NY reflect the effect that climate change may have on stream flow conditions. This higher variability in rise and fall rate of hydrograph may affect aquatic invertebrates inhabiting the littoral zone along the river's edge (Richter et al., 1996; Richter et al., 2003).

Conclusions

This study used SWAT-WB model to simulate streamflow and evaluate effects of climate change on streamflow, and flow regime, including metrics calculated using the IHA tool. These indicators are important for understanding how river flow dynamics will impact the health of the aquatic environment as well as water supply and other infrastructure. The indicator analysis showed that watershed water yield is expected to increase at an annual scale. Winter and spring streamflow will increase but summers will be drier in future. Lower flows indicate a reduced wetted perimeter, which would decrease habitat availability and impact lateral exchanges between the riparian zone and the stream. The magnitude and duration of annual extremes are also expected to increase due to climate change. Baseflow index increase, i.e., decrease in baseflow may result due to the change in projected climate effecting soil moisture and soil water storage. The timing of annual extremes will be shifted for maximum flow by approximately 6 days backward and minimum flow from early winter to late October. Such shifts can affect impact the survival of certain fish species whose larval emergence is timed to avoid high spring flows. Both the rise and fall rates of the hydrograph will increase indicating the increase in flashiness. Changes in land surface hydrology due to changing climate, such as changes in the discharge of large rivers, have potentially far reaching implications both for human populations and for regional-scale physical and ecological processes.

4.6. Impact of Climate Change on the Thermal Structure of Cannonsville and Pepacton Reservoirs

An investigation has been initiated to study the potential impact of climate change on the thermal structure and mixing regimes of the Cannonsville and Pepacton Reservoirs, which are part of the Delaware system of the NYC water supply. This study used climate scenarios representative of current conditions (1980-2000) and two future time periods (2045-2065, 2080-2100). Future climate scenarios were derived by examining the differences between simulations of baseline and future time periods associated with three GCM models (Canadian Center for Climate Modeling and Analysis (CGCM3), European Center Hamburg Model (ECHAM) and Goddard Institute of Space Studies (GISS)) available from the World Climate Research Programme's Coupled Model Intercomparison Project phase 3 (CMIP3) dataset. Based on these differences, single monthly change factors were developed (DEP, 2009) and applied to local records of meteorological data to produce future scenarios of air temperature, precipitation, humidity, solar radiation and wind speed. These data are used to drive the Generalised Watershed Loading Functions-Variable Source Area (GWLF-VSA) watershed model to simulate the future reservoir inflows. A one dimensional hydrothermal model is applied to simulate the vertical water temperature over historical data sets and future scenarios for each reservoir (figure 4.14). Stratification and mixing indices are derived from the simulated water temperature and the wind speed under the different climate scenarios (A1B, A2 & B1) using the lake analyzer program (Read et al. 2011) developed by GLEON network (<http://www.gleon.org/>).

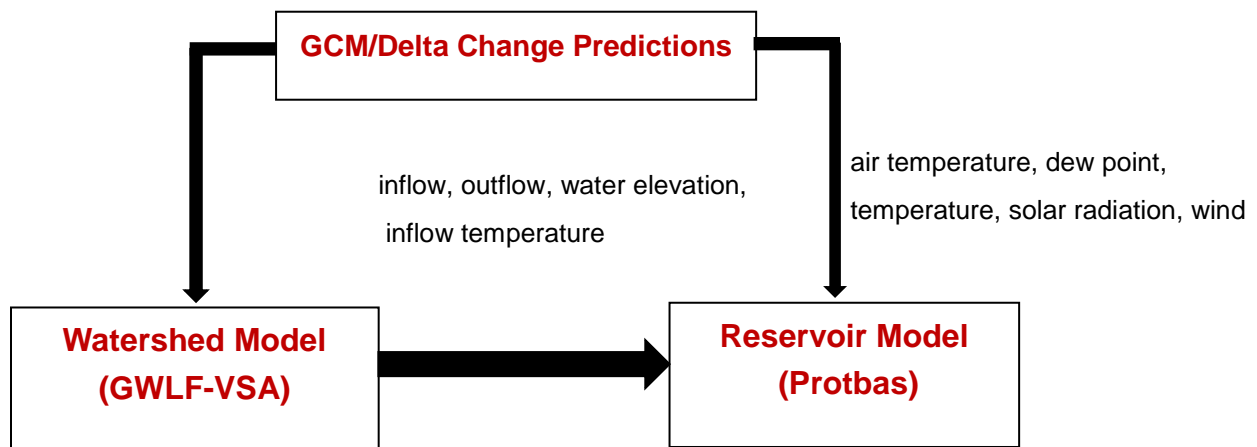


Figure 4.14. Schematic diagram of model connections and dataflow used to simulate reservoir thermal structure

Modeling Water Temperature

The water temperature of lakes and reservoirs is one of the most important factors regulating limnological processes within a system, since temperature affects the rate of biological processes, and density stratification influences the availability of nutrients and light. Other studies have used a variety of one dimensional models to explore the potential impact of climate change on lakes and reservoirs, including studies undertaken by Arvola et al. (2009), Jones et al. (2009), MacKay, et al. (2009), Borowiak et al. (2008), Markensten and Pierson (2007), Hondzo and Stefan (1991). These studies mainly involved sensitivity analyses run over long time scales.

This report examines the output of the hydrothermal sub-model of the DEP one-dimensional Protbas model. Hydrothermal output includes the vertical dynamics of reservoir thermal stratification and related transport regimes, based on changes in such critical (state) variables as meteorological, hydrological and operational conditions. Comparisons between simulations based on present day climate data (baseline conditions) and future simulations (change factor adjusted baseline conditions) are used to evaluate the development and breakdown of thermal stratification, as well as a number of metrics that describe reservoir thermal structure, stability and mixing. As a first step the hydrothermal model was verified by comparison of simulated and measured temperature profiles under current conditions (figures 4.15-4.16). These data clearly demonstrate that the hydrothermal component of the Protbas model is able to simulate vertical and temporal variations in the water temperature of both reservoirs.

Results of Simulated Water Temperature

In figures 4.17-4.18 general features of the simulated changes in thermal structure for the later time period (2080-2100) are presented in the form of temperature isopleths diagrams. These are constructed for each future scenario from a yearly matrix (day 1-365) of mean daily temperature profiles. These temperature isopleths, based on average scenario conditions, suggest that in the future the onset of stratification will begin earlier and end later resulting in a longer period of stratification, particularly under the A1B and A2 emission scenarios that predict greater increases in atmospheric CO₂. The vertical extent of stratification is deeper, and epilimnetic temperatures are also warmer during the future scenarios and again these changes are more pronounced for the A1B and A2 scenarios. Comparing all climate scenarios shows that between 32%-80% of a year undergoes stronger and deeper stratification, as defined by the temperature difference between surface and bottom ($\Delta T = T_s - T_b$) that ranged between 9 to 22 °C.

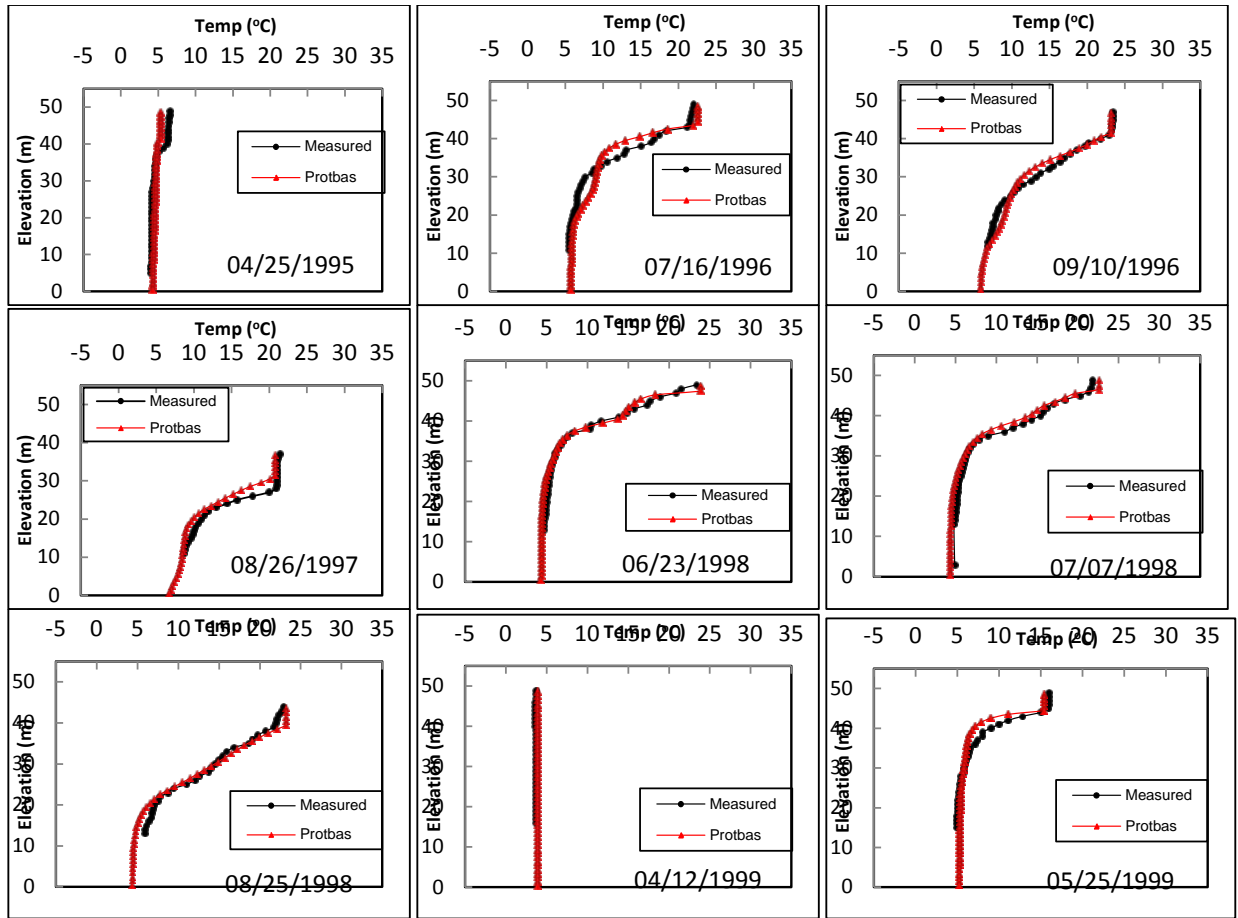


Figure 4.15. Simulated and measured temperature Profiles in Cannonsville reservoir

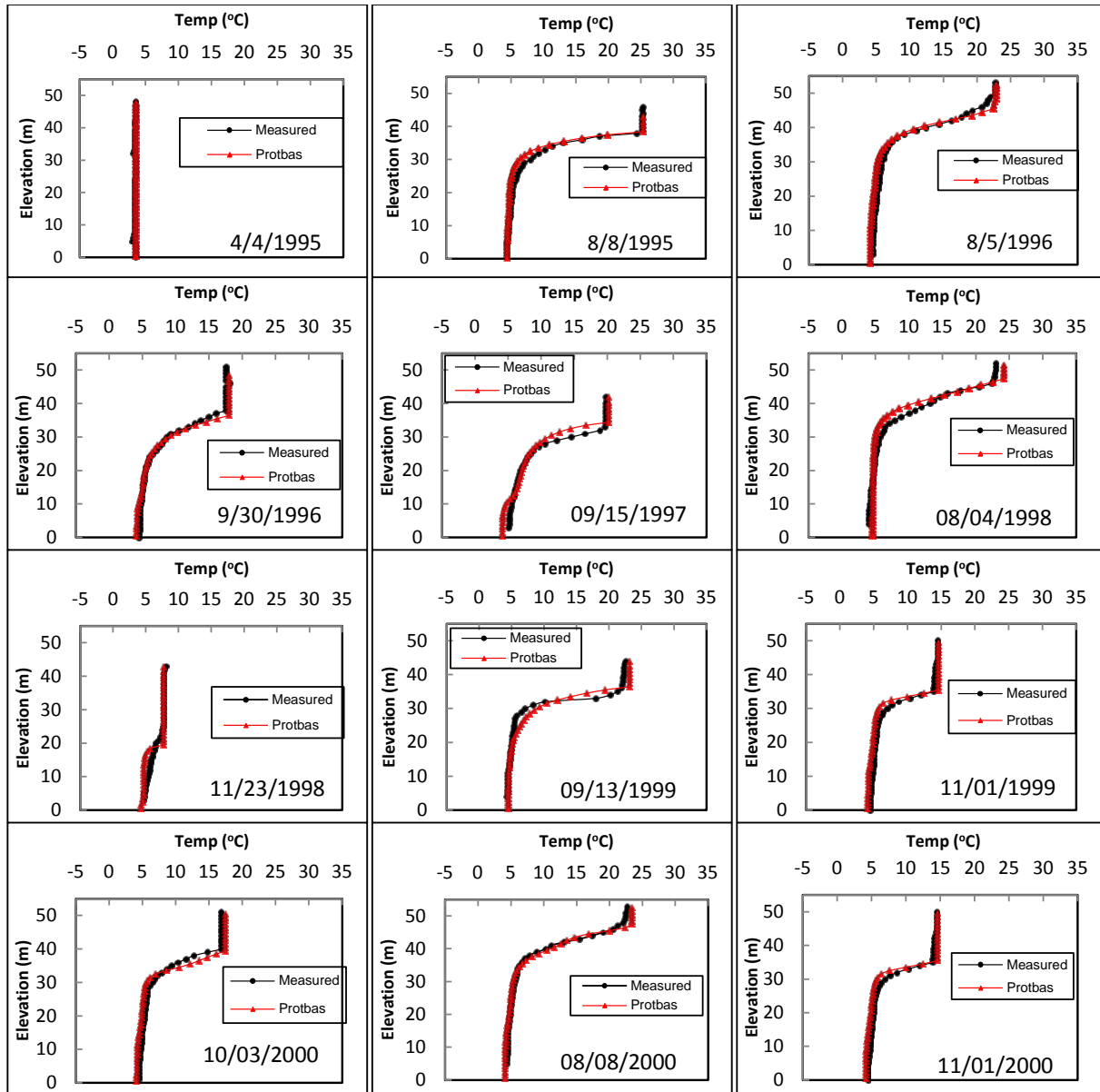


Figure 4.16. Simulated and measured temperature Profiles in Pepacton reservoir

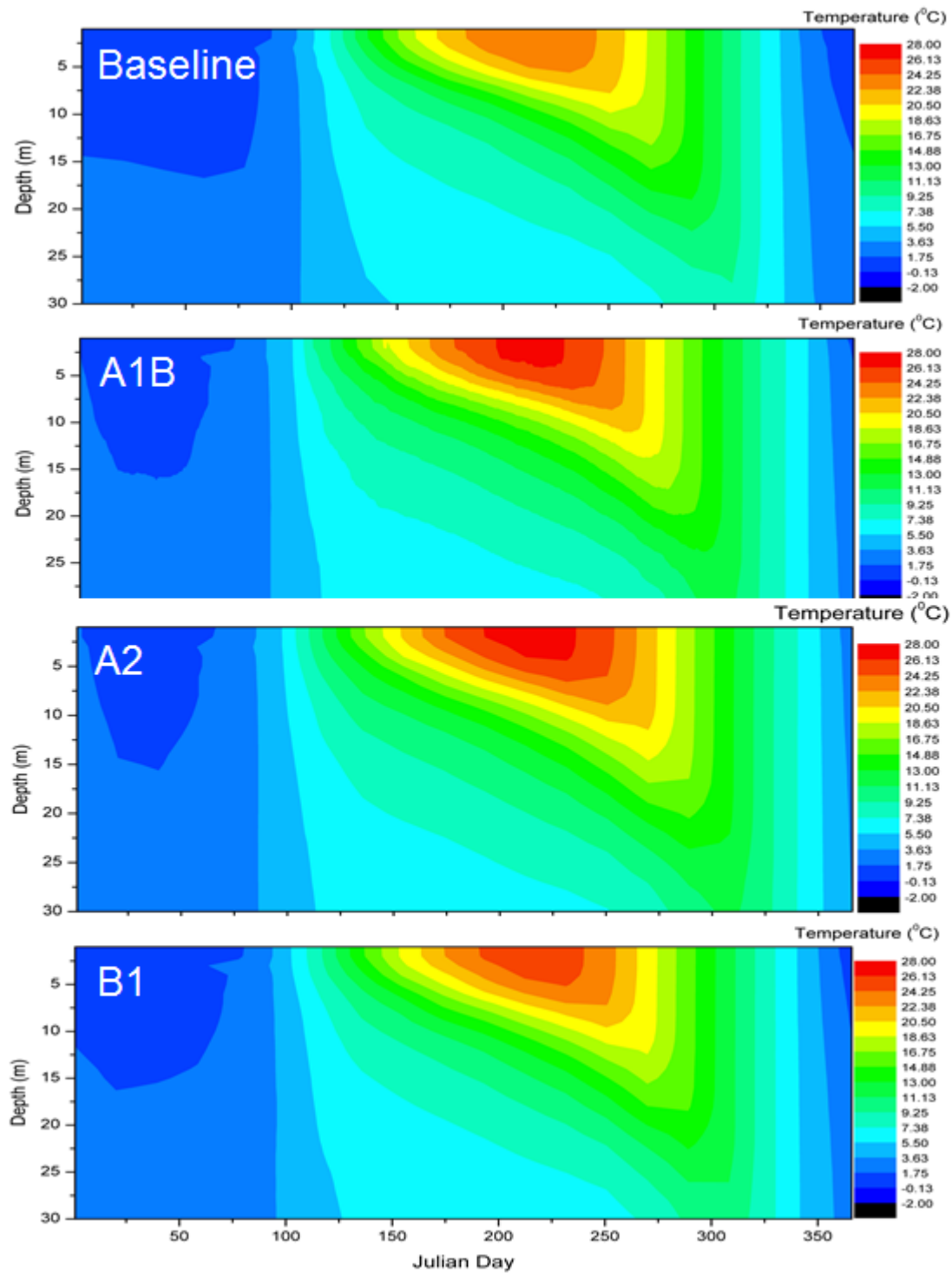


Figure 4.17. Temperature isopleth diagrams for Cannonsville reservoir under simulated baseline and future climate conditions. These represent the average conditions over the 20 year simulation periods.

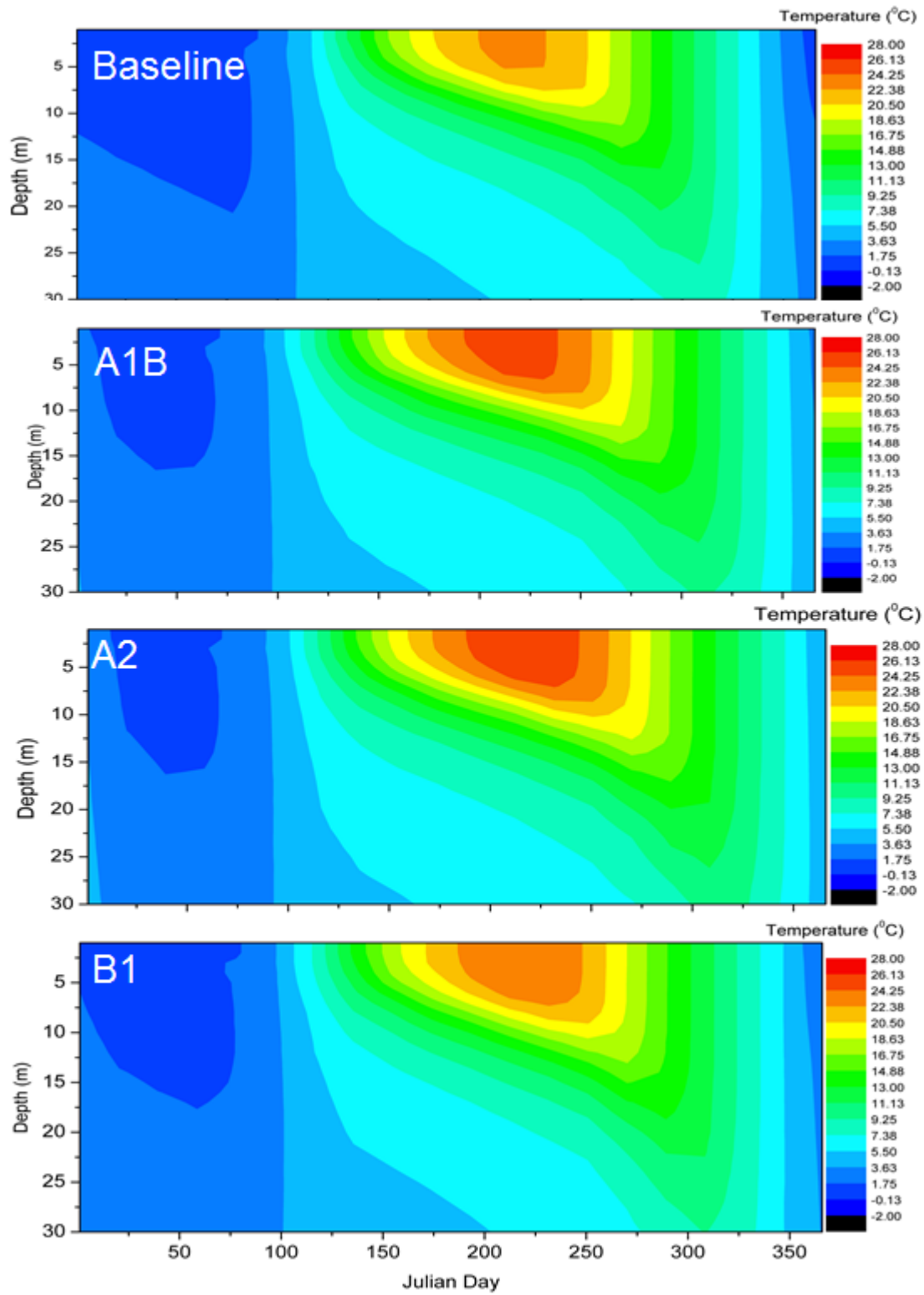
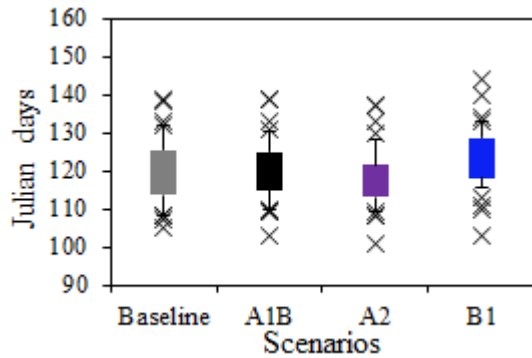
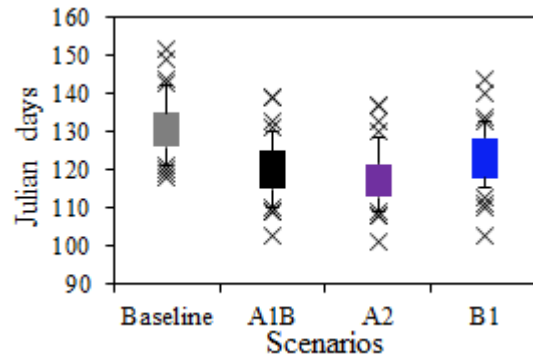


Figure 4.18. Temperature isopleth diagrams for Pepacton reservoir under simulated baseline and future climate conditions. These represent the average conditions over the 20 year simulations periods.

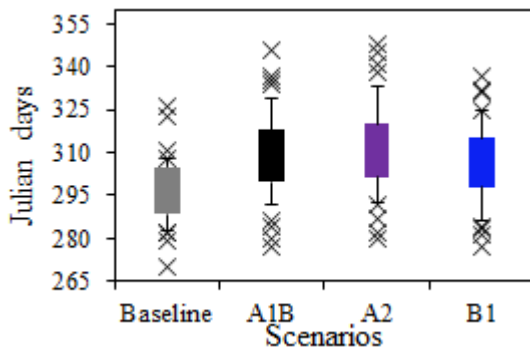
(a) Cannonsville – Onset of Stratification



(b) Pepacton – Onset of Stratification



(c) Cannonsville – Loss of Stratification



(d) Pepacton – Loss of Stratification

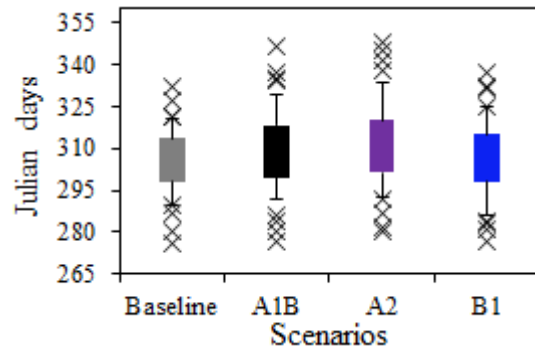
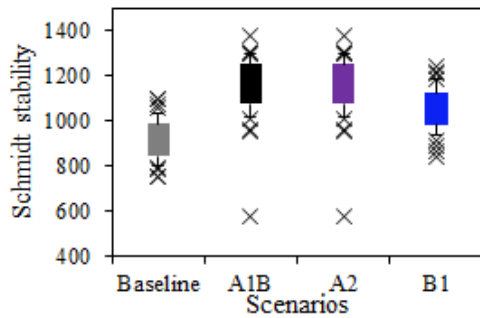
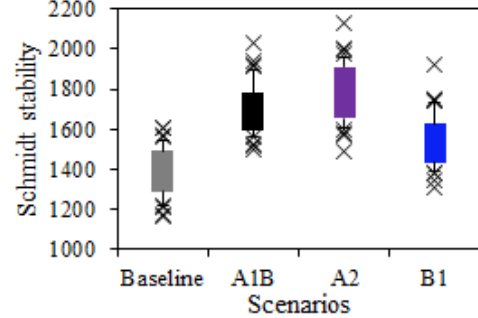


Figure 4.19. Boxplot showing range of Julian day for (a,b) onset and (c,d) loss of stratification for (a,c) Cannonsville and (b,d) Pepacton Reservoirs for Baseline and Future climate scenarios. Future scenarios represent time slice 2080-2100.

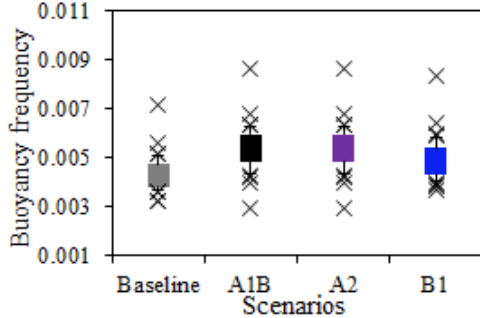
(a) Cannonsville – Schmidt stability ($J \cdot m^{-2}$)



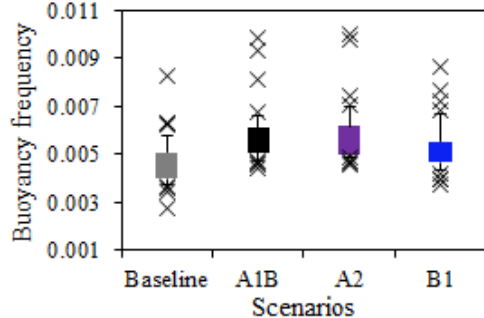
(b) Pepacton – Schmidt stability ($J \cdot m^{-2}$)



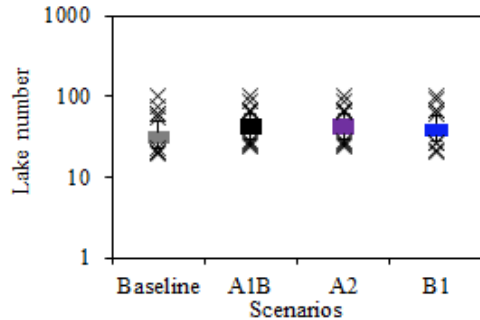
(c) Cannonsville – Buoyancy Frequency (s^{-1})



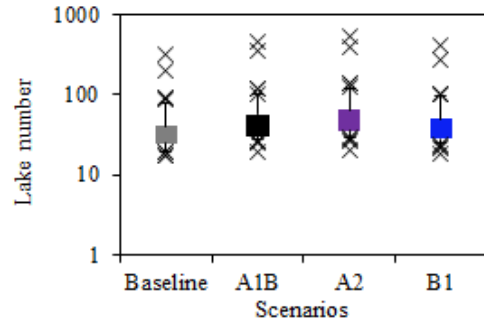
(d) Pepacton – Buoyancy Frequency (s^{-1})



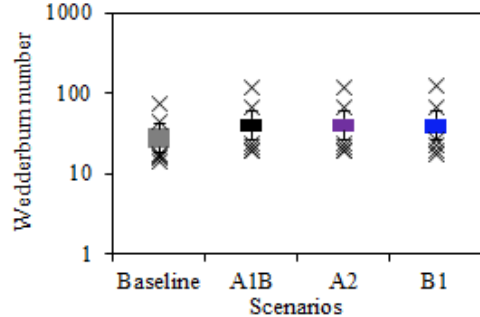
(e) Cannonsville – Lake Number



(f) Pepacton – Lake Number



(g) Cannonsville – Wedderburn Number



(h) Pepacton – Wedderburn Number

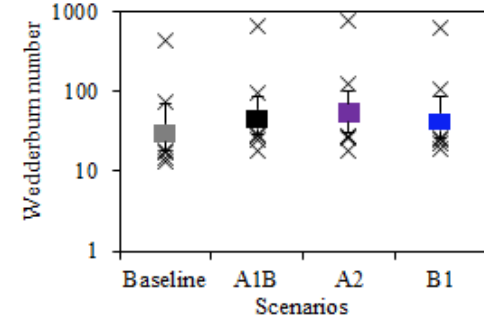


Figure 4.20. Boxplot showing range (a,b) Schmidt stability ($J \cdot m^{-2}$), (c,d) buoyancy frequency (s^{-1}), (e,f) lake number and (g,h) Wedderburn number for (a,c,e,g) Cannonsville and (b,d,f,h) Pepacton Reservoirs. Hydrologic indices were calculated using the Lake Analyzer program. Future scenarios represent time slice 2080-2100.

On average the length of stratification in Cannonsville reservoir is projected to increase by 7 days and 12 days in the case of the A1B and A2 emission scenarios. Water temperature under these different climate scenarios will increase, with the mean surface water temperature is increasing by 10.62% and 12.08% while the mean bottom water temperature is increased by 11.78% and 13.96%. There is a substantial projected increase in both surface and bottom temperatures under different future climate scenarios. For Pepacton reservoir similar results suggest that the length of stratification will increase but by a greater extent of 16 and 21 days in the case of the A1B and A2 emission scenarios. Water temperature under these different climate scenarios will increase, with the mean surface water temperature increasing by 8.07% and 9.8% and the mean bottom water temperature increasing by 5.06% and 6.5%. The statistics of the stratification characteristics in both reservoirs are displayed in figure 4.19.

Results of Reservoir Indices

The daily vertical temperature profiles output from the model and the daily wind speed over the simulation time period was further processed using the Lake Analyzer program (described and developed by Read et al. (2011) to calculate Schmidt stability, lake number and buoyancy frequency on a daily basis. The Schmidt stability (St), which is the resistance to mechanical mixing due to the potential energy in the stratification of the water column was first defined by Schmidt (1928) and later modified by Hutchinson (1957), describes the strength of density stratification. As the stability increases due to gradual warming of the surface waters, and the so called center of gravity of the system moves deeper into the water column as a result of vertical differences in density. The Lake number (Ln), defined by Imberger and Patterson (1990) is a quantitative index of the dynamical stability of the water column and shows the extent of deep turbulent mixing. A higher lake number indicates that the deep turbulent mixing is minimal. The buoyancy frequency (N^2), which represents the local stability of the water column based on the density gradient is given by $N^2 = (g/\rho) (\partial\rho/\partial z)$. The comparisons of results of different indices for both reservoirs are displayed in figure 4.20.

Table 4.5. Increases in thermal stratification and the reservoir indices between present and future (2080-2100) conditions.

Reservoir Climate scenario	Cannonsville Reservoir		Pepacton Reservoir	
	A1B	A2	A1B	A2
Length of stratification (days)	07	12	16	21
Surface temperature (%)	10.62	12.08	8.07	9.8
Bottom temperature (%)	11.78	13.96	5.06	6.5
Reservoir indices				
Schmidt stability (%)	24.5	24.5	24.29	29.4
Buoyancy frequency (%)	23.89	23.89	24.00	25.84
Thermocline depth (%)	8.2	8.2	7.3	13.02

The extent of deep turbulent mixing is reduced during A1B and A2 scenarios as compared with present climate conditions, which is in agreement with the higher Schmidt stability during these periods (Figure 4.20), since stronger stratification dominates the forces introduced by the surface wind energy. The Schmidt stability calculated over the multiple years of baseline and future scenarios was found to increase in Cannonsville by 24.5 % (A1B Scenario and A2 Scenario) whereas the buoyancy frequency showed an increase of 23.9% (A1B scenario and A2 Scenario). In the Pepacton reservoir, the Schmidt stability was found to increase by 24.3 % (A1B Scenario) and 29.4% (A2 Scenario) and buoyancy frequency showed a similar increase of 24.0% (A1B Scenario) and 25.8% (A2 Scenario) in the future scenarios. The Wedderburn number and Lake number, both of which are dimensionless indices explaining the potential for diapycnal (convective) mixing events during periods of thermal stratification, displayed a high amount of variability in Cannonsville and Pepacton reservoirs. Despite this, both indices increased in value under the future climate scenarios suggesting that the reservoirs will experience stronger and longer period of stratification with reduced likelihood of substantial diapycnal mixing during the stable stratification period. The median depth of the thermocline is projected to increase by 8.2% in both the A1B and A2 scenarios in Cannonsville Reservoir, whereas, the projected thermocline depth in Pepacton Reservoir will increase by 7.3% in case of the A1B scenario and 13.0% in case of the A2 scenario. The stable and the stronger stratification for the A1B and A2 scenarios could potentially reduce the extent vertical mixing. The projections of warmer water temperature and longer duration of stratification under future conditions, as indicated by the metrics in figure 4.19 and in Table 4.5, could potentially result in an increase in the net heat flux to the hypolimnion and reduced levels of hypolimnetic dissolved oxygen.

4.7. Vulnerability Assessment and Risk Management Tools for Climate Change: Assessing Potential Impacts and Identifying Adaptation Options

DEP Water Quality Modeling Section is a collaborator in the WRF Project 4262 – Vulnerability Assessment and Risk Management Tools for Climate Change. The goals of the project are to: a) develop a risk assessment and management framework including methods for downscaling GCM data, watershed and water system planning tools to assimilate climate information, and a decision analysis framework to identify climate risk management strategies; and b) pilot test the framework for New York City and Colorado Springs. The collaborators include researchers from Stockholm Environment Institute, Rand Corporation, Hydrologics, Hazen and Sawyer, DEP, and National Center for Atmospheric Research (NCAR).

The NYC pilot test is guided by the “XLRM” organizational framework (Lempert et al., 2003). The XLRM framework structures the analysis of future vulnerability into four main components:

1. Exogenous uncertainties (“X”) are factors deemed to be beyond human control (e.g. future climate, population, land use, and economic change),
2. Levers (“L”) are actions or strategies for reducing vulnerability (e.g. operational modifications, capital investments, water conservation programs),
3. Relationships (“R”) are cause-effect mechanisms (e.g. effect of operational changes on water quality, effect of climate change on reservoir release requirements, effect of water rates on demand, etc.) typically reflected through computer models, and
4. Measures (“M”) are performance standards used for ranking the desirability of various scenarios (e.g. percent of days under a drought condition, probability of refill by June 1, frequency of alum treatment events, etc.)

Application of the XLRM framework entails developing future scenarios that combine uncertainties (X) with alternative actions/strategies for reducing vulnerability (L); running these scenarios thru a suite of watershed and reservoir system models that embody key cause-effect relationships (R) between driving (X,L) factors and system performance; and applying system performance metrics (M) as criteria for evaluating effects of uncertain factors and effectiveness of adaptation strategies. Subsequent statistical analyses to formally evaluate adaptation strategies utilize the Robust Decision Making (RDM) decision analysis framework (Groves and Lempert, 2007).

An initial analysis was set up with the following XLRM components:

- Uncertainties (X)
 - Climate (precipitation and air temperature) under 20th century (20C3M) vs. future periods 2046-2065 and 2081-2100 as projected by 9 GCM models selected based on skill of estimating historical climate, for the A1B SRES scenario. GCM output downscaled using the 25 bin statistical delta method (see elsewhere in report). The 9 GCMs are:
 - (1) CGCM3.1(T47)
 - (2) CGCM3.1 (T63)
 - (3) CSIRO-MK 3.0
 - (4) GISS-AOM
 - (5) GFDL-CM 2.0
 - (6) IPSL-CM4
 - (7) MIROC3.2 (HIRES)
 - (8) ECHAM5/MPI-OM
 - (9) MRI-CGCM 2.3.2
 - Input turbidity levels used to trigger changes in reservoir operations. : Three variations are tested: (1) default levels presently embedded in the DEP OASIS model, (2) 10% lower than default, and (3) 10% higher than default. These are used to account for uncertainty in rating curves that translate watershed modeled streamflow into turbidity load estimates.
 - Average annual daily demand: 3 variations – 1250, 1450, and 1650 MGD.
 - Monthly demand multipliers: 3 variations – flatter, average, sharper, to account for uncertainty in seasonal variation in demand.
- Levers (L)
 - System with planned near-term improvements
- Relationships (R)
 - GWLF Hydrology Models simulate inflows to NYC Catskill, Delaware, and Croton systems. Statistical regression model used to partition Croton system inflows amongst individual East-of-Hudson reservoirs (see Section 5.5)
 - Statistical regression model estimates lower Delaware River inflows
 - Empirical sediment rating curves used to translate simulated inflows to turbidity inputs to reservoirs.
 - NYC OASIS Reservoir system model routes inflows thru system and to simulate reservoir operations.
 - Turbidity surrogates in OASIS model used to simulate operational responses to turbidity events.

- Performance Metrics (M)
 - Volume of water pumped in the system (cost metric)
 - Catskill turbidity events
 - Total number of turbidity event days and alum usage surrogate
 - NYC and upstate shortages
 - Total number of days, average shortage, and maximum year
 - NYCSS drought conditions
 - Total number of days for three drought levels
 - DEL/CAT/CRO and total system usable storage
 - Median levels, refill probability, and probability of drawdown < 50%
 - NYC Delaware Reservoir releases
 - 20th and 95th percentiles
 - Trenton flows
 - Days below 2500 cfs, 2700 cfs, and 3000 cfs levels

In addition to participating in the planning and development of the initial analysis, the DEP Water Quality Modeling Section performed the following tasks to support the project:

- downloaded, regridded, and downscaled GCM output for the 9 GCMs listed above, for 20th century and two future time slices (2046-2065 and 2081-2100), using 25 bin statistical change factor method (see Section 4.2).
- Ran downscaled GCM data thru GWLF watershed models, producing simulated inflow daily time series for each Catskill and Delaware System reservoir and for the Croton System. Croton System inflows were further partitioned to individual East of Hudson reservoirs by statistical regression analysis (see Section 5.5). These were transmitted to Hazen and Sawyer collaborators for further processing.

Initial analysis is underway and results will be forthcoming.

5. Model Development

5.1. Analysis of Turbidity Transport Dynamics in the Esopus Creek Watershed and New Developments in Turbidity Prediction

Introduction

Sediment loads can exert an important control on the use of rivers for water supply and other designated uses (Walling, 2009). High river sediment loads and the resulting sedimentation of water resources is a major water quality issue in the United States (USEPA, 2009). The economic impact of sedimentation in the United States is estimated to be billions of dollars annually (Pimentel et al., 1995). The vast majority of the suspended sediments are transported during high flow events (Wolman and Miller, 1960) and therefore it is important to quantify the sediment flux during these events. Improved capability to quantify such events may help in developing predictive models that can support management of water resources.

Differences between turbidity or suspended sediment loads estimated using discharge rating curves and loads based on actual measurements may be caused by missing explanatory variables in addition to discharge (Colby 1956; Thomas 1988; Syviski et al. 2000), which may also result in inter-event variability in the sediment rating relationship (Asselman, 1999; Lenzi and Marchi, 2000; Seeger et al., 2004; Zabaleta et al., 2007). Recent studies have considered additional predictors of suspended sediment which include antecedent soil moisture conditions and event variables such as maximum stream discharge and precipitation (Seeger et al., 2004; Zabaleta et al., 2007). Hicks et al (1996) observed spatial variability in sediment yield due to variations in rainfall and geology. The underlying assumption is that sediment yield at the watershed outlet is controlled by factors related to sediment supply rather than just transport capacity represented by stream discharge at the outlet. Therefore, inclusion of predictors of sediment supply in addition to measurements of stream discharge may improve the predictive models for event mean turbidity/suspended sediment loads.

A case study from the Catskill region of New York State is presented in this paper, using data collected from the Esopus Creek watershed that is part of the NYC drinking water supply system. The focus of this paper is on the estimation of stream water turbidity and estimates of turbidity loads entering the Ashokan reservoir. Being an optical measurement, turbidity can be measured in situ and at higher sampling frequency than are possible from manual sampling and laboratory analysis of suspended particulate matter (SPM). Automated high frequency monitoring of turbidity (T_n , NTU) can therefore be used to provide high frequency estimates of suspended sediment loads and can also be used to accurately estimate T_n loads that are an important input to predictive models (Gelda and Effler 2007) used to guide reservoir operations and minimize the impact of turbid inputs on water delivered to New York City consumers.

We hypothesize that the event mean turbidity load is determined by a combination of factors such as spatial distribution of precipitation, geologic sources of sediment, antecedent soil moisture condition of the watershed, stream power generated during the event, flow regime, and season. The purpose of this study is to identify the factors that cause variability in the discharge-

turbidity relationship in the Esopus Creek watershed and to develop improved turbidity predictions that include factors in addition to stream discharge.

Methods

Turbidity monitoring

An automated Tn monitoring system was installed on the main tributary entering the Ashokan Reservoir near the confluence of the creek and with the reservoir. Water is pumped into a riverside hut where measurements of Tn , specific conductivity and water temperature are made using a YSI water quality sonde. Water samples are also periodically collected and analyzed for Tn and TSS in the laboratory. These data are then used to correct the automated data to account for drift in the measurements. A nearby U. S. Geological Survey (USGS) gauging station provides discharge data at a daily and 15 min interval. Turbidity measurements are made at intervals between 15 min. and 1 hr. and flow-weighted to provide daily average values, comparable in frequency to the most widely available daily USGS discharge data, and are also the time step used by New York City Department of Environmental Protection (DEP) reservoir water quality models. In this study turbidity events are defined in two time scales; daily (the flow weighted mean daily turbidity for the day that accounted for the greatest proportion of the load during an event) and events (based on the entire hydrograph) whose start times were determined graphically by rise in hydrograph above baseflow and end time determined by the inflection point in the falling limb of the hydrograph similar to the method used by Stuntebeck et al. (2008). Event peak daily turbidity (EPDT) and event mean turbidity (EMT) are calculated by summing the 15 minute turbidity loads derived from measurements of discharge and turbidity collected at a 15 minute frequency (equations 5.1 and 5.2).

$$EPDT = \frac{\sum_{i=1}^{96} [(NTU_i) \times (Q_i)]}{\sum_{i=1}^{96} [(Q_i)]} \quad (5.1)$$

$$EMT = \frac{\sum_{i=1}^n [(NTU_i) \times (Q_i)]}{\sum_{i=1}^n [(Q_i)]} \quad (5.2)$$

where NTU_i is the instantaneous turbidity, Q_i is the instantaneous discharge and n is the number of 15 minute intervals during an event

Loads were calculated for 30 event days (where mean daily turbidity could be calculated) and 27 events (where event mean turbidity could be calculated) between 11/19/2003 and 04/17/2011 where both stream flow and turbidity data were available. Although many events were characterized at both time scales, some events were not captured over the entire hydrograph due

to storm related damage and fouling of turbidity sensors. Turbidity *versus* stream discharge relationships were developed using data from days when the flow diversion from Schoharie Reservoir was less than 20 % of the total Esopus Creek daily discharge. In all cases turbidity inputs to Esopus Creek from the Schoharie watershed were a very small component (<1%) of the event loads.

Analysis of turbidity events

A suite of variables used as possible predictors of event day turbidity include the number of days between events or antecedent dry days (ADD), time of the year (SEASON), mean daily flow at Coldbrook during the previous event (CB_PE), mean daily flow and turbidity at Coldbrook during the day prior to the event (CB_MIN and TURB_MIN). These predictors were used to represent the effect of soil moisture, flow regime, sediment supply and seasonal effect on stream turbidity. In the absence of rain gauges, mean daily stream discharge at the tributaries was used to represent the spatial variability of rainfall and in the contributions of water and sediment from different parts of the watershed, where differences in geologic sources of sediment, and the processes regulating stream channel erosion could occur. For each event day, the mean daily stream discharge at the tributaries ($\text{m}^3 \text{d}^{-1}$) was divided by the corresponding sub-basin area (m^2) to get the mean water yield for the day ($\text{m} \text{d}^{-1}$). Relative water yield (dimensionless) for a tributary was calculated by dividing the tributary water yield with the whole watershed water yield.

Development of Predictive Models

A step-wise regression approach was implemented on the potential predictor variables to determine the optimum combination of variables capable of predicting mean daily turbidity during the 30 identified event days. Separate multiple regression models were developed with the two classes of predictors, and a seasonal term was included in the analysis (0 for May-October and 1 for November-April). This multivariate approach has been used to analyze variations in sediment yield (Restrepo et al., 2006; Tamene et al., 2006). A similar approach was used for predicting the event mean turbidity for the 27 events. To judge the predictive power of the relationship, we compare estimated event turbidity loads with measured event loads derived from a long term (between 2003 and 2011) high frequency (15min. – 1 hr.) data set of stream turbidity and discharge. Direct estimation of the turbidity loads from these high frequency data provide a standard against which the predicted turbidity loads can be judged, and also provide data from which inferences about the processes affecting stream turbidity can be obtained.

Stream discharge- T_n rating curve

T_n loads were estimated based on a relationship between discharge and T_n derived from 415 paired observations of mean daily discharge and flow weighted mean turbidity (Equation 5.3), which allowed T_n to be estimated, and T_n loads to be calculated as the product of discharge and T_n . In the absence of automated T_n monitoring, a common approach to account for intra- and inter-storm variations in T_n (Crawford 1991, Horowitz 2003) expresses mean daily turbidity (NTU) as a function of discharge (Q).

$$\text{Log NTU} = 1.17\text{LogQ} - 0.575 \quad (R^2 = 0.66) \quad (5.3)$$

A rating curve in the form of an ordinary least square (OLS) regression (Equation 5.3 and Figure 5.1) on log-transformed mean daily stream discharge (Q , $\text{m}^3 \text{s}^{-1}$) and log-transformed flow-weighted mean daily turbidity (NTU) was used. A bias correction factor (β) (Ferguson, 1986) estimated based on the variance in the regression equation in the form $\beta = \exp(2.65 \sigma^2)$, was multiplied by the OLS estimated turbidity value to reduce the expected under prediction in loads due to retransformation bias.

Results and Discussion

Hysteresis in discharge-turbidity relationship

Analysis of discharge-turbidity relationship using 15-min high frequency measurements of Tn and stream discharge during each of the individual storm events shows a hysteretic behavior with the rising and falling limbs of the hydrograph transporting turbidity at different rates, and also showed that the pattern of hysteresis varied between events. The most common type of hysteresis, the clockwise hysteresis was observed during most events, indicating that the rate of turbidity transport in the falling limb is lower than the rising limb due to sediment source depletion.

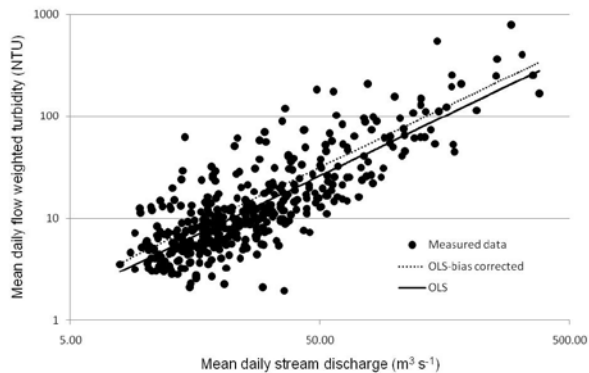


Figure 5.1. Discharge-turbidity relationship at Coldbrook outlet

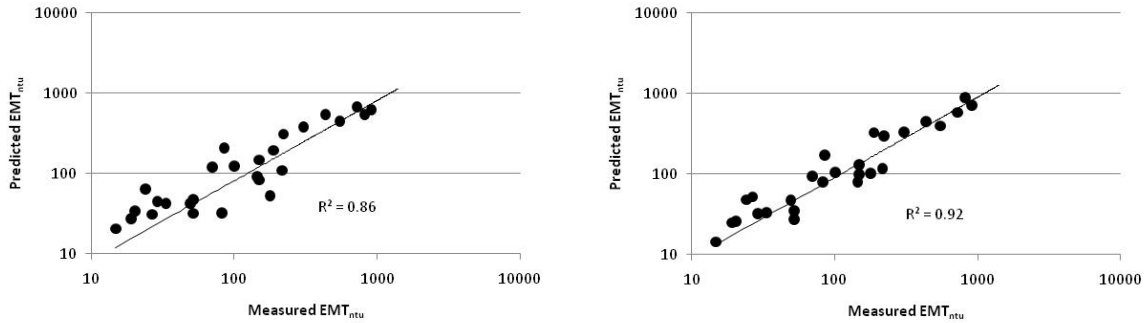


Figure 5.2. Predicted vs. measured event mean turbidity (EMT) using Eq. 6 (left) and Eq. 7 (right)

Table 5.1. Predicted vs. measured event mean turbidity loads for the 27 events and percent deviation from measured

Event #	Date	Event mean discharge	Event mean turbidity	Turbidity load				
		($m^3 s^{-1}$)	(NTU)	($NTU \cdot m^3 s^{-1}$)				
		Measured	Measured	Measured	Eq.6	Eq.6 % deviation	Eq.7	Eq.7 % deviation
1	11/19/2003	106	145	15354	9662	-37.1	8416	-45.2
2	9/17/2004	248	306	76018	94280	24.0	81888	7.7
3	11/28/2004	167	188	31369	32495	3.6	54801	74.7
4	4/22/2006	76	178	13564	3989	-70.6	7762	-42.8
5	5/12/2006	141	149	21085	20913	-0.8	18647	-11.6
6	2/4/2006	67	33	2252	2888	28.3	2258	0.3
7	6/28/2006	307	436	133668	165534	23.8	138644	3.7
8	10/19/2006	52	19	988	1418	43.6	1281	29.7
9	10/28/2006	174	85	14792	36308	145.5	30116	103.6
10	11/8/2006	86	24	2067	5491	165.7	4110	98.9
11	11/16/2006	125	70	8758	15007	71.4	11661	33.2
12	3/14/2007	57	82	4705	1853	-60.6	4561	-3.1
13	3/27/2007	72	52	3722	3407	-8.5	2507	-32.7
14	4/15/2007	220	222	48685	67907	39.5	65026	33.6
15	6/2/2007	67	49	3325	2883	-13.3	3167	-4.7
16	11/15/2007	59	20	1193	1983	66.3	1533	28.6
17	1/7/2008	43	15	643	887	38.0	623	-3.1
18	2/5/2008	57	52	2935	1804	-38.5	1541	-47.5
19	2/18/2008	69	29	2013	3081	53.1	2227	10.6
20	3/4/2008	127	101	12800	15721	22.8	13300	3.9
21	3/9/2009	56	27	1482	1724	16.3	2902	95.8
22	1/25/2010	334	912	304759	208542	-31.6	240371	-21.1
23	3/14/2010	101	149	14958	8393	-43.9	9953	-33.5
24	3/26/2010	275	549	151123	124129	-17.9	109625	-27.5
25	12/1/2010	306	819	250572	164906	-34.2	272866	8.9
26	3/11/2011	350	725	253790	236122	-7.0	204453	-19.4
27	4/17/2011	118	216	25576	13009	-49.1	13923	-45.6

Step-wise multiple regression

Use of additional variables improved the explanatory power of the stream discharge-based turbidity model. The average daily stream discharge, Q_D , ($m^3 s^{-1}$) alone as a predictor could explain only 39% of the variance in EPDT prediction for the 30 event days (Equation 5.4). A multiple regression model (Equation 5.5) that included the variables SEASON and ADD in addition to stream flow could explain 67% of the variance in turbidity prediction during event days.

$$\text{Log(EPDT)} = 1.26 \text{Log}(Q_D) - 0.694 \quad (R^2 = 0.39, P < 0.0001) \quad (5.4)$$

$$\text{Log(EPDT)} = 1.43 \text{Log}(Q_D) - 0.272 \text{SEASON} + 0.0029 \text{ADD} - 1.06 \quad (5.5) \\ (R^2 = 0.67, P < 0.0001)$$

In comparison to turbidity predictions based on stream discharge alone, multiple regression models were able to better capture the variability in stream discharge-turbidity relationship within a given range of flow. This analysis illustrates the multiple factors that may influence stream turbidity during an event, which make predictions using a single explanatory variable inaccurate. However, unlike a stream discharge based rating curve this approach for predicting event turbidity cannot be used for generating a continuous time series of turbidity values over a complete time series of event and inter-event discharges.

While the above analyses explains the importance of multiple factors that may influence daily stream turbidity, event to event variability in total event turbidity load is important in the Esopus Creek watershed, as the magnitude of turbidity loading can impact reservoir operations. We predicted the event mean turbidity (EMT) for 27 events using multiple regressions and compared the results with the measured EMT (Figure 5.2). A predictive relationship of EMT based on event mean stream discharge (Q_E , derived from 15-min data) alone led to a strong predictive relationship ($r^2 = 0.81$), but also a 10% underestimation of the cumulative measured event mean turbidity load calculated as the product of EMT and event mean stream discharge. Using the same relationship, the deviation in predicted event mean turbidity loads ranged from -71% to 166% when compared to the measured loads (Table 5.1). Inclusion of information on the time between events improved the regression equation ($r^2 = 0.89$), reducing the cumulative underestimation to 7%, and also reducing the uncertainty in predicted event mean turbidity loads to -48% to 104%. Other variables that were significant at the daily scale did not improve the regression model at the event scale.

$$\text{Log(EMT)} = 1.67 \text{Log}(Q_E) - 1.43 \quad (R^2 = 0.81, P < 0.0001) \quad (5.6)$$

$$\text{Log(EMT)} = 1.84 \text{Log}(Q_E) + 0.0051 \text{ADD} - 1.92 \quad (R^2 = 0.89, P < 0.0001) \quad (5.7)$$

Comparison of rating curve estimates with automated monitoring

The OLS regression (Equation 5.3) rating curve under-estimated the total measured turbidity loads by 30% for the study period. Use of a retransformation bias correction factor ($\beta = 1.22$) reduced the under prediction to 16%. Most of the under-prediction was due to the two data points

that had the highest turbidity values whose corresponding stream discharge values were not the highest. Without those two points the bias corrected rating curve was able to predict the actual total load with high accuracy whereas the OLS regression rating curve under-estimated the measured load by 18%. A turbidity load duration curve derived from rating curve (Equation 5.3) estimate of daily turbidity showed that as much as 80% of the total turbidity load during the 8 year study period was transported in a short period of the total time (4%) when the stream discharge was $>100 \text{ m}^3 \text{ s}^{-1}$. Therefore, accurate turbidity estimation at high stream discharges is critical as high levels of turbidity inputs lead to water quality problems. Automated turbidity monitoring clearly provides a better estimate of the turbidity inputs to the reservoir under periods of high discharge.

Conclusions

Analysis of factors responsible for the variability in stream discharge-turbidity relationship in the Esopus Creek watershed show that this relationship can be influenced by multiple factors related to turbidity supply and transport. This was illustrated by multiple regression models that showed improved predictions when using variables in addition to only stream discharge. These additional variables, to a certain extent, explain the episodic nature of erosion and its variability in space and time which makes prediction using a single explanatory variable inaccurate. In this study, the period of days between events was the only variable that improved event mean turbidity prediction. With more sampling data from future events we may be able to identify other variables to further improve EMT prediction.

5.2. Sediment Fingerprinting in the Esopus Creek Watershed- Results from a Pilot Study

As part of the Research Experience for Undergraduates (REU) program at SUNY New Paltz, DEP Water Quality Modeling Section was involved in a research project initiated by one of the interns to characterize suspended sediment sources in the Esopus Creek watershed. Potential sediment sources to the creek include glacial and non-glacial fluvial sediments which are subject to channel erosion, and upland sediments that could be mobilized due to surface erosion. In this study a fingerprinting approach was used to track sediment movement within the watershed from the various sources to the stream. The objective was to determine the relative contribution of sources to the total fine sediment load. The underlying principle is the difference in physical or chemical properties among the potential source materials that will be reflected in sediment samples collected from the watershed outlet (Mukundan, et. al. 2010).

Potential sediment sources were characterized for physical and chemical properties. Physical properties included the particle size distribution and the bulk density of each sediment source. Chemical properties included total C and stable isotopes of carbon and nitrogen ($\delta^{13}\text{C}$ and $\delta^{15}\text{N}$) in each sediment source. Stream sediment from the outlet of Esopus Creek at Coldbrook was collected along the rising limb of a storm hydrograph during an event on October 1, 2010 (figure x.1). Interestingly, this event recorded the maximum event mean turbidity (1402 NTU) based on the analysis of event by event turbidity loads between 2003 and 2011. For the preliminary analysis of sources total C and $\delta^{15}\text{N}$ were found to be the useful tracers based on their composition in sources and stream sediment. The total C values in source samples were corrected for particle size and expressed in terms of clay content. This ensured that source and stream sediments were comparable.

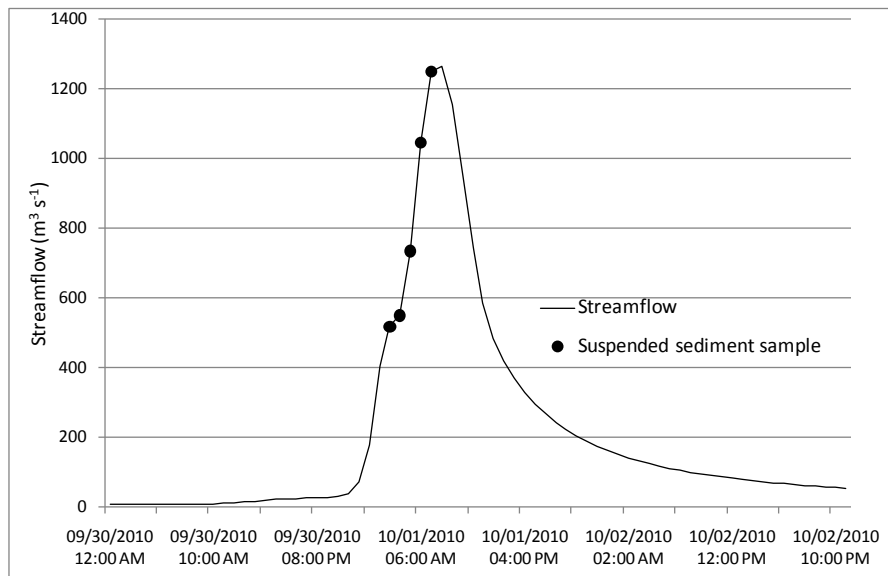


Figure 5.3. Event hydrograph and suspended sediment sampling point for the October 1, 2010 storm event (Coldbrook)

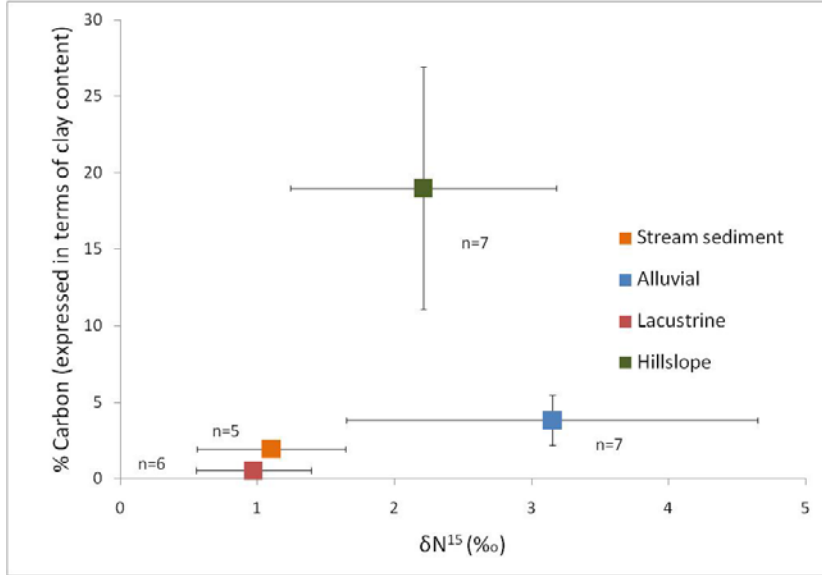


Figure 5.4. Plot of $\delta^{15}N$ vs. total C for 3-end member mixing analysis

A mixing model approach (figure x.2) was used to derive the proportion of stream sediment derived from each of the three potential sources. A set of three simple linear equations were solved as follows:

$$S_{st} = S_a + S_g + S_h \quad (5.8)$$

$$U1_{st}S_{st} = U1_aS_a + U1_gS_g + U1_hS_h \quad (5.9)$$

$$U2_{st}S_{st} = U2_aS_a + U2_gS_g + U2_hS_h \quad (5.10)$$

where, S represents sediment, and $U1$ and $U2$ are the total C and $\delta^{15}N$ values; the subscripts st , a , g , and h represents stream, alluvial, glaciolacustrine, and hillslope respectively.

Results of mixing model indicate glacial sediment from stream channels as the most dominant source contributing about 91% of the stream sediment. Hillslope erosion contributed about 7% and non-glacial channel sediment contributed only about 2% of the total stream sediment. These results are consistent with previous reports of stream channel processes contributing up to 87% of total stream sediment loads in this watershed (DEP, 2008c). Although these findings are sufficient to confirm our hypothesis, in order to derive a more comprehensive conclusion, additional event sampling (3-5) may be required. Moreover, the source samples (hillslope and channel) in the preliminary study were collected primarily from the Stony Clove tributary and used as representative of the watershed. A more rigorous turbidity source sampling from spatially distributed sites within the bigger Esopus Creek watershed combined with more event sampling of suspended sediment from the outlet should comprehend these results.

5.3. Streamflow calibration in Cannonsville Watershed: Application of SWAT-WB Introduction

DEP uses watershed models in conjunction with climate, reservoir, and water supply system models to evaluate the effects of changing conditions of climate, land use/cover, and watershed management on water supply quantity and quality; and is engaged in an ongoing effort to enhance its modeling capabilities to better simulate critical watershed processes that control watershed hydrology and the generation and transport of nutrients and sediment. The USDA Soil and Watershed Assessment Tool (SWAT) (Neitsch et al., 2005) is a widely accepted watershed hydrology and water quality model that is particularly strong in its representation of soil nutrient and plant growth processes, especially in agricultural watersheds. SWAT-WB (Easton et al. 2010a, White et al. 2011) is a version of SWAT that simulates runoff from variable source areas (VSAs) by a process of saturation excess runoff, which is considered the dominant runoff mechanism in the NYC watersheds (Lyon et al., 2004). SWAT-WB thus potentially has a reasonable hydrologic framework for use in NYC water supply modeling. Here we report on work to calibrate the SWAT-WB hydrology model applied to the Cannonsville watershed.

Methods

SWAT-Water Balance model

SWAT-WB is a modified version of the SWAT-2005 model (Neitsch et al., 2005) that incorporates a daily water balance for each Hydrologic Response Unit (HRU) to predict the partitioning of precipitation into runoff and percolation. Once the moisture is portioned, SWAT's existing soil moisture routines are used by SWAT-WB to determine the degree of saturation-deficit for each soil profile for each day of simulation. To include the landscape features most important in runoff generation (e.g., upslope contributing area, soil depth, and slope) a topographic index was integrated with existing soils data to create a soil topographic index (*STI*), which is then used in the SWAT-WB HRU definition process (Easton et al., 2008). This saturation-deficit (in mm of water) is termed the available soil storage, τ_i and is a function of soil properties and watershed soil moisture status (White et al., 2011). The detailed documentation of SWAT model can be obtained from (Neitsch et al., 2005) and SWAT-WB can be obtained from (White et al., 2011) .

HRU definition

The HRUs are defined in SWAT as unique combinations of soil type, land cover, and slope class. However, in basins dominated by variable source area (VSA) hydrology this HRU definition has been insufficient for describing the spatial variations in runoff generating areas (Easton et al., 2008; Schneiderman et al., 2007). To include upslope contributing area while defining HRUs, a topographic index was integrated with existing SSURGO soils data (USDA-NRCS., 2000) to create a soil topographic index (*STI*), which is then used in the SWAT-WB HRU definition process (Easton et al., 2008). Values of *STI* are used to create wetness classes and are used to represent a location's likelihood to saturate. This wetness class map is then substituted for the soils map in the HRU definition process.

SWAT model set up

The model input parameters were developed using a digital elevation model (DEM) of the basin and a land use map which were obtained from DEP. The 19 sub-basins were delineated and further discretized into 554 HRUs based on spatial variations in land use and wetness class. In the baseline simulation the SWAT-WB model was forced with observed temperature and precipitation data obtained from cooperator stations (NCDC, NRCC). The remaining meteorological forcing (solar radiation, and wind speed) are calculated by the SWAT model based on daily temperature and precipitation (Neitsch et al., 2005). The model was calibrated for streamflow at the watershed outlet for the 1991-2000 years. Measured daily streamflow data was obtained from the USGS gauging station (#01423000) located at the watershed outlet near Walton, NY. The calibrated streamflow was used to simulate a historical baseline scenario (1964-2008) of streamflow using measured meteorological data.

Results and Discussions

Model calibration and baseline simulation

In addition to the effective depth coefficient (EDC), twenty parameters (listed in table 5.2) were calibrated which controls the hydrologic processes involved in streamflow generation including partitioning precipitation into infiltration and runoff, baseflow recession, and the rates of snowpack development and depletion. The parameters that were adjusted include a number of factors that account for controls the hydrologic processes involved in streamflow generation. Streamflow parameters such as Manning's n value for main channel (Ch_N2), baseflow alpha factor (Alpha-bf), and snowpack temperature lag factor (TIMP), the parameters surface runoff lag time (SURLAG), threshold depth of water in the shallow aquifer required for return flow to occur (GWQMN), threshold depth of water in the shallow aquifer for revaporization to occur (REVAPMN), soil evaporation compensation factor (ESCO) and other groundwater, channel and basin related parameters were also adjusted. The EDC values ranged from 0.1 to 1.0. The calibrated model simulated streamflow reasonably well as evident from the daily and monthly statistics for the calibration period (figure 5.5). Predicted and measured monthly streamflow for the calibration and baseline periods are presented in figure 5.5. Although the model was able to capture most peaks, it underestimated the measured streamflow during certain periods. The baseline simulation represents observed conditions under current climate scenario. The overall objective of the calibration was to maximize the coefficient of determination (R^2) and Nash-Sutcliffe efficiency (NSE) (Nash and Sutcliffe, 1970), and minimizing the percent bias. In addition, hydrology calibration was optimized so that the runoff and baseflow components of streamflow were simulated reasonably well compared to values derived from measured data using standard baseflow separation techniques (Arnold and Allen, 1999). The final calibrated streamflow for the Cannonsville watershed had a mean absolute bias in the annual flow volume of 8.0%, NSE of 0.63 and R^2 of 0.64 for daily streamflow and NSE of 0.75 and R^2 of 0.77 for monthly streamflow. The mean monthly hydrographs of observed and simulated flow are shown in figure 5.5. SWAT-WB has been found to perform well in simulating streamflow in Cannonsville watershed. The saturation excess runoff process is dominant runoff generation mechanism. Figure 5.6 shows the spatial variability of runoff generated in two sub-basins on

Cannonsville watershed. It is apparent from the figure that the areas with the wettest class with agricultural land uses were the ones that generated the highest runoff.

Conclusions

The SWAT-WB watershed model was calibrated for streamflow in Cannonsville watershed. The model is found to perform well in simulating streamflow in Cannonsville watershed where saturation excess runoff process is dominant runoff generation mechanism. The runoff generating areas were dominant for the wettest class with agricultural land use whereas, the driest class showed the least runoff generation.

Table 5.2. Calibration parameters and their best parameter ranges for SWAT model simulations

SWAT input variables	Description	Parameter Range	Actual Calibrated Parameter Values
ALPHA_BF	Baseflow alpha factor [days]	0.01-0.056	0.054
GW_DELAY	Groundwater delay [days]	0.01-8.0	5.920
GW_REVAP	Groundwater revaporization coefficient	0.01-0.2	0.193
GWQMN	Threshold depth of water in the shallow aquifer required for return flow to occur [mm]	0.01-0.01	0.008
REVAPMN	Threshold depth of water in the shallow aquifer for revaporization to occur [mm]	0-1000	499.7
RCHRG_DP	Deep aquifer percolation fraction	0.15	0.145
GW_SPYLD	Specific yield of shallow aquifer [m ³ /m ³]	0-0.3	0.271
DEEPST	Initial depth of water in the deep aquifer [mm H ₂ O]	0-2700	2681.0
SHALLST	Initial depth of water in the shallow aquifer [mm H ₂ O]	0-600	580.1
SMTMP	Snow melt base temperature [°C]	-5.0-0.08	0.081
SFTMP	Snowfall temperature [°C]	-5.0-0.4	0.343
SMFMX	Melt factor for snow on June 21 [mm H ₂ O/°C-day]	0.01-0.5	0.492
TIMP	Snow pack temperature lag factor	0.01-0.5	0.431
SURLAG	Surface runoff lag time [days]	0-1.0	1.0
LAT_TTIME	Lateral flow travel time [days]	0-0.5	0.015
CH_N2	Manning's n value for main channel	0.01-0.031	0.203
CH_K2	Effective hydraulic conductivity in main channel alluvium [mm/hr]	0.01-85.2	85.13
ESCO	soil evaporation compensation factor	0.01-0.17	0.029
EPCO	plant water uptake compensation factor	0.01-0.815	0.264

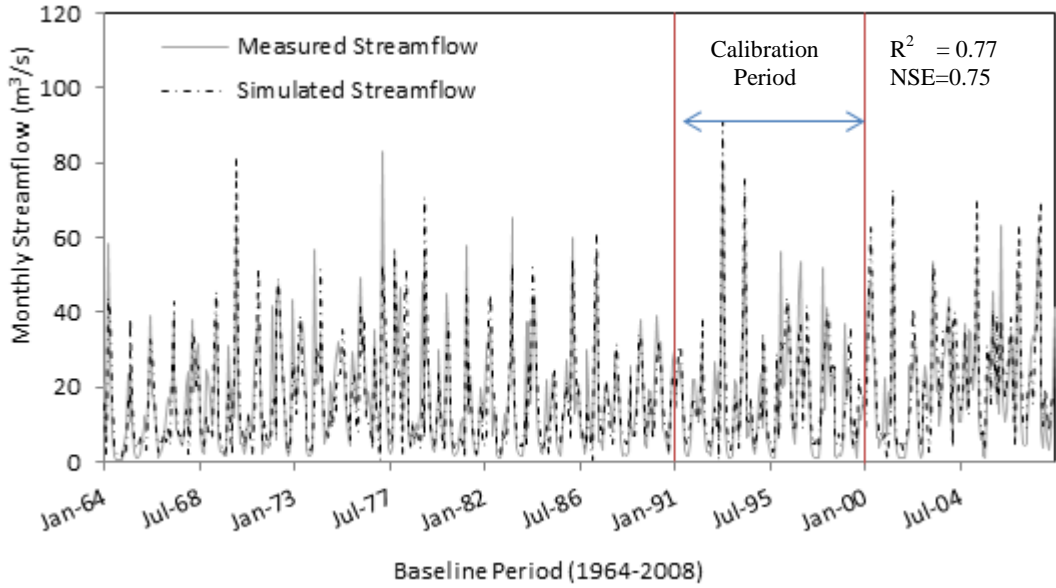


Figure 5.5. Predicted vs. measured monthly streamflow

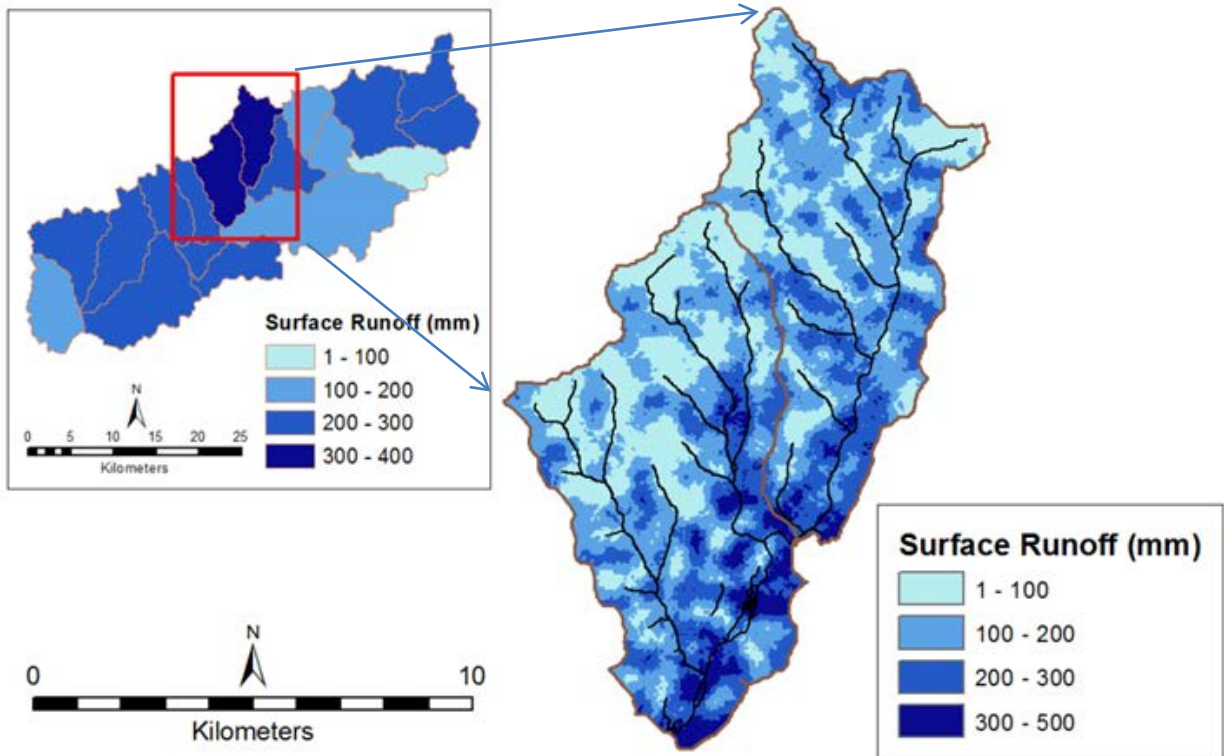


Figure 5.6. Map showing spatial distribution of runoff generating areas at selected sub-basins (inset) and HRUs from the dominant runoff generating region. Values indicated are average annual estimates.

5.4. Influences of Channel Processes on Phosphorus Export

Introduction

Sources of phosphorus (P) in surface waters include agriculture, municipal sewage treatment plants, individual septic treatment systems, decaying plant material, runoff from urban areas and construction sites, stream bank erosion, and wildlife. In Cannonsville watershed, NY, agriculture is known to be a major source of the P entering the streams and reservoir (DEP, 2011). The downstream ecological impacts of P inputs are heavily dependent on the extent to which they are physically retained and/or chemically and biologically processed; but processing of P are often ignored in watershed management studies (Edwards and Withers 2008, Withers and Jarvie 2008). In-stream processing of P may account for the apparent disconnect between measures implemented to reduce P inputs and improvements in water quality and ecology at watershed scale (Sharpley et al. 2009). The understanding of net effects of P release and retention processes in watersheds is important for managing stream water quality and for targeting remediation and restoration measures most effectively. Such knowledge may also be incorporated in water quality models in order to improve nutrient prediction abilities. The goals of this study are to analyze channel P processes at different flow regimes and at different events. This analysis can also be used to examine the scale and variability of p retention and release, as an aid to watershed management and to improvise in-stream processing in existing water quality models.

Methods

Mixing model analysis

In this study, we present a simple empirical approach for quantifying P delivery by using Extended-End Member Mixing Analysis (E-EMMA; (Neal et al. 2010, Jarvie et al. 2010) to explore P net retention and release at the watershed outlet. This approach enables us to utilize water quality monitoring data, and point source data to quantify the impacts of in-stream and watershed P processing on P delivery at the watershed scale. The point source data we used for this study include effluent nutrients data from waste water treatment plants (WWTPs) and nutrients added in-stream by cattle before and after the implementation of watershed management programs in Cannonsville Watershed. For this study, 5 years of data (1997, 2001, 2003, 2005 and 2008) were chosen to evaluate effects of P retention and release on delivery at the watershed outlet.

With E-EMMA, the load of the pollutant (P) is plotted against flow for two end-member component mixing series. The underlying assumption is that there are two dominant and distinct sources of water (both with different P concentrations) contributing to P loads at the watershed outlet: (i) a baseflow end-member source composed largely of effluent and/or groundwater, and (ii) an eventflow end-member source composed of an integrated watershed-wide nonpoint source that, under the highest flows, is delivered directly to the watershed outlet. When the two water sources mix, a linear relationship between baseflow and eventflow P load end-members would indicate that P was behaving conservatively, that is, that P was not undergoing significant net uptake or release as a result of deposition of particulate P, remobilization of P, sorption to

sediments, or interaction with biota. In contrast, a nonlinear mixing series would indicate that P was behaving non-conservatively. Nonlinear behavior under low-flow conditions is assumed to result from within-stream processes, whereas nonlinear behavior under intermediate and higher flows represents the net effects of in-stream and watershed retention/ mobilization. By comparing an observed nonlinear relationship between stream P load and stream flow measurements, with a theoretical linear conservative mixing series between the Baseflow and eventflow end-member P loads, the net effects of P retention and release can be directly quantified.

Phosphorus release and retention calculation

Dissolved and particulate P for USGS gage#01423000 (Walton) were used to illustrate how E-EMMA can be used to estimate net losses and gains of P at the watershed outlet. The baseflow end-member P load ($P_{load_{Baseflow}}$) represents the sources of P to the stream that contribute under dry weather flow conditions. These loads include wastewater treatment plant effluent ($P_{load_{Effluent}}$), direct contributions from cattle in stream ($P_{load_{Cattle}}$), and any background groundwater sources of P, which in this analysis is considered none. The P loads for each upstream wastewater treatment plant were obtained from DEP and P loads for cattle in stream were calculated using the method described in James et al. (2007).

$$P_{load_{Baseflow}} = P_{load_{Effluent}} + P_{load_{Cattle}} \quad (5.11)$$

The eventflow end-member ($P_{load_{Eventflow}}$) is an integration of all the watershed-wide sources of P including non-point and point source and P mobilized from within the stream channel network. For Eventflow Conditions:

$$P_{load_{River}} = P_{Outlet} (Q_{River} - Q_{Baseflow}) + P_{Baseflow} Q_{Baseflow} \quad (5.12)$$

Rearranging above equation:

$$P_{load_{River}} = P_{Outlet} Q_{River} + (P_{Baseflow} - P_{Outlet}) Q_{Baseflow} \quad (5.13)$$

where, $P_{load_{River}}$ is the stream water P load, Q_{River} is the stream flow, $P_{Baseflow}$ is the P concentration at baseflow, and P_{Outlet} is the concentration of P mobilized from an integration of the upstream watershed. Therefore, for the situation where there is conservative mixing of nutrients, the relationship between $P_{load_{River}}$ and Q_{River} should be linear with the gradient equal to P_{Outlet} . $P_{load_{Eventflow}}$ is estimated from the relationship between $P_{load_{River}}$ and stream flow (Q_{River}) by applying a LOESS fit to the $P_{load_{River}}$ vs. Q_{River} relationship.

Given the low water residence times and greatest efficiency of P delivery under highest flows, the impact of P retention on $P_{load_{Eventflow}}$ is likely to be relatively low. Therefore, the $P_{load_{Eventflow}}$ is taken as the reference point for the integrated watershed eventflow end-member, at which there is no net P retention. The gradient (P_{Outlet}) and intercept ($P_{load_{Intercept}}$) of the conservative mixing series were then applied to the observed flow data to derive corresponding $P_{load_{Linear}}$ values.

$$Pload_{Linear} = Q_{River} P_{Outlet} + PLoad_{Intercept} \quad (5.14)$$

To estimate the net P retention or release, $Pload_{River}$ was then compared with the corresponding P load derived from the conservative mixing model ($Pload_{Linear}$). The P load retained or released ($P_{Process}$) is calculated as the difference between $Pload_{River}$ and the P load from the conservative mixing series ($Pload_{Linear}$) predicted $Pload_{River}$ on the LOESS curve at the 99th percentile of the stream flow distribution for the period of investigation.

$$P_{Process} = PLoad_{River} - PLoad_{Linear} \quad (5.15)$$

In this study, we examined differences in average daily $P_{Process}$ under low-flow conditions (the lowest 10% of flows), high-flow conditions (highest 10% of flows), and the intermediate flow conditions, i.e., for moist conditions (10-40%), one covering mid-range flows (40-60%), another for dry conditions (60-90%). These flow conditions were derived from a flow duration curve. A flow duration curve relates flow values to the percent of time those values have been met or exceeded. The analysis at flow regime scale provide a simple differentiation between P retention/release as a result of (i) processes that occur under low flows (within the stream or in near-stream environments) and (ii) wider P processes along the watershed–stream continuum, under intermediate to higher flows.

Results and Discussions

In order to understand the P processes in stream, the net retention and release process was analyzed at different flow components for five years. For all the five studied years, the relationships between stream P load ($Pload_{River}$) and streamflow (Q_{River}) were nonlinear, with none approximating to a conservative mixing series. Such nonlinear relationships indicate that P process in stream is non-conservative. Net P retention or release processes were quantified by comparing the observed curvilinear $Pload_{River}$ versus Q_{River} relationships with corresponding P loads calculated using the corresponding linear mixing model, for each flow regime i.e., low, dry, mid-range, moist and high flows.

Table 5.3. Annual net P retention and release at USGS gage 01423000.

Year	Annual Net P Retention/Release	
	Dissolved P	Particulate P
1997	31%	19%*
2001	39%	47%
2003	36%	44%
2005	62%	>400%*
2008	20%*	21%

* Net P release

Dissolved Phosphorus Processes

At annual scale, there was dissolved P retention with net annual retention (all flow regimes included) ranging from 31% in 1997 to 62% in 2005 (table 5.3). However, there was net release of 20% in 2008 for dissolved P. In considering different flow regimes, there was net retention of dissolved P in low, dry, mid-range and moist flow regimes for all the five years. The high flow regime however showed release of dissolved P in most of the years (figure 5.7). These release processes occurring under high flows will be increasingly dominated by processes linked to flow dynamics, incorporating watershed runoff processes/mobilization/retention effects as well as in-stream sediment storage and remobilization. Dissolved P is subject to intensive biogeochemical processing under low flows and is also affected by stream temperature. Dissolved P retention was greatest under the lowest and intermediate flows, which is strongly indicative of biological processing of P, particularly uptake by algae and/or sorption to sediments. There is also potential for P retention as a result of an increased proportion of total flow being stored in hyporheic sediments under baseflow conditions. There was no evidence of significant net release or remobilization dissolved P loads under low and intermediate flows relative to the linear conservative mixing. This indicates that remobilization of transient in-channel and watershed stores of P was small relative to P load retention under low and intermediate flows. Low flows correspond with highest water residence times (Jarvie et al. 2002) allowing greater interaction with sediments and biota and thus greatest potential for biogeochemical cycling (Jarvie et al., 2010). In-stream processes under low and intermediate flows may regulate delivery of nutrients and modify the timing of delivery in a way that may help to reduce ecological impacts to downstream stream reaches at times of greatest stream eutrophication risk.

Particulate Phosphorus Processes

Particulate P processing in stream showed varied results. At annual scale (all flow regimes included), there was particulate P retention for three studied years with net annual retention ranging from 21% for 2008 to 47% in 2001. There was net release of 19% particulate P in 1997 and greater than 400% release in 2005. The release of particulate P may be attributed to extremely high P load that was observed during certain high flow events during 2005. Particulate P stream processing analysis at different flow regimes showed that during 1997, there was net release of at all the flow regimes and net release at high flow regimes during 2005 and 2008. At low and intermediate flow conditions, there was net retention of particulate P during all the years except 1997 (figure 5.8). The variability can be attributed to many factors such as source availability and mobilization, antecedent conditions, rainfall intensity, and land-use management. Net release of particulate P during 1997 at all flow regimes may be due to activities that might have directly contributed sediment laden P from the stream, and high concentration of effluent and cattle P in the stream. The greatest release of particulate P observed during 2005 may be attributed to few high flow events during spring runoff that produced extremely high P loads to the watershed outlet. The greatest net particulate P retention under low to intermediate flow conditions for 2001, 2003, 2005 and 2008 are likely the result of net deposition of particulate P along the watershed–stream continuum. The watershed management activities, such as stream bank restoration, stream fencing, filter strips and riparian vegetation that were implemented in late 1990s may also have helped in trapping sediment and sediment laden nutrients resulting in net particulate P retention. The release of P during high flow may be attributed to stream bank

erosions following high flow events, that contribute to sediment laden P. P that becomes stored along the stream–watershed continuum (either through physical deposition or by biogeochemical processes such as sorption to sediments or uptake by biota) will subsequently be available for remobilization and thus contribute to the nonpoint-source load (and to the eventflow end-member load) as flows rise (Jarvie et al., 2010).

Conclusions

The relationships between observed P load and discharge exhibited strong non-conservative behavior under the lowest and intermediate flows for both dissolved and particulate P. Given the well-defined baseflow and integrated watershed eventflow end-members derived from the Cannonsville P load–stream flow scatter plot, the interpretation here is that the curvilinear relationship reflects net P retention along the stream–watershed continuum during mixing of the eventflow and baseflow end members. Further study is needed to gain fuller understanding of the balance of processes that determine the eventflow end-member load at intermediate to high flow conditions, especially in watersheds dominated by nonpoint export, such as differential erosion associated with events of different magnitudes, intensities, seasons, and pre-existing conditions; re-deposition and other processing active during overland flow; and in-stream processing.

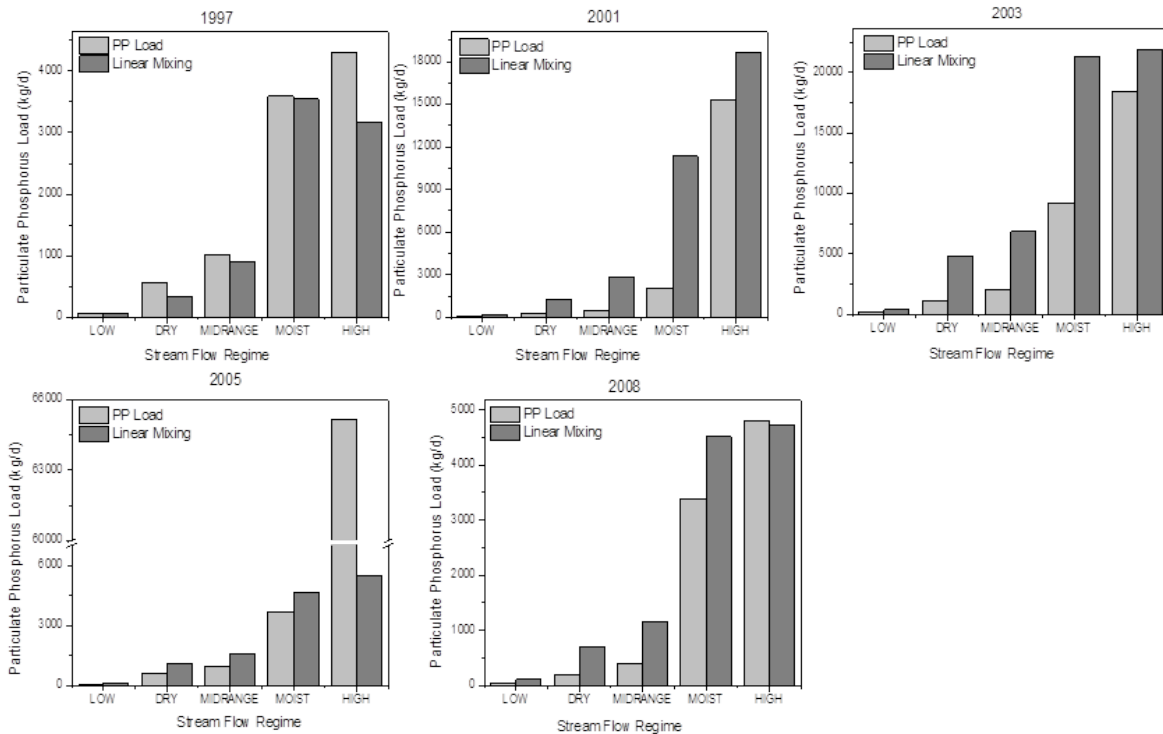


Figure 5.7. Dissolved phosphorus processes for different flow conditions

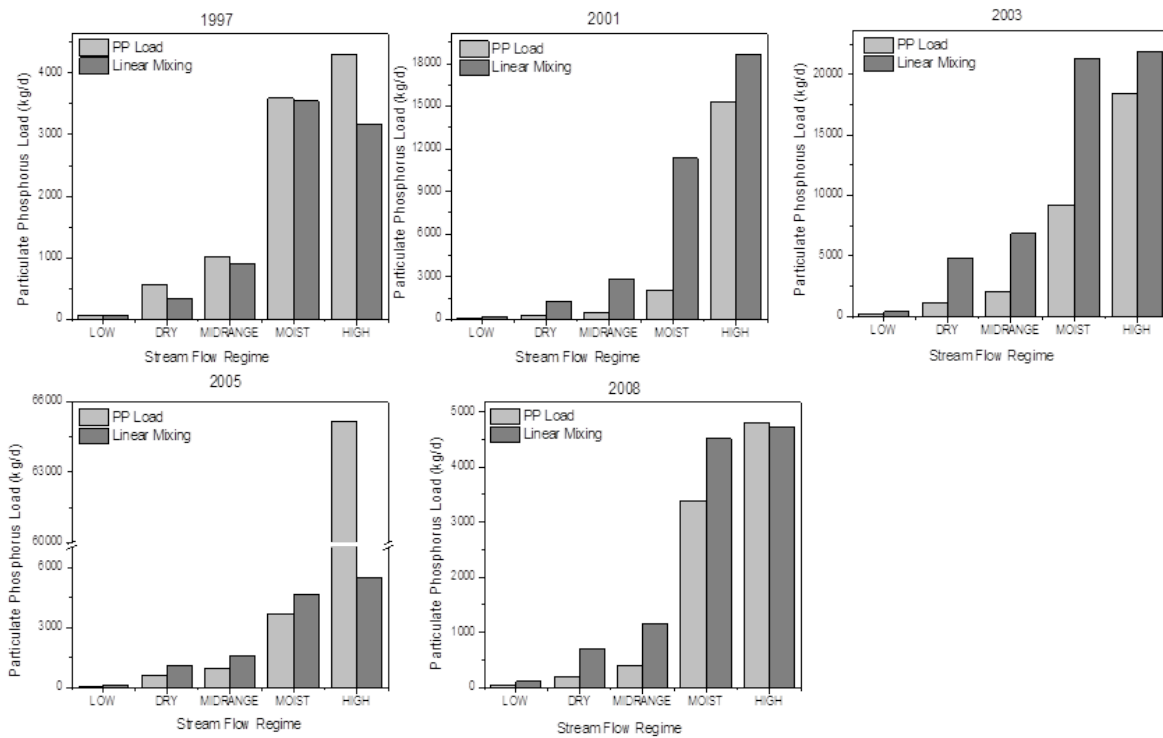


Figure 5.8. Particulate phosphorus processes for different flow conditions

5.5. Developing a Hybrid Approach to Simulate Future East of Hudson Reservoir Inflows

Introduction

Inflows from basins draining to East of Hudson (EOH) reservoirs are required to run simulations with the NYC OASIS reservoir system model. This is also true when performing simulations to study possible impact of climate change on the NYC water supply. During phase I of the DEP “Climate Change Integrated Modeling Project for Water Quantity and Quality” (CCIMP) the assumption was made to maintain EOH inflows during future simulations similar to historical. Though this assumption was fairly acceptable considering that historically the EOH system contributes with less than 10% of total water yield, a more comprehensive study, as planned for CCIMP phase II, will require simulated future EOH inflow as these may affect water routing in the system. A major difficulty with EOH inflows is that no models have been developed or are readily available to simulate future individual EOH inflows. Also, modeling EOH inflows is not an easy task because the area is urbanized with most streamflows being regulated.

This section describes a two-step hybrid approach that was applied to simulate future inflows for each individual EOH reservoir. The methodology combines linear regression models between each individual reservoir inflow and an aggregated inflow for the entire region and the use of the GWLF watershed model to simulate a regional daily inflow time series.

Methodology

Measured streamflow data at each OASIS EOH basin are not available to help develop a model for each basin. A preliminary analysis of historical streamflow from individual EOH basins revealed high correlation coefficient among them. Under this scenario, our option was to apply a hybrid approach that combines a stochastic regression model and GWLF watershed model. This approach can be summarized as following:

1. An aggregate time series was developed consisting of an arithmetic sum of the individual OASIS EOH basins historical inflows. These historical inflow time series were previously estimated and embedded in the OASIS model.
2. Individual regression models were developed for each OASIS EOH basin using the aggregate flow as (the only) explanatory variable.
3. Historical air temperature and precipitation time series representative for the region was used to calibrate the GWLF watershed model to the historical aggregate inflow. Soil radiation and relative humidity that are also required to run GWLF hydrology in addition to air temperature and precipitation were simulated internally in GWLF based on the latitude and longitude of the EOH watershed centroid and the inputs of air temperature and precipitation days.

Linear regression model for each individual OASIS EOH basin

A simple linear regression model is a probabilistic model that relates two variables, an expected dependent variable Y and an independent variable x . The expected value of Y is a linear function of x , but for each fixed x , the variable Y differs from its expected value by a random amount (Devore 2000). The linear relationship between the two variables can be described by the following model equation

$$Y = \beta_0 + \beta_1 x + \varepsilon \quad (5.16)$$

where the intercept β_0 and slope β_1 are model parameters to be determined and ε represents a random error. One important assumption in a linear regression model is that ε does not depend on x , is normally distributed with its mean $E(\varepsilon) = 0$ and has a constant variance $V(\varepsilon) = \sigma^2$. A test statistic when developing a linear regression is based on a null hypothesis $H_0: \beta = 0$, against $H_a: \beta \neq 0$. During the process of model development plotting model residuals against predicted values helps evaluate possible presence of non-linear relationship and heteroscedastic (change in variance) behavior (Devore 2000, Hirsh et al. 1993). The OLS regression approach was applied to develop inflow models for each individual EOH inflow. It is assumed that each individual inflow is linearly related to a total aggregate inflow of the entire OASIS EOH region. When heteroscedasticity is observed weighted least square (WLS) regression can be applied. For WLS β_0 and β_1 are estimated by minimizing

$$f_w(b_0, b_1) = \sum w[y - (b_0 + b_1 x)]^2 \quad (5.17)$$

where the weights w should decrease with increasing x . For the WLS models developed for some of the EOH sites, we selected weights in the form $w=1/x$ which have shown to improve our model results.

Analysis Method

A standard regression analysis technique was employed to determine the parameters for each individual EOH-Inflow basin. The data processing was performed using the Statistics Analysis System (SAS) software. The procedure included following steps. First, PROC UNIVARIATE was used for data description and developing histogram plots. Second, the PROC REG command was used to apply Ordinary Least-Squares (OLS) regression to estimate the coefficients for each individual linear regression model and perform influence diagnostics. Third, a residual analysis and test of normality assumption were conducted by applying PROC UNIVARIATE procedure.

Data

The data available for model development include historical inflows time series for each individual EOH basins. These time series in the current NYC OASIS model covers the period from 1927 to 2008. Time series from 1927 to 2000 were used for model development while the remaining data from 2001 to 2008 was used for model verification.

Regression Models Development

Histogram plots using historical data for each individual EOH site reveal positive skewness. Also, high correlation is observed among individual inflows. Table 5.4 shows the description of the historical inflow for each individual OASIS EOH basin. The numbers in the variable represent ID numbers in the NYC OASIS model associated with inflow nodes where 670 is Boyd Corners, 675 (West Branch), 700 (Kensico), 710 (Middle Branch), 715 (East Branch BogBr), 720 (Croton Div), 725 (Croton Fall), 735 (Titicus), 745 (Amawalk), 750 (Cross River), 755 (Muscoot), and 760 (New Croton).

In table 5.5 we present a summary of model parameters for the OLS regression models for each individual OASIS EOH basin. The models were developed using inflow data from Oct 1927 to Dec 2000 (N = 27029). Except for the intercept for East Branch BogBr (715) and Cross River (750) basins, all parameters in table 5.5 are statistically significant at a 95% confidence level. The R squares and adjusted R squares suggest that model in table 5.5 can explain almost 100% of the data variance.

Table 5.4. Description of individual historical inflow (1927-2008) in current NYC OASIS model. Total-EOH represents the sum of all individual inflows in the EOH region. Units are cfs.

Variable	N	Mean	StDev	Minimum	Median	Maximum
Infl-670	29859	38.17	49.82	0.00	23.98	1326.21
Infl-675	29859	34.35	44.84	0.00	21.55	1193.59
Infl-710	29859	36.26	47.33	0.00	22.74	1259.90
Infl-715	29859	136.3	177.92	0.00	85.55	4752.25
Infl-720	29859	12.09	15.78	0.00	7.580	419.97
Infl-725	29859	28.63	37.36	0.00	17.95	994.66
Infl-735	29859	39.44	51.48	0.00	24.75	1370.42
Infl-745	29859	33.08	43.18	0.00	20.73	1149.38
Infl-750	29859	50.26	65.59	0.00	31.56	1746.18
Infl-755	29859	126.59	165.23	0.00	79.43	4398.60
Infl-760	29859	100.50	131.19	0.00	63.12	3492.35
Total-EOH	29859	635.70	829.70	0.00	399.10	22103.50

Table 5.5. Model parameters for OLS regression models for each individual OASIS EOH basin where TEOH represents the total EOH inflow and R-Std the residual standard deviation. The level of significance for all models is judged using $t_{0.025, n-1} = 1.96$, where n is the sample size and equals 29859. We reject the null hypothesis ($H_0: \beta = 0$) in favor of $H_a: \beta \neq 0$ when the absolute value of the t statistic is greater than 1.96. These models are based on inflow in cu. ft./sec units.

Site Name (OASIS ID number)	Predictor	Parameter	Parameter Value	t-statistic	Significance @95% C.I.? (Pr> t)
Boyd Corners (670)	Intercept	α_{670}	0.00139	3.60	Yes (0.0003)
	TEOH	$\beta_{\text{Total_EOH}}$	0.06005	155516	Yes (<.0001)
	R-Std	σ_{670}	0.05045		
West Branch (675)	Intercept	α_{675}	0.00250	6.52	Yes (<.0001)
	TEOH	$\beta_{\text{Total_EOH}}$	0.05405	140458	Yes (<.0001)
	R-Std	σ_{675}	0.05027		
Middle Branch (710)	Intercept	α_{710}	0.00199	5.24	Yes (<.0001)
	TEOH	$\beta_{\text{Total_EOH}}$	0.05705	149586	Yes (<.0001)
	R-Std	σ_{710}	0.04982		
East Branch BogBr (715)	Intercept	α_{715}	-0.00188	-0.89	No (0.3719)
	TEOH	$\beta_{\text{Total_EOH}}$	0.21432	101123	Yes (<.0001)
	R-Std	σ_{715}	0.27688		
Croton Div (720)	Intercept	α_{720}	0.00452	12.56	Yes (<.0001)
	TEOH	$\beta_{\text{Total_EOH}}$	0.01902	52587.2	Yes (<.0001)
	R-Std	σ_{720}	0.04724		
Croton Fall (725)	Intercept	α_{725}	0.00276	7.30	Yes (<.0001)
	TEOH	$\beta_{\text{Total_EOH}}$	0.04504	118580	Yes (<.0001)
	R-Std	σ_{725}	0.04962		
Titicus (735)	Intercept	α_{735}	0.00234	6.05	Yes (<.0001)
	TEOH	$\beta_{\text{Total_EOH}}$	0.06205	159735	Yes (<.0001)
	R-Std	σ_{735}	0.05075		
Amawalk (745)	Intercept	α_{745}	0.00221	5.81	Yes (<.0001)
	TEOH	$\beta_{\text{Total_EOH}}$	0.05205	135782	Yes (<.0001)
	R-Std	σ_{745}	0.05007		
Cross River (750)	Intercept	α_{750}	0.00119	2.91	Yes (0.0036)
	TEOH	$\beta_{\text{Total_EOH}}$	0.07907	193021	Yes (<.0001)
	R-Std	σ_{750}	0.05352		
Muscoot (755)	Intercept	α_{755}	-0.00828	-13.26	Yes (<.0001)
	TEOH	$\beta_{\text{Total_EOH}}$	0.19917	317185	Yes (<.0001)
	R-Std	σ_{755}	0.08204		
New Croton (760)	Intercept	α_{760}	-0.00451	-8.28	Yes (<.0001)
	TEOH	$\beta_{\text{Total_EOH}}$	0.15814	289101	Yes (<.0001)
	R-Std	σ_{760}	0.07146		

An important assumption in OLS regression is that residuals are normally distributed with a mean equals to zero and constant variance. Residual results show that although a linear relationship may be reasonable (as shown in the fit plot) there is some presence of increasing variance with x. This may also reflect a presence of unusually large values in the time series. The ordinary residual analysis for most of the models reveals distributions with a long tail pointing to the lower values (negative skewness), except sites 715, 720, and 745. Kurtosis values are positive except for site 720. The range of positive kurtosis values is diversified but it is an evidence of a lower and wider peak around the mean than expected for a normally distributed random variable. Most normal probability plots fit a large portion of the normal distribution. Site 720 shows short tails, an indication of less variance than expected from a normal distribution. However, most normal probability plots reveal a long tail in the lower 1 percentile. The Kolmogorov-Smirnov statistic indicate $Pr>D$ less than 0.01 and the Anderson-Darling statistic indicate $Pr>A-Sq$ less than 0.005. These results of residual fit diagnostics and test of normality may be signs of lack of normality in residuals but they are also influenced by extreme values present in our large sample size. Our major concern is with residuals showing a long tails in both lower and upper percentile in sites 715, 755 and 760, suggesting a higher variance in the sample data than expected in a normal distribution. For these reasons we developed weighted least square regression models for these sites. The results are presented in table 5.6.

During regression models application residuals were generated using a polar form of the Box-Muller transformation algorithm and assuming $\varepsilon = N(0, \sigma_\varepsilon^2)$.

Table 5.6. Model parameters for WLS regression models where TEOH represents the total EOH inflow and R-Std the residual standard deviation. The inverse of TEOH ($1/x_i$) was applied as weighting factor.

Site Name (OASIS ID number)	Predictor	Parameter	Parameter Value	t-statistic	Significance @95% C.I.? ($Pr> t $)
East Branch BogBr (715)	Intercept	α_{715}	-1.1078E-12	-0.00	No (0.9999)
	TEOH	β_{Total_EOH}	0.21432	94494.8	Yes (<.0001)
	R-Std	σ_{715}	0.27690		
Muscoot (755)	Intercept	α_{755}	-7.6779E-13	-0.00	No (0.9999)
	TEOH	β_{Total_EOH}	0.19916	134797	Yes (<.0001)
	R-Std	σ_{755}	0.08279		
New Croton (760)	Intercept	α_{760}	7.00393E-14	0.00	No (1.0000)
	TEOH	β_{Total_EOH}	0.15813	115134	Yes (<.0001)
	R-Std	σ_{760}	0.071718		

Final regression model for each individual EOH basin

OLS and WLS were applied to develop regression models for each of the NYC OASIS EOH inflow nodes as a function of the total EOH inflow. The model development was based on historical inflow data from January 1927 to December 2000. Table 5.7 presents the final models for each of 11 (out of 13 total) EOH inflow nodes. The other 2 nodes are Kensico (700) and BQ Aquifer (780) which historical inflows are set to zero.

GWLF model development

The Generalized Watershed Loading Functions (QWLF) model (Schneiderman et al. 2002, 2007) was calibrated to simulate historical total EOH inflow using air temperature and precipitation from Yorktown Heights 1W (NCDC ID# 309670). Solar radiation and relative humidity were simulated internally in the GWLF model. The calibration period started from 1/1/1966 to 12/31/2000. Data from 2001 to 2008 were used for model verification. Delta change factors resulting from applying the 25-bin methodology were applied to historical time series to simulate future regional inflow.

Table 5.7. Final regression models for each of eleven OASIS EOH individual inflow nodes. The model parameters for models marked with ^{*)} were estimated using WLS regression. All parameters for remaining models were estimated using OLS regression. For the WLS the inverse of TEOH ($1/x_i$) was applied as weighting factor.

-
1. **Boyd Corners** (670) = $0.00139 + 0.06005 \text{ TEOH} + \varepsilon$; $\sigma_\varepsilon = 0.05045$
 2. **West Branch** (675) = $0.00250 + 0.05405 \text{ TEOH} + \varepsilon$; $\sigma_\varepsilon = 0.05027$
 3. **Middle Branch** (710) = $0.00199 + 0.05705 \text{ TEOH} + \varepsilon$; $\sigma_\varepsilon = 0.04982$
 4. **East Branch BogBr** (715) = $-1.1078\text{E-}12 + 0.21432 \text{ TEOH} + \varepsilon$; $\sigma_\varepsilon = 0.27690$; $\omega = 1 / \text{TEOH}$ ^{*)}
 5. **Croton Div** (720) = $0.00452 + 0.01902 \text{ TEOH} + \varepsilon$; $\sigma_\varepsilon = 0.04724$
 6. **Croton Fall** (725) = $0.00276 + 0.04504 \text{ TEOH} + \varepsilon$; $\sigma_\varepsilon = 0.04962$
 7. **Titicus** (735) = $0.00234 + 0.06205 \text{ TEOH} + \varepsilon$; $\sigma_\varepsilon = 0.05075$
 8. **Amawalk** (745) = $0.00221 + 0.05205 \text{ TEOH} + \varepsilon$; $\sigma_\varepsilon = 0.05007$
 9. **Cross River** (750) = $0.00119 + 0.07907 \text{ TEOH} + \varepsilon$; $\sigma_\varepsilon = 0.05352$
 10. **Muscoot** (755) = $7.6779\text{E-}13 + 0.19916 \text{ TEOH} + \varepsilon$; $\sigma_\varepsilon = 0.08279$; $\omega = 1 / \text{TEOH}$ ^{*)}
 11. **New Croton** (760) = $7.00393\text{E-}14 + 0.15813 \text{ TEOH} + \varepsilon$; $\sigma_\varepsilon = 0.071718$; $\omega = 1 / \text{TEOH}$ ^{*)}
-

5.6. One-dimensional Reservoir Model Calibration

Introduction

Located in Delaware County, New York, Cannonsville Reservoir was constructed to provide water supply for New York City. The Cannonsville watershed has a relatively high portion of agricultural land use, and there are also a number of small sewage works and other point sources contributing to the rivers entering the reservoir. These factors in the past led to high point and non-point nutrient loading to the reservoir, high average chlorophyll concentrations and frequent phytoplankton blooms. Starting in 1992, the implementation of sewage treatment upgrades, and an aggressive program of agricultural, storm water and other best management practices (BMPs), have reduced nutrient inputs, improved trophic status and reduced the occurrence of phytoplankton blooms (DEP, 2006b).

A one-dimensional hydrothermal and water quality model has been set up to simulate the thermal stratification, nutrients and phytoplankton in the reservoir (Owens 1998; Doerr, 1998; UFI, 2001). The objective of the study is to improve the performance of the reservoir model by automated calibration using long-term measurement data.

Study Area

The Cannonsville watershed has a drainage area of 1178 km². Before the occurrence of land use change and the implementation of watershed management programs, the land use was composed of agriculture (14%), urban areas (3%), non-agricultural grass areas (7%), undeveloped forested and brushland areas (73%), and water and wetland areas (3%) (DEP, 2006b).

The reservoir's capacity is 362 million m³. The surface area of the reservoir is 19.2 km², about 24 kilometers long and 0.8 kilometers wide on average (figure 5.9). Its maximum depth is about 42.7 meters with an average depth of 18.6 meters.

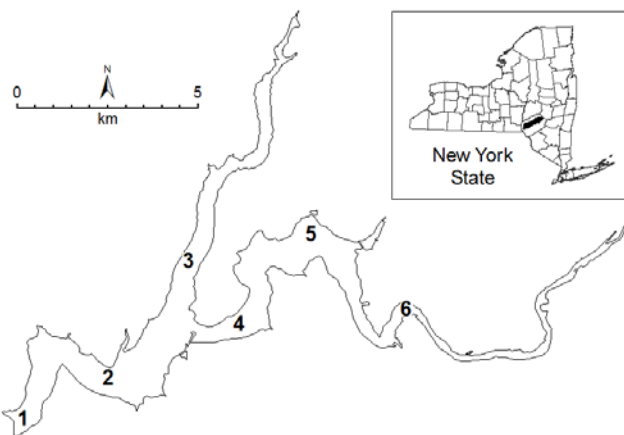


Figure 5.9. Cannonsville reservoir and sampling stations 1-6.

Reservoir Model

A one dimensional reservoir model has been developed to simulate the hydrothermal and water quality conditions in Cannonsville reservoir. The model consists of three components: (1) a hydrothermal sub-model, (2) nutrient sub-models, and (3) a phytoplankton sub-model.

The hydrothermal sub-model simulates the vertical dynamics of reservoir thermal stratification and related transport regimes, based on changes in such critical (state) variables as meteorological, hydrological and operational conditions.

The nutrient sub model describes the transformation and fate of the nutrient loads in the reservoir. The reservoir model distributes nutrients vertically through the water column based on vertical mixing coefficients derived from the hydrothermal sub-model, and the nutrient inputs are partitioned into different forms based on model coefficients.

The PROTBAS (PROtech Based Algal Simulations) (Markensten and Pierson, 2007) model which is based on PROTECH (Reynolds et al., 2001) is used to simulate phytoplankton biomass. In the model, phytoplankton biomass is predicted in terms of algal carbon and is a balance between growth (photosynthesis), and losses due to respiration, grazing, sedimentation and outflow. Chlorophyll *a* is calculated from the algal carbon based on system-specific stoichiometric relationships.

Reservoir model configuration and parameters

To set up the one-dimensional model to simulate the hydrothermal and water quality conditions, the reservoir is discretized vertically into 35 layers with an average thickness of 1.5 meters per layer. The model is fed with daily meteorological data (such as air temperature) and data related to the water balance (water elevation, discharge, dam spill and tunnel outflow). The time series data, such as dissolved phosphorus and nitrogen from non-point and point sources, (which are generated by a watershed model) are taken as input of the model. The model can be configured to output daily simulated values for a large number of variables, such as dissolved oxygen in the epilimnion and hypolimnion layers.

According to the model description (UFI, 2001), 116 hydrothermal and kinetic parameters (also called coefficients) are used in the model. Among them, 52 can be adjusted during model calibration. The Morris method (Morris, 1991; Saltelli et al., 2004) is employed to identify the sensitive parameters in the model. See Huang and Liu (2008) for a detailed description of the method. It was found that 18 parameters were of great importance in determining the simulated values of the variables including temperature (Temp), dissolved oxygen (DO), total phosphorus (TP) and chlorophyll *a* (Chla). These parameters were the focus in model calibration and only their values were adjusted in model calibration. The names and definitions of the 18 parameters, as well as their lower and upper bounds are presented in table 5.8. These bounds were determined according to the recommendations provided by the model developer (UFI, 2001), and adjustments were made to ensure the numerical stability of the model.

Table 5.8. Reservoir model parameters

	Name	Calibrated value	Lower Bound	Upper Bound	Definition
1	aC2CHL	53.000	50.600	100.000	Ratio carbon to chlorophyll (ugC/ugChl)
2	aC2P	150.00	80.00	150.00	Ratio carbon to phosphorus (ugC/ugP)
3	betaw	0.3570	0.3500	0.5000	Surface adsorption fraction
4	emisi	0.9413	0.9000	0.9900	Ice emissivity
5	eta	1.3655	1.0000	1.5000	Wind mixing
6	fardl	0.9923	0.5000	0.9950	Fraction of algal respiration as dissolved labile
7	farpl	0.0077	0.0045	0.0100	Fraction of algal respiration as particle labile
8	htcwi	0.0609	0.0100	0.1000	Ice transfer
9	kc	0.0500	0.0100	0.0500	Chlorophyll multiplier (L/ugChl/m)
10	kldoc	0.0116	0.0100	0.0150	Oxidation of labile DOC (1/d)
11	kldop	0.0173	0.0100	0.1000	Decay of labile DOP (1/d)
12	klpop	0.0600	0.0500	0.0900	Hydrolysis of labile POP (1/d)
13	phir	0.1500	0.0100	0.1500	Respiration multiplier - growth
14	PPvel	1.1589	0.2640	1.4960	Settling organic PP (m/d)
15	rz	0.2973	0.2000	0.6000	Diffusion exponent
16	sod	0.4800	0.3200	0.4800	Sediment oxygen demand (g/m ² /d)
17	trncon	0.0022	0.0020	0.0030	Evaporation multiplier
18	turb	2.2963	2.0000	2.5000	Atmospheric turbidity

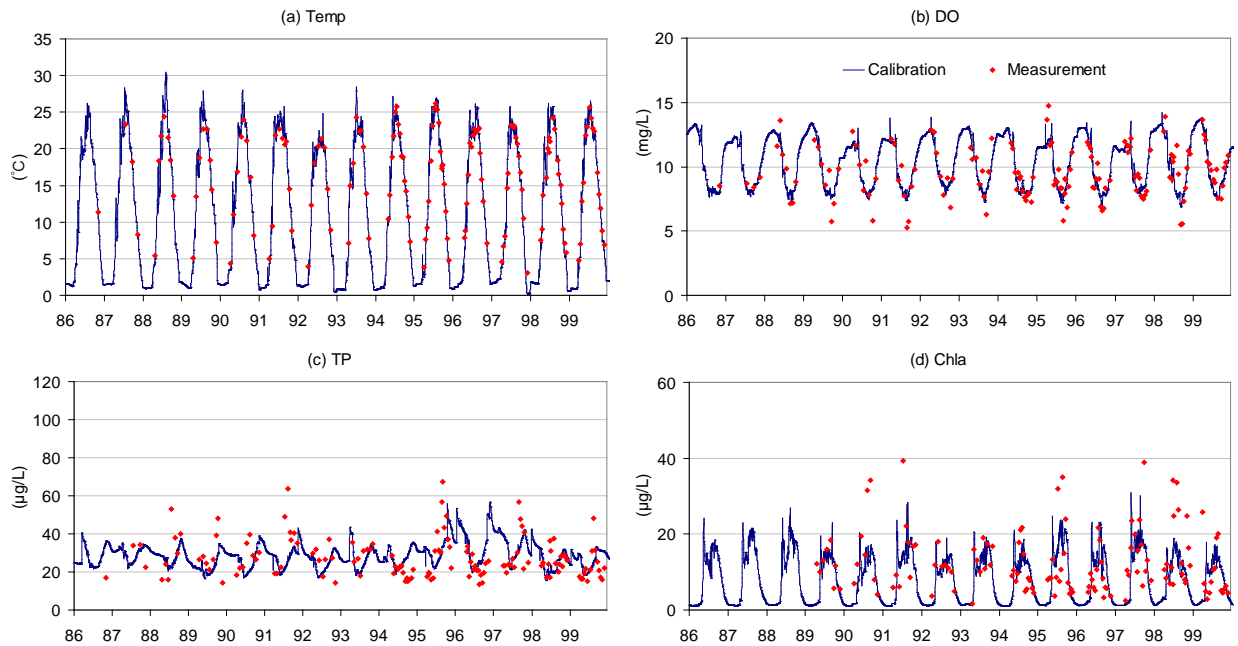


Figure 5.10. Model calibration: Simulated and measured daily Temp and concentrations of DO, TP and Chla in the epilimnion layer, 1986-1999.

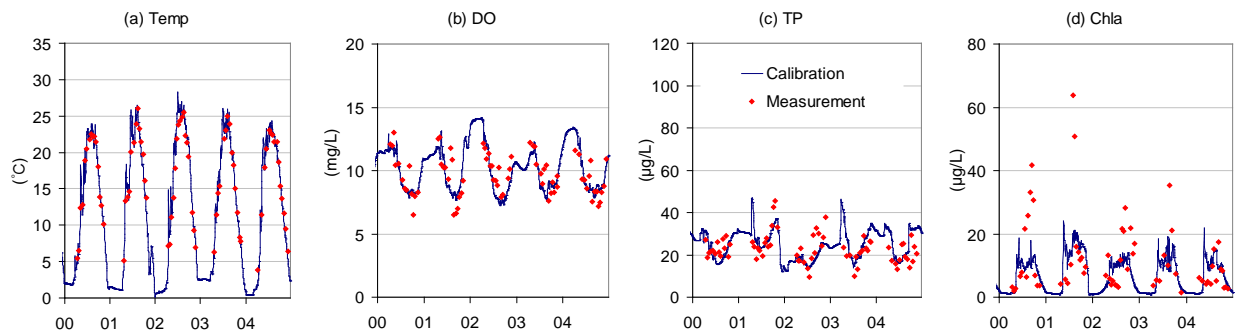


Figure 5.11. Model validation: Simulated and measured daily Temp and concentrations of DO, TP and Chla in the epilimnion layer, 2000-2004.

Reservoir model calibration and validation

In this study, a hybrid genetic algorithm (HGA) consisting of a real-encoded genetic algorithm (a global search method) (Haupt and Haupt, 2004) and the Nelder-Mead simplex (NMS) algorithm (a local search method) (Nelder and Mead, 1965) is used as an optimization algorithm to vary the values of the 18 sensitive parameters. An overall objective function is designed to measure the degree of fitness between the measurements and the predicted values of the selected variables including Temp, DO, TP and Chla. A more detailed description of the HGA and the overall objective function is given by Huang and Liu (2010).

The model was calibrated against the measured data over the time period of 1986-1999, while model validation was performed using 2000-2004 data. The calibrated parameter values are presented in table 5.8. Figure 5.10 depicts (for example) the time series of simulated daily Temp, DO, TP and Chla in the epilimnion layer. It can be observed that the simulated values match the measurements reasonably well for the calibration period.

Figure 5.11 shows the validation results, i.e. simulated and measured Temp, DO, TP and Chla in epilimnion and hypolimnion layers over the validation period. It can also be observed that the simulated values match the measurements reasonably well.

Summary and Conclusions

In this study, an automated procedure is implemented to calibrate a one-dimensional reservoir model which is set up to simulate the hydrothermal structure and water quality of Cannonsville reservoir. The calibrated model produces simulated values that match the observed data reasonably well for calibration and validation time periods.

6. Model Data Acquisition and Organization

6.1. GIS Data Development for Modeling

Water Quality Monitoring Sites

Additional locations were added throughout the reporting period to the ArcSDE feature class of DEP water quality monitoring sites (“aqua.ARCLIB.wq_monitor_site”). The dataset is comprised of DEP stream, reservoir, and keypoint monitoring sites, active and inactive, that are included in the Laboratory Information Management System (LIMS). A spatial view in the geodatabase joins each record of the feature class to attribute data found in LIMS and in the Site Assessment and Management Inventory (SAMI) database. These non-spatial attribute databases are stored in SQL Server. The largest numbers of sites added to the dataset were those indicating East of Hudson WWTP locations and new sampling sites on the lower Esopus Creek downstream of Ashokan Reservoir.

DEP Meteorological Stations

The ArcSDE feature class of DEP meteorological stations was updated to reflect installation of an additional site.

SSURGO2 Soil Data

SSURGO2 soil data were used in conjunction with the Soil Data Viewer extension for ArcGIS to derive additional soil property layers for the West of Hudson watershed. These layers included soil porosity, field capacity, wilting point, and root zone depth. Additionally, these soil property layers were overlaid on a raster of wetness index classes for Hollowtree Brook and Biscuit Brook in order to obtain mean values of each soil property per wetness index class.

Hydrologic Buffer Analyses

The GIS was used for an analysis of agricultural lands within buffers of hydrographic features in the Cannonsville basin. Similarly, an analysis of remediated septic systems was performed within buffers of hydrographic features in the Cannonsville and Pepacton basins.

GWLF Constants Input (CIN) Tool

The GWLF CIN tool implemented in ArcView 3 to derive model input parameters for a user-selected drainage area was used to derive CIN files for the drainage areas of USGS stream gages at Hollowtree Brook, Biscuit Brook, and Richardsville.

Stream Power

Preliminary work began on using ArcGIS ModelBuilder to derive values of stream power, a function of stream gradient and stream discharge, for each cell of raster representations of select tributaries to Esopus Creek in the Ashokan basin. The work continues into the next reporting period.

Additional Support to Staff

Data development efforts of lesser significance and mapping support were provided throughout the reporting period to various members of the DEP modeling unit and other staff of the Watershed Water Quality Science and Research Division. A majority of this support was related to preparation of DEP reports, peer-reviewed publications, conference posters, and conference presentations. Such events included the annual Watershed Science Technical Conference, the Catskill Environmental Monitoring Conference, and the annual meeting of the American Geophysical Union, among others.

6.2. Time Series Data Development

An inventory of time series data used for watershed and reservoir model input and calibration is presented in Tables 6.1 and 6.2, respectively. The time series data includes meteorology, streamflow, water quality, and point source loads for watershed models. For reservoir models the data includes meteorology, streamflow, stream, reservoir and key point water quality and reservoir operations. Data sets are updated as new data become available. Lag times between the current date and the dataset end dates are the result of QA/QC processes at the data source and/or procurement timelines driving the acquisition of any purchased data.

For this reporting period, the following dataset updates have been added to the inventory: Northeast Regional Climate Center Meteorology, USGS Streamflow, DEP Stream and Limnology Water Quality, DEP Key Point and NYSDEC Water Quality through calendar year 2010.

The NYSDEC Water Quality data has provided the Modeling Section with a robust dataset from baseline and storm event sampling of the West Branch of the Delaware River at Beerston from 1992 to the present. Historically the DEC has collected the samples and calculated the nutrient loads. DEP now calculates the nutrient loads and has done so through WY 2010. This dataset has provided the Modeling Section with valuable nutrient load estimates used as inputs into the Cannonsville Reservoir model.

Table 6.1. Inventory of data used for watershed modeling.

Data Type	Data Source	Data Description	Dates*	Modeling Needs
Meteorology	Northeast Regional Climate Center	Daily Precipitation and Max/Min Temperature	Pre 1960-2010	Model Input
Wastewater Treatment Plants	DEP	Monthly WWTP Nutrient Loads	1990-2009	Model Input
Streamflow	USGS	Daily and Instantaneous Streamflow	Pre 1960-2010**	Hydrology Module Calibration / Nutrient and Sediment Loads
Water Quality	DEP	Routine and Storm Stream Monitoring	1987-2010	Nutrient and Sediment Loads for Water Quality Calibration
	DEC	Stream Monitoring at West Branch Delaware River	1992-2010	Nutrient and Sediment Loads for Water Quality Calibration

*Dates represent total span for all data sets combined. Individual station records vary.

** Calendar year 2010 stream flow data is provisional from November to December and will be replaced once the USGS has finalized their water year 2011 dataset.

Table 6.2. Inventory of data used for reservoir modeling.

Data Type	Data Source	Data Description	Dates*	Modeling Needs
Meteorology	DEP	Air Temp., Relative Humidity, Solar Radiation., PAR, Wind Speed, Wind Direction, and Precipitation	1994-June, 2010	Model Input
Key Point and Reservoir Operations	DEP	Tunnel Water Quality, Flow and Temp.; Reservoir Storage, Spill, Withdrawal, and Elevation	1987-2010	Model Input
Streamflow	USGS	Daily and Instantaneous Streamflow	Pre 1960-2010**	Model Input
Stream Hydrology	DEP	Stream Water Quality, Flow and Temperature	1987-2010	Model Input
Limnology	DEP	Reservoir Water Quality, and Temperature Profiles	1992-2010	Model Input

*Dates represent total span for all data sets combined. Individual station records vary.

** Calendar year 2010 stream flow data is provisional from November to December and will be replaced once the USGS has finalized their water year 2011 dataset.

7. Modeling Program Collaboration

7.1. Participation in Ongoing External Research Projects

In the last year the Water Quality Modeling Section has participated in several projects related to the Sections' work on climate change as outlined in DEP's Climate Change Integrated Monitoring Project (CCIMP).

Water Research Foundation Project 4262 - Vulnerability Assessment and Risk Management Tools for Climate Change: Assessing Potential Impacts and Identifying Adaptation Options

The main focus of the CCIMP is to identify potential climate change impacts on the water supply using the structured quantitative framework of water quality models. Project 4262 compliments the CCIMP by going one step further. Once climate change impacts have been identified this project seeks to develop risk management approaches that will help managers prioritize risks and decide on a course of action. During the past year DEP has contributed significantly to this project and a more detailed description of our contribution is given in section 4.7 of this report.

Water Research Foundation Project 4306 – Analysis of Reservoir operations under Climate Change

The OASIS system operation model is being used by the Water Quality Modeling Section to investigate the effects of climate change on water supply storage and reservoir operations. Project 4306 will compliment CCIMP use of the OASIS model. Key to the prediction of system operations is knowledge of the constraints, demands and operating rules which are used by OASIS to predict operations. Analyzing future reservoir operations, and how they differ from those used under current conditions will clearly benefit the CCIMP and allow us to better tailor OASIS to simulation of future conditions,. Project 4306 will also strive to develop adaptive strategies in response to climate change. The modeling section will be well positioned to support this goal due to our past experience in simulating reservoir turbidity to support operational decisions, our support of OST development, and our work with climate change. Hydrologics, the developer of the OASIS model and Hazen and Sawyer the contractor responsible for development of the reservoir operation support tool (OST) will also be participants in project 4306. This insures that DEP will obtain assistance with modeling issues related to CCIMP use of OASIS and the OST, and that project deliverables have direct relevance to DEP's modeling efforts. Work on this project has not yet started, but we expect that the modeling section will participate in this project during 2012.

Water Utility Climate Alliance (WUCA) Piloting Utility Modeling Applications (PUMA)

WUCA is a group of ten of the nation's largest water utilities, whose mission is to improve research on the effects of climates change on drinking water supplies, and to help water supplies to develop strategies to cope with the potential impact of climate change (<http://www.wucaonline.org>). The purpose of the PUMA project is: (1) to identify climate modeling tools and techniques that are appropriate for analysis of climate change impacts on water supplies; (2) develop guidelines for the use of climate data and model simulation data

including methodologies for describing uncertainty; (3) to suggest how these data can be used to support water supply planning and decision making; (4) to build and enhance collaboration between water utilities and NOAA Regional Integrated Sciences and Assessment (RISA) centers; and (5) to identify future research investments that would serve the water utility community. The Water Quality Modeling Section has participated in the WUCA/PUMA project by attending the project kickoff meeting in December 2010, and by participating in regular phone conferences and planning meetings since then. The NYC water supply and the work undertaken as part of the CCIMP will be highlighted as a case study in a white paper that will be product of the PUMA project.

7.2. Modeling Program Contract Management

Presently the Water Quality Modeling Section is managing three contracts which provide data that are used for testing, calibrating and verifying models used by the group. In some cases these contracts also provide support for the development and testing of models used by the group. The modeling section is also managing a contract with the research foundation of the City University of New York (CUNY-RF), which provides technical support for model and data development. These contacts are listed below.

Contractor: Upstate Freshwater Institute.

Contract Title: Integrated Program of Measurement, Process Studies and Modeling for the Turbidity Problem as Schoharie Creek and Esopus Creek.

This contract involves data collection, process studies and the development and testing of turbidity models in Schoharie, Ashokan and Kensico Reservoirs. Models developed by this project are routinely used by the Water Quality Modeling Section to predict turbidity levels in the above reservoirs, and these models have also been incorporated in to the DEP Operation Support Tool (OST). This contract is scheduled to end in December of 2012.

Contractor: Upstate Freshwater Institute.

Contract Title: Robotic Monitoring of Selected New York City Reservoirs and Major Tributaries

This contract involves setting up a network of automated reservoir monitoring buoys and stream water quality monitoring stations through the Catskill reservoir system (Schoharie and Ashokan Reservoirs), Kensico Reservoir and Rondout Reservoir. The emphasis is on turbidity measurements. Near real time turbidity data is collected from three stream monitoring sites and eight reservoir monitoring buoys. Data from this system is used by DEP to monitor reservoir turbidity levels as an aid to operational decisions (particularly at times of elevated turbidity), and to provide data to initialize and verify DEP reservoir turbidity transport models. It is planned that data from the monitoring network will be input to the OST. The contract will end in December of 2011, after which operation of the network will transition to DEP.

Contractor: United States Geological Survey.

Contract Title: Turbidity and Suspended Sediment Monitoring in the Upper Esopus Creek Watershed, Ulster County, NY

This contract involves retrofitting the five existing USGS flow gauges in the Esopus Creek watershed to automatically monitor turbidity at high (15 min) frequency. These five stations will provide a high frequency record of flow and turbidity that will allow the Water Quality Modeling Section to evaluate temporal and spatial variations in turbidity transport within the Esopus creek watershed; develop improved turbidity vs. discharge rating relationships; and collect high quality data that can be used to develop and test watershed sediment erosion and transport models. This project is scheduled to end in 2013.

Contractor: Research Foundation City University of New York.

Contract Title: Scientific Modeling Support

This contract provides CUNY with the funding needed to hire seven post-doctoral research associates (post-docs) who are jointly advised by CUNY faculty and DEP scientists. The post docs are stationed in Kingston, New York working with the Water Quality Modeling Section on a day-to-day basis. The positions are for an initial two year period, with the possibility of an additional two year extension. This project is scheduled to end in 2013.

The present post-doc positions are for

- Climate Data Analysis
- Reservoir system modeling
- Reservoir turbidity modeling
- Reservoir eutrophication modeling
- Watershed nutrient modeling
- Watershed sediment erosion and transport modeling
- Forest ecosystem modeling

7.3. Applications for External Research Funding

During the last year the Water Quality Modeling Section has worked with universities and government agencies to prepare three funding proposals that would support research initiatives that would improve the Water Quality Modeling Section's modeling capability and modeling database. The Water Quality Modeling Section took an active role in planning and formulating these projects and also thoroughly reviewed these projects before they were submitted to the funding agencies. All of these projects are currently under review. If funded the modeling section will participate in the projects and the New York City water supply will be used as a case study region.

Project Proposal : How do Changing Climate Extremes Influence Natural Organic Matter and Turbidity in Drinking Water Systems? Modeling, Experiments, and Insight from New York City, a Representative Unfiltered System

Principle Investigator: Upmanu Lall, Columbia University

Funding Agency : US EPA

There is increasing evidence that the intensity and frequency of extreme precipitation events are increasing, and many future climate scenarios also predict increases in extreme events. The purpose of this project is to develop tools that will better estimate changes in frequency and intensity of extreme events, and also the likelihood of multiple extreme events occurring together in time. The project proposes to examine the effects of the timing and intensity of extreme events on watershed loss (loading) of natural organic matter and turbidity, which will affect reservoir drinking water quality.

Project Proposal: Use of Satellite Data to Improve Model Simulations of Snow, Streamflow, and Water Supply for the NYC Water Supply System

Principle Investigator: Dorothy K. Hall, NASA / Goddard Space Flight Center (GSFC)

Funding Agency: NASA

Snow makes up about 15% of the annual precipitation entering the New York City West of Hudson (WOH) water supply region. Although not a major proportion of the annual precipitation, snow plays an important role in defining reservoir operating policies, and changes in snow accumulation, melt and winter stream flow are some of the major expected effects of climate change on the WOH watersheds. The purpose of this project is to provide DEP with more spatially resolute estimates of snow cover and snow water equivalent (SWE) by using and merging microwave and optical remote sensing products. If successful the data obtained will be used to better refine estimates of watershed snow accumulation and to test and improve modeling algorithms that simulate snow accumulation and melt.

Project Proposal: Application of evapotranspiration and soil moisture remote sensing products to enhance hydrological modeling for decision support in the New York City water supply

Principle Investigator: Nir Y. Krakauer, The City College of New York Center for Remote Sensing of the Earth Science and Technology

Funding Agency: NASA

Soil moisture is a key hydrologic state variable, and evapotranspiration is a key process that affects summer streamflow. Correctly specifying these in our watershed models is important to ensure accurate hydrologic simulations. Furthermore, since soil moisture and evapotranspiration are expected to be influenced by future climate change, correctly representing them in our watersheds models will be critical for simulating the future changes in watershed hydrology, especially during summer periods when low flows and drought conditions could occur. The purpose of this project is to evaluate shortwave, thermal, and microwave remote sensing products that could provide DEP with independent and spatially variable estimates of soil moisture and evapotranspiration. If these products can be obtained, they will be used to test, calibrate and verify watershed hydrologic models in the WOH region under present climate conditions. It is expected that this will lead to more accurate estimate of contemporary summer streamflow and decrease the uncertainty in simulations of future streamflow.

8. Modeling Program Scientific Papers and Presentations

8.1. Published Work

Below is a listing of journal articles in which Water Quality Modeling Section members have been authors during the previous year. Copies of the articles are included in Appendix A of this report.

Anandhi, A., A. Frei, S.M. Pradhanang, M.S. Zion, D.C. Pierson and E.M. Schneiderman. 2011. AR4 climate model performance in simulating snow water equivalent over Catskill Mountain watersheds, New York, USA. *Hydrological Processes*, published online.

Anandhi, A., A. Frei, D.C. Pierson, E.M. Schneiderman, M.S. Zion, D. Lounsbury and A.H. Matonse. 2011. Examination of change factor methodologies for climate change impact assessment. *Water Resources Research*, **47**: W03501

Matonse, A.H., D.C. Pierson, A. Frei, M.S. Zion, E.M. Schneiderman, A. Anandhi, R. Mukundan and S.M. Pradhanang. 2011. Effects of changes in snow pattern and the timing of runoff on NYC water supply system. *Hydrological Processes*, **25**: 3278-3288.

O'Donnell, S.M., R.K. Gelda, S.W. Effler and D.C. Pierson. 2011. Testing and Application of a Transport Model for Runoff Event Inputs for a Water Supply Reservoir. *Journal of Environmental Engineering*, **137**(8): 678-688.

Owens, E.M., R.K. Gelda, S.W. Effler, P.J. Rusello, E.C. Cowen and D.C. Pierson. 2011. Modeling Resuspension in a Dynamic Water Supply Reservoir. *Journal of Environmental Engineering*, **137**(7): 585-595.

Pierson, D.C., G.A. Weyhenmeyer, L. Arvola, B. Benson, T. Blenckner, T. Kratz, D.M. Livingstone, H. Markensten, G. Marzec, K. Petterson and K. Weathers. 2011. An automated method to monitor lake ice phenology. *Limnology and Oceanography: Methods*, **9**: 74-83.

Pradhanang, S.M., A. Anandhi, R. Mukundan, M.S. Zion, D.C. Pierson, E.M. Schneiderman, A. Matonse and A. Frei. 2011. Application of SWAT model to assess snowpack development and streamflow in the Cannonsville watershed, New York, USA. *Hydrological Processes*, **25**: 3268-3277.

Tilahun, S.A., R. Mukundan, B.A. Demisse, C. Guzman, B.C. Tarakegn, T.A. Engda, Z.M. Easton, A.S. Collick, A.D. Zegeye, E.M. Schneiderman, J-Y. Parlange and T.S. Steenhuis. 2011. A Saturation Excess Erosion Model. *International Symposium on Erosion and Landscape Evolution CD-Rom Proceedings*, (18-21 September 2011, Hilton Anchorage, Anchorage Alaska) St. Joseph, Michigan ASABE.

Zion, M.S., S.M. Pradhanang, D.C. Pierson, A. Anandhi, D.G. Lounsbury, A.H. Matonse and E.M. Schneiderman. 2011. Investigation and Modeling of winter streamflow timing and magnitude under changing climate conditions for the Catskill Mountain region, New York, USA. *Hydrological Processes*, **25**: 3289-3301.

8.2. Conference Presentations

During this reporting period members of the Water Quality Modeling Section have made presentations regarding our modeling activities at a number of scientific meetings. Below the presentations and associated abstracts are listed for each of the meetings

Catskill Environmental Monitoring and Research Conference. November 2010. Pine Hill, New York.

Pierson, D.C., E. Schneiderman, M. Zion, A. Anandhi, A. Matonse 2010. *Evaluating the Impacts of Climate Change on New York City Reservoir Watersheds: Program Development and Ongoing Challenges.*

Abstract:

The New York City Department of Environmental Protection (DEP) has developed a suite of computer models that simulate watershed hydrology, sediment and nutrient transport; reservoir eutrophication, turbidity transport; and reservoir system operation. These models when coupled together have been successfully used to evaluate watershed management effects on reservoir water quality. In 2008, DEP adapted its modeling system to evaluate the additional potential effects of climate change on the NYC water supply. The program involved continued testing and improvement to the modeling system, as well as developing expertise in climate data analysis, and forest modeling. The purpose of this talk is to describe the rationale behind the development of our climate change research program, to give some initial results describing potential impacts of climate change on the water supply, and to identify uncertainty in our predictions. Future research challenges are also identified.

Zion, M., E. Schneiderman, D. Pierson and A. Matonse 2010. *Simulation Modeling for NYC Water Supply Operations to Control Turbidity – Spring 2010 Case Study.*

Abstract:

Turbidity is a primary factor that potentially limits use of the NYC Catskill System Water Supply. The impacts of turbidity to the reservoir system can be mitigated by operating the system to minimize turbidity inputs to the terminal Kensico Reservoir while maximizing the storage and settling capacity of the up-basin Catskill System reservoirs. During turbidity events daily decisions are carefully taken to optimize system operations for turbidity control. To support these decisions, simulation models are used to evaluate alternative operational scenarios within a probabilistic framework.

In the spring 2010 a series of storms and accumulation of a deep snowpack lead to elevated levels of turbidity in Catskill System reservoirs, and raised concerns that future runoff could lead to even greater levels of turbidity. Model simulations were performed to analyze the use of the Ashokan waste channel and the blending of Catskill and Delaware System waters to minimize turbidity inputs to Kensico reservoir, and examine the implications of the large snowpack in further increasing turbidity inputs during the snowmelt season. Model results provided guidance for system operations through the spring 2010 season.

American Geophysical Union Meeting. December 2010. San Francisco, California.

Anandhi, A., S.M. Pradhanang, A. Frei, D.C. Pierson, R. Mukundan, A.H. Matonse, E.M. Schneiderman, M.S. Zion and D. Lounsbury 2010. *Uncertainties In Future Climate Over NYC Watersheds In AR4 Model Projections.*

Abstract:

The uncertainties in the future climate from a suite of Global climate models (GCMs), are studied for the west of Hudson (WOH) watersheds of the New York City (NYC) water supply for special report of emission scenarios (SRES A1B, A2 and B1). These WOH watersheds supply 90% of the water consumed by NYC. The uncertainties are studied seasonally for daily timescale for various combinations of meteorological variables. As the confidence in a GCMs future climate scenario depends on its ability or skill to simulate the present day 20th Century climate conditions (20C3M). The objective of this study is to bring out the uncertainties in future climate in relation to GCMs skill in simulating the 20C3M climate. We believe that the uncertainties in future climate of the region would be less for GCMs with high skill score when compared to GCMs with low skill score.

Matonse, A.H., D.C. Pierson, A. Frei, M.S. Zion and R. Mukundan, 2010. *Effects of changes in seasonal precipitation in Catskill Mountain region on NYC water supply system management.*

Abstract:

Simulated future air temperature and precipitation derived from General Circulation Models (GCMs) are used as input to the Generalized Watershed Loading Functions – Variable Source Area (GWLF-VSA) watershed model to simulate future inflows to reservoirs that are part of the New York City Water Supply System (NYCWSS). This ongoing study focuses on the effect of projected changes in temperature and rainfall in the Catskill Mountain region and consequent changes in snow accumulation, snowmelt and the timing of runoff on NYC water supply system storage and operation as simulated by the NYC reservoir system OASIS model. Future scenarios that use current system operation rules and demands, but changed reservoir inflows, suggest that changes in precipitation and snowmelt in this region will affect water availability on a seasonal basis. Despite increased evapotranspiration during non-winter periods, greater runoff earlier in the winter period leads to a reduction in the number of days the system is under drought conditions, and earlier reservoir refill in the spring. Since reservoir storage levels fill up earlier in winter, total volume of water releases and spills also appear to increase during the winter. Of importance is how much (if any) indication of this possible future trend is already captured in current observations and at what level these changes will require operation rules to be adjusted in order to continue to achieve the management objectives of the system.

Mukundan, R., D.C. Pierson, E.M. Schneiderman, D. O'Donnell, A.H. Matonse and M.S. Zion, 2010. *Suspended Sediment Transport Dynamics in the Esopus Creek Watershed, New York*.

Abstract:

Sediment loads of rivers can exert an important control on the use of a river for water supply and other designated uses. The vast majority of the suspended sediments (SS) are transported during high flow events and therefore it is important to quantify the sediment flux during these events. A case study for estimating SS loads in streams from the Catskill region of New York State is presented. Transport of suspended sediment is of concern in the streams of the Esopus Creek Watershed that drains into the Ashokan reservoir, one of the drinking water reservoirs in the New York City water supply system. During and following high stream discharge events, turbidity increased in streams entering the reservoir causing impacts to the reservoir water quality. Turbidity estimation based on a rating curve as a function of stream flow alone tends to show a high level of uncertainty in turbidity load prediction in this watershed. The objective of this study was to understand the underlying factors controlling the uncertainty in the turbidity rating curve at the watershed outlet. Our results clearly indicate that use of additional variables in a stream flow based turbidity rating curve can improve turbidity predictions. These predictor variables relate to spatial variability in runoff and geology, soil moisture condition, and season. Improved capability to quantify turbidity during such events may help in developing predictive models that can support management of water resources.

Pradhanang, S.M., Z.M. Easton, E. Schneiderman, M.S. Zion, T.S. Steenhuis, 2010
Intercomparison of SWAT models in simulating hydrology of Cannonsville Reservoir Watershed.

Abstract:

The Soil and Water Assessment Tool (SWAT) model is a watershed scale hydrologic model created to simulate long term runoff and nutrient losses in rural, agriculturally dominated watersheds. The important model inputs are climate, soil, elevation and land use information. In this study, three versions of SWAT models namely SWAT2005, SWAT2009 and SWAT-WB (water balance) are used to simulate hydrology of the Cannonsville Watershed. The SWAT-2005 and 2009 model hydrologic response units (HRU's) are grouped according to soil type and plant cover while in SWAT-WB a soil topographic index is used to delineate the HRUs. Runoff for each HRU is calculated with the SCS curve number method in SWAT 2005 and 2009. In SWAT-WB the curve number routine is replaced by saturation excess runoff mechanisms where surface runoff occurs when the soils become saturated. These models are calibrated using Dynamically Dimensioned Search and Shuffled Complex Evolutionary & Uncertainty Analysis with 10 years of data for the Cannonsville Watershed and then used to predict an additional eight years of data. The models are evaluated by comparison to the discharge at the watershed outlet as well as the spatial distribution of runoff source area in selected parts of the watershed where the spatial information is available.

**American Water Resources Association, Spring Specialty Conference. April 2011.
Baltimore, Maryland.**

Anandhi, A., M.S. Zion, A. Frei, D.C. Pierson, E.M. Schneiderman, S.M. Pradhanang, D. Lounsbury, R. Mukundan, A.H. Matonse, Y. Huang, N. Samal and G. Tang. 2011. *Estimating the impact of climate change on precipitation, temperature and streamflow over watershed in Catskill Mountain region of New York, USA.*

Abstract:

Understanding the effects of climate change on a water supply involves developing plausible future climate scenarios which can then be used in a hydrologic model to determine water supply specific concerns.

A number of methods are available to derive plausible future scenarios of precipitation and temperatures from Global Climate Models (GCM). For this study two methods based on GCM simulations are explored for the Catskill Mountain region of New York State. The methods are: (1) variant of Change Factor Methodology (CFM), sometimes referred to as “delta change methodology” and (2) bias correction of GCM. The scenarios of daily time series of precipitation and temperature from these two methods are input to Generalized Watershed Loading Function (GWLf) model to estimate future scenarios of streamflow.

The objective of this study is to analyze the future scenarios of daily precipitation, temperatures and streamflow to evaluate the potential effects of climate change on the NYC water supply. This work is part of a program to evaluate the impact of climate change on New York City (NYC) water supply. The Catskill region includes the watersheds for the New York City (NYC) water supply. Analyses are performed for fifteen GCMs contributing to the Fourth Assessment Report of the Intergovernmental Panel on Climate Change (IPCC-AR4) for three emissions scenarios (SRES A1B, A2 and B1). The results demonstrate that climate change impact assessment is dependent on the method that is used to develop future climate scenarios.

Pradhanang, S.M., E.M. Schneiderman, R. Mukundan, A. Anandhi, M. Zion, D. Pierson, A. Matonse, Y. Huang, N.R. Samal, G. Tang and T. Steenhuis, 2011. *The effect of climate change on nitrogen and phosphorus loadings in New York City water supply watersheds.*

Abstract:

Streams transport many biologically important nutrients, of which, nitrogen (N) and phosphorus (P) are known to limit productivity in streams. Studies indicate that higher annual temperatures, increased growing season length, and increased dormant season precipitation are likely to occur across the northeastern United States in response to changing climate. Such changes can have pronounced effect on the hydrologic behavior of the watersheds. Since water movement into the soil profile and across the landscape is the primary mechanism of sediment and nutrient transport, it follows that changes in temperature and precipitation patterns would affect nutrient loadings to streams and reservoirs. This study assesses the potential impacts of climate change on nutrient

loadings in New York City water supply watersheds. Using a Soil and Watershed Assessment (SWAT) model, a baseline scenario with an “as is” distribution of meteorological forcing and current management practices was simulated. The model was then used to simulate changes in nutrient loading under projected climate scenarios and land use managements. The differences in nitrogen and phosphorus loads from future simulations analysis indicate the relative effects that might be expected due changing climate and/or management practices or combination of both.

15th Workshop on Physical Processes in Natural Waters. July 2011. Burlington, Ontario, Canada.

Samal, N.R., D.C. Pierson, Y. Huang, J.S. Read, A. Anandhi, E.M. Owens. 2011. *Impact of climate change on Cannonsville reservoir thermal structure in the New York City Water Supply.*

Abstract:

The thermal structure of lakes and reservoirs is an important regulator of biogeochemical processes, and a property that is well simulated using mechanistic hydrodynamic models. A one-dimensional reservoir model is applied to examine the thermal structure in two deep reservoirs: the Cannonsville and Pepacton reservoirs that are located in Delaware County, approximately more than 100 miles northwest of New York City, and are an important part of the New York City water supply. The impact of climate change on the thermal structure of these reservoirs is investigated as part of a larger study of the effects of climate change on the physical processes occurring within the reservoir system. Future climate data obtained from GCMs is used to produce local (downscaled) scenarios to drive the reservoir models. Comparisons between simulations based on present day climate data and future simulations are used to evaluate a number of metrics that describe reservoir thermal structure, stability and mixing. The development and break down of thermal structure in these systems during various withdrawal scenarios has been considered and possible effects of climate change on the New York City’s drinking water supply system are discussed.

Huang, Y.T., D. Pierson, A. Frei, N. Samal, E. Schneiderman, M. Zion, S.M. Pradhanang, A.H. Matonse, E. Owens, 2011. *Hydrothermal and water quality model calibration and application to the evaluation of land use change and watershed management programs.*

Abstract:

Located in Delaware County, New York, Cannonsville Reservoir was constructed to provide water supply for New York City. A one-dimensional hydrothermal and water quality model has been set up to simulate the thermal stratification, nutrient levels and phytoplankton biomass in the reservoir. This study aims to improve the model performance through automated calibration using a long-term record of measured reservoir water quality data and apply the model to the evaluation of the effects of land

use change and watershed management programs on the water quality in the reservoir. To implement automated model calibration, a hybrid genetic algorithm (HGA) consisting of a real-encoded genetic algorithm and the Nelder-Mead simplex (NMS) algorithm is developed as an optimization algorithm, and an overall objective function is designed to measure the degree of fitness between the measurements and the predicted values of the selected variables including temperature, dissolved oxygen, total phosphorus and chlorophyll a. The HGA and the objective function are used to calibrate the hydrothermal and water quality model by comparison with long-term measured reservoir water quality data. The output of the calibrated model matches the measured values reasonably well. The calibrated model is then used in conjunction with a watershed model to evaluate the effects of land use change and watershed management programs. The watershed model is used to simulate the changes in nutrient loading caused by land use change and watershed management programs. The calibrated reservoir model is used to evaluate the effects of the changes in nutrient loading on reservoir water quality and it predicts the significant improvement of reservoir water quality.

Watershed Science and Technical Conference. September 2011. West Point, New York.

Matonse, A.H., A. Frei, D.C. Pierson, E. Schneiderman. 2011. *Simulated effects of climate change on NYC reservoir system versus historical trends – What can we learn?*

Abstract:

A recent study of the possible effects of climate change on New York City water supply indicates that projected future changes in air temperature and precipitation are likely to have an impact on the streamflow regime in the Catskill region of New York and on NYC reservoir system operations (Matonse et al. 2011). Scenarios that use current system operation rules and water demands together with future simulated Catskill reservoir inflows, suggest that in the future, greater runoff will occur earlier in the winter period, causing the reservoirs to refill earlier in the year. Since reservoir storage levels fill up earlier, total volume of water releases and spills also appear to increase during the winter. Despite increased evapotranspiration during non-winter periods, future simulations suggest that increased precipitation will lead to a reduction in the number of days the system is under drought conditions. Based on these results the NYC water supply will continue to show high resilience, high annual reliability and relatively low vulnerability. This presentation focuses on analyzing the future simulated results in conjunction with statistics and trends developed from local historical data. The central question is how much indication (if any) of the simulated future states of the system can be detected from trends in current observations and if other insights can be obtained from this analysis to improve our modeling methodology and better address the effects of climate change on NYC water supply.

Mukundan, R., D. Pierson, E. Schneiderman and M. Zion. 2011. *Catskill Stream Turbidity Sources and the Effect of Extreme Events*.

Abstract:

Elevated turbidity associated with high stream discharges in the Esopus Creek watershed in the Catskill region of New York State can sometimes limit the use of a part of the drinking water supply from the Ashokan reservoir. Previous analysis indicates that the Esopus Creek watershed contributes over 90% of the annual turbidity load to Ashokan Reservoir, and that as much as 93% of the stream turbidity in the Esopus Creek originates from within the stream channels during large events. The focus of this talk is on methods of quantifying turbidity sources and evaluating the persistence of effects related to extreme events on stream turbidity levels during the low flow periods between events. Low flow periods account for only a small portion of the annual turbidity load, but do account for a large portion of DEP's turbidity monitoring data. Ambient stream turbidity monitoring data from six monitoring stations in the Catskill region were statistically evaluated before and after two extreme events that occurred in 1996 and 2005-2006 period.

After the 1996 event elevated turbidity levels in the Schoharie reservoir and the transport of this turbid water via the Shandaken tunnel resulted in an extended period of elevated low flow turbidity in the Esopus Creek. Tributaries to the Schoharie reservoir also showed significant increases in turbidity during this period. The 2005-2006 events did not result in a prolonged increase in Esopus Creek low flow turbidity. In fact, there was a significant decrease in low flow turbidity that can be attributed to a significant decrease during recent years in the turbidity of the main tributary to Schoharie Reservoir. Tributaries to the Esopus Creek did not show any significant change in turbidity after either event. Such varying watershed responses to extreme events are suggestive of the existence of a geomorphic threshold that could be either intrinsic and related to the geomorphic structure of the system, or extrinsic and related to climate forcing.

Pradhanang, S., E. Schneiderman, D. Pierson and M. Zion. 2011. *Effects of land use and management on dissolved nutrient loads and eutrophication in Cannonsville Reservoir under NYC Filtration Avoidance*.

Abstract:

Since the first NYC Filtration Avoidance Determination (FAD) granted by the USEPA in 1993 NYC has funded an aggressive campaign to reduce nutrient loads and eutrophication in Cannonsville Reservoir. Waste Water Treatment Plants (WWTPs) have been upgraded to reduce point source of nutrients, and watershed management programs have implemented best management practices (BMPs) to control nutrients from agriculture, urban runoff, and septic systems. At the same time a shift in land use towards reduced agriculture and farm livestock has also occurred independently of deliberate land use management. Considerable reductions in nutrient loads and eutrophication in Cannonsville Reservoir have been observed in stream and reservoir water quality monitoring data collected between 1992 and 2009.

Watershed and reservoir simulation models were used to evaluate the factors responsible for the observed changes in Cannonsville water quality. Reductions in dissolved phosphorus (P) loads to the reservoir were mainly attributable to Waste Water Treatment Plant (WWTPs) upgrades, implementation of agricultural BMPs by the Watershed Agricultural Program, and decline in farm livestock. Loading reductions produce improvements in reservoir water quality by not only reducing the long term mean values of epilimnetic chlorophyll, but by also dramatically reducing the frequency of extreme chlorophyll values; which is important since it is extreme events rather than long term averages which actually influence the usability of the reservoirs as sources of drinking water.

M. Zion, A. Matonse, D. Pierson and E. Schneiderman, 2011. *Simulation Modeling for NYC Water Supply Operations to Control Turbidity – 2010 Case Study.*

Abstract:

The New York City Water Supply obtains the majority of its water from the Catskill and Delaware subsystems, and water from these subsystems mix at Kensico Reservoir prior to entering the water supply distribution system. Turbidity is a primary factor that potentially limits use of the Catskill System water. The impacts of this turbidity to the water supply as a whole can be mitigated by operating the system to minimize turbidity inputs to the terminal Kensico Reservoir while maximizing the storage and settling capacity of upstream Catskill System reservoirs. During turbidity events daily decisions are carefully taken to optimize system operations for turbidity control, while ensuring adequate water storage levels. To support these decisions, a combination of watershed, reservoir water quality and water system simulation models are used to evaluate alternative operational scenarios within a probabilistic framework. These simulation models form the basis for the Operational Support Tool currently under development by DEP.

During the fall and winter of 2010 a number of storms caused elevated levels of turbidity in Catskill System reservoirs. As these storm events occurred, various model simulations were performed to analyze the effects of alternative operational strategies on Kensico Reservoir effluent water quality. Operational strategies investigated included use of the Ashokan Reservoir waste channel, implementation of stop shutters in the Catskill Aqueduct to limit flow of turbid water into Kensico Reservoir and the blending of Catskill and Delaware System waters to maintain adequate water quality in Kensico effluents. This presentation describes model simulation results which helped to inform system operation decisions during these periods of elevated Catskill System turbidity.

American Water Work Association – New York Section Edwin C. Tiftt, Jr. Water Supply Symposium. September 2011. Liverpool, New York

Zion, M.S. D.C. Pierson, E.M. Schneiderman, A. Anandhi, A.H. Matonse, S.M. Pradhanang, R. Mukundan, Y. Huang, N. Samal, A. Frei and L. Janus, 2011. *Evaluation of Potential Effects of Climate Change on the New York City Water Supply*

Abstract:

The New York City Department of Environmental Protection (DEP) has developed a Climate Change Assessment and Action Plan (CCAP) that outlines the strategies that DEP is undertaking to address potential climate change effects on the drinking water, stormwater and wastewater systems of New York City.

One element of the CCAP has been expanding the development of an integrated modeling system to further understand the implications of potential future climate changes on the quantity and quality of the New York City (NYC) Water Supply. This modeling project utilizes climate change projections as input to an integrated suite of models including watershed hydrology and water quality models, a water system operations model, and reservoir hydrothermal and water quality models.

Recent predictions of future climate for the northeast U.S. generally indicate greater annual precipitation and increased temperatures compared to current climate conditions. These climate changes could potentially produce longer growing seasons, increased evapotranspiration, earlier snowpack melting, changes in the magnitude of streamflow events, differences in proportion of streamflow due to overland flow, shifts in the timing of sediment and nutrient delivery to the reservoirs, and changes in the timing and intensity of reservoir thermal stratification.

The integrated modeling system can be used to better understand how the interplay of these potential changes will affect the NYC Water Supply System. Utilizing watershed, reservoir, and water system models together provides a framework for evaluating feedback between flows and loads entering the reservoir, reservoir water quality, water demand, and water system operations. Scenarios incorporated within the integrated modeling framework provide a greater understanding of the combined impacts of climate change on the water supply quantity and quality.

Preliminary model simulations are presented that demonstrate how the integrated models are used to investigate climate change effects. Various statistical measures of water system quantity and quality including drought indicators, frequency of occurrence of turbidity limits and frequency of exceeding threshold chlorophyll and phosphorus concentrations are examined in order to place the results in the context of DEP's water supply concerns.

9. References

- Aber, J.D., S.V. Ollinger, C.A. Federer, D.W. Kicklighter, J.M. Melillo, R.G. Lathrop, Jr. and J.M. Ellis. 1995. Predicting the effects of climate change on water yield and forest production in the Northeastern U.S. *Climate Research* **5**, 207–222.
- Allen C.R. and C.S. Holling. 2010. Novelty, Adaptive Capacity, and Resilience. *Ecology and Society* **15**(3): 24. [online] URL: <http://www.ecologyandsociety.org/vol15/iss3/art24/>
- Anandhi, A., A. Frei, D. C. Pierson, E. M. Schneiderman, M. S. Zion, D. Lounsbury, and A. H. Matonse. 2011. Examination of change factor methodologies for climate change impact assessment. *Water Resources Research*, **47**:W03501.
- Arnold, J.G. and P.M. Allen. 1999. Methods for estimating baseflow and groundwater recharge from streamflow. *Journal of the American Water Resources Association*, **35**: 411-424.
- Arvola, L., G. George, D.M. Livingstone, M. Jarvinen, T. Blenckner, M.T. Dokulil, E. Jennings, C.N. Aongusa, P. Noges, T. Noges and G.A. Weyhenmeyer. 2009. The impact of changing climate on the thermal characteristics of lakes, D.G. George (ed.) *The impact of climate change on European lakes, Aquatic Ecology series 4*, DOI 10.1007/978-90-481-2945-4_6, Springer, pp. 85-101.
- Asselman, N. E. M. 1999. Suspended sediment dynamics in a large drainage basin: the River Rhine. *Hydrological Processes*, **13**:1437-1450.
- Auble G.T., J.M. Friedman, S.M.L. 1994. Relating riparian vegetation to present and future streamflows. *Ecological Applications*, **4**:544-554.
- Bagnold, R.A., 1977. Bedload transport in natural rivers. *Water Resources Research*, **13**: 303–312.
- Bates, B.C., Kundzewicz, Z.W., Wu, S., Palutikof, J.P., 2008. Climate Change and Water. Technical Paper of the Intergovernmental Panel on Climate Change. Geneva: IPCC Secretariat.
- Benestad R. 2010. Downscaling precipitation extremes. *Theoretical and Applied Climatology*, **100**: 1-21
- Borowiak, D., J. Baranczuk and K. Nowinski. 2008. The directions of the thermal stratifications of upper Radunskie lake as a result of observed climatic changes., *Balwois 2008-Ochrid, Republic of Macedonia*-**27**, 31 May 2008.
- Bunn S.E. and A.H. Arthington. 2002. Basic Principles and Ecological Consequences of Altered Flow Regimes for Aquatic Biodiversity. *Environmental Management*, **30**:492-507. DOI: 10.1007/s00267-002-2737-0.

Burns D.A., J. Klaus, and M.R. McHale. 2007. Recent climate trends and implications for water resources in the Catskill Mountain region, New York, USA, *Journal of Hydrology*, **336**, 155-170.

Christensen, N.S., A.W. Wood, D.P. Lettenmaier and R.N. Palmer. 2004. Effects of Climate Change on the Hydrology and Water Resources of the Colorado River Basin. *Climatic Change*, **62**, 337–363.

Colby, B. R. 1956. The relationship of sediment discharge to streamflow. *USGS Open File Rep.*, Reston, VA.

Cole, T.M. and E.M. Buchak. 1995. CE-QUAL-W2: A Two-Dimensional, Laterally Averaged, Hydrodynamic and Water Quality Model, Version 2.0. U.S. Army Corps of Engineers, Vicksburg, MS.

Coon, W. 2005. Hydrologic Evidence of Climate Change in Monroe County, NYS., US Geological Survey. OFR 2008-1199.

Crawford, C.G. 1991. Estimation of suspended-sediment rating curves and mean suspended-sediment loads. *J. Hydrol.*, **129**: 1–4.

DEP. 2004. Multi Tiered Water Quality Modeling Program Semi-Annual Status Report – EPA Filtration Avoidance Deliverable Report. New York City Department of Environmental Protection, Valhalla, New York. July 2004.

DEP, 2006a. 2006 Long-Term Watershed Protection Program. New York City Department of Environmental Protection, Valhalla, New York. 2006.

DEP, 2006b. Watershed Protection 2006 Watershed Protection Program Summary and Assessment. New York City Department of Environmental Protection, Valhalla, New York. 2006.

DEP. 2007. Multi Tiered Water Quality Modeling Program Annual Status Report – EPA Filtration Avoidance Deliverable Report. New York City Department of Environmental Protection, Valhalla, New York. October 2007.

DEP. 2008a. Climate Change Program: Assessment and Action Plan. New York, NY. May 2008.

DEP, 2008b. Multi Tiered Water Quality Modeling Program Annual Status Report – EPA Filtration Avoidance Deliverable Report. New York City Department of Environmental Protection, Valhalla, New York. October 2009.

DEP. 2008c. Evaluation of Turbidity Reduction Potential through Watershed Management in the Ashokan Basin. Valhalla, New York. July 2008

DEP, 2009. Multi Tiered Water Quality Modeling Program Annual Status Report – EPA Filtration Avoidance Deliverable Report. New York City Department of Environmental Protection, Valhalla, New York. October 2009.

DEP, 2010. Multi Tiered Water Quality Modeling Program Annual Status Report – EPA Filtration Avoidance Deliverable Report. New York City Department of Environmental Protection, Valhalla, New York. October 2010.

DEP, 2011. 2011 Watershed Protection Program Summary and Assessment. New York City Department of Environmental Protection, Bureau of Water Supply, NY. March 2011.

Devore, J.L. 2000. *Probability and Statistics for Engineering and the Sciences*, 5th Edition, Duxbury-Thomson Learning, CA, USA.

Doerr, S.M., E.M. Owens, R.K. Gelda, M.T. Auer and S.W. Effler. 1998. Development and testing of a nutrient-phytoplankton model for Cannonsville Reservoir. *Lake and Reservoir Management* **14**, 301-321.

Ducré-Robitaille, J.F., L.A. Vincent and G. Boulet. 2003. Comparison of techniques for detection of discontinuities in temperature series, *International Journal of Climatology*, **23**: 1087-1101.

Easton, Z. M., D.R. Fuka, E.D. White, A.S. Collick, B. Biruk Asharge, M. McCartney, S.B. Awulachew, A.A. Ahmed and T.S. Steenhuis, T.S. 2010a. A multi basin SWAT model analysis of runoff and sedimentation in the Blue Nile, Ethiopia. *Hydrology and Earth System Sciences*, **7**: 3837–3878.

Easton Z.M., M.T. Walter, D.R. Fuka, E.D. White and T.S. Steenhuis. 2010b. A simple concept for calibrating runoff thresholds in quasi-distributed variable source area watershed models. *Hydrological Processes*, **25**:3131-3143. DOI: 10.1002/hyp.8032.

Easton Z.M., D.R. Fuka, M.T. Walter, D.M. Cowan, E.M. Schneiderman and T.S. Steenhuis. 2008. Re-conceptualizing the soil and water assessment tool (SWAT) model to predict runoff from variable source areas. *Journal of Hydrology*, **348**:279-291.

Edwards A. C. and P.J.A. Withers. 2008. Transport and delivery of suspended solids, nitrogen and phosphorus from various sources to freshwaters in the UK. *Journal of Hydrology* **350**, 144-153.

Ernstson, H., S.E. van der Leeuw, C.L. Redman, D.J. Meffert, G. Davis, C. Alfsen, T. Elmqvist. 2010. Urban Transitions: On Urban Resilience and Human-Dominated Ecosystems, *AMBIO Report*, doi:10.1007/s13280-010-0081-9, Royal Swedish Academy of Sciences, www.kva.se/en

Fitzjohn, C., J.L. Ternan and A.G. Williams, 1998. Soil moisture variability in a semi-arid gully catchment: Implications for runoff and erosion control. *Catena* **32**, 55–70.

- Ferguson, R. I. 1986. River loads underestimated by rating curves. *Water Resources Research*, **22**: 74–76.
- Gan T.Y. 1998. Hydroclimatic trends and possible climatic warming in the Canadian Prairies. *Water Resour. Res.*, **34**. DOI: doi:10.1029/98WR01265.
- Gannett Fleming & Hazen and Sawyer. 2007. Catskill turbidity control study: Phase III Final Report, Prepared for New York City Department of Environmental Protection, Bureau of Engineering Design and Construction.
- Garmestani A.S., C.R. Allen, and L.H. Gunderson. 2009. Panarchy: discontinuities reveal similarities in the dynamic system structure of ecological and social systems. *Ecology and Society* **14**(1): 15. [online] URL: <http://www.ecologyandsociety.org/vol14/iss1/art15/>
- Gelda, R. K. and S. W. Effler. 2007. Modeling Turbidity in a Water Supply Reservoir: Advancements and Issues. *Journal of Environmental Engineering*, **133**: 139–148.
- Gibson C.A., J.L. Meyer, N.L. Poff, L.E. Hay and A. Georgakakos. 2005. Flow regime alterations under changing climate in two river basins: implications for freshwater ecosystems. *River Research and Applications*, **21**:849-864. DOI: 10.1002/rra.855.
- Groves, D. G., and R. J. Lempert. 2007. A new analytic method for finding policy-relevant scenarios, *Global Environ. Change*, **17**, 73– 85.
- Haith, D. A., R. Mandel, and R. S. Wu. 1992. GWLF: Generalized Watershed Loading Functions User's Manual, Vers. 2.0. (Computer program manual). Cornell University, Ithaca, N.Y.
- Hauer F.R., J.S. Baron, D.H. Campbell, K.D. Fausch, S.W. Hostetler G.H. Leavesley, P.R. Leavitt, D.M. McKnight and J.A. Stanford J.A. 1997. Assessment of Climate Change and Freshwater Ecosystems of the Rocky Mountains, USA and Canada. *Hydrological Processes*, **11**:903-924.
- Haupt, R.L. and S.E. Haupt. 2004. *Practical Genetic Algorithms*. John Wiley & Sons, Inc.
- Hay, L.E., , R.L. Wilby, and G.H. Leavesley. 2000, A comparison of delta change and downscaled GCM scenarios for three mountainous basins in the United States, *Journal American Water Resources Association* **36**(2), 387-397.
- Hicks, D.M., J. Hill, and U. Shankar, 1996. Variation of suspended sediment yields around New Zealand: The relative importance of rainfall and geology, *IAHS Publ.* 236, 149-156.
- Hirsch, M.R., D.R. Helsel, T.A. Cohn and E.J. Gilroy. 1993. Statistical analysis of hydrologic data, In Maidment D R, 1993, *Handbook of Hydrology*, McGraw-Hill Inc., New York, Chapter 17: 1-55.

- Hondzo, M. and H.G. Stefan. 1991. Three case studies of lake temperature and stratification response to warmer climate. *Water Resources Research*, **27**(8):1837-1846.
- Horowitz, A. J., 2003. An evaluation of sediment rating curves for estimating suspended sediment concentrations for subsequent flux calculations. *Hydrological Processes*, **17**:3387-3409.
- Huang, Y.T. and L. Liu. 2008. A hybrid perturbation and Morris approach for identifying sensitive parameters in surface water quality models. *Journal of Environmental Informatics* **12**(2):150-159.
- Huang, Y.T. and L. Liu 2010. Multiobjective water quality model calibration using a hybrid genetic algorithm and neural network-based approach. *Journal of Environmental Engineering* **136**(10), 1020-1031.
- Hutchinson, G.E. 1957. *A Treatise on Limnology, Volume 1*. John Wiley & Sons, Inc, New York. pp. 1015.
- HydroLogics, Inc. 2007 *User Manual for OASIS with OCL*, Columbia, MD
- Imberger J. and J.C. Patterson. 1990. Physical limnology. *Advances in Applied Mechanics* **27**: 303-475
- IPCC. 2007a. Climate Change., 2007: Impacts, Adaptation and Vulnerability. Contribution of Working Group II to the Fourth Assessment Report of IPCC. Cambridge, United Kingdom and New York, NY, USA: Cambridge University Press, 2007.
- IPCC. 2007b. Climate Change 2007: The Physical Science Basis. Contribution of Working Group I to the Fourth Assessment Report of the Intergovernmental Panel on Climate Change., in: S. Solomon, D. Qin, M. Manning (Ed.).
- James, E., P. Kleinman, T. Veith, R. Stedman, and A. Sharpley. 2007. Phosphorus contributions from pastured dairy cattle to streams of the Cannonsville Watershed, New York. *Journal of Soil and Water Conservation* **62**:40-47.
- Jarvie H. P., E. Lycett, C. Neal and A. Love. 2002. Patterns in nutrient concentrations and biological quality indices across the upper Thames river basin, UK. *Science of The Total Environment*, **282-283**: 263-294.
- Jarvie H. P., C. Neal, P.J.A. Withers, D.B. Baker, R.P. Richards and A.N. Sharpley. 2010. Quantifying Phosphorus Retention and Release in Rivers and Watersheds Using Extended End-Member Mixing Analysis (E-EMMA). *J. Environ. Qual.* **40**, 492-504.
- Jones, I., J. Sahlberg and I. Persson. 2009. Modelling the impact of climate change on the thermal characteristics of lakes, D.G. George (ed.) *The impact of climate change on European lakes, Aquatic Ecology series 4*, DOI 10.1007/978-90-481-2945-4_6, Springer, pp. 103-120.

- Lempert, R. J., S. W. Popper, and S. C. Bankes. 2003. *Shaping the Next One Hundred Years: New Methods for Quantitative, Long-Term Policy Analysis*, 187 pp., RAND, Santa Monica, Calif.
- Lenzi, M. A. and L. Marchi. 2000. Suspended sediment load during floods in a small stream of the Dolomites (northeastern Italy). *Catena*, **39**:267-282.
- Lockwood D.R. and J.A. Lockwood. 2008. Grasshopper population ecology: catastrophe, critically, and critique. *Ecology and Society* **13** (1): 34. [online]
URL: <http://www.ecologyandsociety.org/vol13/iss1/art34/>
- Longabucco, P. and M.R. Rafferty. 1998. Analysis of material loading to Cannonsville Reservoir: Advantages of event-based sampling. *Lake and Reservoir Management*, **14**: 197-212.
- Lund, R. and L. Reeves. 2002. Detection of undocumented changepoints: a revision of the two-phase regression model. *Journal of Climate - Notes and correspondence*, **15**: 2547-2554.
- Lyon S.W., M.T. Walter, P. Gérard-Marchant and T.S. Steenhuis T.S. 2004. Using a topographic index to distribute variable source area runoff predicted with the SCS curve-number equation. *Hydrological Processes*, **18**:2757-2771. DOI: 10.1002/hyp.1494.
- MacKay, M. D., P.J. Neale, C.D. Arp, L.N.De. Senerpont Domis, X. Fang, G. Gal, K.D. Joehnk, G. Kirillin, J.D. Lenters, E. Litchman, S. MacIntyre, P. Marsh, J. Melack, W.-M. Mooij, R. Peeters, A. Quesada, S.G. Schladow, M. Schmid, C. Spence and S.L. Stokes. 2009. Modeling lakes and reservoirs in the climate system. *Limnol. Oceanogr.*, **54**(6, part 2): 2315–2329.
- Markensten, H. and D. Pierson. 2007. Weather driven influences on phytoplankton succession in a shallow lake during contrasting years: application of PROTBAS. *Ecological Modelling*, **207**, 128-136.
- Major, D. C., R. Horton, and C. Rosenzweig. 2007. Integrated Modeling Project for Water Quantity and Quality Guidelines for Project. Columbia University Earth Institute, Center for Climate Systems Research.
- Matonse, A. H., D. C. Pierson, A. Frei, M. S. Zion, E. M. Schneiderman, A. Anandhi, R. Mukundan, and S. M. Pradhanang. 2011. Effects of changes in snow pattern and the timing of runoff on NYC water supply system. *Hydrological Processes*, **25**:3278-3288.
- Mauget, S.A. 2003. Multidecadal regime shifts in US streamflow, precipitation, and temperature at the end of the twentieth century. *Journal of Climate*, **16**:3905-3916.
- Mukundan, R., D. E. Radcliffe, J. C. Ritchie., L. M. Risse and R. A. McKinley. 2010. Sediment Fingerprinting to Determine the Source of Suspended Sediment in a Southern Piedmont Stream. *Journal of Environmental Quality*, **39**(4): 1328-1337.

- Mulholland P.J., E.R Marzolf, J.R. Webster, D.R. Hart and S.P. Hendricks 1997. Evidence that hyporrheic zones increase heterotrophic metabolism and phosphorus uptake in forest streams. *Limnology and Oceanography* **42**:443-451.
- McCabe G.J. and D.M. Wolock. 2002. A step increase in streamflow in the conterminous United States. *Geophysics Research Letters*, **29**:2185. DOI: doi:10.1029/2002GL015999.
- Morris, M.D. 1991. Factorial sampling plans for preliminary computational experiments. *Technometrics*, **33**(2): 161-74.
- Mukundan, R., D. E. Radcliffe, J. C. Ritchie., L. M. Risse and R. A. McKinley. 2010. Sediment Fingerprinting to Determine the Source of Suspended Sediment in a Southern Piedmont Stream. *Journal of Environmental Quality*, **39**(4): 1328-1337.
- Nash, J. E., and Sutcliffe, J. V. 1970. River flow forecasting through conceptual models – Part I: a discussion of principles. *Journal of Hydrology*, **10**: 282–290.
- Neal, C., H. P. Jarvie, R. Williams, A. Love, M. Neal, H. Wickham, S. Harman, and L. Armstrong. 2010. Declines in phosphorus concentration in the upper River Thames (UK): Links to sewage effluent cleanup and extended end-member mixing analysis. *Science of The Total Environment* **408**:1315-1330.
- Neitsch, S.L., J.G. Arnold, J.R. Kiniry and J.R. Williams, 2005. Soil and Water Assessment Tool: Theoretical Documentation – Version 2005. Grassland, Soil and Water Research Laboratory, Agricultural Research Service. January 2005
- Nelder, J.A. and R. Mead. 1965. A simplex method for function minimization. *The Computer Journal* **7**, 308-313.
- Nunes, J.P., J. Seixas, J.J. Keizer. 2011. Modeling the response of within-storm runoff and erosion dynamics to climate change in two Mediterranean watersheds: A multi-model, multi-scale approach to scenario design and analysis. *Catena*. doi:10.1016/j.catena.2011.04.001.
- Owens, E.M. 1998. Development and testing of a one-dimensional hydrothermal models of Cannonsville Reservoir. *Lake and Reservoir Management*, **14**, 172-185.
- Parry, M.L., C. Rosenzweig, A. Iglesias, M. Livermore and G. Fischer. 2004. Effects of climate change on global food production under SRES emissions and socioeconomic scenarios. *Global Environmental Change*, **14**, 53-67
- Perreault L., J. Bernier and E. Parent. 2000. Bayesian changepoint analysis in hydrometeorological time series. Part 1. The normal model revised, *J. Hydrol.*, **235**:221-241
- Pimentel, D., C. Harvey, P. Resosudarmo, K. Sinclair, D. Kurz, M. McNair, S.Crist, L. Shpritz, L. Fitton, R. Saffouri, and R. Blair. 1995. Environmental and economic costs of soil erosion and conservation benefits. *Science*, **267**:1117–1123.

Poff, N. and J. Ward. 1990. Physical habitat template of lotic systems: Recovery in the context of historical pattern of spatiotemporal heterogeneity. *Environmental Management*, **14**:629-645. DOI: 10.1007/bf02394714.

Poff, N.L., J.D. Allan, M.B. Bain, J.R. Karr, K.L. Prestegard, B.D. Richter, R.E. Sparks and J.C. Stromberg. 1997. The Natural Flow Regime. *BioScience*, **47**:769-784.

Pradhanang, S.M., A. Anandhi, R. Mukundan, M.S. Zion, D.C. Pierson, E.M. Schneiderman, A. Matonse, A. Frei. 2011. Application of SWAT model to assess snowpack development and streamflow in the Cannonsville watershed, New York, USA. *Hydrological Processes*, **25**:3268-3277. DOI: 10.1002/hyp.8171.

Read, J.S., et al. 2001. Derivation of lake mixing and stratification indices from high-resolution lake buoy data. *Environmental Modelling & Software*, doi:10.1016/j.envsoft.2011.05.006

Restrepo, J.D., B. Kjerfve, M. Hermelin and J.C. Restrepo, 2006. Factors controlling sediment yield in a major South American drainage basin: the Magdalena River, Colombia. *Journal of Hydrology* 316:213-232.

Reynolds, C.S., A.E. Irish and J.A. Elliott. 2001. The ecological basis for simulating phytoplankton responses to environmental change (PROTECH). *Ecological Modelling*, **140**, 271-291.

Richter B.D., J.V. Baumgartner, J. Powell and D.P. Braun. 1996. A Method for Assessing Hydrologic Alteration within Ecosystems. *Conservation Biology* **10**:1163-1174.

Richter B.D., R. Mathews, D.L. Harrison and R. Wigington. 2003. Ecologically sustainable water management: Managing river flows for ecological integrity. *Ecological Applications*, **13**:206-224. DOI: doi:10.1890/1051-0761.

Risbey J.S., D. Entekhabi D. 1996. Observed Sacramento Basin streamflow response to precipitation and temperature changes and its relevance to climate impact studies. *Journal of Hydrology*, **184**:209-223.

Rodionov, S.N. 2004. A sequential algorithm for testing climate regime shifts, *Geophysical Research Letters*, **31**, L09204, doi:10.1029/2004GL019448

Rodionov, S.N. 2006. Use of prewhitening in climate regime shift detection. *Geophysical Research Letters*, **33**, L12707, doi:10.1029/2006GL025904

Rodionov, S. and L. E. Overland. 2005. Application of a sequential regime shift detection method to the Bering Sea ecosystem. *ICES Journal of Marine Science*, **62**: 328-332, doi:10.1016/j.icesjms.2005.01.013

Rood, S.B., J.M. Mahoney, D.E. Reid, L. Zilm. 1995. Instream flows and the decline of riparian cottonwoods along the St. Mary River, Alberta. *Canadian Journal of Botany*, **73**:1250-1260.

Saltelli, A., Tarantola, S., Campolongo, F. and Ratto, R. 2004. *Sensitivity Analysis in Practice: a Guide to Assessing Scientific Models*. John Wiley & Sons Ltd, Chichester.

Scheffer M, J. Bascompte, W.A. Brock, V. Brovkin, S.R. Carpenter, V. Dakos, H. Held, E. H. van Nes, M. Rietkerk and J. Sugihare. 2009. Early-warning signals for critical transitions, Macmillan Publishers Limited, Reviews – *Nature*, **461**:53-59, doi:10.1038/nature08227.

Schmidt, W. 1928. Über Temperatur and Stabilitätsverhältnisse von Seen. *Geographiska Annaler*, **10**, 145-177.

Schneiderman, E.M., D.C. Pierson, D.G. Lounsbury and M.S. Zion. 2002. Modeling the Hydrochemistry of the Cannonsville Watershed with Generalized Watershed Loading Functions (GWLf). *Journal of the American Water Resources Association*, **38**(5):1323-1347.

Schneiderman, E. M., T. S. Steenhuis, D. J. Thongs, Z. M. Easton, M. S. Zion, A. L. Neal, G. F. Mendoza, and M. T. Walter. 2007. Incorporating variable source area hydrology into the curve number based Generalized Watershed Loading Function model. *Hydrol. Process.*, **21**:3420-3430.

Seeger, M., M.P. Errea, S. Beguería, J. Arnáez, C. Martí, J. M. García-Ruiz. 2004. Catchment soil moisture and rainfall characteristics as determinant factors for discharge/suspended sediment hysteretic loops in a small headwater catchment in the Spanish Pyrenees. *Journal of Hydrology*, **288**(3-4): 299-311.

Sharpley A. N., P.J.A. Kleinman, P. Jordan, L. Bergstrom and A.L. Allen. 2009. Evaluating the success of phosphorus management from field to watershed. *Journal of Environmental Quality*. **38**, 1981-1988.

Stuntebeck, T.D., M.J. Komiskey, D.W. Owens, and D.W. Hall. 2008. *Methods of data collection, sample processing, and data analysis for edge-of-field, stream gaging, subsurface-tile, and meteorological stations at Discovery Farms and Pioneer Farm in Wisconsin, 2001-7*. United States Geological Survey, Reston, VA.

Syviski, J. P., M.D. Morehead, D.V. Bahr, and T. Mulder. 2000. Estimating fluvial sediment transport: the rating parameters. *Water Resour. Res.*, **36**(9): 2747–2760.

Tamene, L., S. J. Park, R. Dikau, P. L. G. Vlek. 2006. Analysis of factors determining sediment yield variability in the highlands of northern Ethiopia. *Geomorphology* **76**(1-2): 76-91.

Thomas, R. B. 1988. Monitoring baseline suspended sediment in forested basins: The effects of sampling of suspended sediment rating curves. *Hydrol. Sci. J.*, **33**(5): 499–514.

UFI (Upstate Freshwater Institute). 2001. Calibration, Verification of a One-Dimensional Hydrothermal and Eutrophication Model for Catskill/Delaware Reservoirs.

USDA-NRCS. 2000. Soil Survey Geographic (SSURGO) database for Delaware County, New York

USEPA. 2009. National water quality inventory report to Congress. Available at <http://www.epa.gov/305b/> (verified 23 Sep. 2010).

Walling, D. E. 2009. The Impact of Global Change on Erosion and Sediment Transport by Rivers: Current Progress and Future Challenges. UNESCO-IHP The United Nations World Water Development Report 3 Available at <http://unesdoc.unesco.org/images/0018/001850/185078e.pdf> (Accessed Sept 23, 2010)

Washington-Allen R.A., D.D. Briske, H.H. Shugart and L.F. Salo. 2009. Introduction to special feature on catastrophic thresholds, perspectives, definitions, and applications, *Ecology and Society* **15**(3): 38. [online] URL: <http://www.ecologyandsociety.org/vol15/iss3/art38/>

White, E.D., Z.M. Easton, D.R. Fuka, A.S. Collick, E. Adgo, M. McCartney, S.B. Awulachew, Y.G. Selassie and T.S. Steenhuis. 2011. Development and application of a physically based landscape water balance in the SWAT model. *Hydrological Processes* **25**, 915–925.

Withers P. J. A. and H.P. Jarvie. 2008. Delivery and cycling of phosphorus in rivers: A review. *Science of The Total Environment*, **400**, 379-395.

Wolman, M.G. and J.P. Miller. 1960. Magnitude and frequency of forces in the geomorphic processes. *J. Geol.*, **68**:54–74.

Zabaleta A., M. Martínez, J. Uriarte, and I. Antigüedad. 2007. Factors Controlling Suspended Sediment Yield During Runoff Events In Small Headwater Catchments Of The Basque Country. *Catena*, **71**: 179-190.

Zion, M. S., S. M. Pradhanang, D. C. Pierson, A. Anandhi, D. G. Lounsbury, A. H. Matonse, and E. M. Schneiderman. 2011. Investigation and Modeling of winter streamflow timing and magnitude under changing climate conditions for the Catskill Mountain region, New York, USA. *Hydrological Processes*, **25**:3289-3301.

Appendix A:

Journal Articles by members of Water Quality Modeling Section

Anandhi, A., A. Frei, S.M. Pradhanang, M.S. Zion, D.C. Pierson and E.M. Schneiderman. 2011. AR4 climate model performance in simulating snow water equivalent over Catskill Mountain watersheds, New York, USA. *Hydrological Processes*, published online.

Anandhi, A., A. Frei, D.C. Pierson, E.M. Schneiderman, M.S. Zion, D. Lounsbury and A.H. Matonse. 2011. Examination of change factor methodologies for climate change impact assessment. *Water Resources Research*, **47**: W03501

Matonse, A.H., D.C. Pierson, A. Frei, M.S. Zion, E.M. Schneiderman, A. Anandhi, R. Mukundan and S.M. Pradhanang. 2011. Effects of changes in snow pattern and the timing of runoff on NYC water supply system. *Hydrological Processes*, **25**: 3278-3288.

O'Donnell, S.M., R.K. Gelda, S.W. Effler and D.C. Pierson. 2011. Testing and Application of a Transport Model for Runoff Event Inputs for a Water Supply Reservoir. *Journal of Environmental Engineering*, **137**(8): 678-688.

Owens, E.M., R.K. Gelda, S.W. Effler, P.J. Rusello, E.C. Cowen and D.C. Pierson. 2011. Modeling Resuspension in a Dynamic Water Supply Reservoir. *Journal of Environmental Engineering*, **137**(7): 585-595.

Pierson, D.C., G.A. Weyhenmeyer, L. Arvola, B. Benson, T. Blenckner, T. Kratz, D.M. Livingstone, H. Markensten, G. Marzec, K. Petterson and K. Weathers. 2011. An automated method to monitor lake ice phenology. *Limnology and Oceanography: Methods*, **9**: 74-83.

Pradhanang, S.M., A. Anandhi, R. Mukundan, M.S. Zion, D.C. Pierson, E.M. Schneiderman, A. Matonse and A. Frei. 2011. Application of SWAT model to assess snowpack development and streamflow in the Cannonsville watershed, New York, USA. *Hydrological Processes*, **25**: 3268-3277.

Tilahun, S.A., R. Mukundan, B.A. Demisse, C. Guzman, B.C. Tarakegn, T.A. Engda, Z.M. Easton, A.S. Collick, A.D. Zegeye, E.M. Schneiderman, J-Y. Parlange and T.S. Steenhuis. 2011. A Saturation Excess Erosion Model. *International Symposium on Erosion and Landscape Evolution CD-Rom Proceedings*, (18-21 September 2011, Hilton Anchorage, Anchorage Alaska) St. Joseph, Michigan ASABE.

Zion, M.S., S.M. Pradhanang, D.C. Pierson, A. Anandhi, D.G. Lounsbury, A.H. Matonse and E.M. Schneiderman. 2011. Investigation and Modeling of winter streamflow timing and magnitude under changing climate conditions for the Catskill Mountain region, New York, USA. *Hydrological Processes*, **25**: 3289-3301

AR4 climate model performance in simulating snow water equivalent over Catskill Mountain watersheds, New York, USA

Aavudai Anandhi,^{1*} Allan Frei,^{1,2} Soni M. Pradhanang,¹ Mark S. Zion,³ Donald C. Pierson³ and Eliot M. Schneiderman³

¹ CUNY Institute for Sustainable cities, City University of New York, New York, NY, 10065

² Hunter College, City University of New York, New York, NY, 10065

³ Water Quality Modeling Group, New York City Department of Environmental Protection, 71 Smith Avenue, Kingston, NY, 12401

Abstract:

In this study, we evaluate the ability of GCMs participating in the Intergovernmental Panel for Climate Change's (IPCC) Fourth Assessment Report (AR4) to simulate variability in the snow water equivalent (SWE) in New York City Water Supply watersheds located northwest of NYC in the Catskill Mountains. SWE is estimated using an empirical temperature-based degree day model. Inputs to this model are either measured with historical meteorological (1961–2000) data or a GCM model output for the same historical period. The evaluation of the GCMs is based on a skill score developed using probability distribution functions derived from the time series of simulated snowpack. From the skill scores (SS) calculated, the GCMs are ranked based on their ability to simulate the snowpack. These results have implications for selecting a subset of GCM simulations for climate change impact assessments in New York City's water supply.

Results show that the GFDL 2.0 (gf001) model has the highest SS (0.93) and CCSM (ncc09) model has the lowest SS (0.26). On the basis of the SS, the GCM ensemble members are classified into three categories: high, medium and low performance. The probability density functions for the three performance classes show the largest between-model variability for models in low performance class. Differences between the means and medians of observation-based model simulation and GCM-based simulation were greatest in the low-performance class. Copyright © 2011 John Wiley & Sons, Ltd.

KEY WORDS snow water equivalent; evaluation AR4 models; global climate models; probability-based skill score; temperature-based snowmelt algorithm; GWLF

Received 15 July 2010; Accepted 23 May 2011

INTRODUCTION

Snowmelt runoff is an important source of water in the watersheds of the New York City water supply that provide about ninety percent of the New York City's (NYC) daily water demand. One hydrologic change that has been observed in this region during the period of 1952–2005 is a shift in the timing of snowmelt runoff to earlier in the year (Burns *et al.*, 2007; Zion *et al.*, 2010). As climate continues to change, the contribution of spring snowmelt to streamflow will also change. Given the fact that changes in snowmelt runoff in Catskill Mountain (West of Hudson (WOH)) watersheds have potentially important implications for the water supply of New York City, there is a need to study the potential impacts of climate change on the quantity of snowmelt runoff in these watersheds. For this purpose, data derived from a suite of Global Climate Models (GCMs) are being used to drive watershed models to study snowmelt runoff in the absence of observed snow data.

Presently, the output from GCMs related to snow and snowmelt are only available at monthly timescales. Snow cover fraction (SCF), a GCM output is diagnostically derived from prognostic variables: snow water equivalent (SWE) or snow depth (SD). The details of the studies that have examined GCMs with respect to snow are given in Table I. From the table it can be observed that snow simulations (SWE, surface albedo, SD, SCF, snow mass, snow cover area) from GCMs are evaluated at monthly, seasonal and annual timescales using measures such as annual cycle, frequency distribution, mean, median, decadal scale variability (Foster *et al.*, 1996; Yang *et al.*, 1999; Frei *et al.*, 2003, 2005; Frei and Gong, 2005; Roesch, 2006; Roesch and Roeckner, 2006).

The watershed models used to study the hydrology in the NYC WOH region are run at daily timescales. Higher temporal resolution snow data can be obtained indirectly by modelling SWE at daily timescales using daily simulations derived from GCMs. Different approaches of varying complexity are possible, ranging from simple regression equations, blackbox approaches based only on temperature measurements to physics-based models containing equations for all the processes involved, or complete multilayer models based on an energy balance

* Correspondence to: Aavudai Anandhi, CUNY Institute for Sustainable cities, City University of New York, New York, NY, 10065.
E-mail: aavudaia@dep.nyc.gov

Table I. Literature review

S.N	Variable name	Region of study	Time scale	Evaluation metric	GCMs	References
1	Snow cover, Snow mass	North America, Eurasia	Mean monthly	Climatology plots	Hadley centre, CGCM, GENESIS, ECHAM, GISS, GLA, ARIES	(Foster <i>et al.</i> , 1996)
2	Snow mass, extent	Mid-latitude Grasslands in Russia, California	Month	Monthly time series plots	CCSM (BATS)	(Yang <i>et al.</i> , 1999)
3	Snow cover area (SCA)	North America, Eurasia	Month	Interannual variability	18 GCMs participating in AMIP-1	(Frei <i>et al.</i> , 2003)
4	SCA	North America	Annual, decadal	mean, Decadal scale variability (DSV)	21 GCMs participating in IPCC-AR4	(Frei and Gong, 2005)
5	SWE	North America	Month, seasonal,	Box and whisker plots, monthly mean and standard deviation, Pearson correlation coefficient	18 GCMs participating in AMIP-1	(Frei <i>et al.</i> , 2005)
6	SWE, Snow cover fraction (SCF), surface albedo	North America, Eurasia	Month, seasonal	Annual cycle, biases, frequency distribution	Most GCMs participating in IPCC-AR4	(Roesch, 2006)
7	SCF, SD	Eurasia	Month	Annual cycle, frequency distribution	ECHAM4, ECHAM5	(Roesch and Roeckner, 2006)

(Stewart, 2009; Zeinivand and Smedt, 2009; Debele *et al.*, 2010) have been used to estimate snowmelt. In this study, daily snowmelt is estimated using the temperature-based approach used in the Generalized Watershed Loading Function (GWLF; (Haith *et al.*, 1992) watershed model).

Owing to the relatively large number of GCMs from which output is presently available to researchers, there is a need for GCM evaluations to identify the best models for different applications. For regional applications, there are three general methods by which GCMs can be used. (1) Using all available GCMs for achieving better representation of uncertainty. This may result in an unreasonable number of watershed model simulations. (2) Using a multi-model ensemble mean from a group of climate models. Using this approach, only one 'likely' outcome is produced, without information regarding a range of possible outcomes. (3) Choosing a subset of GCMs which are judged as being 'best' for a particular application. For this third option, an evaluation method must be chosen. Testing the GCM's ability to simulate 'present climate' (including variability and extremes) is considered an important part of model evaluation. However, it should be noted that neither good performance across an arbitrary suite of measures of observed climate, nor agreement in output across a collection of models, provides a rigorous basis for assessing the accuracy of a future prediction. Another evaluation method is to identify groups of models which agree on future climate changes (convergence). However, there are inherent

problems with this last approach as well. These issues and approaches are discussed in Gleckler *et al.* (2008); Knutti *et al.* (2010); Weigel *et al.* (2010).

In this study, GCMs are evaluated by examining the skill of models in simulating present-day climate (Raisanen, 2007; Johnson and Sharma, 2009). A number of studies have used SS and other criteria statistics for evaluating the different meteorological variables available from GCMs simulations (Taylor, 2001; Giorgi and Mearns, 2003; Tebaldi *et al.*, 2004; Murphy *et al.*, 2007; Perkins *et al.*, 2007; Randall *et al.*, 2007; Gleckler *et al.*, 2008; Maxino *et al.*, 2008; Pierce *et al.*, 2009; Errasti *et al.*, 2011). A good review of some of these methods available to evaluate the performance of GCMs is found in Johnson and Sharma (2009).

The objective of this study is to evaluate the ability of daily GCM-derived SWE to simulate daily observation-based model SWE using a probability-based skill score. Daily snow accumulation or snowmelt is estimated using the temperature-based snow algorithm in GWLF watershed model.

STUDY REGION AND DATA USED

The study area encompasses a watershed area of about 4100 km². It consists of six reservoir watersheds namely Cannonsville, Ashokan, Nerversink, Schoharie, Rondout and Pepacton (Figure 1). These watersheds are part of the Eastern Plateau Climate Region of New York. The regional climate is characterized as humid continental

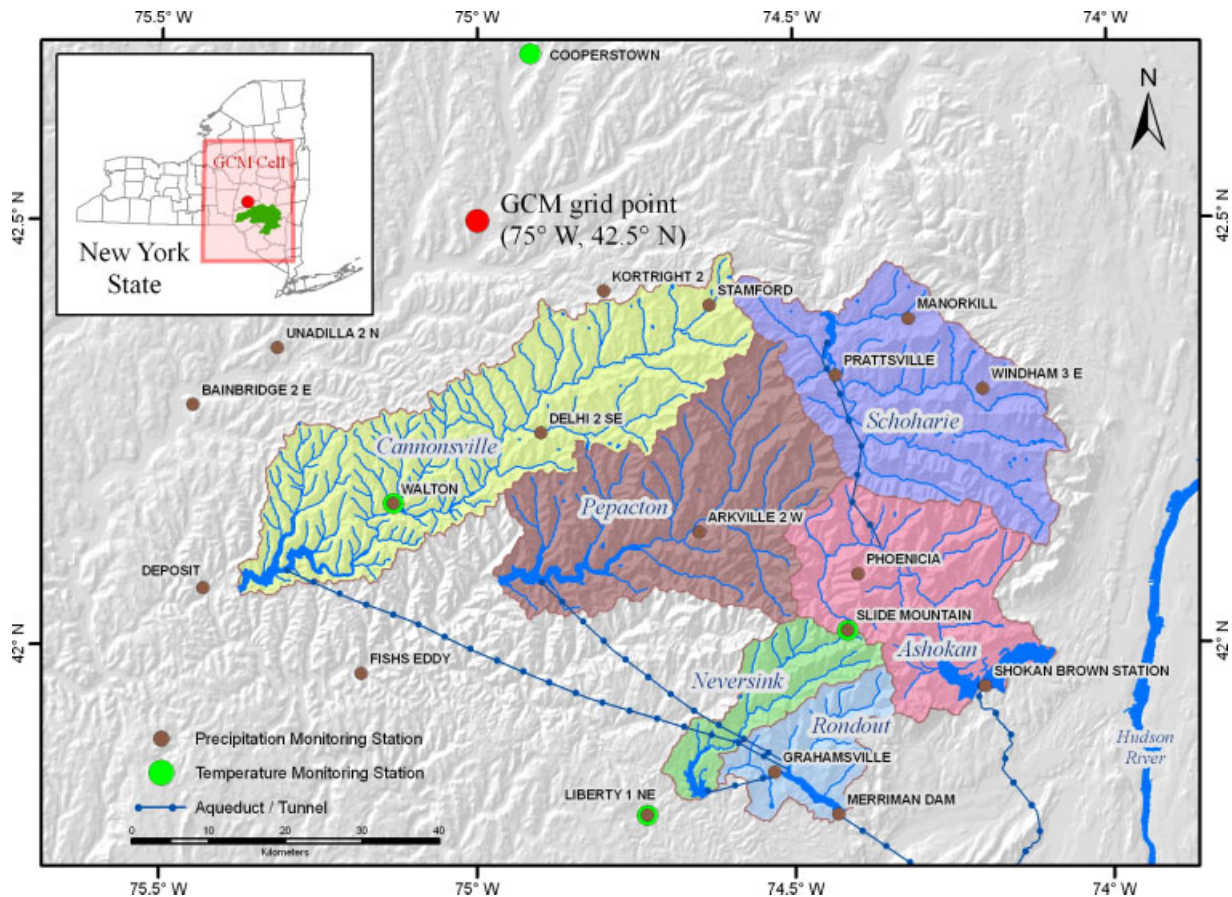


Figure 1. Study region. The six reservoir watersheds provide approximately 90% of NYC's drinking water needs

with cool summers (with average minimum, maximum and mean temperatures of 12, 22 and 18 °C), cold winters (with average minimum, maximum and mean temperatures of -10, 0 and -5 °C), abundant precipitation and snowfall (Figure 2). This region experiences a uniform distribution of precipitation throughout the year. Typically, total precipitation is about 1000–1200 mm per year, with snowfall accounting for approximately 20% of total precipitation. Snow survey data collected by the New York City Department of Environmental Protection (NYCDEP) was used in Table III.

In addition, orography influences the spatial distributions of precipitation and temperature (Frei *et al.*, 2002; Burns *et al.*, 2007).

For each of the 6 WOH watersheds, daily observed data for precipitation from 18 National Climate Data Center cooperative stations were obtained from the Northeast Regional Climate Center (NRCC) (Figure 1). Each watershed was broken into Thiessen polygons based on the location of the nearest precipitation stations. Weights were calculated for each station by dividing the area within each polygon representing a precipitation station to the total watershed area. Then, for each station, the product of precipitation data and its weight were calculated. The average precipitation of each watershed was calculated by the summation of the products for all stations. Using this method the watershed average precipitation is calculated. Average air temperatures are derived from four stations measuring this variable, Cooperstown,

Liberty, Slide Mountain and Walton (Figure 1). Each of these stations has been active since 1960 or earlier. The averaging method includes the application of an environmental lapse rate (6 °C/km) to correct for elevation differences between the station and the mean watershed elevation and use of inverse distance squared weighting averaging of the four stations (NYCDEP, 2004). After processing the observed daily precipitation and average temperatures, a single time series for a variable and watershed is obtained and used in this study. The period of observed data used in this study is 1960–2000.

GCM simulations are obtained from the World Climate Research Programme's (WCRP's) Coupled Model Intercomparison Project Phase 3 (CMIP3) multi-model dataset. The daily baseline scenario (20C3M) GCM simulations are from 20 GCMs (Table II), and for two meteorological variables (precipitation and average temperatures at the surface). A list of the GCM simulations (name and realisation number), used in the study are provided in Table II. The data from all the GCMs for the region surrounding the study region are extracted and interpolated to a common 2.5° grid using bilinear interpolation.

METHODOLOGY

The lack of measured high-quality spatial datasets (Jost *et al.*, 2009) is mainly due to difficulties in extrapolating

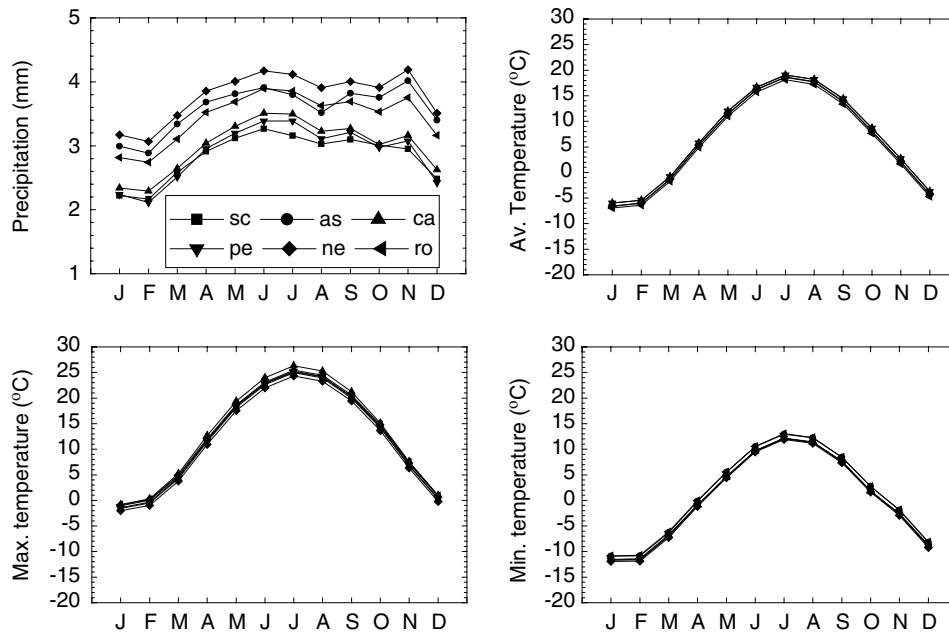


Figure 2. Mean monthly plots for the six WOH watersheds averaged for the period of 1960–2000. In the figure, sc = Schoharie, as = Ashokan, ca = Cannonsville, pe = Pepacton, ne = Neversink, ro = Rondout watersheds

Table II. Names of the climate models, their versions, realisation numbers, acronyms used in the study. The GCMs are classified based on their performance in simulating the SWE are shown. All snow simulations were made using baseline runs associated with these models

S.N	GCM I.D. ^a	Acronym		Country
		GCM name	Realisation number ^b	
1	BCCR-BCM2-0	bcc	01	Norway
2	CCSM3	ncc	01,03,05,06,07,08,09	USA
3	CGCM3-1(T47)	cc4	01,02,03,04,05	Canada
4	CGCM3-1(T63)	cc6	01	Canada
5	CNRM-CM3	cnr	01	France
6	CSIRO-Mk3-0	cs0	01,02,03	Australia
7	CSIRO-Mk3-5	cs5	01	Australia
8	ECHAM5/MPI-OM	mpi	01,04	Germany
9	ECHO-G	miu	01,02,03	Germany, Korea
10	FGOALS-g1-0	iap	01,03	China
11	GFDL-CM2-0	gf0	01	USA
12	GFDL-CM2-1	gf1	02	USA
13	GISS-AOM	gao	01	USA
14	GISS-ER	gir	01	USA
15	INGV-SXG	ing	01	Italy
16	IPSL-CM4	ips	01,02	France
17	MIROC3-2(hires)	mih	01	Japan
18	MIROC3-2(medres)	mim	01,02	Japan
19	MRI-CGCM2-3-2	mri	01,02,03,04,05	Japan

^a As provided by Lawrence Livermore National Laboratory's Program for Coupled Model Diagnosis and Intercomparison (PCMDI): http://www-pcmdi.llnl.gov/ipcc/model_documentation/ipcc_model_documentation.php.

^b Realisation numbers in bold are classified as models having high SS, the numbers in italics represent the models classified as medium SS, and the numbers in black represent models having low SS. This classification is subjective.

data collected from sparse networks of climate stations. The high-resolution daily data are not available especially for mountainous areas where the effects of terrain create spatially and temporally complex climatic patterns (Daly *et al.*, 2007). Also, lack of daily snow measurements for the period of 1960–2000 was one of the problems faced in this study. Further, lack of comparable daily snow parameters in the GCM simulations and comparisons

presented in this paper are based on simulated snow parameters. These simulations are driven using either observed daily mean measurement of air temperature and precipitation or daily GCM data for these variables from the GCM grid cell nearest to the study area and are referred as 'observation-based model' SWE and 'GCM-based simulated' SWE, respectively. The methodology followed in this study is shown in Figure 3.

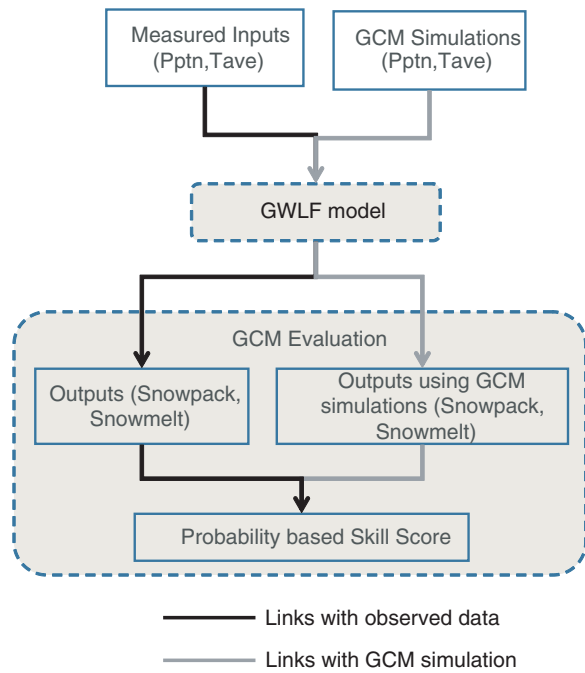


Figure 3. Flow chart showing the methodology for simulating observation-based model and GCM-based SWE

SWE estimation using GWLF model

The GWLF model is a lumped parameter hydrologic model coupled to simple water quality model and details of the model may be found in Haith *et al.* (1992); Schneiderman *et al.* (2002), (2007).

In GWLF, SWE at a given time (t), is a function of SWE at a previous time ($t - 1$), snowfall [$P(t)$] and snowmelt [$P_s(t)$] at time t . If the mean daily temperature $T(t)$ is less than or equal to 0°C , precipitation is assumed to be snowfall. If $T(t) > 0^\circ\text{C}$, snowmelt $P_s(t)$ is calculated based on Equation (1).

$$P_s(t) = M.T(t) \quad (1)$$

Snowmelt is a function of mean daily temperature and a snowmelt parameter or degree day factor (M) given in Equation (1). The units of $P(t)$ and $P_s(t)$ are in cm/day, while the units of $T(t)$ and M are $^\circ\text{C}$ and mm/day/ $^\circ\text{C}$. Air temperature is taken as the measure of the thermal conditions of air masses which are generated by various components (advection, convection, mixing, radiative processes, turnover of latent heat in melting, condensation and evaporation) and is used as input in estimating and modelling energy for melt (Lang and Braun, 1990). The variations in M are attributed to differences in relative importance of individual energy components providing energy for melt (Hock, 2003). M depends on the basin's geographical location, time of year, vegetation, aspect and topography (Maidment, 1993). In general, melt rates in south-facing slopes tend to be higher than north-facing slopes (Harms and Chanasyk, 1998; Pomeroy *et al.*, 2003; Carey and Quinton, 2004; Pohl and Marsh, 2006; Carey and Pomeroy, 2009) due to a greater receipt of solar radiation. In higher-latitude environments, longwave radiation fluxes (from the sky

and surrounding snow-covered landscape) provide similar or higher amounts of radiation to snowmelt processes than shortwave radiation from insolation due to low solar elevation (cosine effect and increased scattering due to long atmospheric path lengths). This effect is magnified in mountains due to shading and longwave emissions from the complex topography (Sicart *et al.*, 2006). The forest canopy absorbs, scatters and reflects the direct beam solar radiation and emits longwave radiation. Owing to the larger downward longwave radiation in the evergreen forest than in the deciduous forest, the daily snowmelt rates in the evergreen forest site were larger than those in the deciduous forest site (Hashimoto *et al.*, 1994). Further, it was observed that the forests had greater snow depth and snow cover compared to agricultural lands in the Cannonsville watershed due to increased sublimation, greater solar radiation and greater winds (Pierson and Kick, 1995) indicating lower melt rates in forest when compared to agricultural lands.

The value for M is calibrated for each of the six WOH watersheds (Table III). The calibrated parameter varies between 0.29 and 0.48 based on the comparison of simulated and measured streamflow. They are within the range of values typical of this region (Maidment, 1993).

GWLF is driven by daily precipitation and temperature data. For six reservoir watersheds, six separate GWLF model applications are driven using watershed-averaged precipitation and air temperature. In the absence of snow measurements, these simulations are used to provide a surrogate for observed SWE and snowmelt corresponding to present day conditions. They are referred to as observation-based model SWE and snowmelt and plot for selected years are shown in Figure 4.

The precipitation and average temperature obtained from GCM simulations were also input into each of the six calibrated GWLF models to obtain snowmelt and SWE for the various combinations of GCM/realisations. These simulations are referred to as GCM-based simulated SWE.

Estimation of probability density functions of SWE

The probability density functions (PDFs) are estimated using 'observation-based model' and 'GCM-based simulated' for the months of December–March (winter to early spring) using MatLab (<http://www.mathworks.com>) for variables SWE, snowpack and mean air temperatures. Six simulated time series for each variable were developed based on observed data (daily basin-wide averaged precipitation and air temperature) for each of the six watersheds. The pooled data from all six watersheds were used to construct a single representative distribution for each parameter in the observation-based model PDF. The PDFs were also calculated for each reservoir watershed using daily grid cell air temperature data for each GCM/realisation.

To estimate the PDFs used in this study, we require bin sizes (S_b) and number of bins (N_b). For each variable, a common value of S_b is used for all analyses;

Table III. Melt coefficients calibrated for the six WOH watersheds

S.N	Name of reservoir watershed	Melt coefficient cm/day/°C	Elevation range, (mean) m	Watershed area (km ²) ^a	Landuse(%) ^b		Snow depth (mm) ^c	SWE (mm) ^c
					Forest	Agriculture		
1	Ashokan	0.29	125–1275 (539)	661	98	1	113.03	19.05
2	Cannonsville	0.41	315–1234 (572)	1177	80	19	171.20	24.64
3	Neversink	0.48	435–1276 (841)	238	98	2	164.85	19.81
4	Pepacton	0.39	353–1181 (633)	961	90	9	134.11	22.61
5	Rondout	0.41	248–1175 (523)	247	96	4	121.16	21.08
6	Schoharie	0.38	315–1234 (632)	817	91	8	127.00	26.16

^a Includes the reservoir area.

^b Values from Mehaffey *et al.* (2005) (Table I).

^c Average values obtained for the watershed calculated based on snow survey data collected by the New York City Department of Environmental Protection (NYCDEP) on 1/21/04.

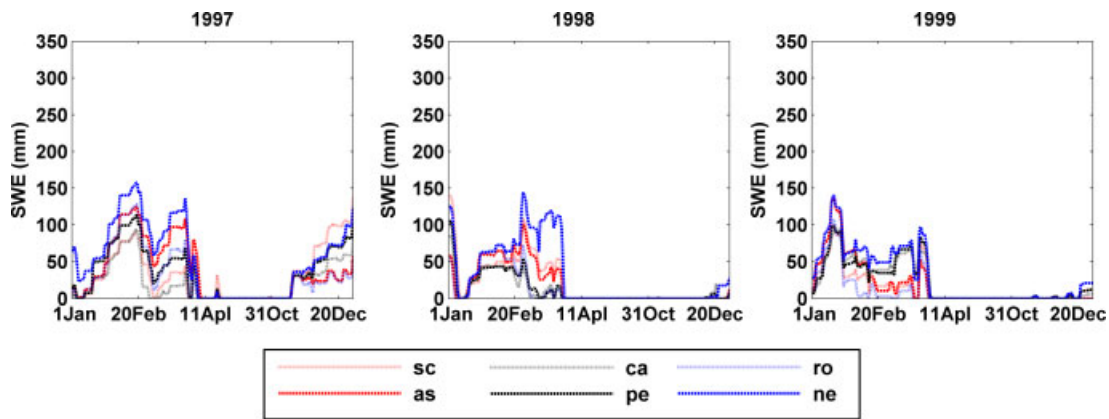


Figure 4. Observation-based model SWE for selected years obtained using GWLF hydrological model. In the figure, sc = Schoharie, as = Ashokan, ca = Cannonsville, pe = Pepacton, ne = Neversink, ro = Rondout watersheds

N_b is then determined based on the range of values (Equation (2)). S_b selected for this study are 0.5 mm/day for SWE, 0.5 mm/day for snowmelt and 0.5 °C for average temperature.

$$N_b = (V_{\max} - V_{\min})/S_b \quad (2)$$

where V_{\max} and V_{\min} is the maximum and minimum value of the variable and vary for the different combinations. The frequencies of values within each bin (n) is then calculated for GCM-based (Fg_n) and observation-based model (Fo_n) data.

Skill score (SS)

The ability of the GCMs to estimate snowmelt and SWE was judged using the skill score (SS) developed by Perkins *et al.*, (2007) which computes the empirical PDFs derived from observation-based model and GCM-based simulation. The advantage of this skill score is its simplicity and applicability across variables, spatial scales and seasons. For each bin n , in the SWE frequency distribution the minimum frequency associated with either the GCM-based (Fg_n) or observation-based model (Fo_n) data is recorded. SS is the summation of these minimum frequency values over all bins (Equation (3)).

$$SS = \sum_{n=1}^{N_b} \min(Fg_n, Fo_n) \quad (3)$$

The value of SS can range between 0 and 1. The SS is close to 1 when the modelled and observed PDFs are similar; close to 0 if there is negligible overlap. For SWE, a SS is calculated by comparing the observation-based model PDF with the PDFs from each GCM/realisation which are then ranked.

RESULTS AND DISCUSSION

The SS for SWE are estimated for 41 GCM/realisations used in the study. The ranks of the GCM are provided in Figure 5 where, the x -axis denotes the rank and y -axis the SS. The GFDL 2.0 (gf001) has the highest SS (0.93) and CCSM (ncc09) has the lowest SS (0.26). On the basis of the SS, the GCMs are classified into three categories high, medium and low performance. The classification is based on the changes in the SS and is subjective. In Table II, the GCMs and realisation number which are classified as high, medium and low performance are shown. It can be observed that the SSs are generally consistent between ensemble members of each GCM, however, in some cases ensemble members fall into adjacent classes but no GCM has one ensemble member in the highest performance group and one in the lowest performance group. The range of the SS in the three categories are high skill score: 0.87–0.93, medium skill score: 0.72–0.83 and low skill score: <0.72 (0.26–0.72).

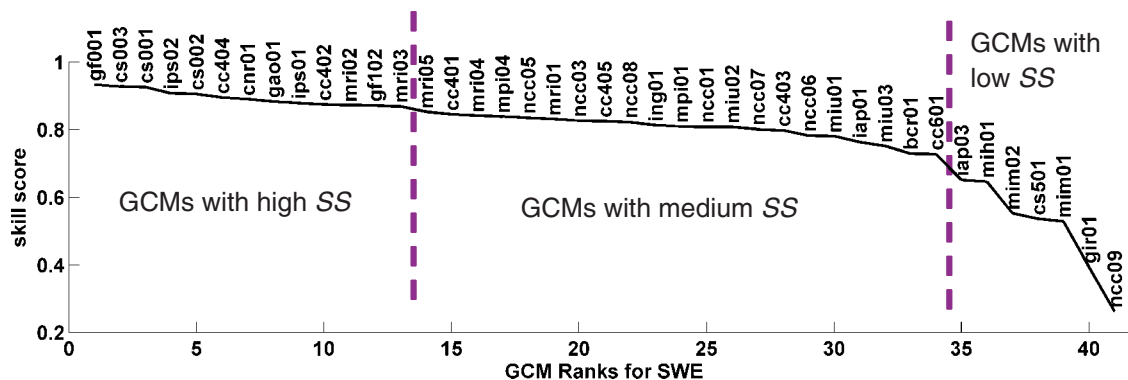


Figure 5. The AR4 climate models are ranked based on average SS for SWE for the season DJFM in each realisation. The GCM with highest skill score is given rank 1, while the GCM with lowest skill score is given the last rank. The GCMs/realisation are classified into high, medium and low classes based on SS

In Figure 6, the PDFs of SWE, snowmelt and air temperature for the three categories defined in Figure 5 are plotted. In Figure 6, a separate row is plotted for each variable and columns represent a different performance class. In each panel, the range of the GCM-based PDFs (shaded region) is shown along with the observation-based model PDF (bold line). For snowmelt and SWE (rows 2 and 3) the x -axis is transformed using a natural log. These figures suggest that the largest between-model variability is found for models in low performance class, and lowest between-model variability is found for models in high performance class.

From the basic statistics (such as mean, median, standard deviation, interquartile range) estimated for all the GCM-based SWE and observation-based model SWEs, it is apparent that the mean statistics in the GCM-based SWE in high performance class were more representative of observation-based model SWEs when compared to the other two performance classes (Figure 7). For the three GCMs selected from the high, medium and low performance classes, the percentage difference between mean statistics from the observation-based model SWE and GCM-based SWE is found to be 3, 29 and 98%, respectively. Further, it can be observed that the range in the GCM-based SWE is less than the observation-based model SWE.

We formed subgroups of models that share common features to make a connection between SS and model characteristics. The model characteristics considered for the analysis include: (1) Horizontal resolutions of the GCMs. (2) Convective scheme employed for precipitation parameterisation; and (3) Flux correction at the ocean–atmosphere interface. On the basis of horizontal resolution, we divided the models into three groups (high, medium and low) and compared them with the SS. In general, the horizontal resolutions of the three groups are >3 , $2-3$ and $<2^\circ$ for high, medium and low groups (Kim *et al.*, 2008). On the basis of the convective scheme used they are divided into four groups namely, RAS (relaxed Arakawa-Schubert), MC (moist convection adjustment), MF (Mass flux-based), AS (Arakawa-Schubert) (Kripalani *et al.*, 2007). On the basis of flux correction at the ocean–atmosphere interface they are

divided into groups with no flux correction (N), heat (H), water (W), momentum (M) (Dai, 2006; Kripalani *et al.*, 2007).

The results of the analysis showed that there is no clear connection between SS and model characteristics, as models with high skill score did not belong to a particular group in terms of horizontal resolution, convective scheme and flux correction. This could be due to the fact that model developers have shared parts of code, input datasets and expertise when developing the GCMs and that some institutions have developed multiple models with some similarities. This may result in some models having similar biases (Jun *et al.*, 2008; Knutti *et al.*, 2010). Hence, it may not be relatively straightforward to associate underlying reasons for high/low SS with the GCM model characteristics that are responsible for the biases.

CONCLUSIONS

Snowmelt runoff is an important source of water for New York City's (NYC) water supply. The GCMs participating in the IPCC's AR4 report are evaluated for their performance in simulating SWE in the water supply watersheds using probability-based SS. In the absence of observed daily SWE or comparable GCM-simulated daily SWE, SWE is estimated using a simple watershed model, which includes a degree-day snow melt parameterisation.

Results show that SSs are generally consistent between ensemble members of each GCM. The GFDL 2.0 (gf001) has the highest SS (0.93) and CCSM (ncc09) has the least SS (0.26). On the basis of the SS, the GCM ensemble members are classified into three categories high, medium and low performance. The range of the SS in the three categories is 0.87–0.93 for high skill score, 0.72–0.83 for medium skill score and <0.72 (0.26–0.72) for low skill score.

The PDFs of snowmelt, SWE and mean temperature for the three performance classes show the largest between-model variability for models in low performance class. Differences between the mean and median from GCM-based PDFs and observation-based model PDFs were also greatest in the low performance class.

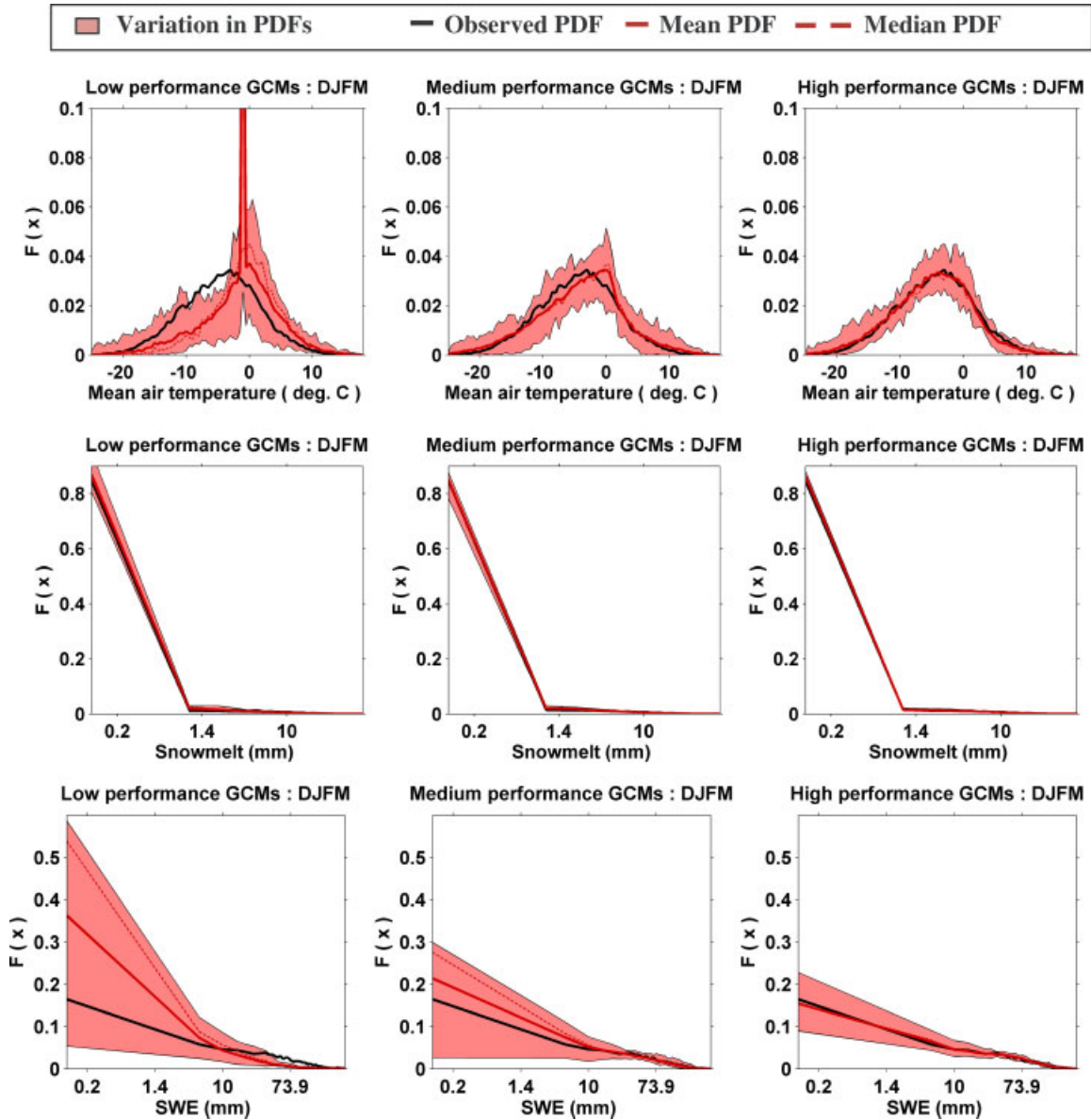


Figure 6. The shaded region represents the variation in Probability Density Functions (PDFs, $F(x)$) for average daily temperature, and daily predictions of snowmelt and SWE for the various AR4 climate models in the three performance classes considered in the study. The PDFs are estimated for the period of 1962–1999 for the DJFM months. In each of the plots, the black bold line represents the PDF obtained using daily observation-based model simulation for the study region. The red dashed line represents the median PDF and the red line shows the mean PDFs for the GCM-based simulation

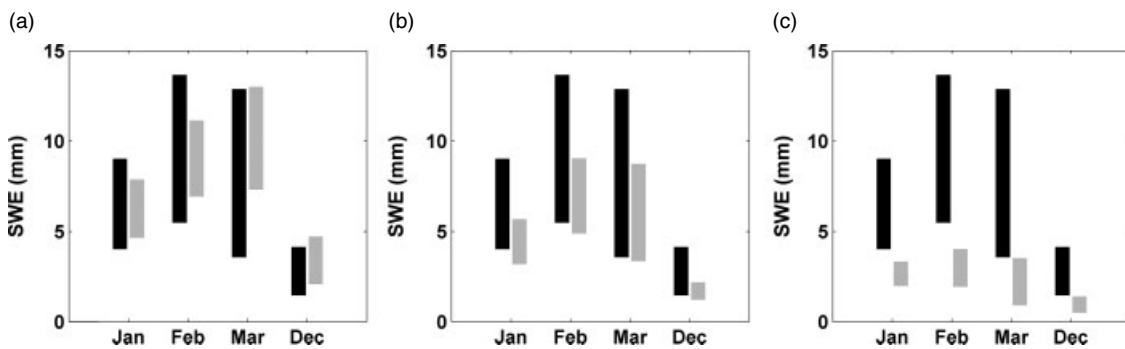


Figure 7. Monthly mean values obtained from simulations (daily GCM-derived SWE, represented as grey bars) and observations (daily observation-based model SWE, represented as black bars) for the six WOH watersheds to show the differences. The GCM-derived SWE in: (a) is from three GCMs (gf001, cs003 and ips01) with high skill score; (b) is from three GCMs (mri05, cc401 and mpi04) with medium skill score; and (c) is from three GCMs (iap03, mih01 and mim02) with low skill score

The statistics (such as mean, median, standard deviation, interquartile range) from the GCM-based SWE simulation were more representative of the observation-based model SWE in high performance class when compared to the other two performance classes.

Evaluation of GCMs by estimating the skill score for individual watersheds is deferred for future work. Analysing the SS for each month in the winter period would help understand the variation of SS in the winter season during pre-melt period (earlier in winter), melt period and post-melt period (later in winter). This is also deferred for future research.

ACKNOWLEDGEMENTS

We acknowledge the modelling groups, the Program for Climate Model Diagnosis and Intercomparison (PCMDI) and the WCRP's Working Group on Coupled Modelling (WGCM) for their roles in making available the WCRP CMIP3 multi-model dataset. Support of this dataset is provided by the Office of Science, US Department of Energy. The GIS support from David G. Lounsbury, and data support from Don Kent, Jim Porter, Glenn Horton, Carrie Olheiser and Anne Sawyer are also acknowledged.

REFERENCES

- Burns DA, Klaus J, McHale MR. 2007. Recent climate trends and implications for water resources in the Catskill Mountain region, New York, USA. *Journal of Hydrology* **336**: 155–170.
- Carey SK, Pomeroy JW. 2009. Progress in Canadian Snow and Frozen Ground Hydrology, 2003–2007. *Canadian Water Resources Journal* **34**: 127–138.
- Carey SK, Quinton WL. 2004. Evaluating snowmelt runoff generation in a discontinuous permafrost catchment using stable isotope, hydrochemical and hydrometric data. *Nordic Hydrology* **35**: 309–324.
- Dai A. 2006. Precipitation Characteristics in Eighteen Coupled Climate Models. *Journal of Climate* **19**: 4605–4630.
- Daly C, Smith JW, Smith JI, McKane RB. 2007. High-Resolution Spatial Modeling of Daily Weather Elements for a Catchment in the Oregon Cascade Mountains, United States. *Journal of Applied Meteorology and Climatology* **46**: 1565–1586.
- Debele B, Srinivasan R, Gosain AK. 2010. Comparison of Process-Based and Temperature-Index Snowmelt Modeling in SWAT. *Water Resources Management* **24**: 1065–1088.
- Errasti I, Ezcurra A, Sáenz J, Ibarra-Berastegi G. 2011. Validation of IPCC AR4 models over the Iberian Peninsula. *Theoretical and Applied Climatology* **103**: 61–79.
- Foster J, Liston G, Koster R, Essery R, Behr H, Dumenil L, Verseghy D, Thompson S, Pollard D, Cohen J. 1996. Snow Cover and Snow Mass Intercomparisons of General Circulation Models and Remotely Sensed Datasets. *Journal of Climate* **9**: 409–426.
- Frei A, Armstrong RL, Clark MP, Serreze MC. 2002. Catskill Mountain Water Resources: Vulnerability, Hydroclimatology, and Climate Change Sensitivity. *Annals of the Association of American Geographers* **92**: 202–224.
- Frei A, Brown R, Miller JA, Robinson DA. 2005. Snow mass over North America: Observations and results from the second phase of the Atmospheric Model Intercomparison Project (AMIP-2). *Journal of Hydrometeorology* **6**: 681–695.
- Frei A, Gong G. 2005. Decadal to century scale trends in North American snow extent in coupled atmosphere-ocean general circulation models. *Geophysical Research Letters* **32**: L18502.
- Frei A, Miller JA, Robinson DA. 2003. Improved simulations of snow extent in the second phase of the Atmospheric Model Intercomparison Project (AMIP-2). *Journal of Geophysical Research* **108**: 4369–4386.
- Giorgi F, Mearns LO. 2003. Probability of regional climate change based on the reliability ensemble averaging (REA) method. *Geophysical Research Letters* **30**: 1629 doi:10.1029/2003GL017130.
- Gleckler PJ, Taylor KE, Dutriaux C. 2008. Performance metrics for climate models. *Journal of Geophysical Research* **113**: D06104.
- Haith DA, Mandel R, Wu RS. 1992. *Generalized Watershed Loading Functions*, Version 2.0, User's Manual. Cornell University: Ithaca, New York.
- Harms T, Chanasyk D. 1998. Variability of snowmelt runoff and soil moisture recharge. *Nordic Hydrology* **29**: 179–198.
- Hashimoto T, Ohta T, Fukushima Y, Ishii T. 1994. Heat balance analysis of forest effects on surface snowmelt rates. *Snow and Ice Covers: Interactions with the Atmosphere and Ecosystems. IAHS Publication* **223**: 247–258.
- Hock R. 2003. Temperature index melt modelling in mountain areas. *Journal of Hydrology* **282**: 104–115.
- Johnson F, Sharma A. 2009. Measurement of GCM skill in predicting variables relevant for hydroclimatological assessments. *Journal of Climate* **22**: 4373–4382.
- Jost G, Dan Moore R, Weiler M, Gluns DR, Alila Y. 2009. Use of distributed snow measurements to test and improve a snowmelt model for predicting the effect of forest clear-cutting. *Journal of Hydrology* **376**: 94–106.
- Jun M, Knutti R, Nychka DW. 2008. Spatial Analysis to Quantify Numerical Model Bias and Dependence. *Journal of the American Statistical Association* **103**: 934–947.
- Kim H-J, Wang B, Ding Q. 2008. The Global Monsoon Variability Simulated by CMIP3 Coupled Climate Models. *Journal of Climate* **21**: 5271–5294.
- Knutti R, Furrer R, Tebaldi C, Cermak J, Meehl GA. 2010. Challenges in Combining Projections from Multiple Climate Models. *Journal of Climate* **23**: 2739–2758.
- Kripalani RH, Oh JH, Chaudhari HS. 2007. Response of the East Asian summer monsoon to doubled atmospheric CO₂: Coupled climate model simulations and projections under IPCC AR4. *Theoretical and Applied Climatology* **87**: 1–28.
- Lang H, Braun L. 1990. On the information content of air temperature in the context of snow melt estimation. In *Hydrology of Mountainous Areas*. Proceedings of the Strbske Pleso Symposium 1990, IAHS Publ. no. 190. Molnar L (ed), 347–354.
- Maidment D. 1993. *Handbook of Hydrology*. McGraw-Hill: New York.
- Maxino CC, McAvaney BJ, Pitman AJ, Perkins SE, Holbrook NJ, McAneney J. 2008. Ranking the AR4 climate models over the Murray-Darling Basin using simulated maximum temperature, minimum temperature and precipitation. *International Journal of Climatology* **28**: 1097–1112.
- Mehaffey MH, Nash MS, Wade TG, Ebert DW, Jones KB, Rager A. 2005. Linking Land Cover and Water Quality in New York City's Water Supply Watersheds. *Environmental Monitoring and Assessment* **107**: 29–44.
- Murphy JM, Booth BBB, Collins M, Harris GR, Sexton DMH, Webb MJ. 2007. A methodology for probabilistic predictions of regional climate change from perturbed physics ensembles. *Philosophical Transactions of the Royal Society A: Mathematical, Physical and Engineering Sciences* **365**: 1993–2028.
- NYCDEP. 2004. "Multi Tiered" Water Quality Modeling Program Semi-Annual Status Report—EPA Filtration Avoidance Deliverable Report. Valhalla, NY: New York City Department of Environmental Protection (NYCDEP).
- Perkins SE, Pitman AJ, Holbrook NJ, McAneney J. 2007. Evaluation of the AR4 Climate Models' Simulated Daily Maximum Temperature, Minimum Temperature, and Precipitation over Australia Using Probability Density Functions. *Journal of Climate* **20**: 4356–4376.
- Pierce DW, Barnett TP, Santer BD, Gleckler PJ. 2009. Selecting global climate models for regional climate change studies. *Proceedings of the National Academy of Sciences* **106**: 8441–8446.
- Pierson D, Kick J. 1995. Use of a GIS to Develop a Stratified Snow Survey in Mountainous Agricultural Landscape. Eastern Snow Conference, June 7–9. Toronto, Ontario, Canada.
- Pohl S, Marsh P. 2006. Modelling the spatial-temporal variability of spring snowmelt in an arctic catchment. *Hydrological Processes* **20**: 1773–1792.
- Pomeroy JW, Toth B, Granger RJ, Hedstrom NR, Essery RLH. 2003. Variation in Surface Energetics during Snowmelt in a Subarctic Mountain Catchment. *Journal of Hydrometeorology* **4**: 702–719.
- Raisanen J. 2007. How reliable are climate models? *Tellus* **59A**: 2–29.
- Randall DA, Wood RA, Bony S, Colman R, Fichefet T, Fyfe J, Kattsov V, Pitman A, Shukla J, Srinivasan J, Stouffer RJ, Sumi A, Taylor KE. 2007. *Climate Models and Their Evaluation*. Cambridge University Press: Cambridge, United Kingdom and New York, NY, USA.

- Roesch A. 2006. Evaluation of surface albedo and snow cover in AR4 coupled climate models. *Journal of Geophysical Research* **111**: D15111.
- Roesch A, Roeckner E. 2006. Assessment of Snow Cover and Surface Albedo in the ECHAM5 General Circulation Model. *Journal of Climate* **19**: 3828–3843.
- Schneiderman EM, Pierson DG, Lounsbury D, Zion MS. 2002. Modeling the hydrochemistry of the Cannonsville watershed with generalized watershed loading functions (GWLF). *Journal of the American Water Resources Association* **38**: 1323–1347.
- Schneiderman EM, Steenhuis TS, Thongs D, Easton Z, Zion MS, Neal A, Mendoza G, Walter M. 2007. Incorporating variable source area hydrology into a curve-number-based watershed model. *Hydrological Processes* **21**: 3420–3430.
- Sicart JE, Pomeroy JW, Essery RLH, Bewley D. 2006. Incoming longwave radiation to melting snow: observations, sensitivity and estimation in Northern environments. *Hydrological Processes* **20**: 3697–3708.
- Stewart IT. 2009. Changes in snowpack and snowmelt runoff for key mountain regions. *Hydrological Processes* **23**: 78–94.
- Taylor KE. 2001. Summarizing multiple aspects of model performance in a single diagram. *Journal of Geophysical Research* **106**: 7183–7192.
- Tebaldi C, Mearns LO, Nychka D, Smith RL. 2004. Regional probabilities of precipitation change: a Bayesian analysis of multimodel simulations. *Geophysical Research Letters* **31**: L24213.
- Weigel AP, Knutti R, Liniger MA, Appenzeller C. 2010. Risks of Model Weighting in Multimodel Climate Projections. *Journal of Climate* **23**: 4175–4191.
- Yang Z-L, Dickinson RE, Hahmann AN, Niu G-Y, Shaikh M, Gao X, Bales RC, Sorooshian S, Jin J. 1999. Simulation of snow mass and extent in general circulation models. *Hydrological Processes* **13**: 2097–2113.
- Zeinivand H, Smedt F. 2009. Hydrological Modeling of Snow Accumulation and Melting on River Basin Scale. *Water Resources Management* **23**: 2271–2287.
- Zion M, Pradhanang S, Pierson D, Anandhi A, Lounsbury D, Matonse A, Schneiderman E. 2010. Investigation and Modeling of Winter Streamflow Timing and Magnitude under Changing Climate Conditions for the Catskill Mountain Region, New York, USA. *Proceedings of the the 67th Annual Eastern Snow Conference*. Hancock, MA, June 8–10, USA.

Examination of change factor methodologies for climate change impact assessment

Aavudai Anandhi,¹ Allan Frei,^{1,2} Donald C. Pierson,³ Elliot M. Schneiderman,³ Mark S. Zion,³ David Lounsbury,³ and Adao H. Matonse¹

Received 19 January 2010; revised 1 August 2010; accepted 16 November 2010; published 1 March 2011.

[1] A variety of methods are available to estimate values of meteorological variables at future times and at spatial scales that are appropriate for local climate change impact assessment. One commonly used method is Change Factor Methodology (CFM), sometimes referred to as delta change factor methodology. Although more sophisticated methods exist, CFM is still widely applicable and used in impact analysis studies. While there are a number of different ways by which change factors (CFs) can be calculated and used to estimate future climate scenarios, there are no clear guidelines available in the literature to decide which methodologies are most suitable for different applications. In this study several categories of CFM (additive versus multiplicative and single versus multiple) for a number of climate variables are compared and contrasted. The study employs several theoretical case studies, as well as a real example from Cannonsville watershed, which supplies water to New York City, USA. Results show that in cases when the frequency distribution of Global Climate Model (GCM) baseline climate is close to the frequency distribution of observed climate, or when the frequency distribution of GCM future climate is close to the frequency distribution of GCM baseline climate, additive and multiplicative single CFMs provide comparable results. Two options to guide the choice of CFM are suggested. The first option is a detailed methodological analysis for choosing the most appropriate CFM. The second option is a default method for use under circumstances in which a detailed methodological analysis is too cumbersome.

Citation: Anandhi, A., A. Frei, D. C. Pierson, E. M. Schneiderman, M. S. Zion, D. Lounsbury, and A. H. Matonse (2011), Examination of change factor methodologies for climate change impact assessment, *Water Resour. Res.*, 47, W03501, doi:10.1029/2010WR009104.

1. Introduction

[2] New York City Department of Environmental Protection (DEP) is undertaking a program to evaluate the potential effects of climate change on the New York City (NYC) water supply. This modeling program utilizes meteorological time series derived from Global Climate Model (GCM) simulations. These time series are provided as input to an integrated suite of models (including watershed hydrology, water quality, water system operations, and reservoir hydrothermal models), to examine the potential effects of climate change on water quantity and quality.

[3] One difficulty encountered in such studies is the mismatch of spatial scales between GCMs on the one hand, and local observations and local impact assessments on the other hand. For example, the area of typical GCM grid cells range between 10,000 km² and 90,000 km², while for the case of

the NYC water supply, model simulations are typically run on watershed areas of 25–1200 km².

[4] A number of techniques have been employed to overcome this problem of mismatched spatial scales. Future climate scenarios have been derived in several ways: (1) based on analogies with different climatic zones or historical time periods, (2) from GCMs using simple manipulation of current climate observations (e.g. Change Factor Methodology (CFM)), and (3) from more sophisticated statistical and dynamical downscaling methodologies [Wilby *et al.*, 2000]. There are three types of statistical downscaling, namely weather classification methods, weather generators, and transfer functions. Weather classification methods group days into a finite number of discrete weather types or “states” according to their synoptic similarity [Anandhi, 2010; Brinkmann, 1999; Wetterhall *et al.*, 2005]. Weather generators are statistical models that provide sequences of weather variables that have similar statistical properties as the observed data on which they are trained [Chen *et al.*, 2010; Mehrotra *et al.*, 2006; Stehlik and Bárdossy, 2002; Wilks, 1998]. Transfer functions capture the relationships between the large scale atmospheric variables (predictors) and the local meteorological variable of interest (predictand) [Anandhi *et al.*, 2008; Anandhi *et al.*, 2009; Tripathi *et al.*, 2006]. In the dynamic downscaling approach, a Regional Climate Model (RCM) is nested in a GCM. Dynamic

¹CUNY Institute for Sustainable Cities, City University of New York, New York, New York, USA.

²Department of Geography, Hunter College, City University of New York, New York, New York, USA.

³Water Quality Modeling Group, New York City Department of Environmental Protection, Kingston, New York, USA.

downscaling can be further subdivided into one-way nesting and two-way nesting [Wang *et al.*, 2004].

[5] Each of the methods has its own set of advantages and pitfalls for generating future climate scenarios [Mearns *et al.*, 2001; Semadeni-Davies, 2004]. The major advantage of CFM (also referred to as delta change factor methodology) is the ease and speed of application, and the direct scaling of the local data in line with changes suggested by the GCM scenario. Hence, CFM is used in many climate change impact assessment studies [Semadeni-Davies *et al.*, 2008] and programs across the world, such as the US Global Change Research Program (available at <http://www.usgcrp.gov/usgcrp/nacc/default.htm>), and in a recent study of the effect of climate change impact on lakes in Europe (CLIME) [George, 2010]. However, there are also some disadvantages to this approach that have been reported in the literature. For example, the temporal sequencing of wet and dry days generally remains unchanged when using single change factor (explained in detail in section 3.1), and so CFM may not be helpful in circumstances where changes in event frequency and antecedent conditions are important to the impact assessment [Diaz-Nieto and Wilby, 2005; Gleick, 1986]. The purpose of this paper is to shed some light on the different types of CFM methodologies under different circumstances, and to provide guidance on how they should be applied.

2. Study Region and Data

[6] Our study region is the Cannonsville reservoir watershed, which is one of the sources of NYC's municipal water supply. Cannonsville is a 1178 km² watershed located in Delaware County, about 160 km northwest of NYC in the Catskill Mountains.

[7] Daily GCM simulation results from three GCMs are downloaded for the grid box closest to the centroid of the watershed. The National Center for Atmospheric Research (NCAR), Goddard Institute of Space Studies (GISS), and European Center Hamburg Model (ECHAM) are the three GCMs used in the study. The GCM simulations were obtained from the World Climate Research Programme's (WCRP's) Coupled Model Intercomparison Project phase 3 (CMIP3) multimodel data set. The NCAR, GISS, and ECHAM results were supplied by Columbia University/GISS as part of an initial climate change contract with DEP [Hornton and Rosenzweig, 2010; Major and O'Grady, 2010]. The scenarios include a baseline scenario (20C3M), three future emission scenarios (A1B, A2, and B1), and two time slices (2046–2065 and 2081–2100). All combinations of future emissions scenarios and time slices are compared to the 1981–2000 baseline period, and nine meteorological variables were examined depending on their availability (precipitation; maximum, minimum and average temperature; meridional wind component; zonal wind component; surface pressure; shortwave solar radiation; and longwave radiation; as discussed in section 4.3). The temperature and winds are at the near surface, usually 2 m height for temperature and 10 m height for wind. The chosen future scenarios coincide with daily data available for most GCMs. The details of the GCMs used in the study are provided in Table 1.

[8] Daily observed data from six meteorological variables (precipitation; maximum, minimum and average

Table 1. GCMs, Emission Scenarios, and Time Slices Applied in This Study^a

GCM	20C3M	Emission Scenarios	Time Slices
ECHAM	1981–2000	A2, A1B, B1	2046–2065, 2081–2100
GISS	1981–2000	A2, A1B, B1	2046–2065, 2081–2100
NCAR	1980–1999	A2, A1B	2045–2064, 2080–2099

^aTime slice refers to the interval of time used in the calculation of change factors.

temperature; wind speed; and shortwave solar radiation) for the period 1981–2000 are used in the more detailed study in section 4.4. For these variables, there was no significant change in the frequency distributions calculated over a 20 (1981–2000) or 40 (1961–2000) year record of observed data.

3. Change Factor Methodologies

[9] There are several types of CFMs. These can be categorized by temporal scale, temporal resolution, mathematical formulation, or number of change factors. The first type of CFM is categorized by the temporal scale and temporal domain from which they are calculated. Temporal scale refers to the timescale (e.g. daily, monthly, seasonal, annual) of values that are included in the analysis. Temporal domain refers to both the time of year (e.g. January, winter, annual) and the beginning and ending dates of the historical observed, historical modeled, and future modeled values to be included in the analysis (e.g. 1981–2000 compared to 2046–2065). In general, the reliability of GCMs decrease at higher frequency temporal scales. The monthly, seasonal, and annual averages of any variable are better simulated than daily values [Grotch and MacCracken, 1991; Huth, 1997]. However, there is also a need for daily hydrometeorological variables in hydrological and ecological impact assessment studies relating to climate change. Studies have evaluated GCM simulations at daily timescales and concluded that some of the GCMs (in AR4 report) show considerable skill at subcontinental scales even when assessed using daily frequency distributions. This builds confidence in using the GCMs for regional assessment [Perkins *et al.*, 2007] and in some cases for assessing extreme events.

[10] The second type of CFM is categorized by its mathematical formulation (additive or multiplicative). In an additive CFM, one calculates the arithmetic difference between a GCM variable derived from a current climate simulation and derived from a future climate scenario taken at the same GCM grid location. This difference is then added to observed local values to obtain the modeled future values. This method, typically used for temperature [Akhtar *et al.*, 2008; Hay *et al.*, 2000; Kilsby *et al.*, 2007], assumes that the GCM produces a reasonable estimate of the *absolute change* in the value of a particular variable regardless of the accuracy of the GCM's current climate simulation. A multiplicative change factor (CF) is similar to an additive CF except that the ratio, rather than arithmetic difference, between the future and current GCM simulations is calculated; the observed values are then multiplied by (rather than added to) the CF. This method assumes that the GCM produces a reasonable estimate of the *relative change* in the value of a variable, and is typically used for precipitation

[Akhtar et al., 2008; Hay et al., 2000; Kilsby et al., 2007]. If CFs are to be applied multiplicatively for temperature values, the Kelvin scale should be used. In some studies change factors are applied incrementally by arbitrary amounts (e.g. +1, +2, +3, +4°C change in temperature). The scenarios obtained are also referred to as synthetic scenarios [Carter et al., 1994], as they do not necessarily present a realistic set of changes that are physically plausible. They are usually adapted for exploring system sensitivity prior to the application of more credible, model-based scenarios [Rosenzweig and Iglesias, 1994; Smith and Hulme, 1998].

[11] There are no clear guidelines available in the literature as to whether CFs are to be estimated additively or multiplicatively for meteorological variables such as wind speed and solar radiation. Nevertheless, these values are sometimes required for impact assessment studies in hydrology. Hence, there is a need to develop a methodology for applying CFs across a wide variety of meteorological variables.

[12] The third type of CFM is categorized based on the number of change factors (single and multiple CFs). Single CFs are calculated identically for all values of the variable, regardless of magnitude [Akhtar et al., 2008; Hay et al., 2000]. Multiple CFs are those that are calculated separately for different magnitudes of the variable [Andréasson et al., 2004; Kilsby et al., 2007; Olsson et al., 2009]. For example, one can calculate separate CFs for percentiles 0–10, 10–20, and so on for the meteorological parameter of interest. There are no clear guidelines available that suggest the appropriate number of CFs.

[13] For any particular CFM analysis, one must choose CF values that are appropriate for the methodology being applied. As an example of a particular analysis, one might consider a temporal scale of daily; a temporal domain that includes all January values for the time period 1981–2000 compared to 2046–2065; and an additive, single CF. It is likely that one might want to do the analysis for each month of the year. In that case, each monthly analysis would be performed independently. The CFs may be obtained from a single GCM grid point or an average of grid points. In the remainder of this section, calculations of CFs are discussed.

3.1. Single CF

[14] The procedure to calculate a single CF, additively or multiplicatively, is explained in this section and illustrated in Figure 1. The first step is to estimate the mean values of GCM simulated baseline and future climates (equations (1) and (2)).

$$\overline{GCMb} = \sum_{i=1}^{Nb} GCMb_i / Nb \tag{1}$$

$$\overline{GCMf} = \sum_{i=1}^{Nf} GCMf_i / Nf \tag{2}$$

[15] In equations (1) and (2) $GCMb$ and $GCMf$ represent the values from a GCM baseline (20C3M) and GCM future climate scenario, respectively, for a temporal domain. \overline{GCMb} and \overline{GCMf} are the mean values from a GCM

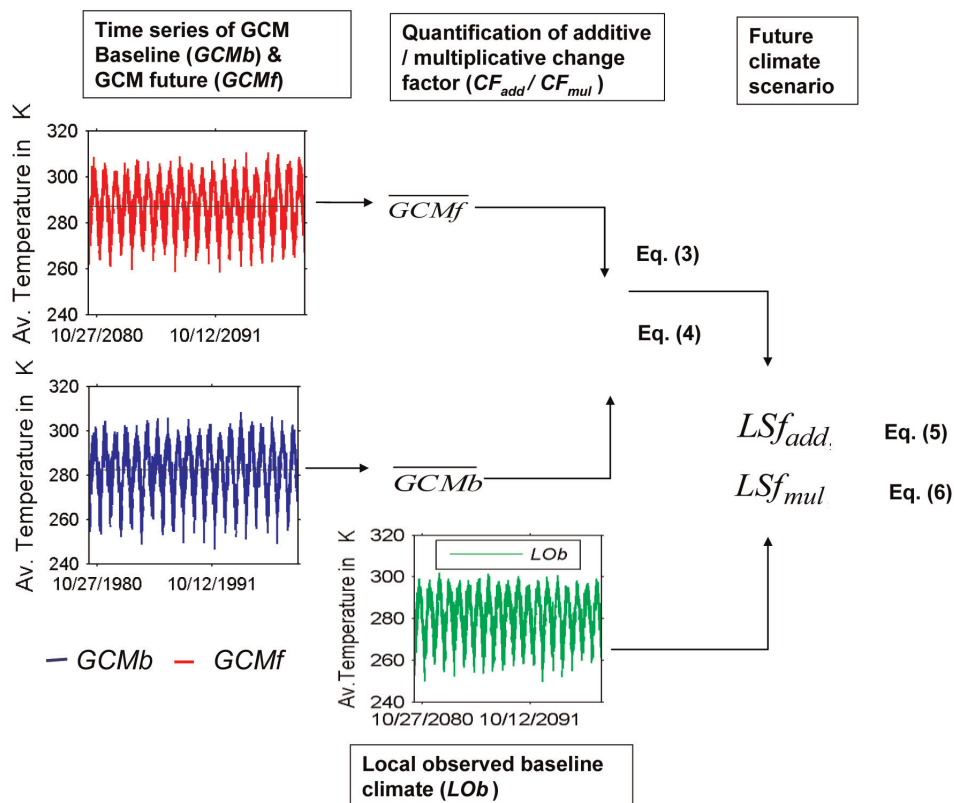


Figure 1. Methodology to estimate future scenarios using “Single additive” and “Single multiplicative” change factors.

baseline and GCM future scenario for the designated temporal domain. Nb and Nf are the number of values in the temporal domain of the GCM baseline and GCM future scenario.

[16] For example, when using a temporal domain corresponding to January 1981–2000, at a daily temporal scale, Nb would be equal to the number of days in all the January months ($Nb = 20 \times 31$) during this time period while for a monthly temporal scale, Nb would be equal to the number of January months ($Nb = 20$). Likewise, for a future temporal domain corresponding to January 2046–2065, at a daily temporal scale, Nf would be equal to the number of days in all the January months ($Nf = 20 \times 31$), and at a monthly temporal scale, Nf would be equal to the number of January months ($Nf = 20$).

[17] Step 2 is to calculate additive and multiplicative change factors (CF_{add} , CF_{mul}) (equations (3) and (4)).

$$CF_{add} = \overline{GCMf} - \overline{GCMb} \quad (3)$$

$$CF_{mul} = \overline{GCMf} / \overline{GCMb} \quad (4)$$

[18] Step 3 is to obtain local scaled future values ($LSf_{mul,i}$ and $LSf_{add,i}$) by applying CF_{add} and CF_{mul} (equations (5) and (6)).

$$LSf_{add,i} = LOb_i + CF_{add} \quad (5)$$

$$LSf_{mul,i} = LOb_i \times CF_{mul} \quad (6)$$

where LOb_i are observed values of the meteorological variable (at the i^{th} time step) at an individual meteorological station, or are the averaged meteorological time series for a watershed for the designated temporal domain. $LSf_{add,i}$ and $LSf_{mul,i}$ are values of future scenarios of the variable obtained using additive and multiplicative formulation of CFM.

3.2. Multiple (Magnitude Dependent) CFs

[19] The procedure to calculate multiple CFs (additively or multiplicatively) is explained in this section. The first step is to estimate the empirical cumulative distribution functions (CDFs) for $GCMf$ and $GCMb$.

[20] Step 2 is to fix the number of bins (n) to be estimated and the resolution of the percentiles (r) in each bin. The bin size may be uniform or nonuniform. In this study the results using six different sets of values for n and r are compared: (1) single CF ($n = 1$, $r = 100$, explained in section 3.1); (2) 3 CFs ($n = 3$, r is variable; 0–25 percentile, 25–75 percentile, and 75–100 percentile); (3) 10 CFs ($n = 10$, $r = 10$); (4) 25 CFs ($n = 25$, $r = 4$); (5) 50 CFs ($n = 50$, $r = 2$); and (6) 100 CFs ($n = 100$, $r = 1$).

[21] Calculations within each bin are analogous to the calculations required for a single CF (section 3.1), so that equations (7)–(12) are analogous to equations (1)–(6), except that the former have subscripts “ n ” denoting that the calculations are specific for each bin. In step 3, for each bin, mean values $GCMf$ and $GCMb$ are estimated using equations (7) and (8).

$$\overline{GCMb}_n = \sum_{i=1}^{Nb} GCMb_{i,n} / Nb \quad (7)$$

$$\overline{GCMf}_n = \sum_{i=1}^{Nf} GCMf_{i,n} / Nf \quad (8)$$

[22] In step 4, calculate the $CF_{add,n}$ and $CF_{mul,n}$ for each bin (equations (9) and (10))

$$CF_{add,n} = \overline{GCMf}_n - \overline{GCMb}_n \quad (9)$$

$$CF_{mul,n} = \overline{GCMf}_n / \overline{GCMb}_n \quad (10)$$

[23] The fifth step is to estimate the CDF for LOb , and divide LOb into the same bin and percentile classes as was used with the GCM data.

[24] The final step is to obtain future scaled climate values ($LSf_{mul,n,j}$ and $LSf_{add,n,j}$) by applying the change factors to the corresponding observed values (j) in each bin in the baseline period LOb using the general equations (11) and (12).

$$LSf_{add,n,j} = LOb_{n,j} + CF_{add,n} \quad (11)$$

$$LSf_{mul,n,j} = LOb_{n,j} \times CF_{mul,n} \quad (12)$$

4. Results and Discussion

[25] In this section the behaviors of different types of CFMs are demonstrated. In the first two sections, theoretical examples of additive and multiplicative methodologies for single (section 4.1) and multiple (section 4.2) CFs are presented. Then a case study using multiple CFs from real observations (section 4.3) is shown, followed by a comparison of single and multiple CF results (section 4.4). Results of additive and multiplicative categories of CFMs are discussed in sections 4.1 to 4.4.

4.1. Theoretical Example of a Single CF

[26] It is shown, using a theoretical example, how the estimated local scaled future value (LSb) depends on (1) the choice of additive or multiplicative CFM; (2) the magnitude of the bias in the baseline period between local observed climate (LOb) and GCM baseline climate (\overline{GCMb}); and (3) the magnitude of the change factor. In the example, the local observed value (LOb) of exactly 1 is assumed. We then estimate the local scaled future climate (LSf_{add} and LSf_{mul}) using both additive and multiplicative CFs based on a range of values for GCM baseline climate (\overline{GCMb} ; x axis in Figure 2) and GCM future climate (\overline{GCMf} ; y axis in Figure 2). The differences (D) between the LSf_{add} and LSf_{mul} obtained additively and multiplicatively, calculated using equation (13), are shown as contours in Figure 2.

$$D = LSf_{mul} - LSf_{add} \quad (13)$$

[27] This example can apply to a single CF, or to a particular bin in a multiple CF. The results shown in Figure 2 demonstrate that when the frequency distribution of GCM baseline simulation is close to the frequency distribution of observed baseline climate (i.e., small bias) or when the

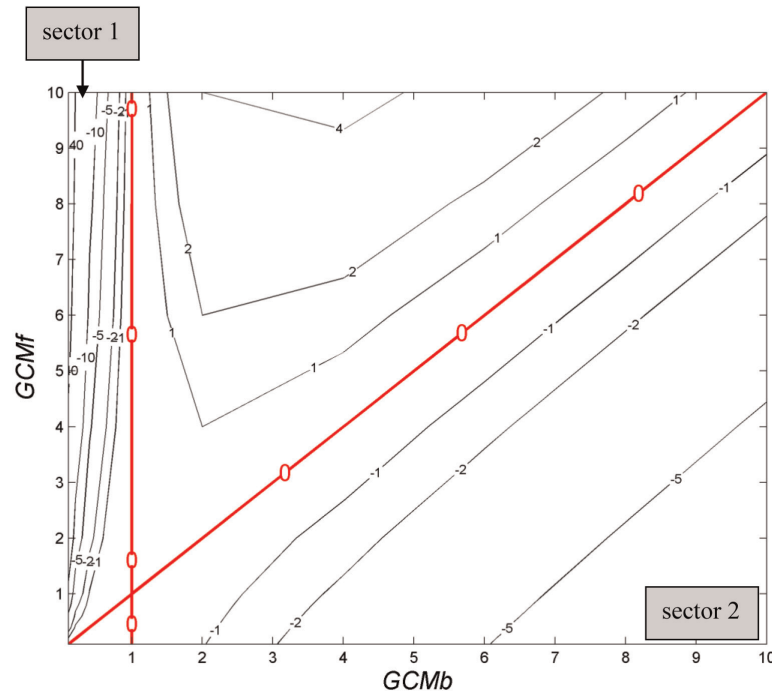


Figure 2. The contour plot of the differences in future scenario values obtained from additive and multiplicative change factors is calculated using equation (13), from the theoretical values of GCM baseline mean ($GCMb$, x axis) and GCM future mean ($GCMf$, y axis). A local observed baseline (LOB) value of exactly 1 is assumed. The 0 contours following the diagonal line represent small bias while those following the vertical line represent small change factors as explained in section 4.1. Contours are not equally spaced. Sectors 1 and 2 are referred to in section 4.4.

mean GCM baseline is close to the mean GCM future simulations (i.e., small change factor), there is little difference between the additive and multiplicative methods. These are areas with a value near 0 (represented in Figure 2 as bold red lines). However, as the bias in the baseline GCM simulation increases, or as the absolute value of the change factor gets larger, the additive and multiplicative methods produce more and more divergent results.

4.2. Theoretical Example of a Multiple CFM

[28] A graphical approach is developed to evaluate multiple CFMs using “difference plots” and “ratio plots,” which are defined here. In this example, CFs are calculated for 100 bins of equal width (i.e., all widths span exactly 1 percentile) using both additive and multiplicative methods (Figure 3). CF values are on the abscissa axis, and percentile values are shown on the ordinate axis. This example shows the simple case where, for all bins, the difference between the current and future climates modeled by the GCM is a constant value. In other words, the additive CF is independent of the magnitude of the values. In such a case, the difference plot is a straight vertical line, and the ratio plot is a curved line.

[29] Figures 3 and 4 show more generally how the difference and ratio plots look for the simple cases where, across bins, there is a constant difference or constant ratio between current and future climates. These plots can be considered theoretical templates against which to compare similar plots derived from GCM output, and which may be useful in determining whether an additive or multiplicative

method is most appropriate. However, it is demonstrated in section 4.3, that results from GCM experiments are unlikely to be as simple or as obvious as the theoretical example shown in Figures 3 and 4.

4.3. Real Example of a Multiple CFM

[30] A real example from the Cannonsville watershed (see section 2) is shown in Figure 5. Difference plots and ratio plots were derived using daily values from three GCMs (NCAR, ECHAM, and GISS), three emission scenarios (A1B, A2, and B1), and two time slices (2046–2065 and 2081–2100, both of which are compared to the 1981–2000 baseline period). Nine meteorological variables (precipitation; maximum, minimum, and average temperature; meridional wind component; zonal wind component; surface pressure; wind speed; shortwave solar radiation; and longwave solar radiation) were examined. From all of these combinations of meteorological variables, time periods, and emission scenarios, a variety of patterns in the ratio and difference plots were observed. Figure 5 shows a selection of difference and ratio plots that are considered illustrative of more general results.

[31] The difference and ratio plots for our study area can be broadly classified into five groups. The five classifications include those in which: (1) the difference plot is close to a straight vertical line, indicating that a single additive CF is appropriate (Figure 5a); (2) the ratio plot is close to a straight vertical line, indicating that a single multiplicative CF is appropriate (Figure 5b); (3) the difference plot is close to multiple straight vertical lines for different percentile

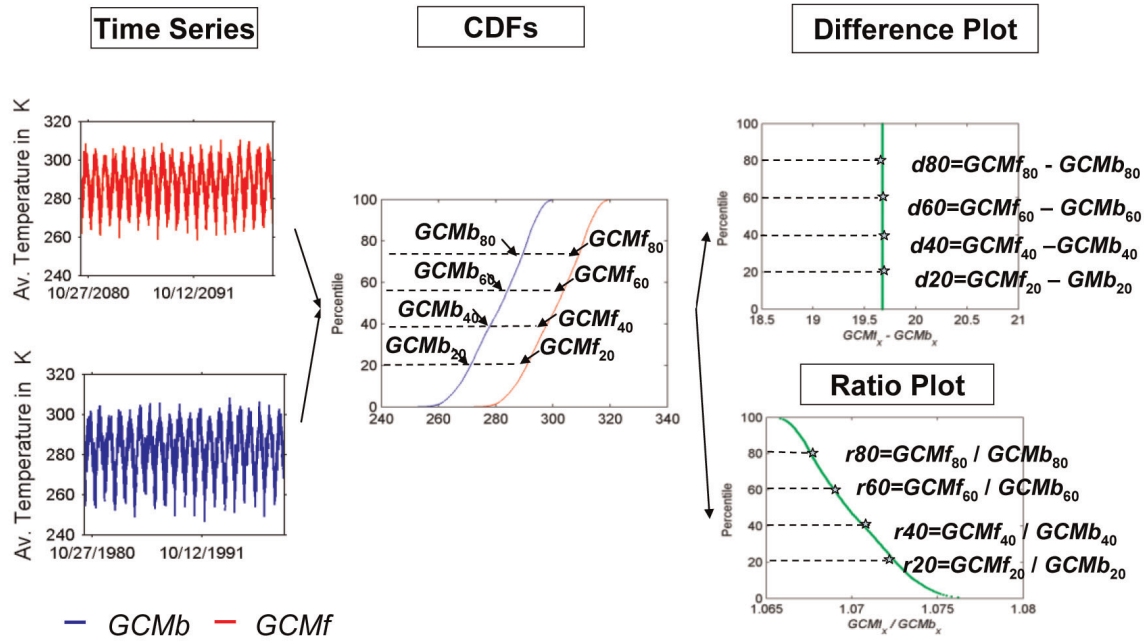


Figure 3. Explains the procedure used to obtain difference plot and ratio plots for use in the graphical approach to study the distribution of the CFs in different magnitudes of the variable. The calculations associated with 4 specific percentiles are illustrated using dashed lines. The difference plot and ratio plot shown in the figure are theoretical templates to guide the choice of change factor methodology (CFM) in cases where an additive CF is appropriate in which case the difference plot will be a vertical line and the ratio plot will be a curved line.

ranges (say 1st through 50th percentiles, 50th through 100th percentiles), indicating that multiple additive CFs are appropriate (Figure 5c); (4) the ratio plot is close to multiple straight vertical lines for different percentile ranges (say 1st through 50th percentiles, 50th through 100th percentiles), indicating that multiple multiplicative CFs are appropriate (Figure 5d); and (5) both the difference and ratio plots are curved, indicating a larger number of multiple multiplicative or additive CFs are probably in order (Figure 5e).

[32] It is found that the shapes of the difference and ratio plots vary depending on meteorological variables, GCMs,

and special report on emission scenarios (SRES) scenarios. Hence, we infer that fixing a single type of CF formulation for use in this region may not be appropriate. We assume that this type of variability in CFs is probably the norm, not the exception. Thus, to apply this methodological analysis for multiple variables/GCMs in a particular region may in many cases be quite cumbersome. This raises the question of how to proceed in such a case, and whether there is a method that can be applied more generally that would circumvent the need for such a cumbersome analysis. This is addressed in section 4.4.

4.4. Comparison of Single and Multiple CF Results

[33] In this section we determine whether one particular method is generally as good as, or better than, the others in all or most circumstances. Using six of the nine meteorological variables (the only ones for which observations were available at this location), both additive and multiplicative CFs were used to estimated future climates either as a single CF or from multiple CFs using 3, 10, 25, 50, and 100 bins. This results in six *LSf* time series derived using the additive method, as well as six *LSf* time series derived using the multiplicative method, for each GCM, emission scenario, and future time period.

[34] For each future scenario, the root mean sum of squares of the differences (RMSD, defined in equation (14)) between the additive and multiplicative *LSf* series are calculated for all bin sizes.

$$RMSD = \sqrt{\sum (LSf_{mul} - LSf_{add})^2} \tag{14}$$

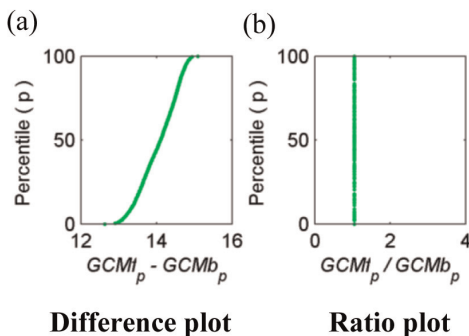


Figure 4. Theoretical templates of difference and ratio plots to guide the choice of change factor methodology (CFM). In cases where a multiplicative CF is appropriate, (a) the difference plot will be a curved line and (b) the ratio plot will be a vertical line.

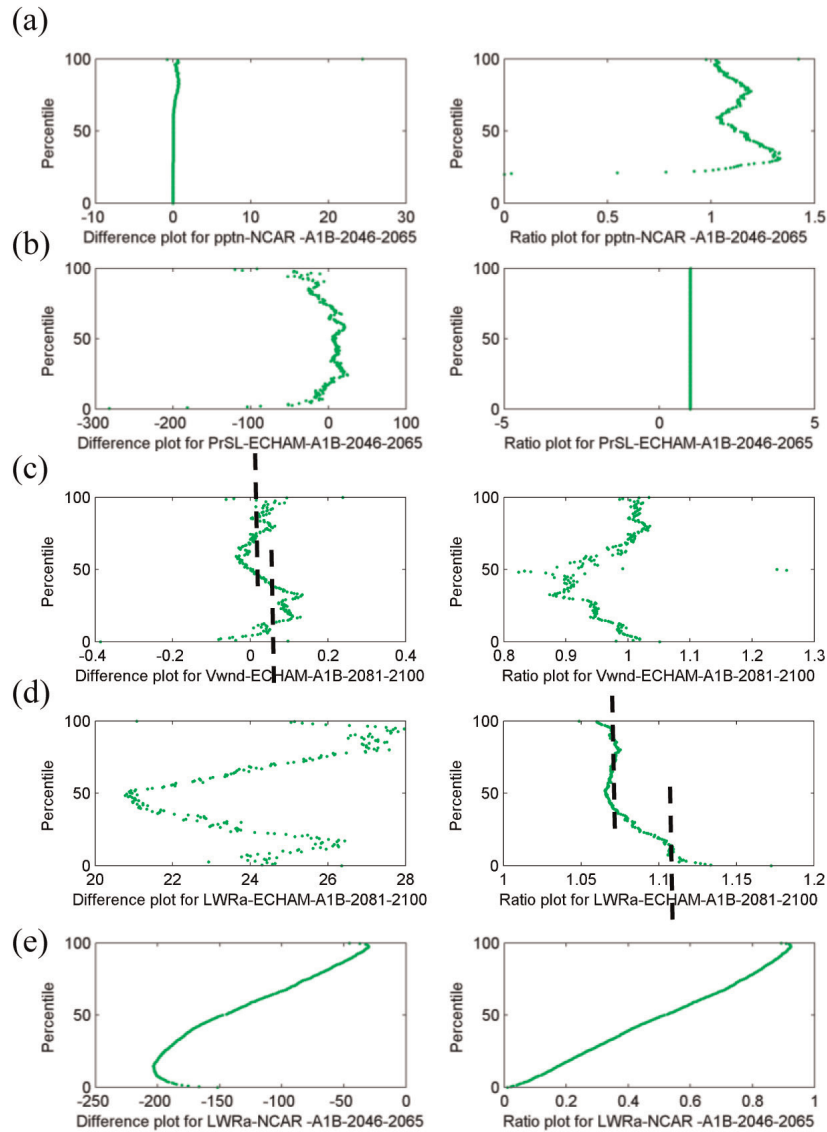


Figure 5. Illustrative examples of difference and ratio plots from a study of the Cannonsville basin. (a) Single additive CFM, where the difference plot is close to a straight vertical line and ratio plot is curved. (b) Single multiplicative CFM, where the ratio plot that is close to a straight vertical line and difference plots is curved. (c) Multiple additive CFM, where the difference plot is close to multiple straight vertical lines within different percentile bands (i.e., 1st through 40th percentiles, 40th through 100th percentiles) and the ratio plot is curved. (d) Multiple multiplicative CFM, where the ratio plot is close to multiple straight vertical lines for different percentile bands (i.e., First through 25th percentiles, 25th through 100th percentiles) and the difference plot is curved. (e) Nondefinitive CFM, where the difference plots and ratio plots are both curved. Pptn, PrSL, Vwnd, LWRa in the panel abscissa titles refer to precipitation, sea level pressure, meridional wind and longwave radiation respectively.

[35] Figure 6 shows how RMSD depends on bin size for one sample scenario (SRES A2). As the number of bins is increased, RMSD always stabilizes to a constant value. Stabilization of values occurs as the number of bins exceeds approximately 25. Furthermore, in most cases RMSD is also minimized with ≥ 25 bins. In some cases RMSD increases with increasing bin size (in the example shown in Figure 6, shortwave radiation for the GISS model). This is because the projected change is large, falling within either the upper left quadrant (sector 1) or lower right quadrant (sector 2) of Figure 2. The multiplicative CFs ($\overline{GCMf}/\overline{GCMb}$) in sector 1

are very high, when the value of \overline{GCMb} is very small when compared to \overline{GCMf} . Such large CFs result in very unrealistic scenarios. Hence additive CFs was recommended. Further, from the difference and ratio plots obtained derived using daily values from three GCMs (section 4.3), it was inferred that fixing a single CF formulation for use in this region may not be appropriate. It may be noted the RMSD values for temperatures and wind speed are very small of the order of 10^{-4} to 10^{-3} K and 10^{-2} m/sec respectively.

[36] Some meteorological variables have upper and/or lower limits of the value they can have. For example,

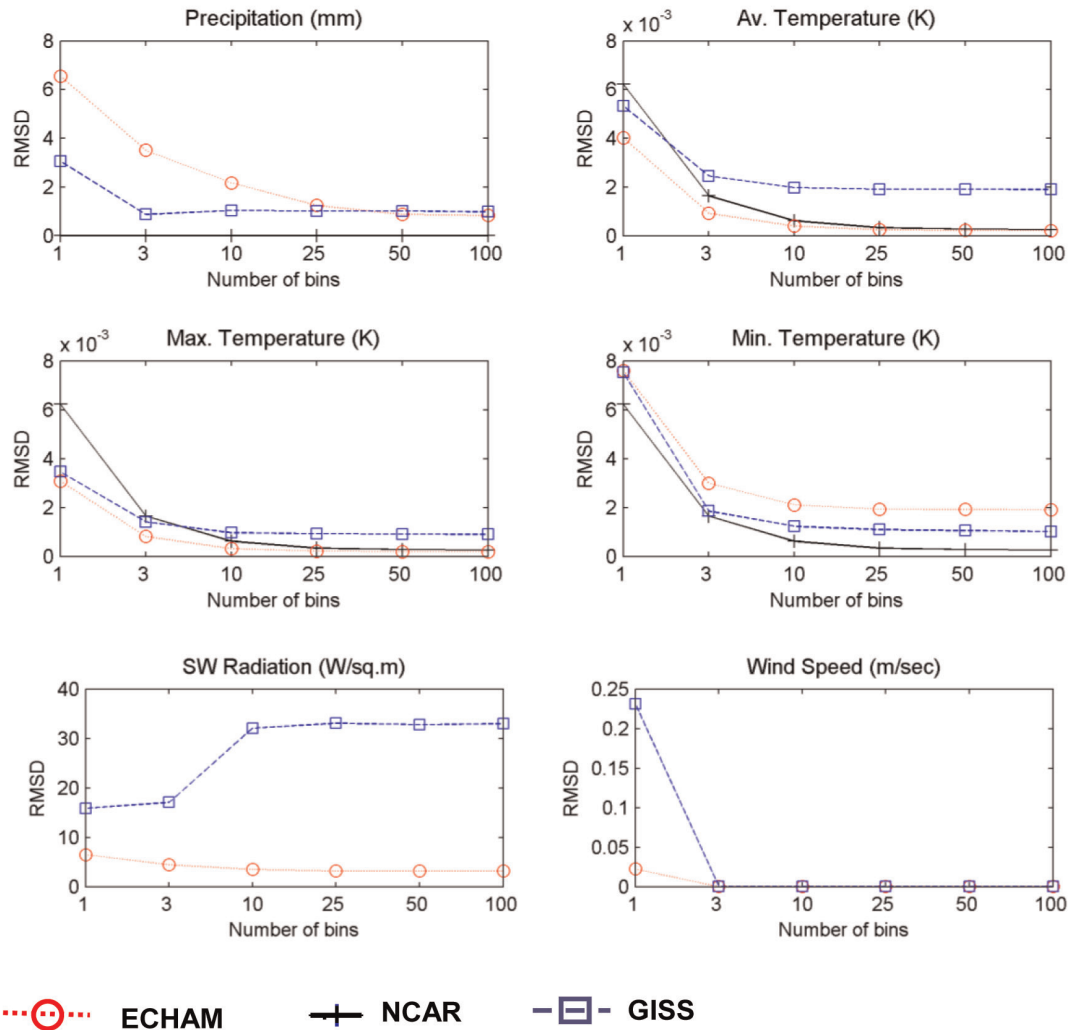


Figure 6. Effect of the number of bins (n) on the difference between additive and multiplicative change factors. On each panel the abscissa shows the number of bins. The ordinate shows the root sum squares of differences (RMSD, equation (14)) between an additive and multiplicative CF. Results taken from three GCMs; A2 emission scenario; base temporal domain is 1981–2000 (January only); future temporal domain is 2046–2065 (January only); six meteorological variables; and daily temporal resolution. In all cases, results stabilize with ≥ 25 bins. In all cases except GISS shortwave radiation, RMSD is minimized with ≥ 25 bins.

precipitation and wind speed have a lower limit of 0 (i.e., positive values only). Surface temperatures in absolute scale have a theoretical lower limit (-273 K), but not realistic, so it can be assumed as not having upper and lower limits because such lower temperatures are not plausible. Solar radiation at the earth’s surface has a lower limit of 0, and an upper limit equal to the top-of-the-atmosphere radiation multiplied by the maximum transmissivity of the atmosphere (these values vary with latitude and time of year). For variables such as precipitation, wind speed, and solar radiation, the *GCMf* or *GCMb* can have values equal or close to 0, causing multiplicative CFs to be either undefined, or unrealistically high or low.

[37] Thus, there are two main results demonstrated in this section. The first result is that the use of multiple bins usually eliminates the difference between additive and multiplicative

CFs. This is because with multiple CFs, the magnitude of the CF in any bin (i.e., for any magnitude of the variable) is independent of the magnitude of CFs in other bins. Thus, multiple CFs can mimic single CFs (when the magnitudes of the CFs for different variable values are dependent on each other) as well as more complicated cases (when the magnitudes of the CFs for different variable values are completely independent). Single CFs can essentially be considered a special case of multiple CFs. Furthermore, when using a sufficient number of bins (25 or more in our analysis) the differences between additive and multiplicative CFs are eliminated.

[38] The second main result is that additive CFs are preferable to multiplicative CFs. This is because of the problem that multiplicative CFs encounter with undefined, or unrealistically small or large, CFs associated with variable

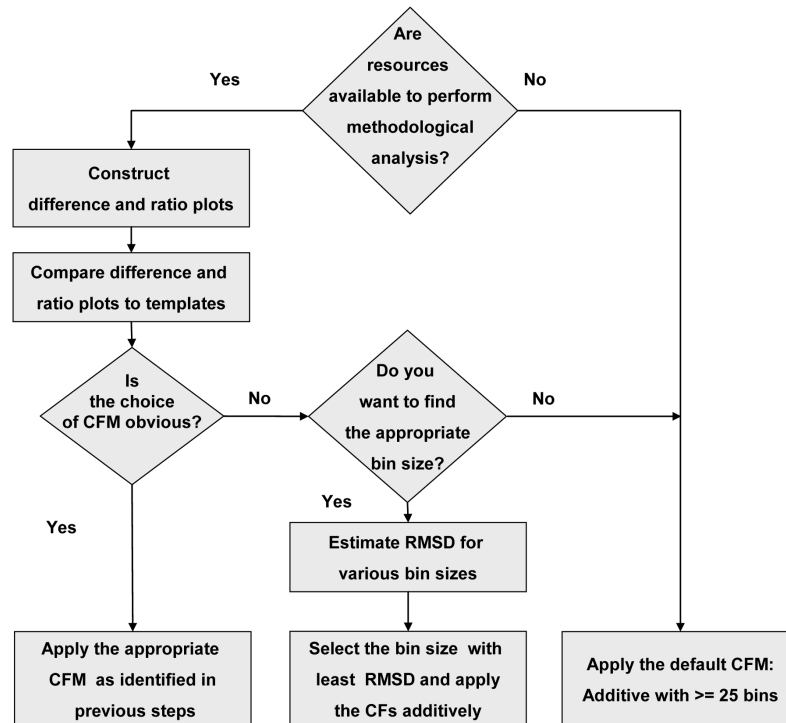


Figure 7. Flowchart of the procedure developed in this study to determine the appropriate type of CFM to be used for a particular variable, location, GCM and scenario. The symbols CFM, CF and RMSD refer to Change factor methodology, change factor and root mean sum of differences respectively.

values near 0. Additive CFs avoid such problems. While using additive CFs, the values of future meteorological variables which have a 0 lower limit should be checked to make sure that they do not get negative values (e.g. precipitation, wind speed, solar radiation).

5. Summary and Conclusions

[39] In this study we compare and contrast different categories of Change Factor Methodology (CFM) when using GCM results to project future climate for subgrid-scale impact analyzes. For some variables, the choice of additive versus multiplicative seems, as inferred by their general usage in the published literature, to be intuitive to researchers (e.g. additive for temperature, multiplicative for precipitation) although the physical reasoning behind these choices has not been adequately explained and is not obvious. For other variables (e.g. wind speed) there seems to be little or no precedent in the literature.

[40] In cases when the frequency distribution of GCM baseline climate is close to the frequency distribution of observed climate (i.e., the GCM climate simulation has a small bias), or when the frequency distribution of GCM future climate is close to the frequency distribution of GCM baseline climate (i.e., the GCM projects only a small climate change), additive and multiplicative single CFMs provide comparable results. However, the greater the difference between modeled and observed baseline climates, or the greater the projected climate change, the greater will be the difference in the local climate change projections made by these two methods. In general, multiple CFMs provide local

climate change projections that are more consistent between the additive and multiplicative methods.

[41] This study suggests two options to guide the choice of change factor methodology: (1) In studies where a detailed methodological analysis is possible, the difference and ratio plots introduced in this study may be useful in determining whether an additive or multiplicative method is most appropriate. Our suggested steps for performing such an analysis are discussed in the results section and outlined in Figure 7. (2) In most circumstances, however, it is likely to be too cumbersome to perform such a detailed study for each of the different locations, GCMs, scenarios, and variables needed in a climate change impact analysis. Also, in many cases the difference and ratio plots may not provide conclusive evidence as to which type of CFM to employ. In all circumstances in which a detailed methodological analysis cannot be performed, or the choice of CFM is not obvious, we recommend that multiple additive CFs with ≥ 25 bins be used. This will minimize the impact of the choice of whether to use the additive or multiplicative method, and remove one source of uncertainty from the analysis.

[42] **Acknowledgments.** We thank the Climate Impacts Group of the Goddard Institute of Space Studies who helped the NYCDEP obtain and analyze GCM model output.

References

Akhtar, M., N. Ahmad, and M. J. Booij (2008), The impact of climate change on the water resources of Hindukush-Karakorum-Himalaya region under different glacier coverage scenarios, *Journal Hydrol.*, 255(1-4), 148–163. doi:10.1016/j.jhydrol.2008.03.015.

- Anandhi, A. (2010), Assessing impact of climate change on season length in Karnataka for IPCC Scenarios *J. Earth Syst. Sci.*, 119(4), 447–460, doi:10.1007/s12040-010-0034-5.
- Anandhi, A., V. V. Srinivas, R. S. Nanjundiah, and D. N. Kumar (2008), Downscaling precipitation to river basin in India for IPCC SRES scenarios using support vector machine, *Int. J. Climatol.*, 28(3), 401–420 doi:10.1002/joc.1529.
- Anandhi, A., V. V. Srinivas, D. N. Kumar, and R. S. Nanjundiah (2009), Role of predictors in downscaling surface temperature to river basin in India for IPCC SRES scenarios using support vector machine, *Int. J. Climatol.*, 29(4), 583–603 doi: 10.1002/joc.1529.
- Andréasson, J., S. Bergström, B. Carlsson, L. P. Graham, and G. Lindström (2004), Hydrological change - Climate change impact simulations for Sweden, *Ambio*, 33(4), 228–234.
- Brinkmann, W. (1999), Application of non-hierarchically clustered circulation components to surface weather conditions: Lake Superior basin winter temperatures, *Theor. Appl. Climatol.*, 63(1–2), 41–56.
- Carter, T. R., M. L. Parry, H. Harasawa, and S. Nishioka (1994), *IPCC Technical Guidelines for Assessing Climate Change Impacts and Adaptations*, 59 pp, Univ. College London, U. K.
- Chen, J., F. P. Brisette, and R. Leconte (2010), A daily stochastic weather generator for preserving low-frequency of climate variability, *J. Hydrol.*, 388(3–4), 480–490, doi:10.1016/j.jhydrol.2010.05.032
- Diaz-Nieto, J., and R. L. Wilby (2005), A comparison of statistical downscaling and climate change factor methods: Impacts on low flows in the River Thames, United Kingdom, *Clim. Change*, 69(2–3), 245–268 doi:10.1007/s10584-005-1157-6.
- George, G. (Ed.) (2010), *The Impact of Climatic Change on European Lakes*, Vol. 4, *Aquat. Ecol.*, 507 pp., Springer, New York.
- Gleick, P. H. (1986), Methods for evaluating the regional hydrologic impacts of global climatic changes, *J. Hydrol.*, 88(1–2), 97–116, doi:10.1016/0022-1694(86)90199-X.
- Grotch, S. L., and M. C. MacCracken (1991), The use of general circulation models to predict regional climatic change, *J. Clim.*, 4(3), 286–303.
- Hay, L. E., R. L. Wilby, and G. H. Leavesley (2000), A comparison of delta change and downscaled GCM scenarios for three mountainous basins in the United States, *J. Am. Water Resour. Assoc.*, 36(2), 387–397, doi:10.1111/j.1752-1688.2000.tb04276.x.
- Horton, R., and C. Rosenzweig (2010), Climate Risk Information, in *Climate Change Adaptation in New York City: Building a Risk Management Response: New York City Panel on Climate Change 2010 Report*, edited by C. Rosenzweig and W. Solecki, appendix A, pp. 147–228, N. Y. Acad. of Sci., New York.
- Huth, R. (1997), Potential of continental-scale circulation for the determination of local daily surface variables, *Theor. Appl. Climatol.*, 56(4), 165–186, doi:10.1007/BF00866425.
- Kilsby, C. G., et al. (2007), A daily weather generator for use in climate change studies, *Environ. Modell. Software*, 22(12), 1705–1719, doi:10.1016/j.envsoft.2007.02.005.
- Major, D. C., and M. O'Grady (2010), Adaptation assessment guidebook, in *Climate Change Adaptation in New York City: Building a Risk Management Response: New York City Panel on Climate Change 2010 Report*, edited by C. Rosenzweig and W. Solecki, appendix B, pp. 229–292, N. Y. Acad. of Sci., New York.
- Mearns, L., et al. (2001), *Climate scenario development, in Climate Change 2001: The Scientific Basis: Contribution of Working Group I to the Third Assessment Report of the Intergovernmental Panel on Climate Change*, edited by J. Houghton, et al., pp. 739–768, Cambridge Univ. Press, Cambridge, U. K.
- Mehrotra, R., R. Srikantha, and A. Sharma (2006), A comparison of three stochastic multi-site precipitation occurrence generators, *J. Hydrol.*, 331(1–2), 280–292, doi:10.1016/j.jhydrol.2006.05.016.
- Olsson, J., K. Berggren, M. Olofsson, and M. Viklander (2009), Applying climate model precipitation scenarios for urban hydrological assessment: A case study in Kalmar City, Sweden, *Atmos. Res.*, 92(3), 364–375.
- Perkins, S. E., et al. (2007), Evaluation of the AR4 Climate Models' Simulated Daily Maximum Temperature, Minimum Temperature, and Precipitation over Australia Using Probability Density Functions, *J. Clim.*, 20(17), 4356–4376, doi:10.1175/JCLI4253.1.
- Rosenzweig, C., and A. Iglesias (1994), Implications of climate change for international agriculture: Crop modeling study, *Rep. EPA-230-B-94-003*, U. S. Environ. Prot. Agency, Policy, Plann. and Eval., Clim. Change Div., Washington D. C.
- Semadeni-Davies, A. (2004), Urban water management vs. climate change: Impacts on cold region wastewater inflows, *Clim. Change*, 64(1–2), 103–126, doi:10.1023/B:CLIM.0000024669.22066.04.
- Semadeni-Davies, A., C. Hernebring, G. Svensson, and L.-G. Gustafsson (2008), The impacts of climate change and urbanization on drainage in Helsingborg, Sweden: Combined sewer system, *J. Hydrol.*, 350(1–2), 100–113, doi:10.1016/j.jhydrol.2007.11.006.
- Smith, J., and M. Hulme (1998), Climate change scenarios, in *Handbook on Methods of Climate Change Impacts Assessment and Adaptation Strategies*, edited by J. Feenstra et al., 40 pp., U. N. Environ. Programme, Inst. Environ. Stud., Amsterdam.
- Stehlik, J., and A. Bárdossy (2002), Multivariate stochastic downscaling model for generating daily precipitation series based on atmospheric circulation, *J. Hydrol.*, 256(1–2), 120–141 doi:10.1016/S0022-1694(01)00529-7.
- Tripathi, S. V. V. Srinivas, and R. S. Nanjundiah (2006), Downscaling of precipitation for climate change scenarios: A support vector machine approach., *J. Hydrol.*, 330(3–4), 621–640.
- Wang, Y., et al. (2004), Regional climate modeling: Progress, challenges, and prospects, *J. Meteorol. Soc. Jpn.*, 82(6), 1599–1628.
- Wetterhall, F., S. Halldin, and C.-Y. Xu (2005), Statistical precipitation downscaling in central Sweden with the analogue method, *J. Hydrol.*, 306(1–4), 136–174, doi:10.1016/j.jhydrol.2004.09.008.
- Wilby, R., et al. (2000), Hydrological responses to dynamically and statistically downscaled climate model output, *Geophys. Res. Lett.*, 27(8), 1199–1202, doi:10.1029/1999GL006078.
- Wilks, D. S. (1998), Multi-site generalization of a daily stochastic precipitation model, *J. Hydrol.*, 210(1–4), 178–191, doi:10.1016/S0022-1694(98)00186-3.

A. Anandhi, A. Frei, and A. H. Matonse, CUNY Institute for Sustainable Cities, City University of New York, New York City, NY 10065, USA. (aswamy@hunter.cuny.edu)

D. Lounsbury, D. C. Pierson, E. M. Schneiderman, and M. S. Zion, Water Quality Modeling Group, New York City Department of Environmental Protection, 71 Smith Ave., Kingston, NY 12401, USA.

Effects of changes in snow pattern and the timing of runoff on NYC water supply system

Adão H. Matonse,^{1*} Donald C. Pierson,² Allan Frei,^{1,3} Mark S. Zion,² Elliot M. Schneiderman,² Aavudai Anandhi,¹ Rajith Mukundan¹ and Soni M. Pradhanang¹

¹ City University of New York, CUNY Institute for Sustainable Cities, New York, NY

² New York City Environmental Protection, Bureau of Water Supply, Kingston, NY

³ Hunter College, City University of New York, Department of Geography, New York, NY

Abstract:

This study focuses on the effect of projected changes in rainfall, snow accumulation and snowmelt, and consequent changes in the timing of runoff on NYC water supply system storage and operation as simulated by the NYC reservoir system Operational Analysis and Simulation of Integrated Systems (OASIS) model. The Generalized Watershed Loading Functions—Variable Source Area (GWL-F-VSA)—watershed model is used with future climate scenarios derived from different General Circulation Models (GCMs) to simulate future inflows to reservoirs that are part of the New York City Water Supply System (NYCWSS). Future scenarios that use current system operation rules and demands, but changed reservoir inflows, suggest that changes in precipitation and snowmelt will affect regional water availability on a seasonal basis. The combined effect of projected increases in winter air temperatures, increased winter rain, and earlier snowmelt may result in more runoff during winter. This will cause reservoir storage levels, water releases and spills to increase during the winter and earlier reservoir refill in the spring. An overall increase in precipitation will result in a reduction in number of days the system is under drought conditions, despite increased evapotranspiration later in the year. Copyright © 2011 John Wiley & Sons, Ltd.

KEY WORDS Climate change; snow and water supply operation; reservoir system OASIS model; reservoir system indicators; watershed modelling

Received 23 July 2010; Accepted 1 April 2011

INTRODUCTION

The New York City Water Supply System (NYCWSS) comprises a total of 19 reservoirs and three controlled lakes. Reservoirs were initially developed east of the Hudson River (EOH) in and adjacent to the Croton River Watershed. In total, 13 reservoirs were built in the EOH portion of the supply, and today these contain approximately 10% of the water stored in the NYCWSS. In 1905, the New York City Board of Water Supply was created by the New York State legislature with the task of identifying and delivering new water sources for the growing NYC metropolis (NYCDEP 2006). Reservoir construction in areas west of the Hudson River (WOH) began with the development of the Catskill subsystem, which was finalized with the completion of the Schoharie Reservoir in 1926. Additional reservoir capacity was added to the system during the 1950s and 1960s with the addition of four reservoirs that form the Upper Delaware subsystem in the NYCWSS WOH region. Today, the total NYC reservoir system which includes both the EOH and WOH regions has the capacity to store up to 219 553.8 ha-m ($2195.5 \times 10^6 \text{ m}^3$) of water (NYCDEP 2006). In a system as diverse as the NYCWSS, the allocation and use of water among the different reservoirs is based on a variety

of factors including the relative differences in water availability, water quality, system infrastructure, and demands. The combined effects of these considerations have been formalized into a rule set describing NYCWSS operation, and this rule set is the basis of the NYC OASIS (Operational Analysis and Simulation of Integrated Systems) (HydroLogics, Inc., 2007) system operations model.

Previous studies have indicated that for mountainous regions like the Catskill Mountains in New York where snow accounts for an important component of the annual precipitation, future changes in temperature and precipitation may lead to changes in winter rainfall, snowpack water equivalent, water loss due to evapotranspiration, and a shift in the timing of runoff (Blake *et al.*, 2000; Frei *et al.*, 2002; Burns *et al.*, 2007; Hayhoe *et al.*, 2007; Brekke *et al.*, 2009). Basing on a study involving Cannonsville and Ashokan watersheds that are part of the NYCWSS Frei *et al.* (2002) estimated that snowfall accounts for 18–21% of total precipitation. Also, when soils are saturated, precipitation and snowmelt are more likely to runoff and becoming less available for evaporation. Given the fact that most of snowmelt occurs during spring, when soils are saturated, the contribution of snow to total runoff is estimated being between 24 and 30% in this region. The effect of snow on runoff is 1.3–1.5 times greater than its contribution to total annual precipitation (Frei *et al.*, 2002). An

* Correspondence to: Adão H. Matonse, CUNY Institute for Sustainable Cities, City University of New York, New York, NY.
E-mail: amatonse@hunter.cuny.edu

earlier peak in snowmelt as suggested by Burns *et al.* (2007) may result in reservoirs filling earlier and more water losses. However, how these changes will impact the NYC water supply will depend on overall water availability, demands, operational rules and system flexibility to adapt to these changes. As part of New York City Department of Environment Protection (NYCDEP) Climate Change Integrated Modeling Project for Water Quantity and Quality (CCIMP) project (NYCDEP 2008) baseline and future climate scenarios have been developed for the WOH region contributing water to the NYCWSS. The projected climate data are used to drive the Generalized Watershed Loading Functions—Variable Source Area (GWL-F-VSA)—watershed model to simulate snowpack, snowmelt and inflows to reservoirs (Haith and Shoemaker, 1987; Schneiderman *et al.*, 2002; Schneiderman *et al.*, 2007). As snowpack represents extra water storage and the timing of snowmelt impacts winter and spring streamflow patterns in this region (Frei *et al.*, 2002; Burns *et al.*, 2007), our objective is to investigate how changes in snowmelt and the timing of runoff due to climate change can affect NYCWSS water storage and operation. GWLF-VSA-simulated reservoir inflow is input into the NYCWSS OASIS reservoir system model to simulate water storage and NYCWSS operation. NYC OASIS generates a selected number of system indicators that are used to represent the instantaneous state of system operations and to assess system performance. These indicators include reservoir storage volume, release and spill, drought conditions occurrence, and probability of reservoirs to refill by 1 June.

Reservoir operation rules have evolved over time, and the current rules in NYC OASIS model are based on knowledge gained during years of historical operation of the system to meet demands, maintain high water quality, and provide regulatory releases while balancing diversion from the Delaware, Catskill, and Croton subsystems. For this study, rules and water demands used with the future climate simulations were considered stationary and equal to present conditions. There are advantages and disadvantages in these assumptions: (i) maintaining current rules helps evaluate the system effectiveness in responding only to changes in climate and hydrology in the WOH watersheds; (ii) simulations with the NYC OASIS model are sensitive to existing demand levels. A preliminary analysis of NYC water demands indicates a decline during recent times, starting in the late 1980s. A continuation of this trend would most likely be in favour of the current system to fulfilling its objectives, however, future changes in population and other socio-economic development can lead to increases in future demand levels and consequent need of new adjustments in system operations. In addition, preliminary analysis of historical data indicates a positive correlation between water demands and high temperature suggesting that climate change can also cause a direct impact on future demands. The incorporation of projections in future water demands is

an important component to be considered for a more comprehensive study of the effects of climate change on NYC water supply and will require a kind of socio-economic analysis that is outside of the scope of the present manuscript.

STUDY SITE

NYCWSS integrates 19 interconnected reservoirs and two aqueducts to supply more than 1 billion gallons of drinking water per day to about 9 million people in NYC and nearby counties (NYCDEP 2006). It is the largest surface water supply in the United States with no mechanical filtration (Daily and Ellison 2002). The system includes the NYC WOH and EOH regions (Figure 1). As illustrated in Figure 1, the WOH portion which is the focus of this study includes the Catskill and Delaware system reservoir watersheds (further called subsystems) and supplies more than 90 percent of NYC water demands. The Delaware subsystem is required to release water to the lower Delaware (LD) watersheds (which serve New Jersey and Pennsylvania) as part of implementing regulatory rules for the Delaware system.

The Catskill subsystem has a total of 53 185 ha-m (approximately $531 \times 10^6 \text{ m}^3$) storage capacity. This includes the Ashokan (46 522 ha-m) and Schoharie (6662 ha-m) reservoirs storages. The Delaware subsystem has a total of 121 284 ha-m ($1.212 \times 10^9 \text{ m}^3$) storage capacity. This capacity includes the available storage at the Pepacton (53 071 ha-m), Cannonsville (36 226 ha-m), Rondout (18 775 ha-m) and Neversink (13 211 ha-m) reservoirs (NYCDEP 2006). The WOH watershed has an approximate area of 4103 square kilometers. The regional hydrology is influenced by snowpack water storage and snowmelt processes that depend on temperature and precipitation patterns. One challenge for the reservoir system operation is the management of peak flows, some of which are associated with snowmelt and flooding events particularly during March and April. According to the 2000 census, the population density is 29 and 499 persons per square mile for WOH and EOH areas, respectively (NYCDEP 2006).

WOH has a humid continental climate with cold winters (typically -5 to 0°C) and cool (typically 15 to 20°C) summers. Being a mountainous region the temperature is strongly impacted by elevation (Burns *et al.*, 2007) which rises to approximately 1200 m from the Hudson River. Previous studies (such as Burns *et al.*, 2007) have found that a 0.6 degree Celsius increase in mean annual temperature, and 136 mm increase in yearly cumulative precipitation have occurred over the past 50-year period for the Catskill Mountain region. This manuscript examines how further changes in climate and a shift in snow processes as simulated by the GCMs and scenarios applied in this study will affect future water availability in the region, and the status and operation of the NYCWSS.

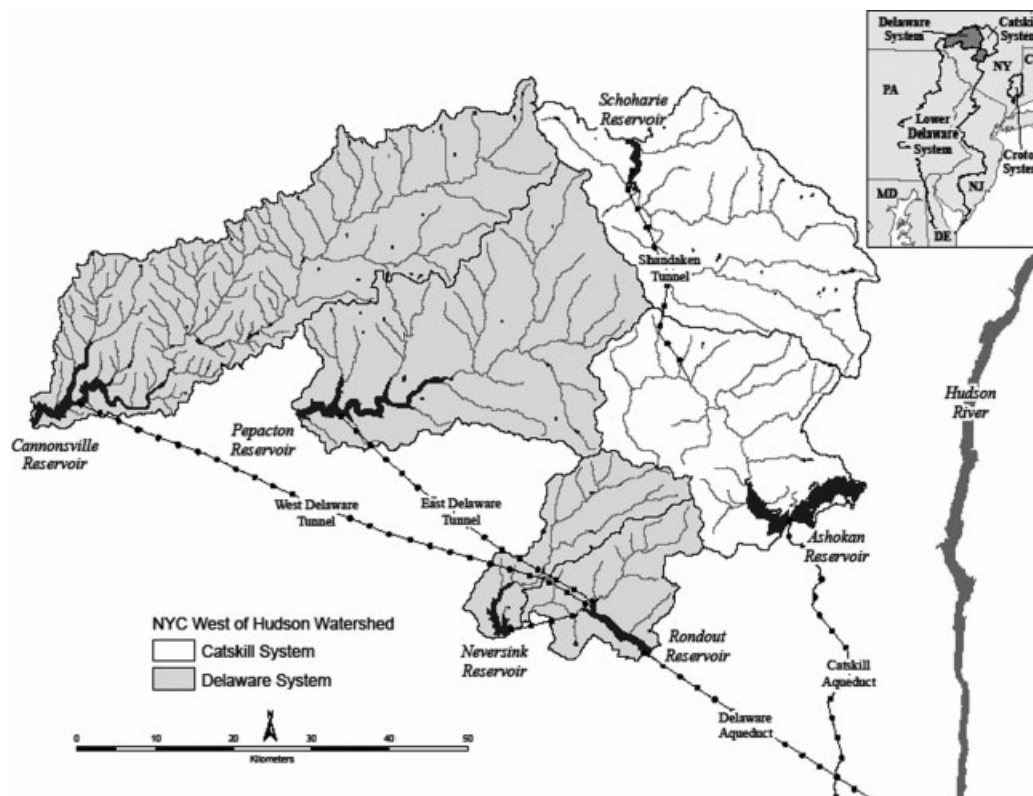


Figure 1. NYC WOH reservoir watersheds and aqueducts schematic. The location view at the top right corner of this figure shows an overview of the entire NYC water supply system including the EOH (Croton), WOH and LD parts of the system. There are release requirements from the WOH to LD. However, LD does not contribute water to NYC water supply

METHODOLOGY

Simulated baseline and future air temperature and precipitation were derived from GCMs and a monthly delta change methodology (as described by Anandhi *et al.*, 2011) and used as input to the GWLF-VSA watershed model. In the past, the delta change methodology has been applied in many climate change studies including Gleick (1986), Hey *et al.* (2000), Kilsby *et al.* (2007), Lettenmaier and Gan (1990), and Maurer and Duffy (2005). GWLF-VSA (Schneiderman *et al.*, 2007) is a lumped parameter model based on the original GWLF model (Haith and Schoemaker 1987) that simulates daily streamflow discharge and monthly sediment and nutrient loads at a watershed scale. The GWLF model accounts for dissolved (originated from point sources, ground water and rural runoff) and solid-phase (from rural and urban runoff) nitrogen and phosphorus in streamflow. Runoff is calculated using the USDA Soil Conservation Service (SCS) runoff Curve Number (CN) methodology. The CN is an empirical parameter for estimating direct runoff or infiltration excess runoff. CN value can range from 30 to 100 depending on the hydrologic soil group, land cover type, land treatment, hydrologic condition, and antecedent runoff condition (Rawls *et al.*, 1993). Streamflow results from contributions of runoff and baseflow. Daily snowmelt is estimated based on temperature degree-day, with a daily updating of a single watershed-wide snowpack. The model accounts for an unsaturated, shallow saturated, and deep saturated zones.

A daily mass balance for the unsaturated shallow (U_{t+1}) and saturated (S_{t+1}) zones are a function of shallow saturated (S_t) and unsaturated zone (U_t) soil moistures at the beginning of day t , the watershed runoff (Q_t), evapotranspiration (E_t), percolation into the shallow zone (PC_t), groundwater discharge to the stream (G_t) and seepage flow to the deep saturated zone (D_t), as represented in Equations (1) and (2).

$$U_{t+1} = U_t + R_t + M_t - Q_t - E_t - PC_t \quad (1)$$

$$S_{t+1} = S_t + PC_t - G_t - D_t \quad (2)$$

Inputs to GWLF include daily precipitation and air temperature data, runoff sources, nutrient data and a number of parameters describing transport processes. One important modification was introduced in GWLF-VSA version of the model (Schneiderman *et al.*, 2007) by accounting for surface runoff distribution across the landscape based on a saturation-excess interpretation of the SCS Curve Number equation and a topographic index of saturation probability. This modification is important since saturation-excess is a dominant process in the studied watersheds. GWLF-VSA development included model calibration against measured streamflow data from 10 USGS gauge stations in the study region namely: West Branch Delaware River at Walton, NY (01 423 000; 0.89); Schoharie Creek at Prattsville, NY (01 350 000; 0.8); Manor Kill at West Conesville Near Gilboa, NY (01 350 080; 0.7); Neversink River near Claryville, NY

(01 435 000; 0.82); East Branch Delaware River at Margaretville, NY (01 413 500; 0.81); Mill Brook near Dunraven, NY (01 414 500; 0.8); Temper Kill near Andes, NY (01 414 500; 0.83); Esopus Creek at Coldbrook, NY (01 362 500; 0.88); Esopus Creek at Allaben, NY (01 362 200; 0.79) and Rondout Creek near Lowes Corner, NY (01 365 000; 0.79). The first number in the parentheses indicates the USGS gauge station identification number while the second number represents the Nash-Sutcliffe efficiency coefficient (NS) value for the calibration period. Calibration was performed to fit measured streamflows on a monthly time interval for the period 1991–2000. For this study, GWLF-VSA was used to simulate future evapotranspiration, snowpack, snowmelt, and streamflow discharge for all the reservoir watersheds in the WOH part of the NYCWSS system. For the EOH portion of the system, historical inflows to reservoirs were maintained throughout all simulations. Historical daily inflows to EOH reservoirs were developed using measured monthly inflows to Croton system available from 1927 through 1992, daily streamflow from a nearby USGS station (Prattsville, 1902–2002), weights based on drainage basin areas for individual EOH reservoirs, and a mass balance method. For this study EOH inflows were not adjusted to account for future climate change. This assumption was considered reasonable since EOH contributes less than 10% to NYC water supply requirements.

Simulated GWLF-VSA stream discharge data were subsequently used as inputs to the NYC OASIS reservoir system model to simulate system operations and evaluate system performance. OASIS (HydroLogics, 2007) is a generalized model that was developed to simulate the operations of interconnected reservoir systems, and that simulates daily changes in storage and the transfer of water within the reservoir system by solving a linear program. An operations control language built into OASIS is used to set system operating rules, and a graphical user interface is available to represent the current elements of the system and system interconnections. The NYC OASIS model reflects the infrastructure and operation rules that are specific to the NYCWSS. The OASIS model seeks to balance Catskill, Delaware, and Croton subsystems, in a process that is based on storage levels, the probability of the system to refill by 1 June and season. Also, a number of rules specific to regulatory requirements for downstream releases, water quality requirements and system operational needs are encoded within the OASIS rule set.

Simulations for this study focused on changes in WOH inflow as a result of the different climate change scenarios while assuming EOH and LD inflows, system operation rules and water demands are stationary and identical to present day. System indicators are used in this study to help evaluate the NYCWSS response to the simulated changes in WOH inputs. These indicators are generated for the Catskill and Delaware subsystems and include volumes of reservoir storage, controlled releases, and uncontrolled spills; the occurrence of drought conditions;

and the probability of reservoir to refill by 1 June. Looking at changes in inflow, storage, release, and spill provides information on how the current system (with current rules and demands) can respond to changes in WOH inflow that can be expected under future climate conditions and helps to identify sensitive parts of the system that will require further investigation and analysis.

Drought occurrence is based on the volume of water or available storage in the water supply system and different thresholds of storage are used to define three drought levels: watch, warning, and emergency. Drought occurrence can be used as a measure of the NYC system performance, as it indicates the number of days per year a particular subsystem is likely to be under drought conditions. The call for a particular drought level is based on a comparison between the total present day storage of the subsystem with average yearly patterns of storage for each individual subsystem and predefined thresholds indicating drought conditions. The combination of the drought conditions in Delaware and Catskill subsystems determine the drought state for the entire NYCWSS. Drought status can affect the operation of the water supply and lead to voluntary and mandatory water conservation policies.

Given the importance of extended periods of low streamflow in determining downstream minimum releases and drought conditions (Matonse and Kroll, 2009; Vogel and Fennessey, 1995) we examined low-flow indices. For this study we selected one of the most commonly used low-flow indices in the United States, the 7-day, 10-year ($7Q_{10}$ or $Q_{7,10}$) statistic which is based on 7-day annual minimum flow series (Kroll and Vogel, 2002; Matonse, 2009). The $7Q_{10}$ is a statistical estimator of the lowest 7-day streamflow that on average will be exceeded 9 out of 10 years (Stedinger and Thomas, 1985). We applied a frequency analysis to baseline historical and future simulated average daily annual maximum streamflow values based on a log-Pearson Type III distribution assumption (Stedinger *et al.*, 1993). The log-Pearson Type III distribution was chosen because it has shown to describe annual minimum low flows in the United States relatively well (Vogel and Wilson, 1996) and it has been applied by the United States Geological Survey (USGS) to describe low flow time series (Reilly and Kroll, 2003). Here, we compare average $7Q_{10}$ from individual Catskill and Delaware basins. The low-flow statistics were developed using 1971–2000 baseline, and 2036–2065 and 2071–2100 simulated future streamflow series for each individual basin.

The probability of refill (PR) by 1 June is an indicator of the state of the NYC system at a given period of the year. This indicator is a function of: (i) the current day's storage deficit; (ii) expected future water diversions and releases (determined using historical data average values from 1987 to 2004); and (iii) system-wide inflow forecasts between today and 1 June (also determined using historical data). This indicator can assume values from 0 to 1, with 1 being the best or the most desired state.

Table I. General Circulation Models, emission scenarios and time slices applied in this study. The time slices reflect the extent of data available for this study. 20C3M represents baseline simulations or a series of experimental runs where greenhouse gases are considered to change as observed through the 20th century (IPCC 2007). Period 2046–2065 is further referred as ‘future_4665’, and periods 2080–2099 and 2081–2100 are referred as ‘Future_8100’

GCM	20C3M	Emission Scenario	Time Slices
ECHAM	1981–2000	A2, A1B, B1	2046–2065, 2081–2100
GISS	1981–2000	A2, A1B, B1	2046–2065, 2081–2100
NCAR	1980–1999	A2, A1B	2046–2065, 2080–2099

INPUT DATA DESCRIPTION

Table I summarizes the climate scenarios and time periods used in this study. The model acronyms ECHAM stands for the European Centre Hamburg Model, GISS for the Goddard Institute for Space Studies, and NCAR for the National Centre for Atmospheric Research. The GCM data were provided by Columbia University/GISS as part of a contract with the NYC Environmental Protection (Horton and Rosenzweig, 2010; Major and O’Grady, 2010). Future climate scenarios were derived using a delta change methodology (Anandhi *et al.*, 2011), which calculated monthly change factors based on comparisons between GCM baseline and future scenarios. Additive factors for air temperature and multiplicative factors for precipitation were applied to the historical time series of daily data associated with each reservoir watershed, in order to produce reservoir-specific future climate scenarios. Historical air temperature and precipitation for 1927–2004 were available for the study site. From this dataset, the period 1981–2000 was used as baseline to derive future scenarios simulation. ‘Future_4665’ and ‘Future_8100’ are used in this manuscript to refer to the future simulated 2046–2065, and 2081–2100 (and 2080–2099 for NCAR GCM) periods, respectively. For the NYC WOH reservoirs, the historical temperature and precipitation time series were developed combining data from NWS meteorological stations located in or adjacent to the WOH watershed area and archived at the Northeast Region Climate Center (NRCC) at Cornell University, NY. Data from these stations were combined by applying inverse distance weighting and Thiessen polygons methods. Also, correction factors were used together with modelled daily air temperature to account for elevation variation and a regression methodology was applied to fill missing measurements of daily precipitation data. Inflows to the reservoirs constitute major inputs to NYC OASIS model. Future scenarios of air temperature and precipitation were used in GWLF-VSA to derive basin-wide inflows for each of the different climate scenarios, and present day (baseline conditions).

Precipitation, air temperature and snowpack

For figures 2 through 6 the Box-plots represent the 25th (Q1) and 75th (Q3) quartiles (or the interquartile range) from all 8 climate change scenarios. For the future_4665 (white box plots) and future_8100 (gray box plots) time periods; the whiskers representing the lowest and highest data values within the lower ($Q1 - 1.5 \times (Q3 - Q1)$) and upper ($Q3 + 1.5 \times (Q3 - Q1)$) limits; the dark horizontal lines in the box-plots represent the median and the asterisks represent outliers. The box plots in Figure 2(a) show the medians and the level of variability of monthly precipitation changes as simulated by the different GCM model scenarios. This variability reflects the high uncertainty associated with GCM simulation of precipitation. On average precipitation is simulated to increase during most months except for May and August. The average annual precipitation calculated using data from all models is simulated to increase by 12.7 and 15.3% for future_4665 and future_8100 periods, respectively. Winter (December, January, and February (DJF)) precipitation is projected to increase in average by 27% for both periods, while summer (June, July, and August (JJA)) precipitation is projected to increase only by 4.6 and 5.5% for future_4665 and future_8100 periods, respectively.

Air temperature is projected to increase over the WOH region under future GCM climate (Figure 2(a)). The difference in simulated air temperature by the different scenarios appears slightly higher for the future_8100 period than the future_4665 period. On average (all models combined), air temperature is projected to increase +2.2 (+3.4) annually, +2.7 (+3.7) during DJF, and +1.9 (+3.3) during JJA by future_4665 (and future_8100) periods. These values are consistent with seasonal trends in historical temperature where average increases in winter temperature are higher than during summer (Hayhoe *et al.*, 2007). Also, these values are within the ranges of future changes projected from a different set of GCMs by Hayhoe *et al.* (2007) for the US Northeast, except for DJF, future_4665 period where our predicted average value is slightly higher than their average estimated from the B1, A2, and A1 emission scenarios.

Higher temperature during winter resulted in a large reduction in snowpack snow water equivalent as simulated by GWLF-VSA (Figure 2(c)). Snowfall and snowpack are projected to greatly decrease during the winter months as increased temperature causes more of the precipitation to fall as rain and since the snowpack that does develop tends to melt faster and earlier in the year. This is consistent with the results shown in Figure 2(c) where relative reductions in snowpack are lower during January and highest during March and April. Between the two simulated future periods the future_8100 period exhibits higher decreases in snowpack than the future_4665 period due to the higher temperature increase predicted for the future_8100 period. Average changes in snowpack

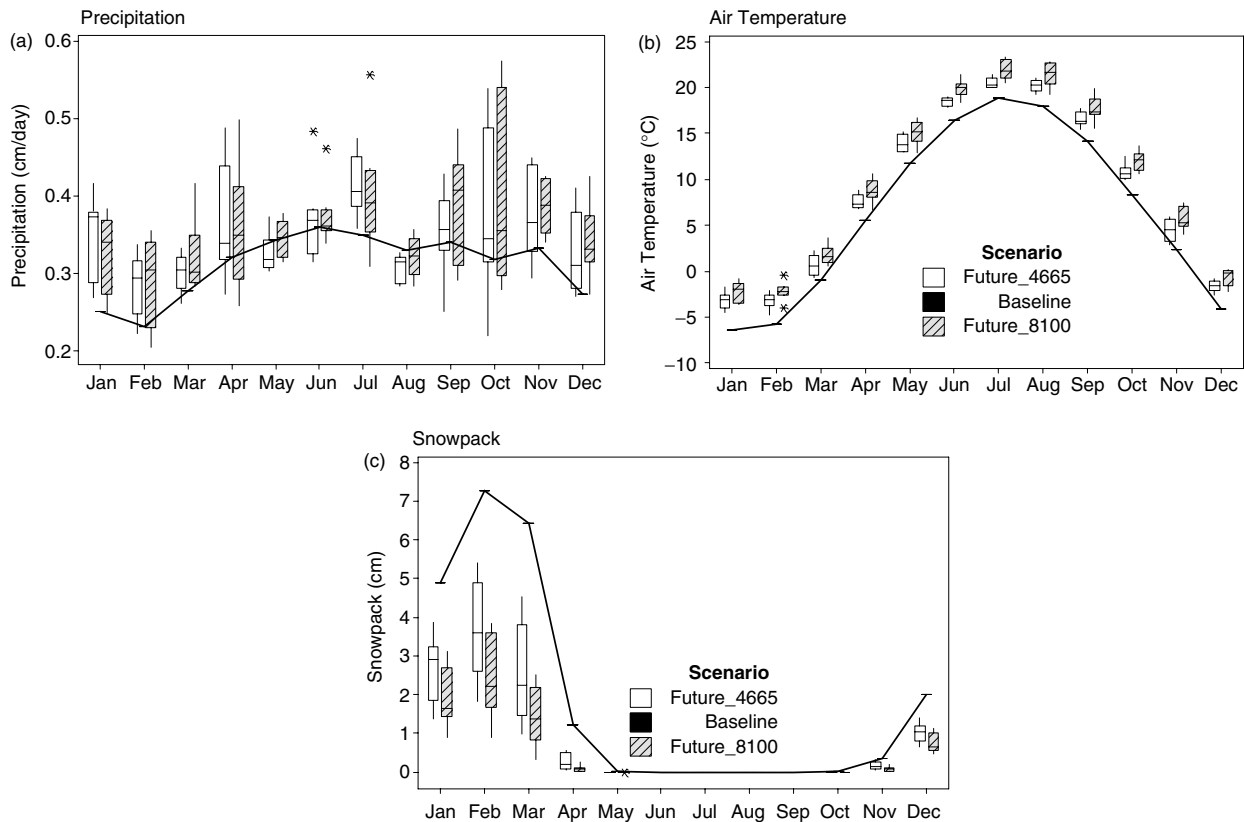


Figure 2. Monthly average daily precipitation (a), air temperature (b), and snowpack (c) for baseline and future scenarios. These data are areal averages for all NYC WOH watersheds. The solid line represents the baseline scenario. Box-plots represent the interquartile range from all 8 climate change scenarios for the future_4665 (white box plots) and future_8100 (gray box plots) time periods; the whiskers represent the lowest and highest data values within the lower and upper limits. The dark horizontal lines in the box-plots represent the median and the asterisks represent outliers

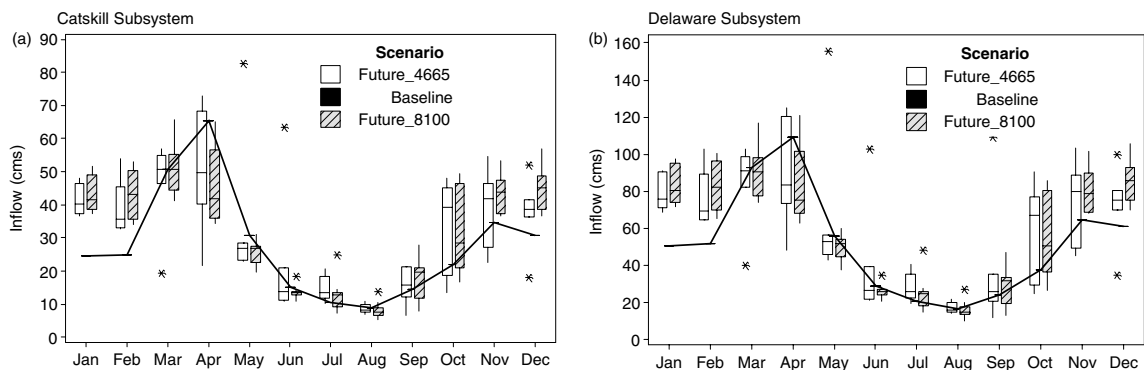


Figure 3. Average monthly inflow (in cubic meters per second) for the baseline (solid line) and simulated future_4665 (white box plots) and future_8100 (gray box plots) periods for the Catskill (a) and Delaware (b) subsystems. Box-plots represent the interquartile range from all eight climate change scenarios by simulated time period, the whiskers represent the values within the upper and lower limits. The dark horizontal lines in the box-plots represent the median and the asterisks represent outliers

between January and April from different scenarios range from 45% to 80% decrease for the future_4665 period and from 60% to 93% decrease for the future_8100 period. The percentage change increases from January to April suggesting a potential positive feedback process that may occur as a result of a reduction in snow coverage area. This pattern is further illustrated in Figure 7(a). Snowfall follows a similar pattern but with slightly lower magnitude of percent changes. The average snowfall percent change from November to April varies from 0 to 43% for the simulated future_4665 and from 26 to 65% for the

simulated future_8100. For both simulated future periods snowfall reduction is lowest during January and it increases as we move backward toward November or forward toward April.

Simulated future inflow to WOH reservoirs

Most GCMs project increased winter and reduced early spring reservoir inflow due to earlier future snow melt (Figure 3). These results are consistent with previous climate change studies in the region (Blake *et al.*, 2000; Neff *et al.*, 2000; Frei *et al.*, 2002; Burns *et al.*, 2007;

Hayhoe *et al.*, 2007; Brekke *et al.*, 2009) that project an increase in late winter and spring runoff and earlier spring snowmelt. There are particularly strong indications that levels of winter streamflow will increase since future predictions all fall well above simulations of contemporary conditions from December to February. This is true for both the Catskill and Delaware subsystems. The disagreement between streamflows from the different GCM simulations is high for April, October, and November in particular when simulating the time period 50 years forward. These monthly patterns reflect a large disagreement (and uncertainty) among the different GCMs used for this study in simulating precipitation (Figure 2(b)). Also, most of the simulated April, October, and November precipitation becomes quickly available for runoff due either to high relative reductions in the April snowpack (80–90% reduction for April) or a lack of snow (close to zero cm during October and November). Annual inflow is higher for most future scenarios but also with large variations in magnitude between estimates from different GCMs. On average, simulations associated with different GCMs indicate an increased 7Q10 for the future_4665 and future_8100 periods in both Catskill and Delaware watersheds (Table II). These values represent average statistics over the NYC WOH region where values for the later period appear to be slightly less than future_4665, a result that can be related to the difference in average evapotranspiration for the two periods and the impact of extreme climate scenarios. If the shift in runoff timing associated with earlier snowmelt was the only effect of climate change, one would expect less water being available during low flows periods due to more water

being lost during winter. The simulated future 7Q10 suggest that for low flows the combined effect of earlier snowmelt and increased rainfall are more important leading to potentially more water being available for the reservoirs throughout the entire year.

RESULTS ON SYSTEM INDICATORS AND DISCUSSION

Reservoir storage, release, and spill

Simulated future reservoir storage, release, and spill show a pattern that is directly related to changes in snowmelt amount and timing of runoff. As shown in Figure 4, the combined effect of changes in snowmelt and timing of winter—spring runoff for simulated future scenarios leads to the reservoirs filling earlier in the year. Future simulated results also suggest that there will be increased future storage levels throughout the year. However, the increase is more pronounced during winter months than during summer.

The disagreement in the simulated average storage among the different GCM simulation scenarios is greater during late fall and earlier winter than during the summer, and reflects the uncertainty associated with future precipitation simulation. The relationship between snowpack, snowmelt, and reservoir releases is complex, given that OASIS attempts to maintain a void in reservoir storage of 50% of the estimated watershed snow water equivalent. Higher projected winter inflows cause the reservoirs that usually reach their 90% storage capacity in April under historical conditions to, on average, fill up one or two

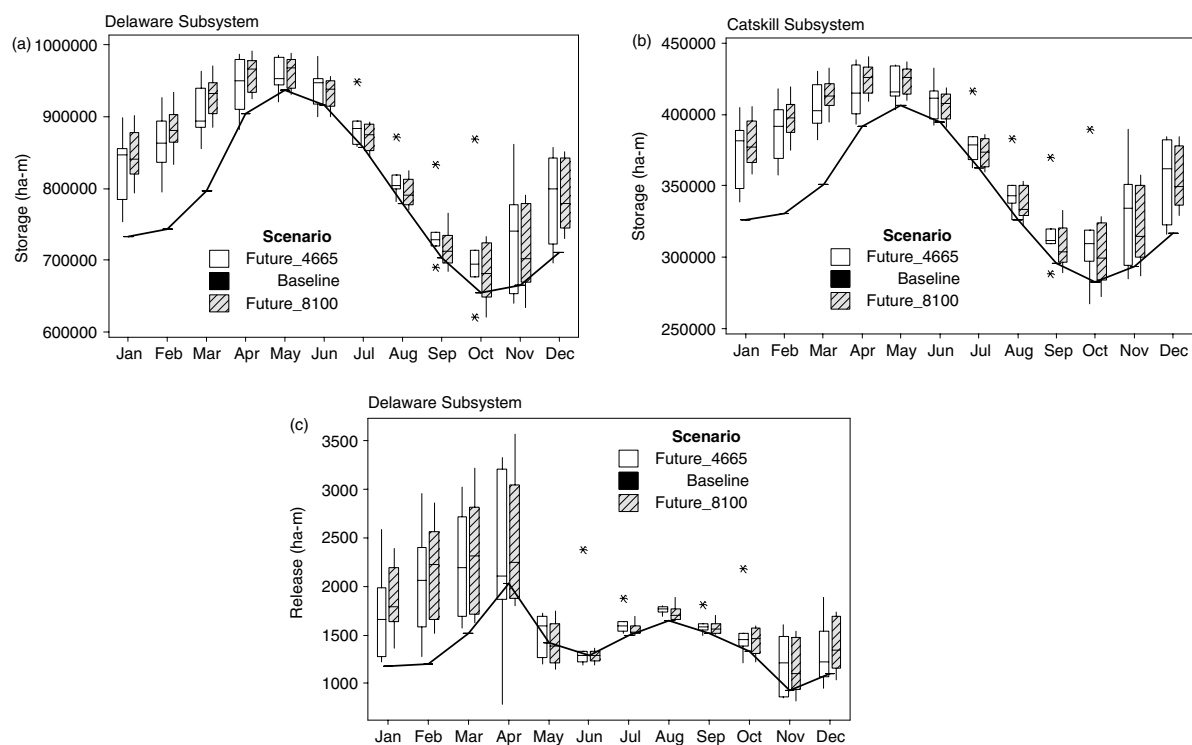


Figure 4. Storage patterns for Delaware (a) and Catskill (b) subsystems and Delaware release (c) for the baseline (solid line), future_4665 (white box plots) and future_8100 (gray box plots) scenarios. Box plots show the median, interquartile range, upper and lower whiskers and outliers

months earlier respectively for the 4664 and 8100 scenarios (Figure 5), and as a result, OASIS increases spills and releases in order to maintain a void in the reservoirs. However, since the snowpack is also projected to decrease in the future, the size of the required void also decreases making it possible to maintain reservoirs at a higher level. The overall effect is an increase in controlled releases and spills during winter and early spring, but also, more water stored at the beginning of the summer months that despite subsequent lower changes in inflow (except for July) offset any increases in evapotranspiration. Figure 5 further illustrates how reservoirs fill earlier and maintain higher levels throughout the year under future simulated climate. It is striking that the Catskill system reservoirs are projected to reach a 90% storage level two months earlier 100 years into the future. Under the assumption of no change in LD inflows the effect is somewhat less pronounced in Delaware subsystem, since as described above, this subsystem is also expected to show an increased release of water to the lower Delaware watershed.

Figure 6 shows box-plots for the spill volume from November (previous year) to before March. The volume of spill during this period increases in both subsystems under the simulated future scenarios. This increase is slightly more pronounced for the future period 100 years

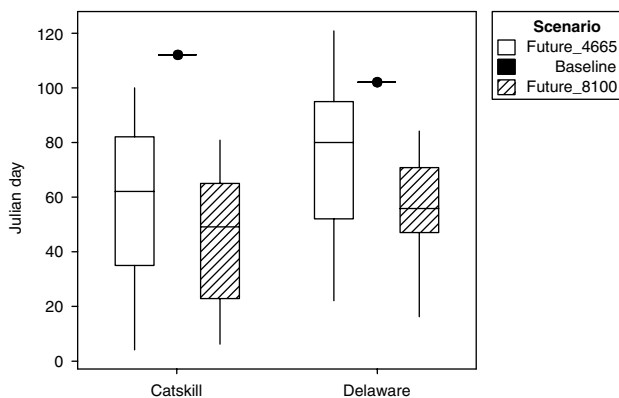


Figure 5. First Julian day when reservoirs in Catskill and Delaware subsystems pass the level of 90% of the total storage capacity. The lines with dark dots represent the average baseline values. The box-plots represent simulated data by time period. Box plots show the median, interquartile range, upper and lower whiskers

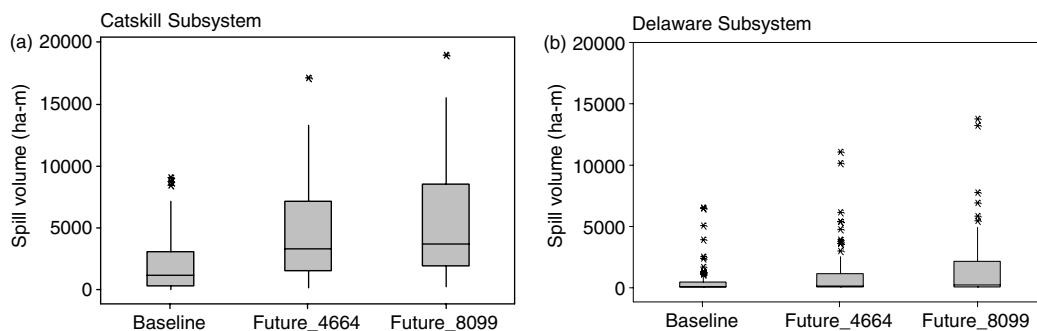


Figure 6. Yearly volume of spill from November to 1 March for the Catskill (a) and Delaware (b) subsystems for the baseline and future periods. Box plots show the median (horizontal line) and interquartile range, whiskers show the extend of the upper and lower limits and the asterisks represent outliers

forward. It is important to note that the increase in volume of spill does not directly address any issue related to flooding, which was not part of this study, but rather is an indicator of water that would no longer be available in the system for water supply. The increased water loss from the water supply system is of course, related to greater winter stream discharges (Figure 3) that lead to the reservoirs filling earlier and spilling more. This is ultimately a consequence of the projected increase in snow melt and a decreased amount of water stored in the snowpack. Also, higher winter inflows may occasionally result in elevated turbidity, which under extreme circumstances, may trigger a reduction in the use of the Catskill subsystem resulting in greater simulated spills.

In Figure 7, we show baseline and future estimates of the storage of water in the reservoir system, snowpack, and the combination of the two. From these data, it is apparent that while future scenarios show the reservoir system to fill earlier, this occurs at the expense of snow storage. This, when combined with greater levels of evapotranspiration later in the year, might have potentially led to decreased reservoir storage levels during summer. However, as shown in Figure 7(c), the future storage levels are increased as a result of an overall increased precipitation (Figure 2(b)). This result also explains the slight improvements in simulated 7Q10 low flow statistics particularly for the future_3665 period (Table II) and reduction in drought conditions occurrence (next section). It is worth noting that the uncertainty in future projections of precipitation is large, so that the loss of snow storage still could be an issue of concern.

Drought conditions occurrence and probability of refill by 1st June

On average, simulated future conditions may result in a reduction in average number of days per year the system is under Drought Watch, Warning and Emergency (Figure 8) even though there was high variability between GCM predictions. Also, both the Catskill and Delaware subsystems show an increased probability of refill by 1 June for future scenarios compared to present conditions. The probability of refill by 1 June is an indicator used in NYCWSS to help with the decision making

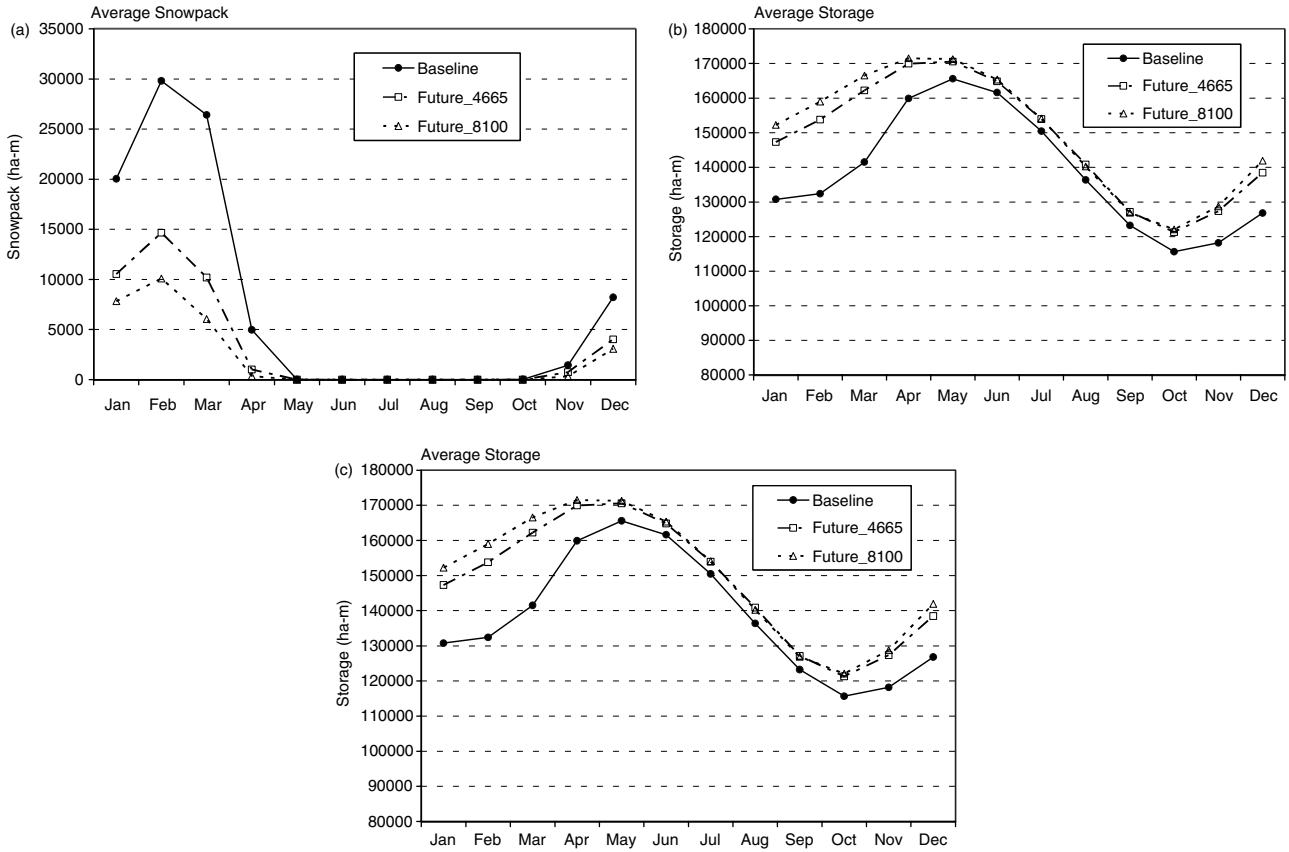


Figure 7. Baseline and average over future scenarios of monthly snowpack (a), storage (b) and storage plus snowpack (c) for the WOH system

Table II. 7Q10 low-flow statistics for the baseline and future simulated periods. The values represent an average over the NYC WOH region

	Catskill (m ³ /s)	Delaware (m ³ /s)
Baseline historical	0.19	0.97
Future_3665	0.25	1.24
Future_7100	0.19	1.03

in 7Q10 low flow statistic and more water availability during the traditional summer low flow (Figure 7(c)).

SUMMARY AND CONCLUSIONS

The state of the NYCWSS described by the water balance between streamflow inputs, storage, release, and spill is complex and dependent on various rules and constraints within the system. In NYC OASIS, the total daily withdrawal of water from the system must account for NYC demand, all other required releases, and any changes in system storage. The NYC OASIS model was used to model baseline historical and future climate simulated water supply system operation. Simulated changes

process of moving water from and between reservoirs during the operation of the system. This reduction in drought conditions occurrence and increase in probability of refill by 1 June are consistent with an average increase

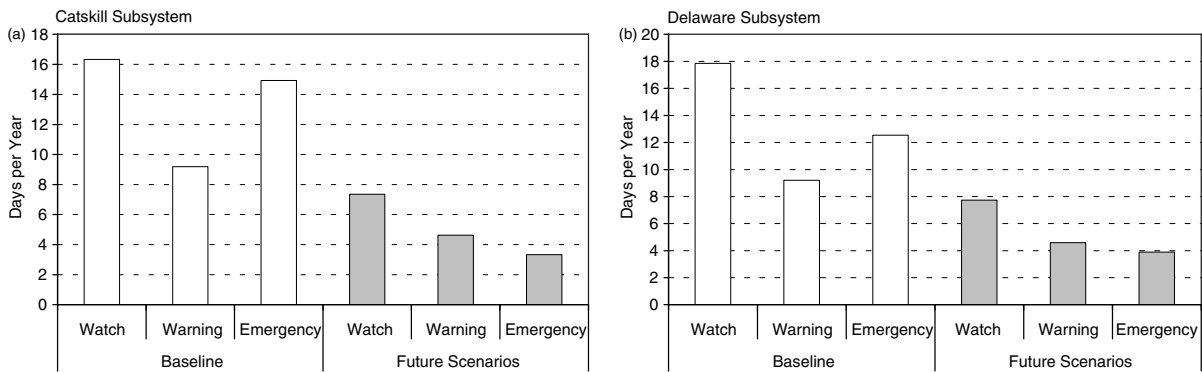


Figure 8. Baseline and simulated future average number of days per year the Catskill (a) and Delaware (b) subsystems are in watch, warning and emergency drought conditions

in snowmelt and runoff derived from GWLF-VSA and climate inputs from three GCMs in this study indicate an increase in winter streamflow with a shift in the historical April streamflow peak to earlier in the year and a reduction in snowpack accumulation that is consistent with an increase in temperature simulated by the GCMs for the region. These results are consistent with historical trends (Hodgkins *et al.*, 2003; Burns *et al.*, 2007) and previous climate change studies for the Northeast US (e.g. Frei *et al.*, 2002; Hayhoe *et al.*, 2007) and Mid-Atlantic (Neff *et al.*, 2000) regions. However, our results do not show an overall decrease in runoff as suggested by Frei *et al.* (2002) that would occur if increased evaporation rates offset any surplus precipitation. Changes in snowmelt and runoff timing appear to have an effect of increasing reservoir storage levels, spill, and releases during winter and early spring. Despite relatively small changes in inflow and higher evapotranspiration rates during most of the summer period, higher simulated storage levels during winter and spring and more precipitation throughout the year result in improving the probability of refill by 1 June and decreasing the number of days the system is likely to be under watch, warning, and emergency drought conditions. These positive effects come at the expense of a loss in snow water storage that would otherwise persist longer into the year, drain into the reservoirs at a slower rate, and would more likely be stored in the reservoir than lost as spill during winter. In terms of the total winter storage, the loss of snow storage is relatively small in volume compared to gain in runoff, and this loss of potential spring runoff water is apparently compensated for by the reservoirs filling earlier (and at higher levels than under baseline conditions) and a projected overall increase in precipitation.

These results are preliminary because of assumptions concerning EOH and LD inflows, stationary rules, and water demands, and are limited to the performance of the applied GCM models and other modelling approaches. Simulations with the NYC OASIS reservoir system model are sensitive to inflows that are driven by precipitation and air temperature inputs from GCM models. Climate change simulations are dependent on selected GCM models and scenarios because different GCMs represent different physical processes and feedbacks differently resulting in high uncertainty particularly in simulated future precipitation at a regional scale (Neff *et al.*, 2000; Annan *et al.*, 2005; Gleckler *et al.*, 2008; Hayhoe *et al.*, 2007). Despite these constraints, our results show how the NYCWSS can adjust to simulated changes in climate and how an increase in both temperature and rainfall can potentially result in a reduced frequency of drought. Future work will make use of a larger set of GCM models and climate change scenarios, account for future projected water demands and will examine whether or not future changes will require changes in reservoir operation policies to optimize use of the NYCWSS under future climate conditions.

ACKNOWLEDGEMENTS

The authors are grateful to the New York City Department of Environmental Protection (NYCDEP) for providing funding for most of the research that led to this manuscript. This paper does not necessarily reflect the official views of NYCDEP, and no endorsement should be inferred. Also, the authors wish to thank the Columbia University Center for Climate Systems Research, and the NASA Goddard Institute for Space Studies, for providing the NCAR, GISS, and ECHAM GCM data used in this study (Major *et al.*, 2007). Our acknowledgement is extensive to Donald Kent and David Lounsbury for their technical support during preparation of this manuscript.

REFERENCES

- Anandhi A, Frei A, Pierson DC, Schneiderman EM, Zion MS, Lounsbury D, Matonse AH. 2011. Examination of change factor methodologies for climate change impact assessment. *Water Resources Research* **47**: W03501, DOI:10.1029/2010WR009104.
- Annan JD, Hargreaves JC, Edwards NR, March R. 2005. Parameter estimation in an intermediate complexity earth system model using an ensemble Kalman filter. *Ocean Model* **8**: 135–154.
- Blake R, Khanbilvardi R, Rosenzweig C. 2000. Climate change impacts on the New York City's water supply system. *Journal of the American Water Resources Association* **36**: 279–292.
- Brekke LD, Maurer EP, Anderson JD, Dettinger MD, Townsley ES, Harrison A, Pruitt T. 2009. Assessing reservoir operations risk under climate change. *Water Resources Research* **45**: W04411, DOI:10.1029/2008WR006941.
- Burns DA, Klaus J, McHale MR. 2007. Recent climate trends and implications for water resources in the Catskill Mountain region, New York, USA. *Journal of Hydrology* **336**: 155–170, DOI:10.1016/j.jhydrol.2006.12.019.
- Daily GC, Ellison K. 2002. *The new economy of nature: the quest to make conservation profitable*, Island Press: Washington DC, 3: 61–85.
- Frei A, Armstrong RL, Clark MP, Serreze MC. 2002. Catskill Mountain Water Resources Vulnerability, Hydroclimatology, and Climate-Change Sensitivity. *Annals of the Association of American Geographers* **92**(2): 203–224.
- Gleckler PJ, Taylor KE, Doutriaux C. 2008. Performance metrics for climate models. *Journal of Geophysical Research* **113**: D06104, DOI:10.1029/2007JD008972.
- Gleick PH. 1986. Methods for evaluating the regional hydrologic effects of global climate changes. *Journal of Hydrology* **88**: 97–116.
- Haith DA, Shoemaker LL. 1987. Generalized watershed loading functions for stream flow nutrients. *Water Resources Bulletin* **23**(3): 471–478.
- Hay LE, Wilby RL, Leavesley GH. 2000. A comparison of delta change and downscaled GCM scenarios for three mountainous basins in the United States. *Journal of the American Water Resources Association* **36**(2): 387–397.
- HydroLogics Inc. 2007. *User Manual for OASIS with OCL*, Columbia, MD.
- Hayhoe K, Wake CP, Huntington TG, Luo L, Schwartz MD, Sheffield J, Wood E, Anderson B, Bradbury J, DeGaetano A, Troy TJ, Wolfe D. 2007. Past and Future Changes in Climate and Hydrological Indicators in the US Northeast. *Climate Dynamics* **28**: 381–407.
- Hodgkins GA, Dudley RW, Huntington TG. 2003. Changes in the timing of high river flows in New England over the 20th century. *Journal of Hydrology* **278**: 244–252.
- Horton R, Rosenzweig C. 2010. Climate Risk Information. In *Climate Change Adaptation in New York City: Building a Risk Management Response: New York City Panel on Climate Change 2010 Report*, Rosenzweig C, Solecki W (eds), Appendix A, pp. 147–228. N.Y. Acad. of Sci.: New York.
- IPCC- Intergovernmental Panel on Climate Change. 2007. *IPCC Fourth Assessment Report: Climate Change 2007*, Cambridge University Press: Cambridge, United Kingdom and New York, NY, USA.
- Kilsby CG, Jones PD, Burton A, Ford AC, Fowler HJ, Harpham C, James P, Smith A, Wilby RL. 2007. A daily weather generator for

- use in climate change studies. *Environmental Modelling & Software* **22**(12): 1705–1719, DOI:10.1016/j.envsoft.2007.02.005.
- Kroll CN, Vogel RM. 2002. Probability distribution of low streamflow series in the United States. *Journal of Hydrologic Engineering* **7**(2): 137–146.
- Lettenmaier DP, Gan TY. 1990. Hydrologic sensitivities of the Sacramento-San Joaquin river basin, California, to global warming. *Water Resources Research* **26**: 69–86.
- Major DC, O'Grady M. 2010. Adaptation assessment guidebook. In *Climate Change Adaptation in New York City: Building a Risk Management Response: New York City Panel on Climate Change 2010 Report*, Rosenzweig C, Solecki W (eds), Appendix B, pp. 229–292. N.Y. Acad. of Sci.: New York.
- Matonse AH. 2009. *New Investigations of Baseflow Processes*, PhD. dissertation, State University of New York College of Environmental Science and Forestry, Syracuse, NY **1**: 1–14.
- Matonse AH, Kroll CN. 2009. Simulating low streamflows with hillslope storage models. *Water Resources Research* **45**: W01407, DOI:10.1029/2007WR006529.
- Maurer EP, Duffy PB. 2005. Uncertainty in projections of streamflow changes due to climate change in California. *Geophysical Research Letters* **32**(3): L03704 DOI:10.1029/2004GL021462.
- Neff R, Chang H, Knight CG, Najjar RG, Yarnal B, Walker HA. 2000. Impact of climate variation and change on Mid-Atlantic Region hydrology and water resources. *Climate Research* **14**: 207–218.
- NYCDEP. 2006. *New York City Water Supply System Reference Guide*, NYCDEP Bureau of Water Supply, Valhalla, New York.
- Rawls WJ, Ahuja LR, Brakensiek DL, Shirmohammadi A. 1993. Infiltration and Soil Water Movement. In *Handbook of Hydrology*, McGraw-Hill, Inc.: USA; chapter **5**: 1–51.
- Reilly CF, Kroll CN. 2003. Estimation of 7-day, 10-year low-streamflow statistics using baseflow correlation. *Water Resources Research* **39**(9): 1236, DOI:10.1029/2002WR001740.
- Schneiderman EM, Pierson DC, Lounsbury DG, Zion MS. 2002. Modeling the Hydrochemistry of the Cannonsville Watershed with Generalized Watershed Loading Functions (GWLf). *Journal of the American Water Resources Association* **38**(5): 1323–1347.
- Schneiderman EM, Steenhuis TS, Thongs DJ, Easton ZM, Zion MS, Neal AL, Mendoza GF, Walter MT. 2007. Incorporating variable source area hydrology into the curve number based Generalized Watershed Loading Function model. *Hydrological Processes* **21**: 3420–3430.
- Stedinger JR, Thomas Jr. WO. 1985. Low-flow frequency estimation using base-flow measurements. *U.S. Geological Survey Open-file Rep.*, 85–95, U.S. Geological Survey, Reston, VA.
- Stedinger JR, Vogel RM, Foufouls-Georgiou E. 1993. Frequency Analysis of Extreme Events, in Maidment DR. 1993. *Handbook of Hydrology*, McGraw-Hill, Inc.: USA; chapter **18**: 1–66.
- Vogel RM, Fennessey NM. 1995. Flow duration curves II: a review of applications in water resources planning. *Water Resources Bulletin* **31**(6): 1029–1039.
- Vogel RM, Wilson I. 1996. Probability distribution of annual maximum, mean, and minimum streamflows in the United States. *Journal of Hydrologic Engineering* **1**(2): 69–76.

Testing and Application of a Transport Model for Runoff Event Inputs for a Water Supply Reservoir

Susan M. O'Donnell¹; Rakesh K. Gelda²; Steven W. Effler³; and Donald C. Pierson⁴

Abstract: Effective simulation of the fate and transport of runoff event inflows is an important goal of many water quality modeling initiatives. The set-up and testing of a two-dimensional hydrodynamic transport model is documented for a water supply reservoir, Schoharie Reservoir, New York, that uses specific conductance (SC) as a conservative tracer and focuses on fate and transport of runoff event inputs, particularly the plunging of density currents in summer and fall. Model testing is supported by temporally detailed measurements of meteorological, operational, and tributary (temperature and SC) model drivers, and temporally and spatially repetitive in-reservoir patterns of SC following multiple runoff events, obtained with a combination of robotic monitoring platforms and gridding with rapid profiling instrumentation. Specific conductance is demonstrated to be an ideal tracer because of the distinct tributary signals and subsequent in-reservoir signatures imparted from runoff events and its close coupling to turbidity patterns that are primary water quality concerns for managers. The model is demonstrated to perform well in simulating in-reservoir signatures of SC following multiple runoff events over the spring to fall interval of 2003, including vertical, longitudinal, and temporal patterns, and features of the thermal stratification regime for the same interval. The validated model is applied in a probabilistic manner on the basis of a 61-year record (239 runoff events) of model drivers to provide a robust representation of the transport of runoff event inputs relative to the location of the water supply intake. This application demonstrates the entry of runoff event inflows as plunging density currents in summer and fall is a recurring phenomenon for this reservoir. DOI: 10.1061/(ASCE)EE.1943-7870.0000378. © 2011 American Society of Civil Engineers.

CE Database subject headings: Hydrodynamics; Hydrologic models; Reservoirs; Water quality; New York; Runoff.

Author keywords: Hydrodynamic model; Specific conductance; Schoharie Reservoir; Plunging currents.

Introduction

Most mechanistic water quality models can be partitioned into transport and kinetic submodels. Design or selection of an appropriate transport model that serves as the physical framework for the overall water quality model is a critical first step; i.e., “the first step.... is to determine *where the water goes* and how water movement affects the concentrations of dissolved and suspended materials” (Martin and McCutcheon 1999, p.7). A primary issue for the transport submodel is the physical dimensions (e.g., 1, 2, or 3) necessary to describe the spatial features of impact (Martin and McCutcheon 1999). One-dimensional models that consider vertical differences in lakes and reservoirs are often appropriate when autochthonous (internal production) processes dominate, such as for nutrient-eutrophication modeling (Chapra 1997). However, substantial two- or three-dimensional structure is often manifested

where allochthonous (external) inputs are important in imparting spatial signatures, such as from spills (Chung and Gu 1998) or runoff event-driven loads (Canale et al. 1993; Effler et al. 2006).

Density differences, particularly thermally-based, often prevail between tributaries and receiving lakes and reservoirs associated with divergent rates of heating and cooling of proximate lotic and lentic waters (Martin and McCutcheon 1999). Moreover, streams often remain cooler, and therefore more dense, than the upper waters of receiving lentic systems in summer from the effects of canopy and ground water inputs (O'Donnell and Effler 2006; Effler et al. 2009). If local mixing in the region of a dense inflow is inadequate to eliminate density differences, the density current (plunging inflow) will plunge and travel along the sloping bottom as an underflow (Fischer and Smith 1983; Martin and McCutcheon 1999). If a depth is encountered in a stratified lake or reservoir in which the density of the underflow equals that of the water column, the neutrally buoyant density current will separate from the bottom and intrude into that layer as an interflow (Fischer et al. 1979; Martin and McCutcheon 1999). The plunging phenomenon is accompanied by entrainment of ambient water (Akiyama and Stefan 1984; Alavian et al. 1992; Gu and Chung 1998).

Density currents have been documented for a number of lakes (Serrya 1974; Hamblin and Carmack 1978; Effler et al. 2009) and reservoirs (Hebbert et al. 1979; Johnson and Merritt 1979; Ford and Johnson 1983; LaBounty and Horn 1997; Effler et al. 2006; Gelda et al. 2009). Moreover, the phenomenon is probably unrecognized in many lentic systems. The submerged river channels of reservoirs (thalwegs) promote preservation of underflows, a feature that contributes to it being more common in reservoirs than lakes (Martin and McCutcheon 1999). The density current phenomenon can have important water quality implications by routing external loads to stratified depths. Accordingly, this can diminish the effective

¹Research Engineer, Upstate Freshwater Institute, P.O. Box 506, Syracuse, NY 13214 (corresponding author). E-mail: susanod@upstatefreshwater.org

²Research Engineer, Upstate Freshwater Institute, P.O. Box 506, Syracuse, NY 13214. E-mail: rkgelda@upstatefreshwater.org

³Research Engineer, Upstate Freshwater Institute, P.O. Box 506, Syracuse, NY 13214. E-mail: sweffler@upstatefreshwater.org

⁴Section Chief, Water Quality Modeling, New York City Dept. of Environmental Protection, 71 Smith Ave., Kingston, NY 12401. E-mail: dpierson@dep.nyc.gov

Note. This manuscript was submitted on May 17, 2010; approved on March 2, 2011; published online on March 4, 2011. Discussion period open until January 1, 2012; separate discussions should be submitted for individual papers. This paper is part of the *Journal of Environmental Engineering*, Vol. 137, No. 8, August 1, 2011. ©ASCE, ISSN 0733-9372/2011/8-678-688/\$25.00.

external loading of constituents to epilimnia in which issues of primary production and public health issues are of concern (Effler et al. 2009). Conversely, conditions within the density current may be of concern, such as oxygen depletion (Romero and Imberger 2003) or turbidity levels relative to withdrawal depths for water supply reservoirs (Effler et al. 2006). The behavior of density currents and the spatial patterns in constituents imparted by the phenomenon dictates the adoption of either a two- (Gu and Chung 1998) or three-dimensional (Dallimore et al. 2003) transport model to represent related features and dynamics of water quality concern.

Ideally, testing of a transport submodel is separated from, and conducted before, that of the overall water quality model (Chapra 1997; Martin and McCutcheon 1999). This avoids embedding transport effects within the calibration of kinetic coefficients. Conservative tracers are invaluable in supporting the testing of transport models (Martin and McCutcheon 1999). Application of a “nearly” conservative dye is a common practice, although such interventions are generally limited in representing the effects of a robust range of driving conditions. Passive, system-specific, tracers offer greater potential in that regard, where opportunities exist. Potential natural or site-specific tracers include chloride (Richardson 1976; Effler et al. 1989; Doerr et al. 1994), salinity, specific conductance, and sodium (Martin and McCutcheon 1999). Coupled dynamics in inflow concentrations and loads (e.g., the “signal”) and in-reservoir spatial patterns (e.g., the “signature”) offer the opportunity to test the performance of a transport model. Manual sampling and laboratory measurements can place practical limitations on temporal and spatial resolution of such patterns. However, patterns of specific conductance (SC), an aggregate metric of ionic content (Clesceri et al. 1998), can now be resolved in great detail in time and space with deployed robotic (O’Donnell and Effler 2006; Effler et al. 2009) and rapid profiling (Effler et al. 2006) instrumentation. A dilution effect on ionic content (i.e., decrease in SC) is observed widely in tributaries during runoff events (Manczak and Florczyk 1971; Matthews and Effler 2003; Effler et al. 2009) that represents an opportunity to track the transport of these lower SC inputs within the receiving lentic system.

This paper describes the setup and testing of a two-dimensional hydrodynamic/transport model for a water supply reservoir that focuses on simulation of the fate and transport of turbid density currents formed during runoff events. Model testing is supported by temporally replete data sets for the dynamics of tributary flow, reservoir operations, meteorological drivers, and tributary and in-reservoir patterns of temperature (T) and a conservative tracer, SC. Testing against observed in-reservoir patterns of SC, as well as T , is documented for the spring to fall interval of a single year, which included a wide range of runoff events and ambient stratification conditions. The validated model is used to investigate the influence of the completeness of the supporting data and features of model set up on model performance. Finally, the validated transport model is applied for a long-term (61 years) driver data set to develop robust probabilistic representations of features of runoff event-driven transport, including turbid density currents, in the vicinity of the water supply intake.

Study System

Schoharie Reservoir is located in the Catskill Mountains of southeastern New York (latitude 42°23' N; longitude 74°26' W), approximately 190 km from New York City [Fig. 1(a)]. This impoundment is part of a network of 19 reservoirs that supplies drinking water to 9 million people in the New York City area. The reservoir is 8 km long with a maximum width of 1 km; it lacks

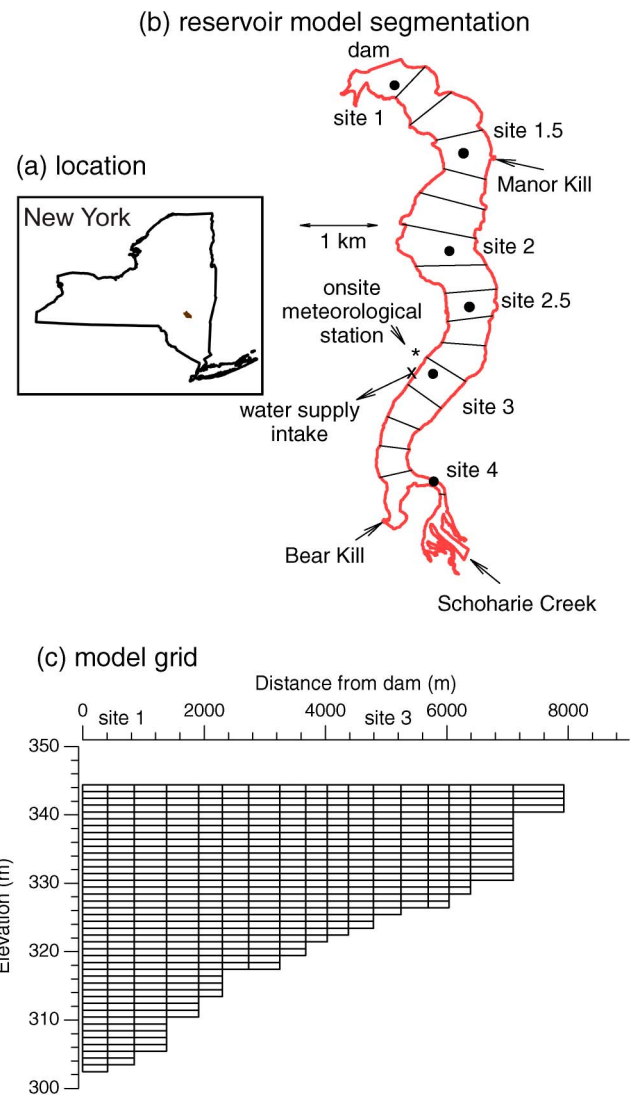


Fig. 1. Schoharie Reservoir: (a) location within New York; (b) reservoir shoreline for full conditions with dam, water supply intake, meteorological monitoring sites, tributary (Schoharie Creek, Bear Kill, and Manor Kill) entry points, long-term monitoring sites, robotic profiling platform sites for 2003, and longitudinal model segments; and (c) longitudinal profile of model segmentation (longitudinal segments and vertical layers)

dendritic complexities [Fig. 1(b)] and has a dimictic density stratification regime. The reservoir has a surface area of 4.3 km², a volume of 79 × 10⁶ m³, and a maximum depth of 41 m when full. However, these morphometric features vary seasonally and year-to-year associated with the drawdown of its surface in response to withdrawals for the water supply and natural variations in runoff. The reservoir’s primary tributary, Schoharie Creek (drains 75% of the 815 km² watershed), enters the southern end of the basin [Fig. 1(b)]. The second largest tributary, Manor Kill, drains 11% of the watershed and enters along the eastern shore [Fig. 1(b)]. The maximum longitudinal slope along the thalweg of the basin is 2%. Schoharie Reservoir flushes 10.1 y⁻¹ on average on a completely mixed basis. This impoundment is described as an upstream reservoir within the overall system because water withdrawn for the water supply (intake is 19 m deep when full, effective elevation = 326.9 m) travels through a tunnel, then a stream, and two downstream reservoirs before delivery to New York City.

The reservoir suffers from the problem of high turbidity following runoff events associated with inputs received through the tributaries, but especially Schoharie Creek (Effler et al. 2006). This turbid water has been documented to enter as a density current at certain times because of lower stream temperature (O'Donnell and Effler 2006) manifested as subsurface turbidity peaks with substantial longitudinal gradients, but with limited and short-lived lateral differences (Effler et al. 2006). Significant longitudinal differences in thermal stratification are not observed in this system (Gelda and Effler 2007a). Management alternatives to abate turbidity levels have been considered including: (1) reductions in external inputs; (2) a variety of in-reservoir engineered structures to reduce transport of turbidity toward the intake; and (3) effective positioning and operation of the intake(s) to avoid the withdrawal of turbid layers. A mechanistic predictive turbidity model is required to provide quantitative guidance for management deliberations. A representative hydrodynamic transport model that can accurately simulate the behavior of runoff event inputs, including transient turbid density currents, is an essential component (submodel) of such a turbidity model.

Modeling Strategy, Model Description, and Specification of Inputs and State Variable Patterns

The selection of the transport model was influenced by multiple factors: (1) the need to represent the primary longitudinal spatial features of the impacts of runoff events on in-reservoir turbidity patterns; (2) the management alternatives under consideration; (3) the need to integrate the water quality model with a water supply (hydrologic) model; (4) the need to support robust model simulations; and (5) the principle of parsimony. According to the principle of parsimony, the adopted framework should only be as complex as necessary to address the problem (Chapra 1997; Martin and McCutcheon 1999). The selection of a two-dimensional hydrodynamic/transport model that serves as the submodel of CE-QUAL-W2 (designated W2/T) for this work is consistent with these factors. More complete, but complex, three-dimensional models have distinct disadvantages for this situation. First, extended (e.g., seasonal) simulations are problematic because of over-mixing manifested in three-dimensional model simulations for long narrow basin configurations such as Schoharie Reservoir. Second, these models are much more computationally demanding. Two features of the modeling initiative for this reservoir make this limitation particularly problematic: (1) the planned integration of the water quality model with a water supply system model (OASIS; Hydrologics 2003); and (2) the planned model application strategy of long-term simulations (61 years) to provide robust representations of behavior and variability to be expected (Gelda and Effler 2008). The integration with the system/operations model is necessary because management alternatives that affect this reservoir's operations need to be considered in the context of the effects on the overall water supply system (i.e., all 19 reservoirs).

W2/T is a dynamic, laterally averaged two-dimensional (longitudinal and vertical) model (Edinger and Buchak 1975; Cole and Wells 2002) that is based on the finite-difference solution of partial differential equations for laterally averaged fluid motion and mass transport. The basic equations of the model that describe horizontal momentum, hydrostatic pressure, continuity, free water surface elevation, equation of state, and constituent transport have been presented previously (Chung and Gu 1998; Gu and Chung 1998; Cole and Wells 2002). Vertical velocities are assumed to be sufficiently small for the vertical momentum equation to be simplified to the hydrostatic equation. The heat budget of W2/T that supports

Table 1. Coefficient Values for Two-Dimensional Hydrodynamic and Transport Model W2/T for Schoharie Reservoir

Coefficient	Value
Longitudinal eddy viscosity	$1 \text{ m}^2 \text{ s}^{-1}$
Longitudinal eddy diffusivity	$10 \text{ m}^2 \text{ s}^{-1}$
Chezy coefficient	$70 \text{ m}^{0.5} \text{ s}^{-1}$
Wind sheltering coefficient	0.8
Fraction of incident solar radiation absorbed at the water surface	0.45
Coefficient of bottom exchange	$7.0 \times 10^{-8} \text{ W m}^{-2} \text{ C}^{-1}$

simulation of the thermal stratification regime includes terms for short- and long-wave radiation, convection, conduction, evaporative heat loss and back radiation (Cole and Wells 2002).

The model represents the reservoir as a grid of longitudinal segments and vertical layers [Fig. 1(c)]. The lateral dimension is described as the average cross-sectional width. Features of outflow structures are represented including the spillway length of the dam and elevations of the water supply withdrawal and dam outlet. The withdrawal envelope is represented by a relationship (Cole and Wells 2002) that describes the decreasing contributions from water column depths with increasing distance from the intake. Inputs for W2/T include wind speed and direction, air temperature, dew point temperature, solar radiation, the light attenuation coefficient, inflows, inflow temperature, and outflows. The model has six coefficients (Table 1) that are subject to calibration. The values of the coefficients for longitudinal eddy viscosity, eddy diffusivity, wind shelter, and the Chezy coefficient directly affect simulated hydrodynamics and in turn affect the distribution of heat. The other two coefficients, the fraction of incident solar radiation absorbed at the water surface and the coefficient for bottom heat exchange, directly affect the heat budget calculations.

Schoharie Reservoir is represented by 17 longitudinal segments with layer thickness of 1 m [Fig. 1(c)] consistent with the guidelines of Cole and Wells (2002). Morphometric features of the grid were established by a digitized bathymetric map obtained in a 1997 survey from analysis with Geographical Information Systems (GIS) software (IDRISI 2005). Inflows and outflows directly enter and exit model segments according to their locations. Ninety-five percent of the watershed was gauged for flow rates (U.S. Geologic Survey) through monitoring at Schoharie Creek, Manor Kill, and Bear Kill [Fig. 1(b)]. Available time steps of these flow measurements that were considered in this study included 15 min, 60 min, and 24 h averages; 15 min information supported model testing. Ungauged (~5%) inflows were assumed to have dynamics of flow and other conditions that tracked those of Schoharie Creek. Outflows and water surface elevation of the reservoir were specified at a 1-day time step as the daily average values reported from monitoring by the New York City Department of Environmental Protection (NYCDEP). A wide range of magnitudes of runoff events occurred in the study interval of 2003 [Fig. 2(a)]. Fifteen events were identified (Table 2); two of these contained two distinct (but closely spaced in time) peaks. The recurrence frequencies of the peak flows ranged from 33 y^{-1} (a minor event, i.e., that on average occurs 33 times per year) to 1 y^{-1} (major event; Table 2), with peak Schoharie Creek flows of 15.7 to $385.5 \text{ m}^3 \text{ s}^{-1}$.

Meteorologic measurements [Figs. 2(b)–2(d)] of model inputs were made at two sites, one on the reservoir adjoining the intake location (Site 3, reservoir site designations from NYCDEP), the other at the intake facility [Fig. 1(b)]. The measurements were available at 15 min time steps (as average values over that interval); time series of air temperature [Fig. 2(b)], wind speed [Fig. 2(c)],

Table 2. Runoff Events, Identification, and Description

Event number	Date of peak Q	Peak ^a Q ($\text{m}^3 \text{s}^{-1}$)	Recurrence y^{-1}
1	May 2	76.2	7
2	May 12	34.6	16
3	May 27	32.2	22
4	June 1	134.3	5
5	June 22	65.9	9
6	July 22	15.7	33
7	August 3	61.5	15
8	August 10	104.6	10
9	September 4	130.3	11
10	September 15	53.4	11
11	September 19	45.6	17
12	September 23	200.2	4
13	September 28	241.0	1
14	October 15	57.1	15
15	October 27	385.5	1

^aHourly resolution.

and solar radiation [Fig. 2(d)] are presented for the 2003 study interval. Measurements of temperature [Fig. 2(e); accuracy $\pm 0.15^\circ\text{C}$, resolution 0.01°C], SC [Fig. 2(f); accuracy $\pm 5\%$, resolution $1 \mu\text{S cm}^{-1}$], and turbidity [T_n , nephelometric turbidity units (NTU), Fig. 2(g); accuracy $\pm 5\%$ of reading or 2 NTU, resolution 0.1 NTU] were made near the mouth of Schoharie Creek at 15 min intervals for the study interval with a robotic monitoring unit (O'Donnell and Effler 2006). Although T_n is not modeled in this study, observations are included to establish a coupling between SC and T_n tributary signals and in-reservoir signatures. Temperatures of other tributaries were specified as equal to those measured at Schoharie Creek. Values of SC for Manor Kill and Bear Kill were predicted from tributary-specific SC-flow relationships developed from NYCDEP's fixed frequency (twice per month) monitoring program.

In-reservoir patterns of the model state variables of T and SC, and T_n (and a surrogate metric of T_n , the beam attenuation coefficient; Effler et al. 2006) and downwelling irradiance (to specify the attenuation coefficient, Table 1) were obtained with a combination of rapid profiling instrumentation (0.25 m vertical resolution; Effler et al. 2006) and solar-powered robotic profiling platforms (1 m vertical resolution; O'Donnell and Effler 2006). "Gridding" was conducted with rapid profiling instrumentation by collecting profiles at ~ 30 sites throughout the reservoir (within ~ 8 h) on multiple occasions following runoff events to provide spatially replete patterns to support model testing. Lateral transects were included and generally supported the two-dimensional framework selection (Effler et al. 2006). The profiling platforms provided more frequent (2–4 profiles day^{-1}) representations, but at fewer sites [Fig. 1(b)].

Modeling Opportunity

Schoharie Creek was colder than the upper layers of the reservoir for much of the May–October period of 2003 but particularly starting in August [Fig. 2(e)], and thus had the propensity to plunge during those intervals. The diurnal variations in the stream's T , associated with cyclic changes in heat input within a day (Webb and Walling 1988; Sinokrot and Stefan 1993), were often substantial relative to this propensity.

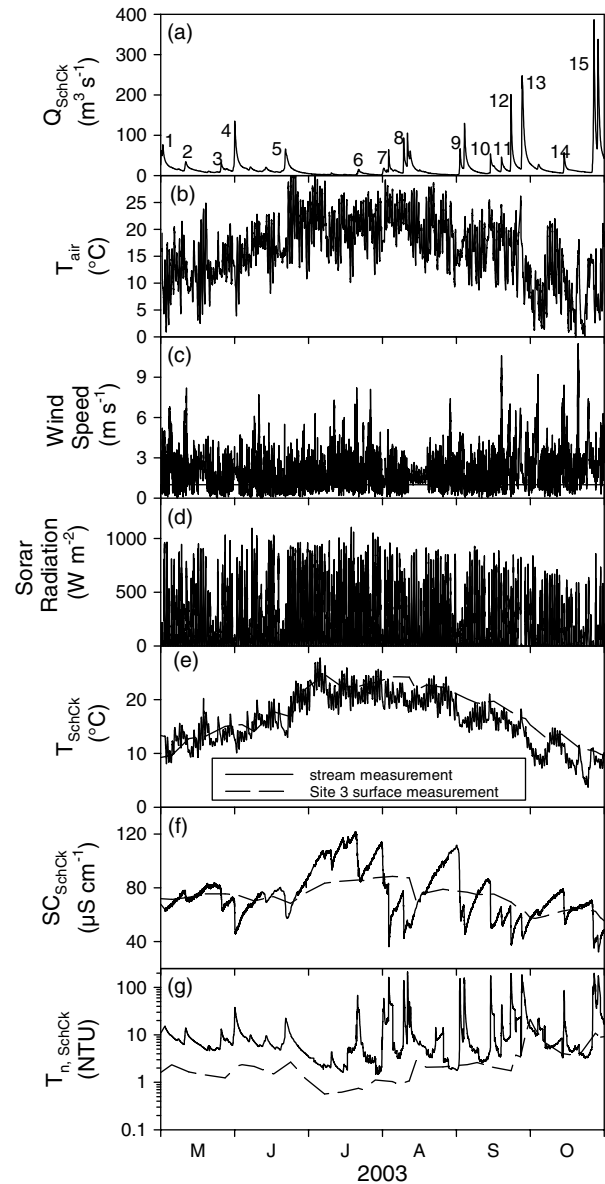


Fig. 2. Time series for transport modeling interval of 2003, drivers, comparisons to reservoir surface conditions, and turbidity: (a) hydrograph for Schoharie Creek, daily average values, with runoff events numbered; (b) air temperatures (T), 15 min average values; (c) wind speed, 15 min average values; (d) solar radiation, 15 min average values; (e) Schoharie Creek T , 15 min average values and Schoharie Reservoir surface T , daily average values, (f) Schoharie Creek specific conductance (SC) hourly average values and Schoharie Reservoir surface SC, daily average values; and (g) Schoharie Creek turbidity (T_n), 15 min average values, and Schoharie Reservoir surface T_n , daily average

The runoff events [Fig. 2(a)] caused temporally coupled perturbations for SC and T_n in Schoharie Creek that were characterized by abrupt decreases in SC [Fig. 2(f)] and increases in T_n [Fig. 2(g)]. Accordingly, each runoff event sent pulselike signals of decreased SC and increased T_n that accompanied the increased flow to the reservoir. These decreased levels of SC were usually lower than the upper waters of the reservoir [Fig. 2(f)], thereby often offering an opportunity to use SC as a tracer to track the transport of runoff flows within the water column. The temporal patterns of SC and T_n in the upper waters of the reservoir were uniform by comparison,

with much lower T_n levels compared to Schoharie Creek, and consistent with the entry of this stream as a turbid density current.

Clear signatures of the entry of turbid density currents with lower SC were documented in response to most runoff events as illustrated for two events with robotic profiles collected adjoining the intake before and soon after the arrival of the turbid subsurface plume [Figs. 3(a)–3(d)]. The density currents entered metalimnetic depths in both cases, and the plume was relatively thick for both the early June and mid-August events. The SC signatures mirrored those of the T_n patterns in both cases [Figs. 3(a)–3(d)]. Thus, the coupled dynamics of SC in the inflows and the reservoir water column offer an excellent opportunity to support testing of a transport model with particularly strong signatures available for the important water quality issue of the behavior of turbid density currents.

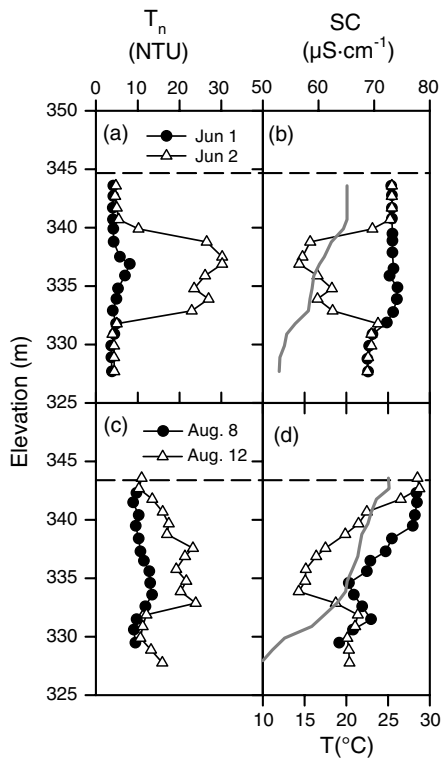


Fig. 3. Vertical profiles bracketing the maximum signatures for runoff-event density currents at Site 3 in Schoharie Reservoir in 2003: (a) turbidity (T_n), June 1 and 2; (b) specific conductance (SC) and temperature (T), June 1 and 2; (c) T_n August 8 and 12; and (d) SC, and T , August 8 and 12; thermal stratification presented as solid lines in (b) and (d)

Execution and Performance Evaluation

The model's autostepping algorithm (Cole and Wells 2002) calculates a maximum time step within a specified range based on hydrodynamic numerical stability requirements, and then uses a fraction of this value for the actual time-step calculations. The minimum and maximum time steps used were 1 s and 1 h, respectively. Initial conditions were those measured on May 5. Overall model validation was based on continuous simulation over the May 5–November 15 interval. The same set of model coefficients (Table 1) was used throughout the simulation period; these coincided with the values used in long-term (14 y) testing of the framework for thermal stratification performance for this reservoir for an earlier period (1989–2002; Gelda and Effler 2007a). Moreover, these coefficient values correspond closely to those adopted elsewhere for this model (Martin 1988; Gelda et al. 1998) and recommended by Cole and Wells (2002).

The primary focus of testing was performance in simulating the transient patterns of SC in time and space following the runoff events of the study period. Salient features of performance evaluation include spatial (in both the vertical and longitudinal dimensions) and temporal (from events to seasonal) patterns. However, because transport, particularly of density currents, in lakes and reservoirs is highly dependent on the attendant stratification regime (Martin and McCutcheon 1999), accurate simulation of thermal stratification for the study interval of 2003 with the hydrodynamic/transport model was also a necessary goal. Model performance was evaluated both qualitatively (i.e., graphically as vertical profiles, spatial, and temporal contours) and quantitatively [root mean square error (RMSE); Thomann 1982].

Model Performance

W2/T performed very well in simulating the thermal stratification regime of Schoharie Reservoir over the study period of May–November of 2003 as depicted by the comparisons of observed and predicted T profiles from selected days in each month for Site 1 (Fig. 4). Systematic longitudinal differences in thermal stratification were not observed or predicted. The RMSE for the entire simulation interval of 2003 resulting from the paired observations (rapid profiling instrumentation) and predictions made at multiple depths at each of the long-term primary monitoring sites [numbers 1–4; see Fig. 1(a)] was 0.63°C. This compares favorably to the annual values reported for the 1989–2002 period for Schoharie Reservoir (0.85–1.75°C; Gelda and Effler 2007a), and other systems for which this metric of performance was reported for seasonal simulations of the stratification regime (Gelda et al. 1998; Owens 1998; O'Donnell et al. 2010).

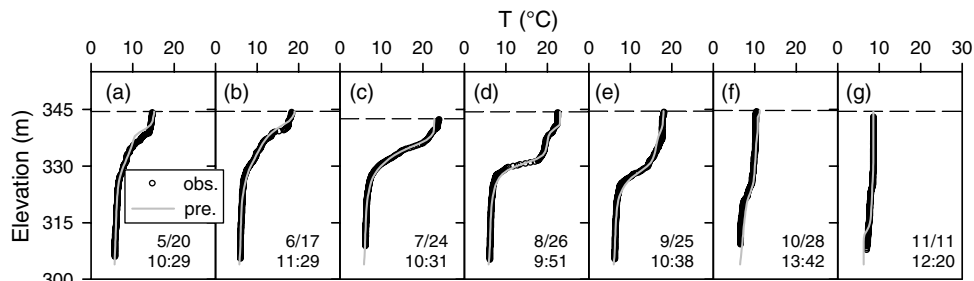


Fig. 4. Model performance for thermal stratification in Schoharie Reservoir (Site 1) for selected days in 2003: (a) May 20; (b) June 17; (c) July 24; (d) August 26; (e) September 25; (f) October 28; and (g) November 11

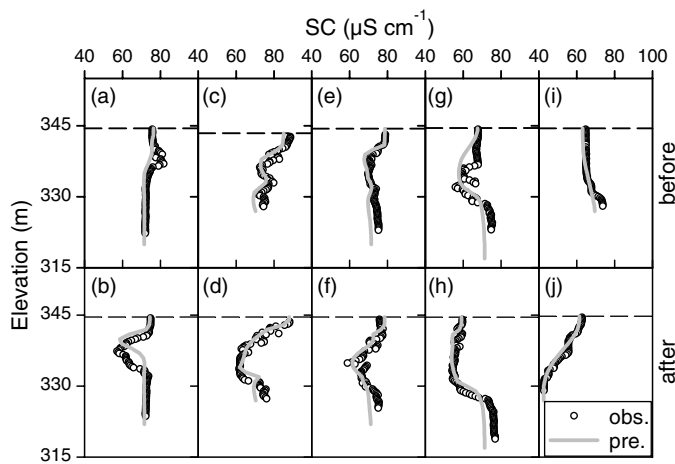


Fig. 5. Model performance for specific conductance (SC) in Schoharie Reservoir for the selected day in 2003 bracketing the effects of runoff events: (a) before event number 1 (May 28), Site 2.5; (b) after event number 1 (June 2), Site 2.5; (c) before event number 9 (August 8), Site 3; (d) after event number 9 (August 12), Site 3; (e) before event number 10 (August 26), Site 2.5; (f) after event number 9 (September 5), Site 2.5; (g) before event number 14 (September 27), Site 2; (h) after event number 14 (October 1), Site 2; (i) before event number 16 (October 21), Site 3; and (j) after event 16 (October 28), Site 3

The fate and transport of density currents from runoff events were also well simulated as evidenced in comparisons of observed and predicted SC patterns. The observed substantial changes imparted in vertical profiles were well simulated as represented for five runoff events (Fig. 5). The depth axis is elevation in these presentations, rather than depth from the surface, to accommodate variations in water surface elevation although drawdown was limited in this year because of the generally high runoff. The elevation of the water surface when the reservoir is full is 344 m; the corresponding depth of water column at Site 3 under these

conditions is 20 m. Vertical patterns were well predicted both before [Figs. 5(a), 5(c), 5(e), 5(g), and 5(i)] and soon after [Figs. 5(b), 5(d), 5(f), 5(h), and 5(j)] these events at various sites. The vertical character of the signatures differed substantially for these cases, offering a robust test. Density current behavior, manifested as a subsurface decrease in SC from an interflow, was well simulated for the May [Figs. 5(a) and 5(b)] and August [Figs. 5(c)–5(f)] events. In contrast, the late September runoff event (number 3) entered the upper waters [Figs. 5(g) and 5(h)], consistent with the lack of substantial T differences between the stream and upper waters of the lake. The simulations for late October [Figs. 5(i) and 5(j)] represented another density current case when the plunging inflow acted as an underflow at Site 3 because the epilimnion had deepened substantially by that time [Fig. 4(f)].

Longitudinal differences in SC imparted by runoff event density currents were also well predicted as illustrated by comparison of observed and simulated longitudinal/elevation contours of SC for two and four days after a September event [number 12; Figs. 6(a)–6(d)]. The general patterns, including vertical position and longitudinal extent of lower SC waters, were well predicted although the simulated leading edge [Figs. 6(b) and 6(d)] was shifted somewhat further downstream than the observations [Figs. 6(a) and 6(c)]. The model also performed well in simulating the combined vertical and temporal patterns of SC at different locations in the reservoir, and is illustrated in this study through comparison of observed (robotic) and predicted time/elevation isopleths of SC for Site 3 [Figs. 7(a) and 7(b)]. Both temporal and vertical features were well simulated, including occurrences of subsurface (metalimnetic) minimums associated with the entry of density currents. The RMSE for SC predictions for the overall simulation interval of 2003, resulting from paired observations and predictions from the long-term monitoring sites was $5.0 \mu\text{S cm}^{-1}$, a value that was $< 10\%$ of the overall observed average value.

Validation of W2/T has been demonstrated for Schoharie Reservoir by the successful simulation of the fate and transport of inflows from multiple runoff events throughout the reservoir in 2003 established on predictions of SC and the thermal stratification regime for the same interval. The testing was robust in the

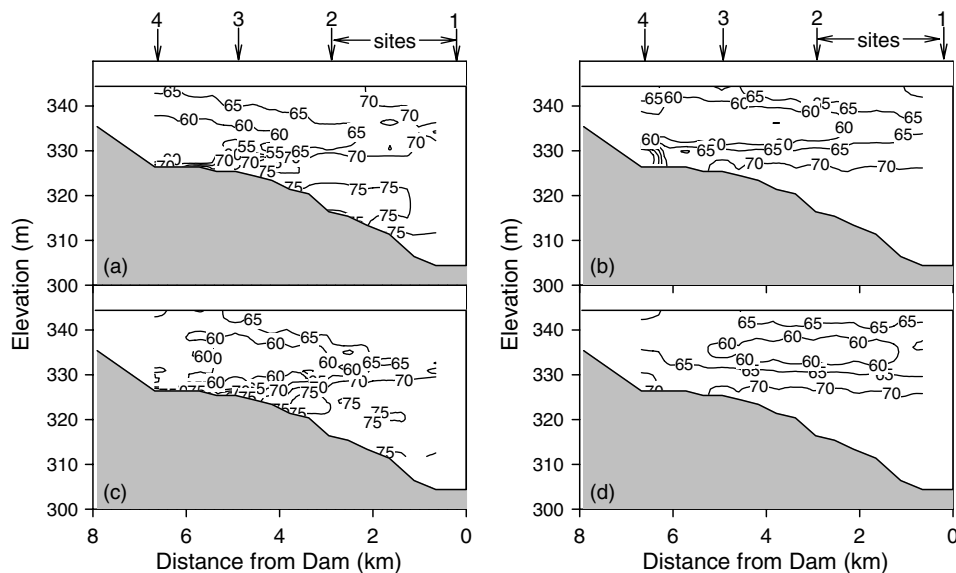


Fig. 6. Model performance for specific conductance (SC) in Schoharie Reservoir for selected days in 2003 following runoff event number 13, as elevation—longitudinal contours along the reservoir primary axis: (a) observed, September 25, based on gridding with rapid profiling instrumentation; (b) predicted, September 25; (c) observed, September 27, based on gridding with rapid profiling instrumentation; and (d) predicted, September 27

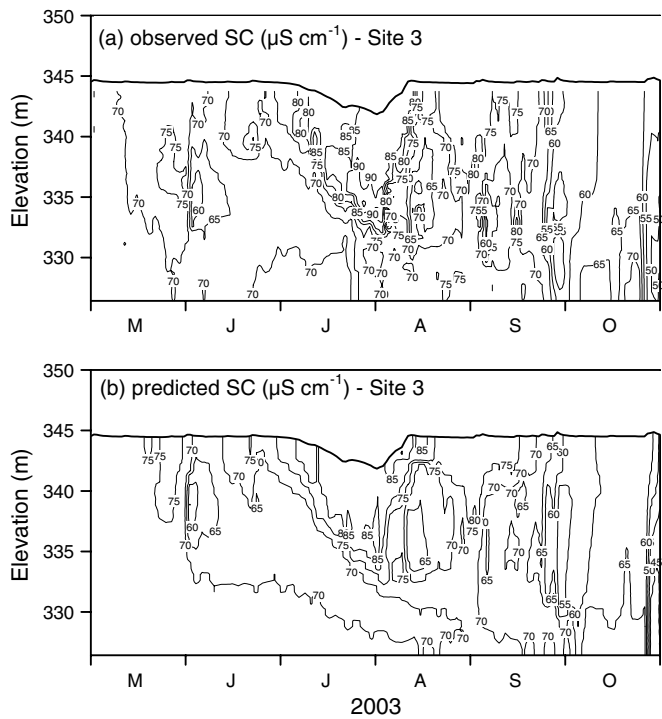


Fig. 7. Model performance for specific conductance (SC) in Schoharie Reservoir as elevation-time contours (e.g., isopleths) at Site 3 for the May-October interval of 2003: (a) observed; and (b) predicted

context of the number of events, differences in the magnitudes of the events, and differences in the vertical position of the entry of the inflow into the water column of the reservoir. The good performance of W2/T for this conservative metric supports the framework

to conduct mass balance calculations and to serve as the physical transport submodel for a water quality model (Chapra 1997; Martin and McCutcheon 1999). Moreover, it supports the representativeness of the various inputs that are embedded in these calculations and that are critical to their success; e.g., levels of SC in the inflows and the reservoir, inflow and outflow rates, and bathymetry. Resolution of the inflow density and SC signal and in-reservoir stratification and SC (model state variable) patterns was made possible through the implementation of a program of robotic monitoring and gridding with rapid profiling instrumentation. Additional independent support for W2/T for Schoharie Reservoir was provided by the reported similarity of model predictions and instrument (acoustic Doppler velocimeter) measurements of bed (bottom) stress at an upstream position in the basin along the thalweg (Owens et al. 2010).

Sensitivity Analyses

Sensitivity analyses were conducted with the validated model to evaluate the effects of the protocols adopted to specify inputs, model segmentation, and initialization of the model. RMSE values obtained with the validated model are compared with those for the sensitivity scenarios (Table 3), established on eight sites along the reservoir's main axis that include long-term Sites 1–4 [Fig. 1(b)]. The first three analyses (Table 3) focus on selected days and runoff events to depict sensitivity in predicting short-term patterns and are consistent with the transient character of the effects of these events. These address the needs for specifying tributary inputs. Specifications of the minor (other than Schoharie Creek) tributary *T* and SC inputs according to the temporally limited (biweekly) observations, instead of the adopted protocols, caused noteworthy deterioration in the RMSE metric of performance for

Table 3. Results of Sensitivity Analyses with Validated Transport Model for Schoharie Reservoir

Run number	Description	Root mean square error (RMSE)			
		Temperature (°C)		Specific conductance ($\mu\text{S cm}^{-1}$)	
		Validation run	Sensitivity run	Validation run	Sensitivity run
1	Minor tributaries: use biweekly <i>T</i> observations instead, October 30 (Event number 15)	0.41	0.35	7.0	8.7
2	Minor tributaries: use biweekly SC observations instead, September 5 (Event number 9)	0.59	0.59	4.0	8.4
3	Alternate measurement frequency for Schoharie Creek, <i>T</i> and SC, September 5 (Event number 9)				
	A. daily	0.59	0.66	4.0	3.7
	B. weekly	0.59	0.96	4.0	10.2
	C. bi-monthly	0.59	0.96	4.0	12.3
4.	Land-based meteorological measurement instead	0.63	0.74		5.18
5.	Alternate segmentation schemes				
	A. 17×0.5	0.63	0.66	5.05	5.03
	B. 34×1.0	0.63	1.05	5.05	5.77
	C. 35×0.5	0.63	1.06	5.05	5.77
6.	Reinitialize model for each event instead				
	A. June 1–9	0.71	0.76	6.64	3.93
	B. July 22–24	0.71	0.76	6.64	3.93
	C. August 3–8	0.56	0.56	5.56	3.87
	D. August 10–15	0.65	1.04	5.59	4.45
	E. September 4–9	0.57	0.74	3.89	3.47
	F. September 23–October 3	0.63	0.62	4.06	3.33
	G. October 27–November 3	0.47	0.54	6.70	4.76

SC but not T (Table 3). These results are generally consistent with the need for temporally detailed specifications of these model inputs to effectively simulate the transient in-reservoir patterns of SC. The importance of temporally detailed measurements of the major input (Schoharie Creek) was illustrated through comparison of the RMSE values for the validated model (15 min) versus results from measurement time steps instead of daily, weekly and biweekly (Table 3). These results indicate substantial deterioration in performance with measurements less frequent than daily. Only modest differences in performance were observed when meteorological data from a nearby land-based position were used instead of the observations from the robot at Site 3 (Table 3).

The adopted model segmentation scheme [Fig. 1(c); i.e., 17×1] is supported by the results of sensitivity analyses conducted with different ($n = 3$) segmentations (17×0.5 , 34×1.0 , and 34×0.5). Each of the three alternatives represented more detailed spatial resolution of the reservoir. No systematic improvements in RMSE were observed (Table 3). Accordingly, the adopted segmentation provides an appropriate spatial representation of this reservoir that avoids noteworthy numeric errors. The continuous simulation approach through the study period adopted in this work is an inherently more rigorous test of the model than an approach that (re)initializes before each runoff event. The latter approach would have essentially no benefit for T performance. However, the RMSE for SC would have been somewhat lower with reinitialization; approximately 30% lower on average for the seven considered events (Table 3).

Model Application

It is important to acquire a robust representation of the fate and transport of runoff event turbid inflows within water supply reservoirs, particularly relative to intake locations, to identify recurring patterns, associated risks, and expected variability. These attributes are resolved for Schoharie Reservoir through application of the validated transport submodel, and by conducting coupled simulations for thermal stratification and a hypothetical conservative tracer (i.e., a numerical dye study) for runoff events. The tracer concentration was set at $1,000 \text{ mg L}^{-1}$ at the peak flow in Schoharie Creek for each runoff event, a concentration that provided adequate in-reservoir signatures over the full range of runoff events considered. Model simulations were carried out for each event individually to avoid “carry-over” effects of injected tracer from one event to subsequent events. A probabilistic modeling strategy (Gelda and Effler 2008) was adopted, which incorporates model simulations for 61 years of historical conditions and utilizes paired long-term records of meteorology, hydrology, operations, and empirical models to specify stream water T and SC for that period. This long-term simulation approach (Owens et al. 1998; Gelda et al. 2001; Gelda and Effler 2008; O'Donnell et al. 2010) has the advantages of: (1) providing a robust probabilistic context for predictions; and (2) predictions are inherently representative because the model drivers correspond to actual historical conditions for the site. The empirical stream T model that is critical to the buoyancy of the tributaries (i.e., density current versus overflow behavior) and established on stream flow and air T , was demonstrated to perform well for Schoharie Creek (Gelda and Effler 2008).

A total of 239 runoff events were identified in the 61-year hydrologic record for Schoharie Creek. The highest peak flow was $740 \text{ m}^3 \text{ s}^{-1}$ and the median peak flow was $130 \text{ m}^3 \text{ s}^{-1}$; secondary peaks within events were not considered. Simulations were initiated on January 1 of the year of each event and continued for six months after the tracer injection. Model simulations were

analyzed for features of transport for runoff event inflow, including density currents and predictions of travel time (t_r) for the effects of the peak tracer concentrations to reach the water supply intake. A schematic representation of predictions for one event (mid-August 2004), along with specified tracer plume characteristics, serve to identify the features described in this probabilistic analysis [Fig. 8(a)]. The in-reservoir characterizations correspond to predicted conditions in the model segment that contains Site 3 adjoining the intake. These predictions for the tracer generally track those for the peak T_n impacts because spatial patterns of T_n have been demonstrated to be transport-driven immediately following the events (Gelda and Effler 2007b; Gelda et al. 2009). Divergence between T_n and the tracer concentrations increases with time following an event from the operation of the settling loss process and is consistent with the behavior observed for T_n and SC following events (O'Donnell and Effler 2006).

Seasonal characterizations of the elevation of c_{max} [peak tracer concentrations; Fig. 8(b)] and b [thickness of plume; Fig. 8(c)] are presented in a box plot format (5, 10, 25, 50, average, 75, 90, 95 percentiles shown). Wide variability is predicted for most months although these representations are not robust for July (particularly) and August because runoff events have been relatively rare in these months over the 61 year record. Wide interannual variations in the extent and timing of drawdown [i.e., elevation not depth for y-axis, Fig. 8(b); Gelda and Effler 2008] contribute to the predicted variability in these features of the fate of runoff event inputs, particularly over the July–November interval. The particularly wide variations in the c_{max} elevation predicted during turnover and ice cover (November–April) is consistent with the combined effects of no, or modest, vertical density differences within the reservoir and variability in the relative buoyancy of stream inputs [Fig. 8(b)]. Deeper and recurring plunging in the basin was predicted for the late summer through early fall interval approaching the intake depth [Fig. 8(b)], which indicates the seasonal recurrence of the density current phenomenon addressed in detail for 2003 (Figs. 5–7). The deepening through this interval generally tracks that of the metalimnion with the approach to fall turnover (Gelda and Effler 2007a). The thicknesses of the runoff event plumes are predicted to usually be less than 10 m during summer stratification (May–October) and ice cover (January and February) and often less than 5 m [Fig. 8(c)]. This feature is predicted to be much more variable during intervals of turnover. Cases of $b \sim 19$ m correspond to the runoff event input being distributed throughout the water column and is expected when the entering water density equals that of the water column during turnover.

Runoff event density currents have most often entered the metalimnion but above the thermocline depth (z_r ; maximum density gradient). The depth of intrusion of a density current (z_i) relative to z_r is described by z_r [$= z_i - z_r$; Fig. 8(a)]; a negative z_r indicates entry above z_r . Approximately 45% of the events were predicted to have z_r values within the range of -5 to 0 m [Fig. 8(d)]. Events with more negative z_r values ($< 25\%$) correspond to those that either enter as overflows or are well mixed into the epilimnion, conditions that occur most often in spring when T increases occur more rapidly in the stream than in the reservoir. The higher z_r values [5 – 15 m; Fig. 8(d)] generally correspond to runoff events when the associated density current is an underflow at Site 3, which is an undesirable condition because of proximity to the intake. The predicted intrusion depth for runoff event density currents was predicted to usually be somewhat shallower than the reservoir water column depth in which the T equals that of the creek during the event [$z_{\text{eq}T}$; see Fig. 8(a)]. This is consistent with the effects of the entrainment mixing process that operates on density currents (Akiyama and Stefan 1984; Alavian et al. 1992) and

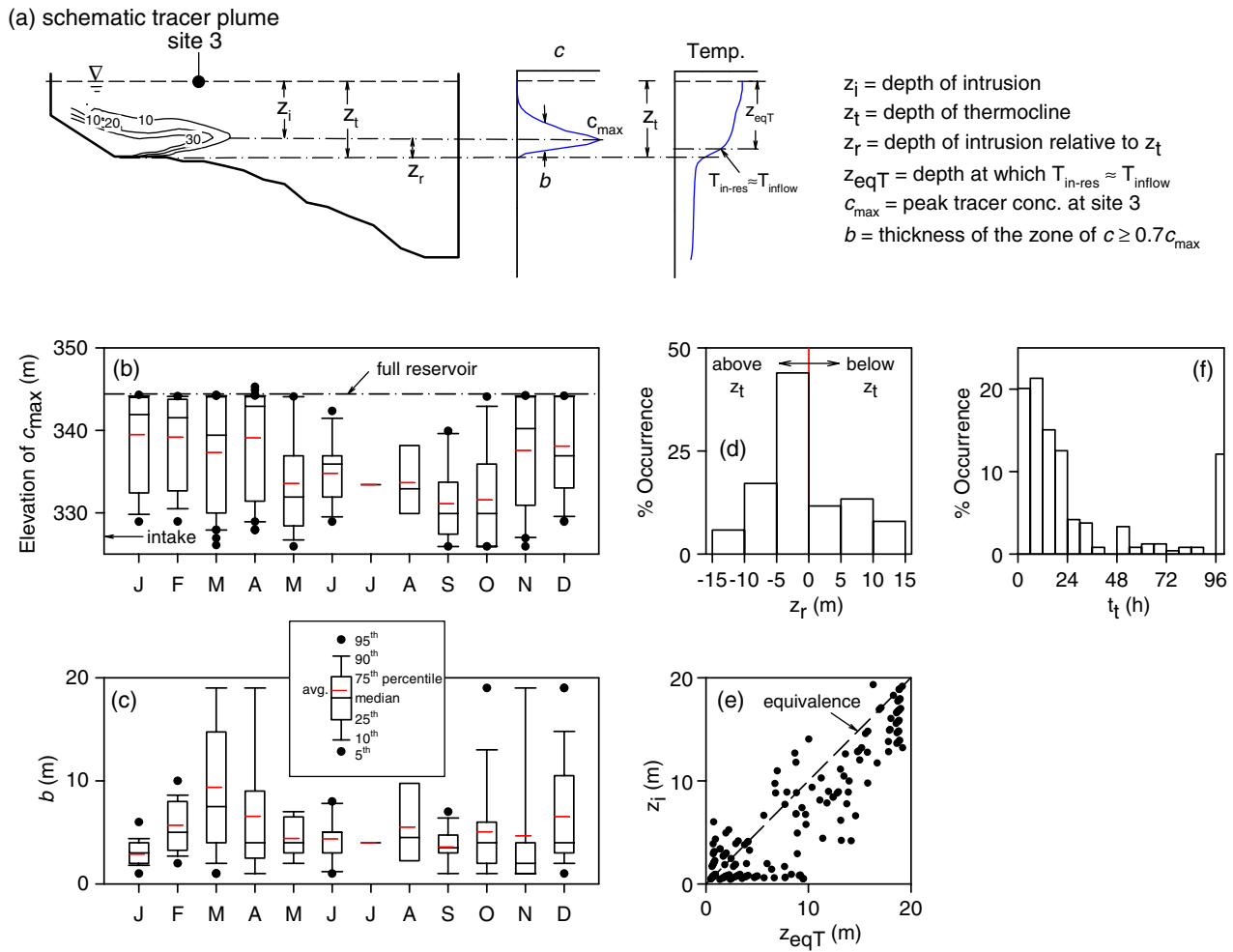


Fig. 8. Model applications for a conservative tracer for 61 years of historical runoff events ($n = 239$) for Schoharie Reservoir to describe fate and transport of runoff event inflows at Site 3 and the water supply intake: (a) schematic representation of the predicted tracer transport for the August 13, 2004 runoff event, as an example, with specification of selected descriptive features; (b) predicted seasonal pattern of the elevation of the peak tracer concentration (c_{max}), as a box plot; (c) predicted seasonal pattern of the thickness of the runoff event plume (b), as a box plot; (d) predicted distribution of z_r , the depth of intrusion of the runoff event plume (z_i) relative to the thermocline depth (z_t ; $z_r = z_i - z_t$); (e) relationship between z_i and z_{eqT} , the reservoir depth at which the T equals the inflow T ; and (f) the distribution of the travel time (t_t) for the effects of the peak stream flow tracer to reach the intake

diminishes T and density differences as the plume is transported down-reservoir.

The effects of runoff event inflows can reach the water supply intake of Schoharie Reservoir rapidly. The travel time, t_t , the time from the peak of a runoff event in the Creek to the time when the maximum effect is observed in the withdrawn water, was predicted to be within 12 h for ~40% of the events and within 24 h for 70% of the events [Fig. 8(f)]. The noteworthy percentage > 96 h reflects the effects of changes in operating strategy embedded in the 61-year record when the intake was shut down during major runoff events to reduce the transport of turbid water downstream.

Summary

The hydrodynamic/transport model W2/T has been validated for Schoharie Reservoir, New York, established from the successful simulation of in-reservoir patterns of SC and T for a 7-month interval with multiple ($n = 15$) events. In particular, the model performed well in simulating the plunging behavior of density currents, a prominent feature of the transport of runoff event inflows over the summer through fall interval in this reservoir.

The model testing effort was supported by a comprehensive monitoring program of model drivers, including meteorological, hydrological, operational and tributary density and SC levels, and detailed in-reservoir patterns of the state variables SC and T . The average RMSE for predictions of these patterns over the entire study interval was $5.0 \mu\text{S cm}^{-1}$, or < 10% of the average SC, and 0.63°C , respectively. Testing of the transport model was robust because of the number of runoff events addressed, the range of magnitudes of the events, and differences in the depth(s) of entry of the inflows. The demonstrated performance of W2/T supports its use to serve as the physical transport submodel for a water quality model for the reservoir that particularly addresses the reservoir's turbidity issue.

The validated transport model was applied through simulations of thermal stratification and conservative tracer concentrations to characterize the fate and transport of runoff event inflows that are relative to the reservoir's single intake for a 61-year historical record (239 events) of driving conditions. The results of these simulations provided a robust probabilistic representation of an array of related attributes including: (1) the entry elevation of runoff event inflows into the water column; (2) the thickness of the inflow

plume (interflow); (3) the depth of entry relative to the thermocline; and (4) the time of travel for effects of a runoff event to reach the water supply intake. Key findings of this analysis included: (1) the recurrence of the density current phenomenon; (2) density current thicknesses of 5–10 m and entry within the metalimnion (but above the thermocline) in late summer; and (3) travel times of less than one day for the effects of most (70%) runoff events to reach the intake.

Effective simulation of the fate and transport of runoff event inflows and independent testing of the transport submodel are common goals in water quality modeling initiatives for many lakes and reservoirs that have been met in this study. Features of the integrated program of monitoring and modeling described in this study are transferable to meet such goals for many other systems. For example, a two-dimensional framework that is capable of representation of the behavior of density currents, such as W2/T, is an appropriate and parsimonious choice for many systems, but particularly those with long narrow configurations. Specific conductance (SC) is expected to be a viable conservative tracer to track runoff event inflows in many cases because the dilution effect during events reported in this study occurs widely. This state variable choice can be supported by modern robotic and rapid profiling instrumentation, such as implemented in this work, which enables the necessary resolution of the transient tributary signals and in-reservoir signatures to support testing. Finally, long-term historical records of model drivers exist for many sites that should be used to support application of validated models to investigate recurring features and variability in the fate and transport of runoff event inflows.

Acknowledgments

Support for this study was provided by the New York City Department of Environmental Protection. Field sampling and measurements were conducted by M. Spada, B. Wagner, and T. Prestigiacomo. This is contribution No. 236 of the Upstate Freshwater Institute.

References

- Akiyama, J., and Stefan, H. G. (1984). "Plunging flow into a reservoir: Theory." *J. Hydraul. Eng.*, 110(4), 484–499.
- Alavian, V., Jirka, G. H., Denton, R. A., Johnson, M. C., and Stefan, H. G. (1992). "Density currents entering lakes and reservoirs." *J. Hydraul. Eng.*, 118(11), 1464–1489.
- Canale, R. P., Auer, M. T., Owens, E. M., Heidtke, T. M., and Effler, S. W. (1993). "Modeling fecal coliform bacteria—II. Model development and application." *Water Res.*, 27(4), 703–714.
- Chapra, S. C. (1997). *Surface water-quality modeling*, McGraw-Hill, New York.
- Chung, S. W., and Gu, R. (1998). "Two-dimensional simulations of contaminant currents in stratified reservoir." *J. Hydraul. Eng.*, 124(7), 704–711.
- Clesceri, L. S., Greenberg, A. E., and Eaton, A. D. (1998). *Standard methods for the examination of water and wastewater*, 20th Ed., American Public Health Association, American Water Works Association, Water Environment Federation, Washington, DC.
- Cole, T. M., and Wells, S. A. (2002). "CE-QUAL-W2: A two-dimensional, laterally averaged, hydrodynamic and water quality model, version 3.1." *Instruction Rep. EL-2002-1*, U.S. Army Engineering and Research Development Center, Vicksburg, MS.
- Dallimore, C. J., Hodges, B. R., and Imberger, J. (2003). "Coupling an underflow model to a three-dimensional hydrodynamic model." *J. Hydraul. Eng.*, 129(10), 748–757.
- Doerr, S. M., Effler, S. W., Whitehead, K. A., Auer, M. T., Perkins, M. G., and Heidtke, T. M. (1994). "Chloride model for polluted Onondaga Lake." *Water Res.*, 28(4), 849–861.
- Eddinger, J. E., and Buchak, E. M. (1975). *A hydrodynamic, two-dimensional reservoir model: The computational basis*, U.S. Army Engineer Division, Ohio River, Cincinnati.
- Effler, S. W., et al. (2009). "Tributary plunging in an urban lake (Onondaga Lake): Drivers, signatures, and implications." *J. Am. Water Resour. Assoc.*, 45(5), 1127–1141.
- Effler, S. W., Auer, M. T., and Johnson, N. A. (1989). "Modeling Cl concentration in Cayuga Lake, USA." *Water Air Soil Pollut.*, 44(3–4), 347–362.
- Effler, S. W., Prestigiacomo, A., Peng, F., Bulygina, K. B., and Smith, D. G. (2006). "Resolution of turbidity patterns from runoff events in a water supply reservoir, and the advantages of in situ beam attenuation measurements." *Lake Reservoir Manage.*, 22(1), 79–93.
- Fischer, H. B., List, E. J., Imberger, J., Koh, R. C., and Brooks, N. H. (1979). *Mixing in inland and coastal waters*, Academic Press, New York.
- Fischer, H. B., and Smith, R. D. (1983). "Observations of transport to surface waters from a plunging inflow to Lake Mead." *Limnol. Oceanogr.*, 28(2), 258–272.
- Ford, D. E., and Johnson, M. C. (1983). "Assessment of reservoir density currents and inflow processes." *Tech. Rep. E-83-7*, Environmental Laboratory, Waterway Experimental Station, Vicksburg, MS.
- Gelda, R. K., and Effler, S. W. (2007a). "Testing and application of a two-dimensional hydrothermal model for a water supply reservoir: Implications of sedimentation." *J. Environ. Eng. Sci.*, 6(1), 73–84.
- Gelda, R. K., and Effler, S. W. (2007b). "Modeling turbidity in a water supply reservoir: Advancements and issues." *J. Environ. Eng.*, 133(2), 139–148.
- Gelda, R. K., and Effler, S. W. (2008). "Probabilistic model for temperature and turbidity in a reservoir withdrawal." *Lake Reservoir Manage.*, 24(3), 219–230.
- Gelda, R. K., Effler, S. W., and O'Donnell, S. M. (2001). "Probabilistic model of ammonia and toxicity status for urban lake." *J. Water Resour. Plann. Manage.*, 127(5), 337–347.
- Gelda, R. K., Effler, S. W., Peng, F., Owens, E. M., and Pierson, D. C. (2009). "Turbidity model for Ashokan Reservoir, New York: Case Study." *J. Environ. Eng.*, 135(9), 885–895.
- Gelda, R. K., Owens, E. M., and Effler, S. W. (1998). "Calibration, verification, and an application of a two-dimensional hydrothermal model [CE-QUAL-W2(t)] for Cannonsville Reservoir." *Lake Reservoir Manage.*, 14(2–3), 186–196.
- Gu, R., and Chung, S. W. (1998). "Reservoir flow sensitivity to inflow and ambient parameters." *J. Water Resour. Plng. and Mgmt. Div.*, 124(3), 119–128.
- Hamblin, P. F., and Carmack, E. C. (1978). "River induced currents in a fjord lake." *J. Geophys. Res.*, 83(2), 885–899.
- Hebbert, R., Imberger, J., Loh, I., and Patterson, J. C. (1979). "Collie River underflow into the Wellington Reservoir." *J. Hydraul. Div.*, 105(5), 533–546.
- Hydrologics. (2003). *User manual for OASIS with OCL*, Hydrologics, Inc, Columbia, MD.
- IDRISI [Computer software]. (2005). "GIS and image processing software." Clark Labs, Clark Univ., Worcester, MA.
- Johnson, N. M., and Merritt, D. H. (1979). "Convective and advective circulation of Lake Powell, Utah-Arizona during 1972–1975." *Water Resour. Res.*, 15(4), 873–884.
- LaBounty, J. F., and Horn, M. J. (1997). "The influence of drainage from the Las Vegas Valley on the limnology of Boulder Basin, Lake Mead, Arizona-Nevada." *Lake Reservoir Manage.*, 13(2), 95–108.
- Manczak, H., and Florczyk, L. (1971). "Interpretation of results from the studies of pollution of surface flowing waters." *Water Res.*, 5(8), 575–584.
- Martin, J. L. (1988). "Application of two-dimensional water quality model." *J. Envir. Eng. Div.*, 114(2), 317–336.
- Martin, J. L., and McCutcheon, S. C. (1999). *Hydrodynamics and transport for water quality modeling*, Lewis Publishers, Boca Raton, FL.
- Matthews, D. A., and Effler, S. W. (2003). "Decrease in pollutant loading from residual soda ash production waste." *Water Air Soil Pollut.*, 146(1/4), 55–73.

- O'Donnell, D. M., and Effler, S. W. (2006). "Resolution of impacts of runoff events on a water supply reservoir with a robotic monitoring network." *J. Am. Water Resour. Assoc.*, 42(2), 323–335.
- O'Donnell, S. M., O'Donnell, D. M., Owens, E. M., Effler, S. W., Prestigiacomo, A. R., and Baker, D. M. (2010). "Variations in the stratification regime of Onondaga Lake: Patterns, modeling, and implications." *Fundam. Appl. Limnol.*, 176(1), 11–27.
- Owens, E. M. (1998). "Development and testing of one-dimensional hydrothermal models of Cannonsville Reservoir." *Lake Reservoir Manage.*, 14(2-3), 172–185.
- Owens, E. M., et al. (1998). "A strategy for reservoir model forecasting based on historic meteorological conditions." *Lake Reservoir Manage.*, 14(2-3), 322–331.
- Owens, E. M., Gelda, R. K., Effler, S. W., Russelo, P. J., Cowen, E. A., and Pierson, D. C. (2010). "Modeling resuspension in a dynamic water supply reservoir." *J. Environ. Eng.*, in press.
- Richardson, W. L. (1976). "An evaluation of the transport characteristics of Saginaw Bay using a mathematical model for chloride." *Modeling biochemical processes in aquatic ecosystem*, R. P. Canale, ed., Ann Arbor Science, Ann Arbor, MI, 113–140.
- Romero, J. R., and Imberger, J. (2003). "Effect of a flood underflow on reservoir water quality: Data and three-dimensional modeling." *Arch. Hydrobiol.*, 157(1), 1–25.
- Serruya, S. (1974). "The mixing patterns of the Jordan River in Lake Kinneret." *Limnol. Oceanogr.*, 19(2), 175–181.
- Sinokrot, B. A., and Stefan, H. G. (1993). "Stream temperature dynamics: Measurements and modeling." *Water Resour. Res.*, 29(7), 2299–2312.
- Thomann, R. V. (1982). "Verification of water quality models." *J. Envir. Engrg. Div.*, 108(5), 923–940.
- Webb, B. W., and Walling, D. E. (1988). "Modification of temperature behaviour through regulation of a British river system." *Regul. Rivers Res. Manage.*, 2(2), 103–116.

Modeling Resuspension in a Dynamic Water Supply Reservoir

Emmet M. Owens, M.ASCE¹; Rakesh K. Gelda²; Steven W. Effler³; P. J. Rusello⁴; Edwin C. Cowen⁵; and Donald C. Pierson⁶

Abstract: Enhancements to the two-dimensional lake and reservoir water quality model W2Tn to simulate the effects of currents and waves on sediment resuspension and turbidity are described. Bed stress attributable to currents was computed by the hydrothermal component of W2Tn, whereas a surface wave component was added to W2Tn to determine bed stress owing to waves. Resuspension flux is computed from bed stress and is included as a source of turbidity to the water column. The model is tested through application to Schoharie Reservoir, a drinking water supply that experiences episodes of elevated turbidity caused by runoff events and exacerbated by drawdown. Model predictions of bed stress attributed to currents are validated by using measurements obtained from acoustic Doppler instrumentation. The surface wave component of the model is established on a framework that has been previously validated for Schoharie Reservoir. Testing of the enhanced turbidity component of W2Tn was completed for a 3.5-year period of historical observations, which included a number of runoff events covering a range of severity and variations in reservoir drawdown. The enhanced model performed well in simulating observed conditions in the water column. The resuspension mechanism made a significant contribution to the predicted turbidity during periods of reservoir drawdown and during a severe runoff event. The model also performed well in simulating the observed turbidity of the drinking water withdrawal. Resuspension of particles contributing to turbidity was largely attributable to reservoir currents with surface wave-induced resuspension playing a smaller role. The potential application of this model to other water bodies and water quality issues is discussed. **DOI:** [10.1061/\(ASCE\)EE.1943-7870.0000358](https://doi.org/10.1061/(ASCE)EE.1943-7870.0000358). © 2011 American Society of Civil Engineers.

CE Database subject headings: Reservoirs; Mathematical models; Turbidity; Water supply.

Author keywords: Reservoirs; Mathematical models; Turbidity; Resuspension.

Introduction

Suspended particles in surface waters are a common problem in environmental engineering. Pollutants such as nutrients, toxic organics, or metals may be associated with particles so that the fate and transport of such pollutants is closely linked to that of particles. In other water bodies, the particles themselves are of concern. One such case is the problem of turbidity in drinking water supplies. Turbidity (Tn) is a common measure of light-scattering by suspended particles. In supplies that receive filtration, the dosage of coagulant or disinfectant depends on the raw water Tn . In unfiltered

supplies, the federal Safe Drinking Water Act (USEPA 1996) limits the Tn of delivered water. In dealing with water bodies that experience elevated Tn , mathematical models may aid in understanding the processes that affect suspended solids or turbidity and may be useful in the evaluation of water quality management alternatives.

Tributary streams are often a significant source of particles to the water column of lakes or reservoirs. Resuspension of particles from a lake or reservoir bottom also occurs in virtually all such systems, although its magnitude relative to tributary inputs varies substantially (Bloesch 1995). Resuspension occurs when the bed shear stress associated with water motion exceeds the critical stress of the sediment bed. Consistent with models of motion in surface waters, the driving force for bed stress may be divided into current and surface wave components (Martin and McCutcheon 1999). Wind-driven surface waves are the most commonly cited mechanism for resuspension in lakes and reservoirs. Surface waves generate significant bed stress when the water depth is less than approximately half the wavelength (Dean and Dalrymple 1991). Separate models have been used to predict motion and bed stress associated with “currents,” which effectively includes all motion not attributable to surface waves including motion driven by barotropic and baroclinic pressure gradients and wind shear (Martin and McCutcheon 1999).

One, or in some cases both, of these mechanisms have been considered in models of resuspension in lakes and reservoirs. A simple model that assumed the water column to be well mixed vertically and neglected horizontal particle transport has been applied to simulate wave-induced resuspension in shallow lakes (Luettich et al. 1990; Hawley and Lesht 1992). Similarly, James et al. (1997) simulated wave-induced resuspension in a depth-averaged model of a shallow lake, but included the horizontal advection and

¹Research Engineer, Upstate Freshwater Institute, P.O. Box 506, Syracuse, NY 13214 (corresponding author). E-mail: emowens@upstatefreshwater.org

²Research Engineer, Upstate Freshwater Institute, P.O. Box 506, Syracuse, NY 13214. E-mail: rkgelda@upstatefreshwater.org

³Research Engineer, Upstate Freshwater Institute, P.O. Box 506, Syracuse, NY 13214. E-mail: sweffler@upstatefreshwater.org

⁴Graduate Student, DeFrees Hydraulics Laboratory, Cornell Univ., Ithaca, NY 14850. E-mail: pjr25@cornell.edu

⁵Associate Professor and Director, DeFrees Hydraulics Laboratory, Cornell Univ., Ithaca, NY 14850. E-mail: eac20@cornell.edu

⁶Section Chief, Water Quality Modeling, York City Dept. of Environmental Protection, 71 Smith Ave., Kingston, NY 12401. E-mail: dpierson@dep.nyc.gov

Note. This manuscript was submitted on April 16, 2010; approved on January 6, 2011; published online on January 8, 2011. Discussion period open until December 1, 2011; separate discussions must be submitted for individual papers. This paper is part of the *Journal of Environmental Engineering*, Vol. 137, No. 7, July 1, 2011. ©ASCE, ISSN 0733-9372/2011/7-585-595/\$25.00.

dispersion of suspended material. Currents alone drove resuspension in a reservoir model study (Ziegler and Nisbet 1995), whereas Lick et al. (1994) and Lou et al. (2000) considered the combined effects of waves and currents.

Both two (2D) and three-dimensional (3D) models that include resuspension have been used previously to describe spatial variations in the water column of lakes and reservoirs. In shallow water bodies that do not experience significant stratification, it is reasonable to assume vertical uniformity in the water column. For this type of system, a depth-averaged 2D model has been successfully applied (Lick et al. 1994; Ziegler and Nisbet 1995; James et al. 1997). The more general 3D models consider spatial variation and particle transport in the vertical direction also (Lou et al. 2000; Jin and Ji 2004). However, when the focus is on water quality in the water column or outflow, many lakes and reservoirs may be accurately simulated by using a 2D vertical-longitudinal approach (Martin and McCutcheon 1999). Typically, these water bodies are sufficiently deep so that thermal stratification occurs, and they have a long, narrow shape so that water quality does not vary significantly in the lateral direction. Vertical-longitudinal models have been widely used in the analysis of such water bodies (Gu et al. 1996; Chung and Gu 1998; Ahlfeld et al. 2003). Although the use of a 3D model may be appealing simply because it is not based on an assumption of lateral homogeneity, these models have practical limitations. If iterative model simulations are to be made in an effort to optimize operation of a multiple-reservoir system to maximize the quality of delivered water, the computational or run-time requirements of a 3D model may be impractically high.

The model W2Tn, which predicts the dynamics of Tn associated with multiple particle size classes within a 2D vertical-longitudinal framework, was recently presented (Gelda and Effler 2007a). This model was applied to Schoharie Reservoir, a water supply reservoir that experiences episodes of elevated turbidity triggered by runoff events. W2Tn performed well in reproducing observed conditions during a year that the reservoir remained at nearly full storage (Gelda and Effler 2007a). However, field studies indicate that resuspension is significant when the reservoir is drawn down (Effler et al. 2008).

This study describes enhancements to W2Tn to allow simulation of resuspension as a source of turbidity to the water column. These enhancements build on the earlier version of W2Tn (Gelda and Effler 2007a; Gelda et al. 2009), which considered tributary input, advective and dispersive transport, settling, and export in the simulation of turbidity associated with multiple particle size classes. A previously-tested surface wave model (Owens 2009) was added to W2Tn to provide predictions of bed stress associated with surface waves. The enhanced model was tested for a 3.5-year period of historical conditions at Schoharie Reservoir that includes a wide range of drawdown and runoff events, allowing the importance of the resuspension source to be evaluated. The applicability of this framework to address management options for turbidity control at Schoharie Reservoir, and broader particle-related water quality issues, is considered.

Reservoir Description and Turbidity Events

Schoharie Reservoir is located in southeast New York State [Fig. 1(a)], 190 km northwest of New York City. It is one of 19 reservoirs that supply drinking water to 9 million people in and around New York City, the largest unfiltered water supply in the United States. Water withdrawn for supply (single intake located at a depth of 23 m with the reservoir full) travels through a stream,

three reservoirs (the east and west basins of Ashokan and Kensico), and several aqueducts before reaching New York City. When full, the basin is 8 km long, 1 km wide, has a 4.6 km² surface area, and mean and maximum depths of 17 and 42 m, respectively. These morphometric features vary seasonally and year-to-year as a result of drawdown and refilling [Fig. 1(c)]. The reservoir has a dimictic stratification regime (Gelda and Effler 2007b) and flushes ~10 times per year on a completely mixed basis.

Schoharie Creek, which drains 75% of the watershed, enters at the southern end of the basin and is the largest source of water and sediment [Fig. 1(b); Gelda and Effler 2007a]. High concentrations of inorganic sediment are carried by the stream from erosion of glacial and fluvial material in the banks (Gelda and Effler 2007a). During much of the year, Schoharie Creek is cooler than the surface waters of the reservoir and so tends to plunge (O'Donnell and Effler 2006). In addition to the drinking water withdrawal, outflow occurs over a spillway adjacent to the dam at the north end [Fig. 1(b)]. Spillway flow averages 56% of reservoir inflow.

The water quality problem of interest in this study is the increase in Tn in the reservoir water column and drinking water withdrawal in response to runoff events (Effler et al. 2006a; 2008). Although the turbidity increases reservoir-wide after such events, significant spatial patterns exist. Schoharie Creek enters as an underflow, flowing downslope and following the thalweg of its drowned channel. When the reservoir is stratified, the underflow intrudes into the water column in the vicinity of the thermocline (O'Donnell and Effler 2006). Under these conditions, maximum turbidity levels are found at the depth of this interflow (Effler et al. 2006a). Substantial longitudinal structure in Tn is observed (O'Donnell and Effler 2006; Prestigiacomo et al. 2008), because of advection of the turbid interflow and accompanying mixing and particle deposition (Effler et al. 2006b). At most times, lateral variations in Tn were generally not present; when observed, lateral gradients were modest and persisted less than a day. Tn generally diminishes within several days after the end of an event in Schoharie Reservoir, although elevated turbidity may persist for weeks or months following severe events (Prestigiacomo et al. 2008). Various management alternatives are being evaluated to reduce the high Tn levels in the reservoir and withdrawal following runoff events.

Supporting Data

Monitoring and Particle Characterization

Detailed monitoring data were available to support application and testing of a turbidity model for Schoharie Reservoir. Available hydrologic and meteorological data included: (1) streamflow from 3 USGS gauges (Schoharie Creek and 2 other tributaries), gauging 95% of the reservoir drainage area; (2) reservoir operations [New York City Department of Environmental Protection, (NYCDEP)], including water surface elevation (WSE), withdrawal and spill flow rates, and (3) on-site [buoy at Site 3; Fig. 1(b)] meteorology (wind speed and direction, air temperature and humidity, and incident solar radiation). Routine Tn measurements (5 per week) were made by NYCDEP of the drinking water withdrawal from Schoharie Reservoir, the location of greatest concern for drinking water quality. Robotic monitoring (4 observations/h) was conducted at the mouth of Schoharie Creek (O'Donnell and Effler 2006; Prestigiacomo et al. 2008). Three solar-powered vertical profiling units were moored along the longitudinal axis of the reservoir [Sites 1, 2, and 3; Fig. 1(b)], collecting at least 2 profiles each day at a 1-m-depth interval (Prestigiacomo et al. 2008). In addition,

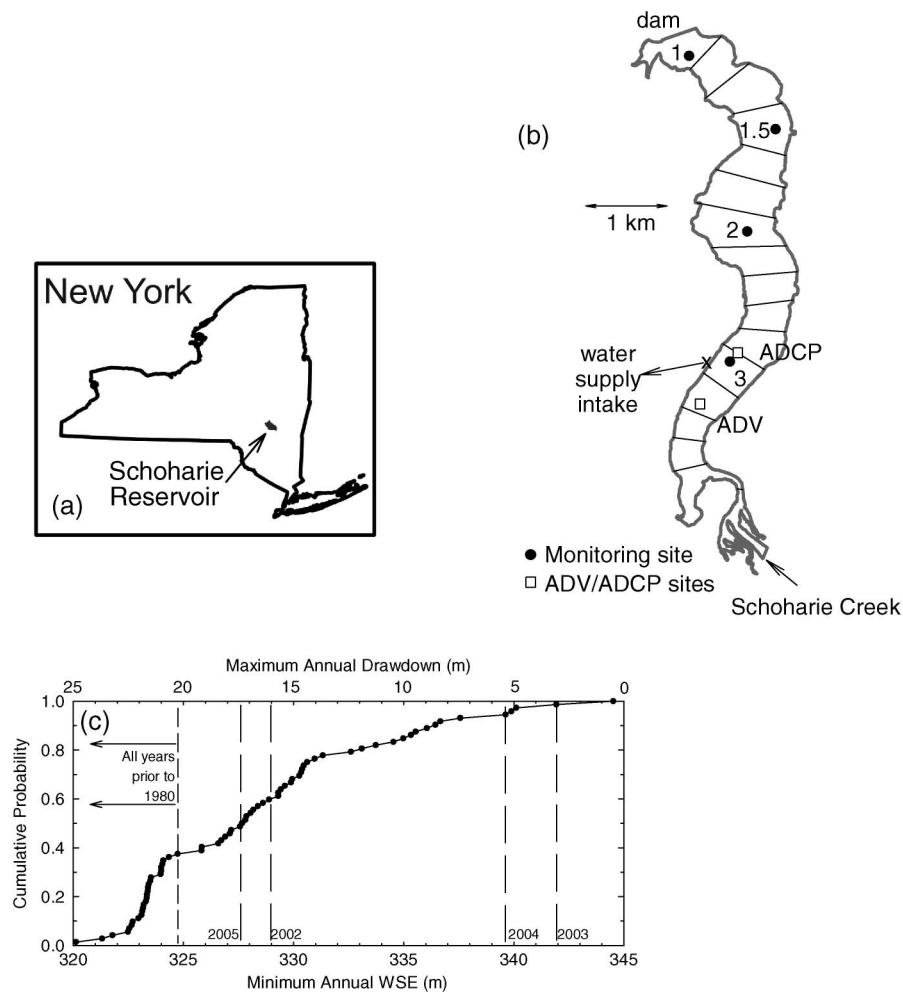


Fig. 1. (a) Schoharie Reservoir location in New York State; (b) reservoir features, monitoring locations, and model longitudinal segmentation; (c) frequency of occurrence of minimum annual reservoir water surface elevation (WSE) and maximum annual drawdown; and all years for which maximum annual drawdown exceeded 20 m occurred before 1980

manual drops of a rapid-profiling instrument cluster were made at multiple sites (usually ≥ 25) in the days following runoff events (Effler et al. 2006a, b, 2008). Stream and reservoir monitoring included Tn , temperature (T), and specific conductance (SC). Although many Tn observations were made directly, others were computed from direct measurements of the beam attenuation coefficient (Effler et al. 2006a), an alternate measure of light scattering. Neither suspended nor dissolved solids concentrations significantly affect buoyancy in this reservoir.

Extensive characterization of particles (number, concentration, size distribution, and composition) and associated light scattering in Schoharie Creek (Effler et al. 2007), Schoharie Reservoir (Peng and Effler 2007), and Ashokan and Kensico Reservoirs (Peng et al. 2009) were conducted with scanning electron microscopy interfaced with automated X-ray microanalysis and image analysis (SAX). In these waters, almost all of the particles that contribute to turbidity were found to be inorganic (minerogenic) and of terrigenous origin (Peng and Effler 2007). The contribution of particles within various size classes was determined, establishing that Tn is primarily associated with clay minerals, 1–10 μm in diameter (Peng and Effler 2007; Peng et al. 2009). This direct characterization of the turbidity-causing particles was invaluable in guiding and constraining the specification of particle behavior in the model (Gelda et al. 2009).

Resuspension Process Measurements

Deployments of two acoustic Doppler instruments were made in the late summer of 2004 to investigate physical processes that lead to bed stress and resuspension. A 6 MHz Nortek Vector acoustic Doppler velocimeter (ADV) was deployed in the southern portion of the basin along the thalweg [Fig. 1(b)] for August 10–17; water depth at the site was ~ 10 m. The cabled probe head of the ADV was deployed in an upward-looking configuration with the measurement volume located 0.2 m above the bed. The ADV operated in burst-mode, collecting a 10-min burst at 8 Hz each hour. The ADV allowed direct determination of the turbulent bed stress components $-\overline{\rho u'w'}$ and $-\overline{\rho v'w'}$, where ρ is the water density, u' and v' are the orthogonal horizontal turbulent velocity fluctuations about their mean values, w' is the vertical velocity fluctuation about its mean value, the overbar indicates the average over a burst interval, and the bed stress $\tau_B = \rho\sqrt{\overline{u'w'^2} + \overline{v'w'^2}}$. The ADV simultaneously measures acoustic backscatter intensity, a surrogate for suspended sediment concentration. In addition, a 600 kHz Teledyne RD Instruments Workhorse acoustic Doppler current profiler (ADCP) was deployed in an upward-looking mode, in approximately 17 m of water [Fig. 1(b)] near the lateral midpoint of the basin for the September 1–22 interval. The ADCP was operated in Mode 1 (broadband) collecting 1,024 samples at 2 Hz in hourly bursts.

The instrument was configured with 35 bins (each 0.5 m in depth), and hence profiled the entire water column.

The August 2004 deployment captured two moderate runoff events [Fig. 2(a)]; Schoharie Creek was plunging throughout the deployment, and the ADV was within the underflow formed by the plunging creek. The dynamics in backscatter across the 3 beams [Fig. 2(b)] showed strong correlation ($r = 0.72$, $p < 0.001$) with the creek discharge [Fig. 2(a)] during the events on August 12–13 and August 16–17. The 6-h lag between the peaks in the hydrograph and backscatter is a result of travel time between the two locations and was accounted for in determining the correlation. Increases in backscatter on August 11–12 in the absence of substantial discharge [Figs. 2(a) and 2(b)] depict the effects of first-mode baroclinic (internal) seiche, which is also apparent in the ADV burst-mode average velocity data (not shown). Baroclinic seiche motion has been observed to drive resuspension elsewhere (Pierson and Weyhenmeyer 1994). The similarity in the time series of backscatter and discharge results from a combination of turbid inflow from the watershed and local resuspension caused by the bed stress caused by the underflow. The variation of the observed bed stress τ_B [Fig. 2(c)] clearly indicates that runoff events lead to increases in τ_B (August 13, 16, and 17). Such levels of τ_B have been found to be sufficient to initiate resuspension in other water bodies (James et al. 1997; Lick et al. 1994).

A consistent pattern was observed in the ADCP data from September when two larger runoff events occurred [Fig. 2(d)].

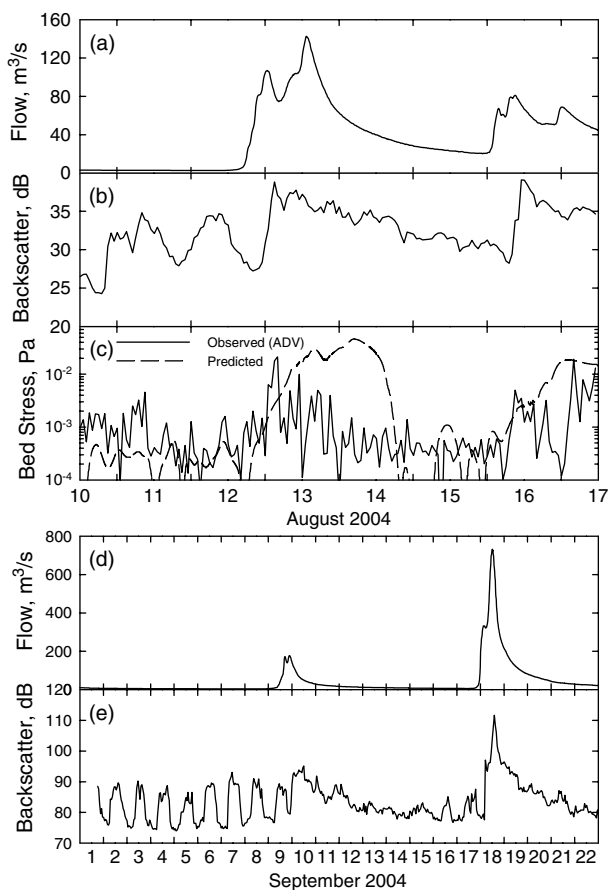


Fig. 2. Schoharie Creek streamflow, ADV, and ADCP observations in Schoharie Reservoir in 2004: (a) Schoharie Creek streamflow; (b) ADV acoustic backscatter; (c) turbulent bed stress observed by the ADV and predicted by the model at the ADV site; (d) Schoharie Creek streamflow; and (e) ADCP acoustic backscatter at 1.0 m above the bed

Increases in backscatter associated with the event on September 7, and particularly the larger event on September 17, again depict the combined effects of tributary input and local resuspension [Fig. 2(e)]. Local resuspension or advection driven by motion associated with the first-mode baroclinic seiche, with a period of ~ 2 days, is suggested by the cyclic backscatter pattern observed in portions of the deployment. A simple, two-layer first-mode seiche calculation for the observed stratification conditions yields a period of 2 days.

Existing Model and Enhancements

Model Components

The turbidity model W2Tn described in this study has three components. The hydrothermal component, which computes water motion (including motion associated with plunging inflow and internal seiche), temperature, diffusion/dispersion coefficients, bed stress, WSE, and selective withdrawal, was directly adopted from the U. S. Army Corps of Engineers model CE-QUAL-W2 (Cole and Wells 2002). No modifications to the hydrodynamic, thermal, or transport aspects of this public-domain code were made. The turbidity component was originally described by Gelda and Effler (2007a), and is advanced in this study to include resuspension. The third component deals with surface waves. A portion of this component, dealing with the prediction of wave characteristics as a function of wind and basin characteristics, has been described and tested previously (Owens 2009). Calculation of the bed stress associated with predicted wave characteristics has been added to the surface wave component.

The selection of a laterally-averaged, 2D approach for simulating turbidity in this reservoir was motivated by two considerations. Most importantly, observations of turbidity, throughout the seasonal cycle and over a wide range of hydrologic, meteorological, and operating conditions, indicate that lateral gradients in turbidity usually do not exist and are of modest magnitude and short duration when observed (Effler et al. 2006b). In addition, there are serious shortcomings associated with use of a 3D approach given the intended management application of this model. This model of Schoharie will be integrated with similar models of the two basins of Ashokan (Gelda et al. 2009) and Kensico Reservoirs. Linked simulations for these basins will be integrated within a larger reservoir system model; iterative model solutions will be made to determine optimal system operation subject to specified objectives, rules, and constraints, including reservoir T_n levels simulated by the W2Tn model. Long-term planning applications of this tool will involve simulations for the record (currently 57 years; Gelda and Effler 2008) of historical hydrologic and meteorological conditions. The computational burden associated with this approach would make use of a 3D model extremely impractical.

Hydrothermal Component of W2Tn

The hydrothermal component of W2Tn is established on laterally-averaged conservation equations for longitudinal momentum, water volume, and temperature; hydrostatic pressure is assumed in the vertical direction. This model has been applied to a number of systems, including the simulation of plunging inflows in deep, narrow basins (Chung and Gu 1998; Ahlfeld et al. 2003). A grid of 17 longitudinal segments [Fig. 1(b)], and layers 1 m in thickness were used to describe spatial variations. As a result of accurate simulation of observed seasonal variation in water column and withdrawal temperature for a 14-year period (Gelda and Effler 2007b) and of the behavior of density currents in 2003

(Gelda and Effler 2007a), the hydrothermal component of the model has been validated for Schoharie Reservoir.

Turbidity Component of W2Tn

Aside from resuspension, the structure of the turbidity component of W2Tn is identical to an earlier version used to study Tn at Schoharie (Gelda and Effler 2007a; Gelda and Effler 2008). The model uses Tn as the state variable and thus assumes that this optical property behaves in a conservative manner. By using this approach, good model performance has been achieved in simulating turbidity events in Ashokan Reservoir (Gelda et al. 2009) and for full reservoir conditions in Schoharie Reservoir (Gelda and Effler 2007a). Total turbidity is assumed equal to the sum of turbidity associated with one or more particle classes; settling velocity differentiates the classes. In this study, three particle classes, represented by Stokes equivalent sizes (diameters) of 1.0, 3.1, and 8.1 μm , respectively, were used. These are the same as recently adopted for downstream Ashokan Reservoir (Gelda et al. 2009) based on equivalent light scattering characteristics of turbidity-causing particles in the two reservoirs (Peng et al. 2009). Moreover, these particle sizes are consistent with the contributions of various size classes to Tn in Schoharie Reservoir determined by SAX measurements (Peng and Effler 2007; Peng et al. 2009). These specifications for particle classes represent an upgrade from the earlier application of W2Tn to Schoharie (Gelda and Effler 2007a), in which these features were more calibration-based and less consistent with SAX observations. Model calibration, guided by the findings for the primary tributary to Ashokan Reservoir (Gelda et al. 2009), was used to determine the fraction of total turbidity in stream inflow associated with the three particle classes.

The starting point for the enhancements associated with resuspension is the two-dimensional “turbidity conservation” equation

$$\begin{aligned} & \frac{\partial}{\partial t}(BTn_i) + \frac{\partial}{\partial x}(BUTn_i) + \frac{\partial}{\partial z}[B(W - W_{Si})Tn_i] \\ & = \frac{\partial}{\partial x}\left(BE \frac{\partial Tn_i}{\partial x} \right) + \frac{\partial}{\partial z}\left(BD \frac{\partial Tn_i}{\partial z} \right) + \frac{dB_R}{dz} \varepsilon_{Ri} + \frac{dB_L}{dz} \varepsilon_{Li} \quad (1) \end{aligned}$$

where Tn_i = turbidity associated with particle class i ; B = cross section width; t = time; U = longitudinal velocity; x = longitudinal position; W = vertical velocity; W_{Si} = settling velocity of particle class i ; z = vertical position; E = longitudinal dispersion coefficient; D = vertical diffusion coefficient; B_R , B_L = width of cross section to right and left of centerline ($B_R + B_L = B$); and ε_{Ri} , ε_{Li} = resuspension flux of turbidity associated with particle class i to right and left of centerline. Separate resuspension expressions for the right and left sides of the cross section were included to allow for wave-induced resuspension to be different on the two sides, which may occur because of differences in flux or bathymetry. This two-dimensional equation assumes that Tn_i is uniform in the lateral direction over the width B . However, the fluxes ε_{Ri} and ε_{Li} vary with z and thus with lateral position. Tn does not affect density and is transported as a passive scalar.

The resuspension fluxes ε_{Ri} and ε_{Li} are computed by

$$\varepsilon_{Ri} = \varepsilon_{RWi} + \varepsilon_{Ui} \quad (2a)$$

$$\varepsilon_{Li} = \varepsilon_{LWi} + \varepsilon_{Ui} \quad (2b)$$

where ε_{RWi} and ε_{LWi} = surface wave-induced resuspension on the right and left sides of the cross section; and ε_{Ui} = current-induced resuspension, each for particle class i . These components of resuspension are computed by

$$\varepsilon_{RWi} = \begin{cases} C_1 \left(\frac{\tau_{RW} - \tau_{Ci}}{\tau_{Ci}} \right)^{C_3}, & \text{for } \tau_{RW} > \tau_{Ci} \\ 0, & \text{for } \tau_{RW} < \tau_{Ci} \end{cases} \quad (3a)$$

$$\varepsilon_{LWi} = \begin{cases} C_1 \left(\frac{\tau_{LW} - \tau_{Ci}}{\tau_{Ci}} \right)^{C_3}, & \text{for } \tau_{LW} > \tau_{Ci} \\ 0, & \text{for } \tau_{LW} < \tau_{Ci} \end{cases} \quad (3b)$$

$$\varepsilon_{Ui} = \begin{cases} C_1 \left(\frac{\tau_U - \tau_{Ci}}{\tau_{Ci}} \right)^{C_3}, & \text{for } \tau_U > \tau_{Ci} \\ 0, & \text{for } \tau_U < \tau_{Ci} \end{cases} \quad (3c)$$

where τ_{RW} and τ_{LW} = surface wave-induced bed stress on right and left sides; τ_U = current-induced bed shear stress; C_1 and C_3 = empirical coefficients; and τ_{Ci} = critical bed stress for particle class i .

The total resuspension rate was computed as the sum [Eq. (2)] of the rates associated with the two mechanisms (currents and surface waves) that generate bed stress. A more general approach would be to calculate a single resultant stress that considers both components of motion with proper accounting for differences in magnitude and direction of the components and the oscillatory nature of wave motion (Grant and Madsen 1979; Lick et al. 1994). The approach expressed by Eq. (2) was used in this study for two reasons. First, this model predicts water motion only in the longitudinal direction. Procedures for combining current and wave-driven motion to determine a resultant bed stress (e.g., Grant and Madsen 1979) require the magnitude and direction (in the horizontal plane) of each component of motion be known. Using this approach requires the use of a 3D hydrodynamic model that is not otherwise justified for this reservoir. More importantly, calculation of the two components of bed stress in Schoharie Reservoir shows that the current-induced (τ_U) and surface wave-induced (τ_{RW} , τ_{LW}) bed stresses very rarely reach significant ($\sim \tau_{Ci}$) levels at the same time and location as demonstrated subsequently. In other words, at any particular time and location, only one of the fluxes on the right side of Eq. (2) is significant. The current-induced bed stress is computed by

$$\tau_U = \frac{\rho g}{C_B} U^2 \quad (4)$$

where C_B = Chezy roughness coefficient; and g = acceleration of gravity.

Surface Wave Component of W2Tn

The prediction of surface wave characteristics in W2Tn was accomplished by using a framework based on the Donelan/GLERL wave model (Schwab et al. 1984). The application and testing of this framework for Schoharie Reservoir has been described elsewhere (Owens 2009), and is summarized briefly in this work. A model grid, consisting of 1,812 fifty-meter squares, was used to represent the reservoir water surface at full storage with a bottom elevation assigned to each grid square. The effect of changing water-surface elevation was considered by allowing individual squares to become inactive during drawdown and reactivated during refilling. The steep nearshore bottom slopes, together with relatively small wavelength (maximum ~ 1 m), indicate that wave-induced bed stress occurs in a narrow shallow strip along the leeward shore. The width of this strip is less than the 50-meter grid size so that the transition from deep water to the shoreline, and the accompanying wave shoaling and refraction, was not simulated by the model. The model was validated by comparing predictions to field wave measurements made in the fall of 2002, a period that included several wind events (Owens 2009).

Previous lake or reservoir water quality models that simulate surface wave-induced resuspension have been applied to shallow water bodies (Luettich et al. 1990; Hawley and Lesht 1992; Lick et al. 1994; James et al. 1997; Jin and Ji 2004). In these models, the gradual increase in τ_W moving from deep water toward the shoreline was considered in the calculation of resuspension. In Schoharie, this transition occurs over distance less than the size of a 50-meter grid square and makes the calculation of bed stress associated with local wave characteristics and water depth problematic. W2Tn computes the average bed stress over the nearshore region from the rate of dissipation of wave energy determined from deep-water wave characteristics. The wave power per unit length of shoreline F was computed from wave model predictions (Dean and Dalrymple 1991)

$$F = \frac{1}{16} \rho g^2 \frac{H^2}{\omega} \cos \Delta\theta_S \quad (5)$$

where H and ω = significant wave height and frequency; and $\Delta\theta_S$ = angle of incidence of waves relative to shoreline ($|\Delta\theta_S| \leq \pi/2$). The average bed stress over the nearshore region is

$$\tau_W = \frac{F}{B_W C_g} = \frac{\rho g}{8 B_W} H^2 \cos \Delta\theta_S \quad (6)$$

where B_W = width of resuspension zone; τ_W = average bed stress over B_W ; and C_g = wave group velocity. Predictions of wave height, period, and direction were used in Eq. (6) to compute τ_W for each of the grid squares located at the shoreline. Average values of τ_W were computed for the grid squares located along the right and left shorelines in each longitudinal segment in the 2D model, yielding values of τ_{RW} and τ_{LW} for each segment. These bed stresses were then used in the turbidity component of the model [Eqs. (3a) and (3b)] to determine resuspension.

Model Testing

W2Tn was tested for the conditions that occurred at Schoharie Reservoir from September 2002 through December 2005. This interval includes a severe runoff event (April 3, 2005; the daily average Schoharie Creek streamflow of 439 m³/s ranked eighth in the 106-year streamflow record) and another major event (September 18, 2004; the daily average flow of 422 m³/s ranked tenth in the record). Both of these events, and a series of moderate events in spring 2003 and fall of 2003 and 2004, occurred at full reservoir storage [Figs. 3(a) and 3(b)]. Significant drawdown occurred in the summer–fall interval of 2002 and 2005 [Fig. 3(b)]; the 16–17 m maximum drawdown that occurred in these two years was

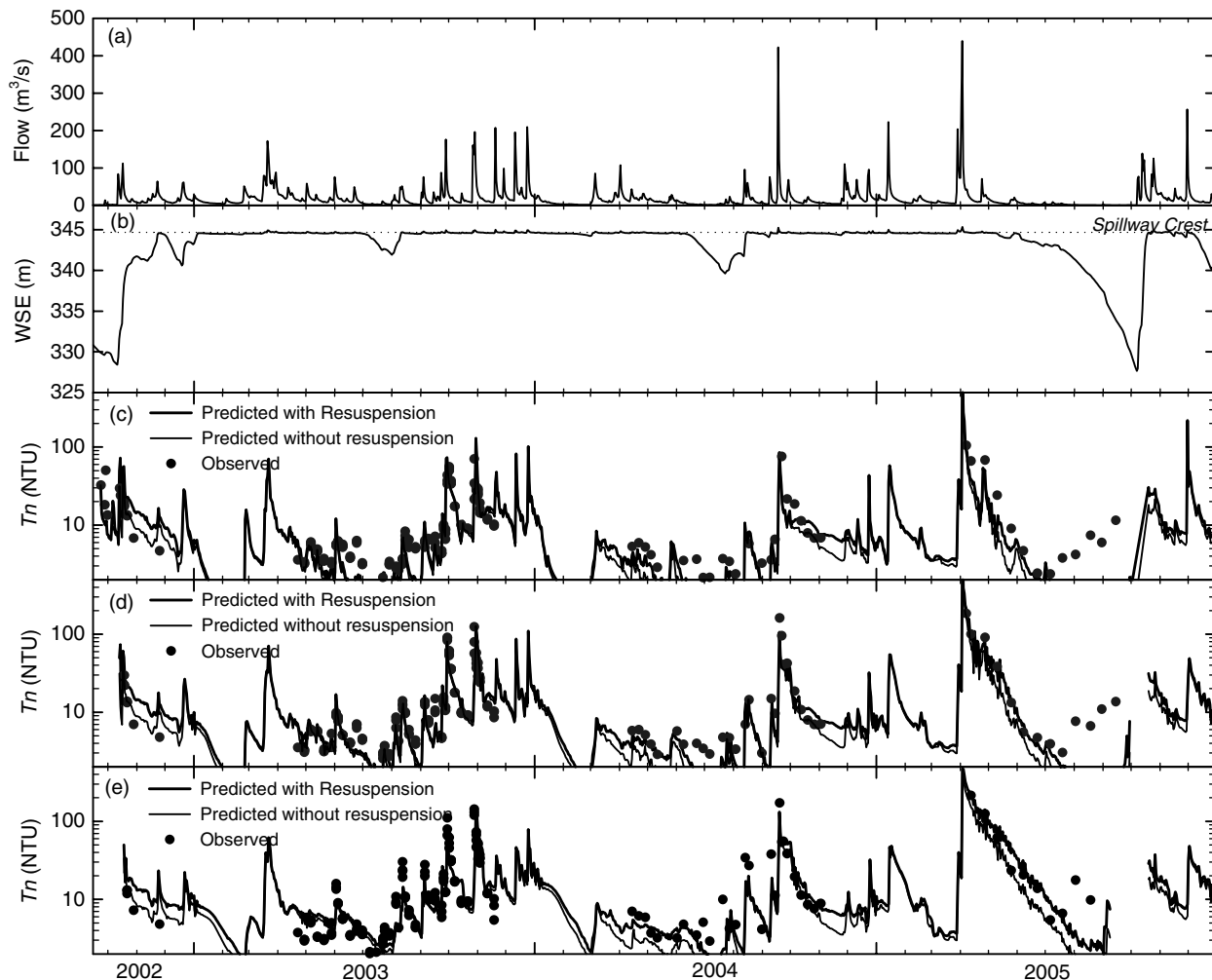


Fig. 3. Selected model inputs and predictions for September 2002–December 2005: (a) daily Schoharie Creek streamflow; (b) reservoir WSE; (c) observed and predicted T_n averaged over the depth range 0–5 m at Site 3; (d) observed and predicted T_n averaged over the depth range 5–10 m at Site 3; and (e) observed and predicted T_n averaged over the depth range 10 m to bottom at Site 3

Table 1. Turbidity Particle Size Class Coefficients Not Related to Resuspension

Particle Class	Stokes equivalent size, (μm)	Settling velocity at 18°C W_{si} , (m/day)	Deposition time scale, t_{Di} , (day)	Tributary load fraction (%)	
				$Q < 40 \text{ m}^3/\text{s}$	$Q > 40 \text{ m}^3/\text{s}$
Class 1 (small)	1.0	0.075	220	10	10
Class 2 (medium)	3.1	0.75	22	65	45
Class 3 (large)	8.1	5.0	3.3	25	45

exceeded in approximately half the years of the record [Fig. 1(c)]. Modest runoff events in the fall of both years quickly refilled the reservoir [Fig. 3(a) and 3(b)].

A further validation of the previously tested (Gelda and Effler 2007a) hydrothermal component of the model was completed by comparison of the ADV-observed bed stress to the model prediction [Eq. (4)] at the deployment location [Fig. 1(a)]. The predicted and

observed bed stress compared well for the August 10–17, 2004 interval [Fig. 2(c)], providing direct validation of the use of $C_B = 70$ [Eq. (4)], and more generally of the ability of the laterally averaged 2D model to predict local water motion and bed stress conditions.

The Ashokan model (Gelda et al. 2009) and the earlier work at Schoharie (Gelda and Effler 2007a) established that multiple particle classes and the associated settling velocities are required to simulate the dynamics of impact and recovery of the water column caused by runoff events; although three particle classes were moderately better than two, more than three produced little additional benefit. The Stokes equivalent sizes for the three particles classes determined for Ashokan Reservoir (Gelda et al. 2009) were adopted for Schoharie (Table 1). These velocities, and the related time scale for particle deposition $t_{Di} = \bar{h}/W_{si}$ in which \bar{h} is the mean depth of the basin, vary significantly for the three classes (Table 1). Initial testing focused on April 2003–December 2004,

Table 2. Values of Resuspension Coefficients for Schoharie Reservoir

Coefficient	Value
C_1 ($\text{NTU} \cdot \text{m} \cdot \text{s}^{-1}$)	1×10^{-5}
C_3 (dimensionless)	2.6
τ_{C1} (Pa; small fraction)	0.08
τ_{C2} (Pa; medium fraction)	0.10
τ_{C3} (Pa; large fraction)	0.20

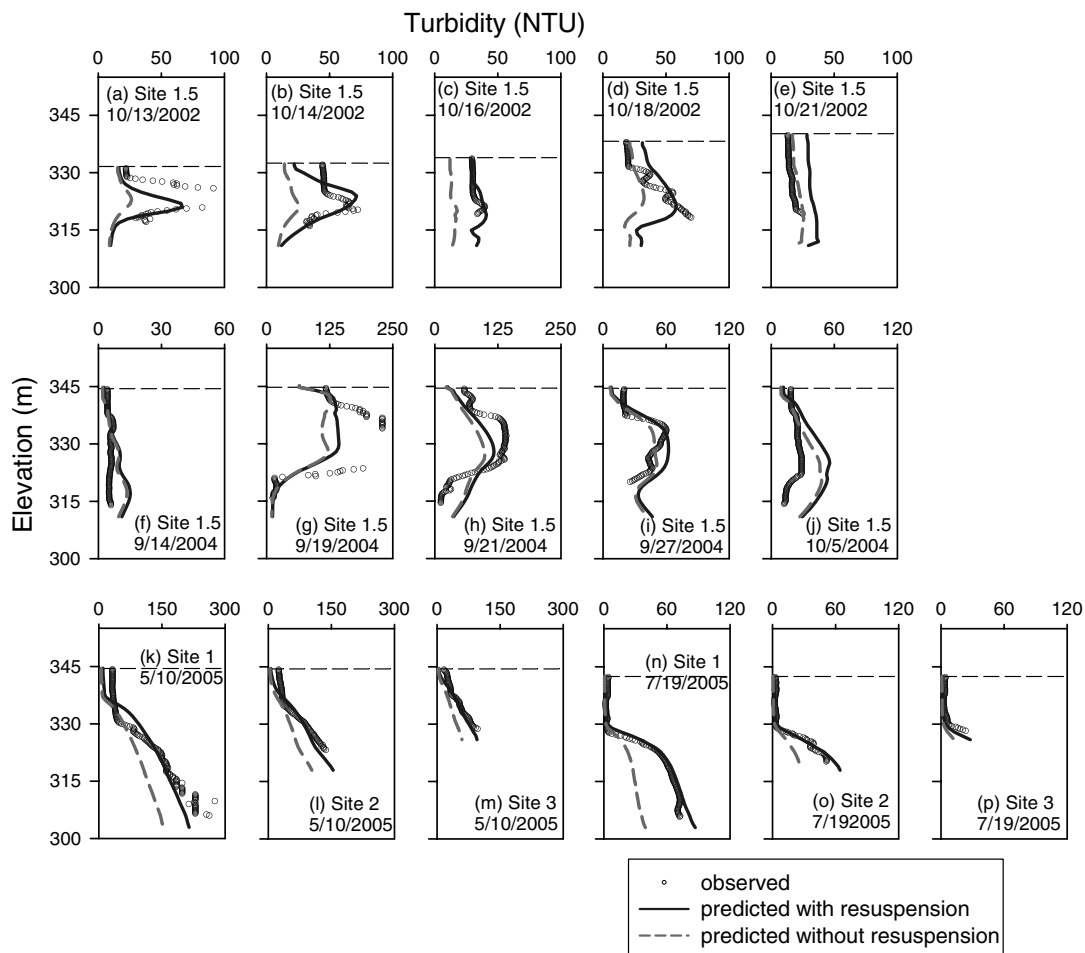


Fig. 4. Selected vertical profiles of observed and predicted turbidity: (a)–(e) at Site 1.5 on October 13, 2002; (f)–(k) at Site 1.5 on September 18, 2004; and (l)–(p) at Site 2 on April 3, 2005

when the reservoir was full $\sim 90\%$ of the time [Fig. 3(b)]. Model performance for this period was good without invoking resuspension associated with currents or surface waves, a result consistent with the earlier application of W2Tn to Schoharie (Gelda and Effler 2007a). The fraction of the observed Schoharie Creek inflow turbidity assigned to each particle size class (Table 1) was adjusted to maximize model performance for this period. A modest shift in the fractions was made for days when the daily average Schoharie Creek flow exceeded $40 \text{ m}^3/\text{s}$ (Table 1). This allowed the model to simulate the large April 2005 event accurately. These fractional contributions, including the shift for high flow, were qualitatively consistent with SAX observations for Schoharie Creek and the effect of elevated streamflow and resulting bed stress on particle size distributions (Effler et al. 2007).

The model generally underpredicted the observed turbidity in the water column and reservoir withdrawal for the drawdown periods in the fall of 2002 and 2005 when resuspension was not simulated [$C_1 = 0$, Eq. (3)]. Preliminary calibration of the resuspension coefficients C_1 and C_3 , and the critical shear stress τ_{Ci} [Eq. (3)], lead to values of $C_1 \approx 10^{-5}$ NTU-m/s, $C_3 = 2.6$, and $\tau_{Ci} \approx 0.1$ Pa. With the critical stress equal for the three classes, equal amounts of turbidity are resuspended from the bed for each class. Final calibration of the critical bed stress, accounting for events occurring during drawdown and the April 2005 event, yielded values of the critical shear stress that differed for the three classes (0.08, 0.1, and 0.2 Pa for the small, medium, and large Stokes equivalent size classes, respectively; Table 2).

Predictions shown in this study (Figs. 3–6) are based on a continuous simulation for September 2002 through December 2005, by using the observed water column T and Tn for initial conditions. Comparison of predicted and observed Tn , averaged vertically over three portions of the water column, indicate the model performed well in simulating the peaks associated with events, the recovery from peaks, and the overall dynamics of turbidity in the reservoir at Site 3 near the intake structure [Figs. 3(c)–3(e)]. The focus is on the prediction of Tn at levels of water quality concern in this reservoir (> 10 NTU), which only occur in response to runoff events [Fig. 3(a)]. When the Tn predictions are viewed as a time series at one depth or a range of depths, the effect of resuspension is most obvious during the period of recovery from events [Figs. 3(c)–3(e)].

The effect of resuspension is seen more clearly when the predictions are viewed as vertical profiles (Fig. 4). At the onset of the runoff event of October 12, 2002, the reservoir was drawn down approximately 16 m [Fig. 3(b)]. At Site 1.5 [Fig. 1(a)], as throughout the deeper stratified portion of the reservoir, the maximum turbidity was observed at ~ 7 m depth, attributable to the turbid interflow from Schoharie Creek [Figs. 4(a) and 4(b)]. The model captured the observed subsurface peak. This feature of model performance depended critically on accurate prediction of mixing associated with the plunging inflow, and the depth of the interflow, by the hydrothermal component of the model. The magnitude of Tn was also simulated well, in large part because of the effect of resuspension, particularly in the early portion of the event (difference in simulations with and without resuspension; Figs. 4(a)–4(c)). The greatest increase in turbidity associated with resuspension occurred at the subsurface peak. This indicates that resuspension was predicted to occur in the upper portion of the reservoir where Schoharie Creek flows through a reduced cross-sectional area because of drawdown, thus creating large velocity U , shear stress τ_U [Eq. (4)], and resuspension ε_U [Eq. 3(c)]. This resuspended material is effectively added to the turbidity “load” from the watershed and enters the water column as an interflow. Resuspension also improved the model predictions for the slightly larger event of October 17 [Fig. 4(d)] and in the recovery following both October events

[Figs. 4(c) and 4(e)]. The model also performed well in simulating the interflow-driven vertical distribution of Tn for the September 2004 event at Site 1.5 [Figs. 4(f)–4(j)] when the reservoir was at full storage [Fig. 3(b)]. As a result, the impact of resuspension on the predicted Tn was less than in the fall of 2002. As under drawdown conditions, the impact of resuspension was greatest at the subsurface peak [Figs. 4(g)–4(i)]. The recovery of the water column to lower Tn levels following the event was simulated well by the model [Fig. 4(j)].

The highest turbidities observed in the reservoir during the 2002–2005 interval occurred following the severe runoff event on April 2–3, 2005. As in the 2002 and 2004 events, Schoharie Creek was cooler and plunged. However, because of the lack of thermal stratification in the water column, the plunging, turbid stream flowed down the sloping bottom into the deepest portions of the reservoir and formed a thick, highly turbid (peaks ~ 300 NTU) underflow layer over the length of the basin [Figs. 4(k)–4(p)]. This event was also unusual in that elevated Tn persisted in the lower waters for approximately four months following the event [Figs. 3(c)–3(e)], despite a lack of significant additional runoff [Fig. 3(a)]. The model performed well in simulating the thickness of the turbid layer and the vertical distribution of Tn [Figs. 4(k)–4(p)]. Resuspension had a significant impact on the predictions, both weeks [Figs. 4(k)–4(m)] and months [Figs. 4(n)–4(p)] after the event.

Resuspension driven by surface waves occurs at depths less than approximately 1 m in Schoharie Reservoir, where the rather small waves (Owens 2009) cause significant bed stress. The effect of resuspension in this range of depth was relatively small throughout the simulation period (Fig. 4), indicating that current-induced resuspension was more significant than that caused by surface

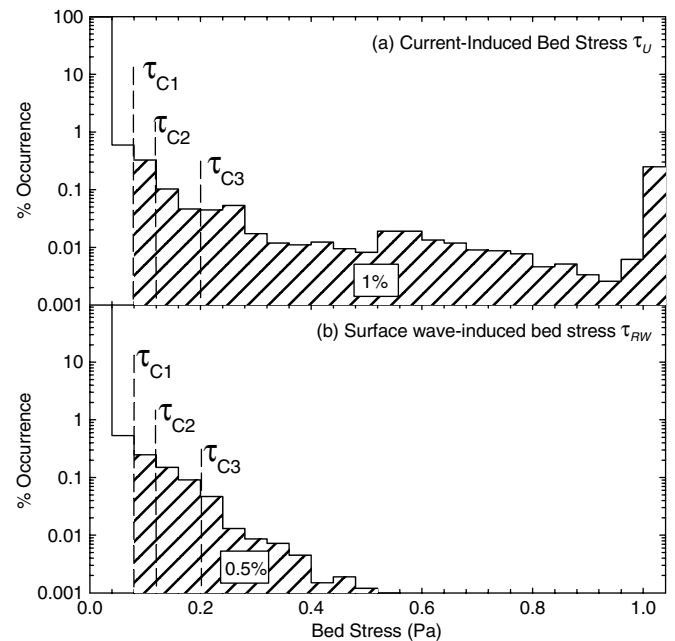


Fig. 5. Frequency of occurrence of various levels of predicted bed stress at selected points in the reservoir for the September 2002–December 2005 simulation: (a) current-induced bed stress, τ_U , in the thalweg at the site of the ADV deployment ($\tau_U > 1.0$ Pa for 0.25% of the simulation period); (b) surface wave-induced bed stress on the right side, τ_{RW} , at the segment containing Site 2, which is on average the location of maximum surface wave effect; and the critical shear stress for resuspension for the 3 particle classes considered in the model (τ_{C1} , τ_{C2} , and τ_{C3}) are shown

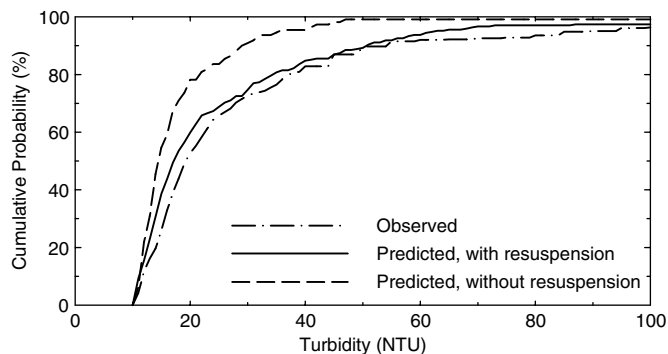


Fig. 6. Percentage of withdrawal turbidity (T_{n_w}) values that are less than a given value for the September 2002–December 2005 simulation period; observed turbidity less than 10 NTU were not included; only those model predictions (with and without resuspension) of withdrawal turbidity exceeding 10 NTU and corresponding to a time at which a measurement was made were included in the predicted curves

waves. At a site on the east shoreline of the reservoir near Site 2, where average wave impact is largest, the wave-induced bed stress (τ_{RW}) exceeded the critical stress $\tau_{C1} = 0.08$ Pa only 0.5% of the time, and peak values of τ_{RW} were less than for τ_U [Fig. 5(b)]. At the site of the ADV deployment in the upstream portion of the reservoir [Fig. 1(a)], the bed stress associated with currents (τ_U) exceeded the lowest critical shear stress for resuspension ($\tau_{C1} = 0.08$ Pa) approximately 1% of the time over the entire September 2002–December 2005 simulation period [Fig. 5(a)]. Thus, resuspension is an infrequently occurring, episodic process, although its impact may persist for weeks or months after resuspension has ceased while the slowly settling fraction remains suspended in the water column [Figs. 4(k)–4(p)].

The frequency of occurrence of various levels of high (> 10 NTU) withdrawal turbidity (T_{n_w}) predicted by the model compared very well with the corresponding frequency distribution of observed T_{n_w} for the September 2002–December 2005 period (Fig. 6). Accurate prediction of high T_{n_w} levels serves as an additional validation of predictions of T_n in the water column and of the model's selective withdrawal algorithm used to mix water and T_n from various layers at and near the elevation of the intake to determine T_{n_w} . Including resuspension in the model increased the accuracy of predictions of T_{n_w} (Fig. 6). Average levels of model error (Table 3) were similar to those achieved in the model application to Ashokan Reservoir (Gelda et al. 2009) and indicate the improved accuracy resulting from consideration of resuspension.

Discussion

Resuspension was generally the dominant source of particles to the water column in previous modeling studies of lake and reservoirs

that considered resuspension (Hawley and Lesht 1992; Lick et al. 1994; James et al. 1997; Luettich et al. 1990). Relative to Schoharie Reservoir, these water bodies are much more shallow and with greater fetch so that surface waves induce resuspension over most of, or the entire, bottom area. In Schoharie Reservoir, the primary source of particles and turbidity to the water column is loading from tributaries. Resuspension occurs over a small fraction of the reservoir bottom—primarily along the thalweg in the shallow upstream areas during runoff events (current-induced) and secondarily in shallow regions along the leeward shore (surface wave-induced). Resuspension plays a secondary, but nonetheless significant, role as a source of particles to the water column. The importance of resuspension is greatest during runoff events that are either very severe (e.g., the April 2005 event) or occur during periods of draw-down (late summer–fall of 2002 and 2005).

Many reservoirs and some lakes are bathymetrically similar to Schoharie Reservoir because impoundment and storage of a large water volume is achieved by construction of a high dam in a relatively narrow valley. The 2D framework of W2Tn would be applicable to water quality problems associated with suspended particles in such reservoirs. For a problem such as eutrophication, the framework may be simplified to simulate a single particle class, and Eq. (3) may be recast to represent resuspension of particle mass rather than turbidity, as generally done in shallow lake eutrophication models (James et al. 1997). Resuspension has been found to play a role in reservoir eutrophication in a reservoir similar to Schoharie (Effler and Matthews 2004).

Of course, deep lakes and reservoirs exist for which the assumption of lateral homogeneity is not valid and may require a three-dimensional approach. In such systems, the general resuspension approach taken in this study may be used. If the conditions are such that current and surface wave-induced bed stress occur simultaneously over significant portions of the bed, then the predicted bed stress caused by currents, predicted by a 3D hydrodynamic model, may be combined with the predicted bed stress from a surface wave model (Grant and Madsen 1979) to generate a total stress to drive resuspension [Eq. (3)].

No simulation of characteristics of the sediment bed was included in the described model. Sediment bed components have been included in resuspension models and may quantify the local accumulation of mass from deposition, loss from resuspension, armoring of the bed by preferential resuspension of individual size fractions, and time-dependent cohesive effects on the resuspension rate (Lick et al. 1994; Ziegler and Nisbet 1995). Simulation of sediment mass in the bed allows for resuspension to be limited by the supply or availability of particles at the bed surface. Although including these processes in a model potentially provides additional predictive capability, such advantages can only be realized if these processes are important in regulating the conditions of practical interest and if data are available to quantify rates or coefficients used to simulate these processes. W2Tn effectively assumed that the

Table 3. Performance of the Turbidity Model W2Tn in Simulating Reservoir Water Column and Withdrawal T_n with ($C_1 = 1 \times 10^{-5}$) and without ($C_1 = 0$) Simulation of Resuspension

Period	Normalized root mean square error in T_n (%)			
	Water column		Withdrawal	
	With resuspension	No resuspension	With resuspension	No resuspension
Drawdown was significant: September–December 2002, July–December 2005	20	34	17	32
Full reservoir (drawdown was small): January 2003–June 2005	17	16	14	15

Note: Normalized root mean square (rms) error is the rms error relative to the observed peak turbidity for the most recent runoff event.

resuspension rate [Eq. (3)] is not limited by the supply of sediment on the bed. Model testing of W2Tn for Schoharie Reservoir indicates that sediment resuspension can be adequately simulated by using a simpler framework that does not include a bed component.

Accurate prediction of the turbidity peaks for the various events [Figs. 3(c)–3(e)] indicates that the total quantity of turbidity input to the water column from watershed loading and resuspension is simulated accurately. Also of interest is the predicted 4-month-long recovery of the water column from the peak for the April 2005 event. In approximately the first 2 weeks after the event, deposition is dominated by large particles ($t_{D3} = 3.3$ days; Table 1). From approximately 2 weeks to 2 months after the event, the large particles are mostly absent from the water column and deposition of medium class ($t_{D2} = 22$ days) dominates. After 2 months, particles in the water column are predominantly of the small class ($t_{D1} = 220$ days). The model generates accurate predictions of the recovery over each of these three portions of the 4-month recovery period [Figs. 3(c)–3(e)], indicating that the relative contribution of the three classes to watershed loading and resuspension was simulated accurately. These model predictions are also consistent with the observed slow attenuation of ADV backscatter peaks.

Summary

A model (W2Tn) that simulates the fate and transport of particles that contribute to turbidity in the water column of a lake or reservoir is described with emphasis on enhancements to include particle resuspension. W2Tn uses a two-dimensional, laterally averaged approach to represent conditions in the water column, and so is well suited to simulate turbidity in deep, narrow lake and reservoir basins. The model has hydrothermal, surface wave, and turbidity components. The hydrothermal component is adopted directly from CE-QUAL-W2, a 2D lake and reservoir model, and predicts longitudinal and vertical water motion, advective and dispersive transport, water surface elevation, and temperature, and simulates selective withdrawal of reservoir outflows. The surface wave component, added in the enhanced model, predicts wave characteristics (significant height and period) over the surface of the water body, and bed stress because of waves. Lastly, the turbidity component computes this optical property in the water column and is enhanced to include simulation of the resuspension of turbidity-causing particles driven by currents and surface waves.

The model was tested for Schoharie Reservoir, an 8-km-long, 42-m-deep water supply reservoir located in the Catskill region of New York State, for a 3.5-year period. This reservoir experiences episodes of elevated turbidity caused by runoff events in its tributary streams. Measurements of environmental conditions, including meteorology, reservoir operations (water withdrawal and spill), and tributary inflow (flow, temperature, and turbidity) were used as model inputs. Water column turbidity, temperature measurements from robotic and manual monitoring programs, and measurements of withdrawal turbidity and temperature provided data for model validation. Measurements of bed stress, which were obtained by using an ADV deployed in the drowned channel of the major tributary, found that variations in bed stress were correlated with streamflow, and good comparison was found with current-induced bed stress predicted by the model. Physical and chemical characterization of collections of individual particles from Schoharie Reservoir and its major tributary also supported testing of the model.

Three classes of turbidity, differentiated by settling velocity or Stokes equivalent particle size, were used in this model application. Site-specific values of three model coefficients used to quantify resuspension were determined by optimizing the agreement between

predicted and observed turbidity in the reservoir water column and withdrawal. The validated model generated predictions of turbidity in the water column and reservoir withdrawal that agreed well with observations over the 3.5-year period, which included two severe and numerous moderate runoff events and two periods of significant reservoir drawdown. The model accurately simulated subsurface peaks in the water column associated with plunging stream inflow to the reservoir, longitudinal variations in turbidity, and the return to low turbidity levels following events. Resuspension was found to contribute importantly to turbidity in the water column during periods of drawdown and for severe runoff events. W2Tn may be applied to the analysis of turbidity in other water bodies where the two-dimensional approach is applicable. Moreover, the enhanced model is appropriate to support robust simulation of the effects of resuspension for various water quality issues associated with particles.

Acknowledgments

The New York City Department of Environmental Protection provided support for this study. This is contribution number 273 of the Upstate Freshwater Institute, Inc. 232

Notation

The following symbols are used in this paper:

- B = cross section width;
- B_L, B_R = cross section width to the left and right of centerline;
- B_W = width of resuspension zone;
- C_1, C_3 = empirical resuspension coefficients;
- C_B = Chezy roughness coefficient;
- D = vertical diffusion coefficient;
- E = longitudinal dispersion coefficient;
- g = acceleration of gravity;
- H = significant wave height;
- \bar{h} = mean depth of reservoir basin;
- t = time;
- t_D = deposition time scale;
- U = longitudinal current velocity;
- W = vertical velocity;
- W_{Si} = settling velocity of particle class i ;
- x = longitudinal position;
- z = vertical position;
- $\Delta\theta_S$ = angle of incidence of waves relative to the shoreline;
- $\varepsilon_{Li}, \varepsilon_{Ri}$ = resuspension flux of particle class i to left and right of centerline;
- ε_{Ui} = current-induced resuspension of particle class i ;
- ρ = water density;
- τ_{Ci} = critical bed stress for resuspension of particle class i ;
- τ_{LW}, τ_{RW} = surface wave-induced bed stress on the left and right side of centerline;
- τ_U = current-induced bed stress; and
- ω = significant wave frequency.

References

- Ahlfeld, D., Jaquin, A., Tobiason, J., and Mas, D. (2003). "Case study: Impact of reservoir stratification on interflow travel time." *J. Hydraul. Eng.*, 129(12), 966–975.
- Bloesch, J. (1995). "Mechanisms, measurement and importance of sediment resuspension in lakes." *Mar. Freshwater Res.*, 46(1), 295–304.

- Chung, S. W., and Gu, R. (1998). "Two-dimensional simulations of contaminant transport in stratified reservoir." *J. Hydraul. Eng.*, 124(7), 704–711.
- Cole, T. M., and Wells, S. A. (2002). "A two-dimensional, laterally-averaged, hydrodynamic and water quality model, Version 3.1." *Instruction Report E-03-1*, U.S. Army Engineering and Research Development Center, Vicksburg, MS.
- Dean, R. G., and Dalrymple, R. A. (1991). *Water wave mechanics for engineers and scientists*, World Scientific, Hackensack, NJ.
- Effler, S. W., et al. (2008). "Insights for the structure of a reservoir turbidity model from monitoring and process studies." *Lake Reservoir Manage.*, 24(1), 69–86.
- Effler, S. W., and Matthews, D. A. (2004). "Sediment resuspension and drawdown in a water supply reservoir." *J. Amer. Water Resour. Assoc.*, 40(1), 251–264.
- Effler, S. W., Matthews, D. A., Kaser, J., Prestigiacomo, A., and Smith, D. G. (2006a). "Runoff event impacts on a water supply reservoir: Suspended solids loading, turbid plume behavior, and sediment deposition." *J. Am. Water Resour. Assoc.*, 42(6), 1697–1710.
- Effler, S. W., Peng, F., and Gelda, R. K. (2007). "Size distribution and light scattering features of minerogenic particles in a stream during runoff events." *J. Environ. Eng.*, 133(9), 931–940.
- Effler, S. W., Prestigiacomo, A., Peng, F., and Smith, D. G. (2006b). "Resolution of turbidity patterns from runoff events in a water supply reservoir, and the advantages of in situ beam attenuation measurements." *Lake Reservoir Manage.*, 22(1), 79–93.
- Gelda, R. K., and Effler, S. W. (2007a). "Modeling turbidity in a water supply reservoir: Advancements and issues." *J. Environ. Eng.*, 133(2), 139–148.
- Gelda, R. K., and Effler, S. W. (2007b). "Testing and application of a two-dimensional hydrothermal model for a water supply reservoir: Implications of sedimentation." *J. Environ. Eng. Sci.*, 6(1), 73–84.
- Gelda, R. K., and Effler, S. W. (2008). "Probabilistic model for temperature and turbidity in a reservoir withdrawal." *Lake Reservoir Manage.*, 24(3), 219–230.
- Gelda, R. K., Effler, S. W., Peng, F., Owens, E. M., and Pierson, D. C. (2009). "Turbidity model for Ashokan Reservoir, New York: Case Study." *J. Environ. Eng.*, 135(9), 885–895.
- Grant, W. D., and Madsen, O. S. (1979). "Combined wave and current interaction with a rough bottom." *J. Geophys. Res.*, 84(C4), 1797–1808.
- Gu, R., McCutcheon, S. C., and Wang, P. (1996). "Modeling reservoir density underflow and interflow from a chemical spill." *Water Resour. Res.*, 32(3), 695–705.
- Hawley, N., and Lesht, B. M. (1992). "Sediment resuspension in Lake St. Clair." *Limnol. Oceanogr.*, 37(8), 1720–1737.
- James, R. T., Martin, J., Wool, T., and Wang, P. F. (1997). "A sediment resuspension and water quality model of Lake Okeechobee." *J. Am. Water Resour. Assoc.*, 33(3), 661–680.
- Jin, K. R., and Ji, Z. G. (2004). "Case study: Modeling of sediment transport and wind-wave impact in Lake Okeechobee." *J. Hydraul. Eng.*, 130(11), 1055–1067.
- Lick, W., Lick, J., and Ziegler, C. K. (1994). "The resuspension and transport of fine-grained sediment in Lake Erie." *J. Great Lakes Res.*, 20(4), 599–612.
- Lou, J., Schwab, D. J., Beletsky, D., and Hawley, N. (2000). "A model of sediment resuspension and transport dynamics in southern Lake Michigan." *J. Geophys. Res.*, 105(C3), 6591–6610.
- Luetlich, R. A., Harleman, D. R. F., and Somlyódy, L. (1990). "Dynamic behavior of suspended sediment concentrations in a shallow lake perturbed by episodic wind events." *Limnol. Oceanogr.*, 35(5), 1050–1067.
- Martin, J. L., and McCutcheon, S. C. (1999). *Hydrodynamics and transport for water quality modeling*, Lewis, Boca Raton, FL.
- O'Donnell, D. M., and Effler, S. W. (2006). "Resolution of impacts of runoff events on a water supply reservoir with a robotic monitoring network." *J. Am. Water Resour. Assoc.*, 42(2), 323–335.
- Owens, E. M. (2009). "Observation and simulation of surface waves in two water supply reservoirs." *J. Hydraul. Eng.*, 135(8), 663–670.
- Peng, F., and Effler, S. W. (2007). "Suspended minerogenic particles in a reservoir: Light scattering features from individual particle analysis." *Limnol. Oceanogr.*, 52(1), 204–216.
- Peng, F., Effler, S. W., Pierson, D. C., and Smith, D. G. (2009). "Light-scattering features of turbidity-causing particles in interconnected reservoir basins and an intervening stream." *Water Res.*, 43(8), 2280–2292.
- Pierson, D. C., and Weyhenmeyer, G. A. (1994). "High resolution measurements of sediment resuspension above an accumulation bottom in a stratified lake." *Hydrobiologia*, 284(1), 43–57.
- Prestigiacomo, A. R., Effler, S. W., O'Donnell, D. M., Smith, D. G., and Pierson, D. C. (2008). "Turbidity and temperature patterns in a reservoir and its primary tributary from robotic monitoring: Implications for managing the quality of withdrawals." *Lake Reservoir Manage.*, 24(3), 231–243.
- Schwab, D. J., Bennett, J. R., Liu, P. C., and Donelan, M. A. (1984). "Application of a simple numerical wave prediction model to Lake Erie." *J. Geophys. Res.*, 89(C3), 3586–3592.
- U.S. Environmental Protection Agency (USEPA). (1996) "Safe Drinking Water Act (SDWA)." (<http://water.epa.gov/lawsregs/rulesregs/sdwa/index.cfm#sdwafs>) (May 31, 2011).
- Ziegler, C. K., and Nisbet, B. S. (1995). "Long-term simulation of fine-grained sediment transport in a large reservoir." *J. Hydraul. Eng.*, 121(11), 773–781.

An automated method to monitor lake ice phenology

D.C. Pierson^{1*}†, G. A. Weyhenmeyer², L. Arvola³, B. Benson⁴, T. Blenckner⁵, T. Kratz⁴, D.M. Livingstone⁶, H. Markensten⁷, G. Marzec¹, K. Pettersson⁵, and K. Weathers⁸

¹New York City Department of Environmental Protection, Kingston, New York, USA

²Department of Limnology, Uppsala University, Uppsala, Sweden

³Lammi Biological Station, University of Helsinki, Finland

⁴Center for Limnology, University of Wisconsin, Madison, Wisconsin, USA

⁵Erken Laboratory, Department of Limnology, Uppsala University, Uppsala, Sweden

⁶Swiss Federal Institute of Environmental Science and Technology, Dübendorf, Switzerland

⁷Department of Aquatic Sciences and Assessment, Swedish Agricultural University, Uppsala, Sweden

⁸Cary Institute of Ecosystem Studies, Millbrook, New York, USA

Abstract

A simple method to automatically measure the date of ice-on, the date of ice-off, and the duration of lake ice cover is described. The presence of ice cover is detected by recording water temperature just below the ice/water interface and just above the lake bottom using moored temperature sensors. The occurrence of ice-on rapidly leads to detectable levels of inverse stratification, defined as existing when the upper sensor records a temperature at least 0.1°C below that of the bottom sensor, whereas the occurrence of ice-off leads to the return of isothermal mixing. Based on data from 10 lakes over a total of 43 winter seasons, we found that the timing and duration of inverse stratification monitored by recording temperature sensors compares well with ice cover statistics based on human observation. The root mean square difference between the observer-based and temperature-based estimates was 7.1 d for ice-on, 6.4 d for ice-off, and 10.0 d for the duration of ice cover. The coefficient of determination between the two types of estimates was 0.93, 0.86, and 0.91, respectively. The availability of inexpensive self-contained temperature loggers should allow expanded monitoring of ice cover in a large and diverse array of lakes. Such monitoring is needed to improve our ability to monitor the progression of global climate change, and to improve our understanding of the relationship between climate and ice cover over a wide range of temporal and spatial scales.

For lakes, changes in the timing of ice-on and ice-off, along with changes in the duration of ice cover, have been clearly

*Corresponding author: E-mail: dpierson@dep.nyc.gov

†This paper was originally conceived by Pierson and Weyhenmeyer using data from Lake Erken. Later the paper was expanded to include additional sites, and the remaining co-authors contributed data and assisted in preparing the manuscript. Because of equal contributions the remaining authors are listed alphabetically.

Acknowledgments

This work benefited from use of data from the Global Lake Ecological Observatory Network (GLEON). We thank the field staff at the Erken Laboratory, particularly Björn Matsson, for many years of support and assistance in maintaining the Erken meteorological station and in conducting the water temperature measurements. We also thank the Lake Sunapee Protective Association (LSPA) for developing, funding, and maintaining a GLEON buoy, and for providing us with data. We are thankful for temperature data and ice cover surveys obtained by Allison Bennett, Kim Nezelek, Karen Moore, and Chris Nadeski of the New York City Department of Environmental Protection. We also thank Peter Adams who reviewed an earlier version of the manuscript.

DOI 10:4319/lom.2011.9.74

established as sensitive indicators of climate change (e.g., Magnuson et al. 2000). Long-term trends toward later ice-on and earlier ice-off, presumably associated with global warming, have been detected in Canada (Skinner 1993; Duguay et al. 2006), Finland (Palecki and Barry 1986; Korhonen 2006), Switzerland (Livingstone 1997), and in the New England (Hodgkins et al. 2002) and North Central regions of the United States (Robertson et al. 1992; Johnson and Stefan 2006; Jensen et al. 2007). Simulations of future ice cover dynamics based on Global Climate Model (GCM) output also suggest that the duration of lake ice cover will decrease as result of global warming (Fang and Stefan 1998, 1999; Stefan et al. 1998).

Because changes in the timing and duration of ice cover influence lake biology and biogeochemistry, they can be expected to be an important mechanism through which the effects of global warming are transferred to lake ecosystems (Blenckner 2005). The timing of ice-off has been shown to influence the timing, magnitude, and composition of the phytoplankton spring bloom (Pettersson 1990; Adrian et al. 1999; Weyhenmeyer et al. 1999), and winter oxygen concentrations

(Fang and Stefan 1997; Wiedner and Nixdorf 1998; Phillips and Fawley 2002). The timing of ice-out may also influence spring and summer lake water temperatures (Austin and Colman 2007, 2008), with longer-term effects on hypolimnetic temperatures following thermal stratification (Livingstone 1993; Gerten and Adrian 2001; Straile *et al.* 2003).

Ice phenology data are still most commonly recorded by visual observation. The use of satellite remote sensing for this purpose is becoming more and more common (Wynne *et al.* 1996; Wynne *et al.* 1998; Latifovic and Pouliot 2007), and it has been shown that satellite-derived estimates of ice cover phenology, particularly ice loss, are close to observer-based estimates (Wynne *et al.* 1996). The utility of satellite remote sensing, however, is limited by the occurrence of cloud cover and by the fact that it is generally only suitable for large lakes (e.g., >10 km²). While ice phenology is strongly related to global and regional climatic forcing, local conditions such as topography, lake basin morphometry, and snow accumulation patterns also play a role (Williams *et al.* 2004). Monitoring the ice cover of a large number of lakes over a large spatial extent would therefore, allow the mechanisms responsible for local variations in ice cover to be better understood, and would also allow estimates of regional variations in ice cover to be made that more adequately account for local variability. When surveying regional variations in ice cover, it can be especially important to include lakes of all size and remote lakes in sparsely populated areas where dedicated human observers are not available and where frequent sampling is not possible.

To increase the consistency of ice cover measurements, and to make it possible to record routinely the timing and duration of ice cover on large numbers of lakes, a simple automated method to detect ice cover is needed. We demonstrate the utility of a method based on automatic water temperature measurements that uses the timing of the beginning and end of inverse thermal stratification as an indicator of the timing of ice-on and ice-off. This simple method for estimating the timing and duration of ice cover is tested on a number of lakes and reservoirs, most of which are part of the Global Lakes Ecological Observatory Network (GLEON; www.gleon.org). Given the simplicity of the method, the availability of inexpensive autonomous temperature loggers, and the clear need for expanded lake ice monitoring, we suggest that such temperature-based ice-phenology measurements can supplement present efforts to monitor lake ice. The purpose of this article is to systematically compare estimates of the onset, loss, and duration of ice cover based on the proposed temperature-based estimation method and estimates based on visual observation. We also examine the effects of using two different temperature sensor deployments with the proposed temperature-based method; a surface temperature sensor moored at a shallow depth that freezes into the ice cover, or a surface sensor moored just below the maximum depth of the ice.

Materials and procedures

The lakes and reservoirs included in this study are listed in Table 1. All have systems for recording lake water temperatures automatically that are deployed during the winter ice season, and all have independent, observer-based estimates of the timing and duration of lake ice cover. For all lakes, relevant meteorological data, such as wind speed, solar radiation, and air temperature, are available that are measured either on the same monitoring buoy that carries the water temperature measuring system or at a nearby meteorological station. At Lake Erken, Sweden, from which much of our data were obtained, the water temperature is measured at 3 depths (1.0, 3.0, and 15 m) using thermocouple sensors that are moored year-round in the lake (Table 2); in addition, there is a permanent lake monitoring station located on a small island approximately 500 m from shore and 100 m from the deepest part of the lake at which a number of routine meteorological measurements are made.

A number of relatively inexpensive (approximately \$150-\$200) autonomous temperature logging systems are commercially available that would be suitable for detecting ice cover as we describe here. Two such systems (manufactured by Vemco and Onset) are used at sites included in this study (Table 2). These systems are hermetically sealed, contain a long-life battery, and are capable of logging water temperature data over at least a six-month period. Once retrieved, data can be downloaded as an optical signal transmitted through the temperature logger housing. The great advantage of these systems is that they can be rapidly deployed and do not require underwater cabling and an onshore data logger installation, as used at Lake Erken. These systems could, therefore, be deployed in large numbers of lakes to provide a better understanding of local and regional variability in lake ice phenology.

Two different mooring configurations were used at the different lake sites listed in Table 1. At some sites, the uppermost sensor was deployed at a depth just below the expected maximum depth of ice cover. In Lake Erken, for example, the uppermost sensor was permanently moored at a depth of 1 m (Fig. 1), so ice movements had no effect on the installation. Sensors at Lake Erken have performed reliably without maintenance for periods of up to 10 y. An alternative is to place one sensor at a shallow depth (e.g., 0.1 m) and for the mooring buoy to be deployed at, rather than below, the surface. This mooring configuration is more precise in detecting the timing of ice-on and ice-off, but requires greater maintenance, and also requires sensors that can withstand being frozen into the ice. It is well suited for autonomous temperature loggers, as the recorded data must be retrieved from these regularly, allowing the mooring to be checked and redeployed immediately after data retrieval.

From the water temperature time series, the period of ice cover can be discerned as the period during which inverse thermal stratification is continually recorded. The boundary between isothermal and inversely stratified conditions is quite

Table 1. Details of ice phenology estimates. Mean values are calculated for both estimates of onset, loss, and duration of ice cover and the difference between methods. Means also show 95% confidence interval. The root mean square of the differences is calculated.

Lake	Location	Winter	Data from temperature sensors			Visual observations			Observed determined minus temperature determined estimates		
			Onset	Loss	Duration	Onset	Loss	Duration	Onset	Loss	Duration
Erken	Sweden	1988-1989	2-Dec-88	5-Feb-89	65	1-Dec-88	3-Feb-89	64	-1	-2	-1
Erken	Sweden	1989-1990	6-Dec-89	7-Dec-89	6-Feb-90	61	1				
Erken	Sweden	1990-1991	14-Jan-91	27-Mar-91	72	11-Jan-91	21-Mar-91	69	-3	-6	-3
Erken	Sweden	1991-1992	23-Jan-92	22-Mar-92	59	25-Jan-92	12-Mar-92	47	2	-10	-12
Erken	Sweden	1992-1993	18-Mar-93	21-Feb-93	18-Mar-93	25		0			
Erken	Sweden	1995-1996	29-Nov-95	16-Apr-96	139	28-Nov-95	15-Apr-96	139	-1	-1	0
Erken	Sweden	1996-1997	20-Dec-96	18-Mar-97	88	18-Dec-96	13-Mar-97	85	-2	-5	-3
Erken	Sweden	1997-1998	2-Feb-98	1-Feb-98	4-Apr-98	62	-1				
Erken	Sweden	1998-1999	20-Dec-98	4-Apr-99	105	20-Dec-98	9-Apr-99	110	0	5	5
Erken	Sweden	1999-2000	22-Dec-99	27-Mar-00	96	29-Dec-99	16-Apr-00	109	7	20	13
Erken	Sweden	2000-2001	13-Jan-01	9-Apr-01	86	19-Jan-01	9-Apr-01	80	6	0	-6
Erken	Sweden	2001-2002	23-Dec-01	29-Mar-02	96	15-Dec-01	4-Apr-02	110	-8	6	14
Erken	Sweden	2002-2003	7-Dec-02	8-Dec-02	5-Apr-03	118	1				
Erken	Sweden	2003-2004	30-Dec-03	1-Apr-04	93	30-Dec-03	14-Apr-04	106	0	13	13
Erken	Sweden	2004-2005		8-Apr-05		27-Jan-05	11-Apr-05	74		3	
Erken	Sweden	2005-2006	4-Jan-06	22-Apr-06	108	1-Jan-06	24-Apr-06	113	-3	2	5
Erken	Sweden	2006-2007	27-Jan-07	24-Mar-07	56	24-Jan-07	1-Apr-07	67	-3	8	11
Erken	Sweden	2008-2009	6-Jan-09	10-Apr-09	94	3-Jan-09	14-Apr-09	101	-3	4	7
Mälaren/Galten	Sweden	1998-1999	22-Nov-98	10-Apr-99	139	19-Nov-98	8-Apr-99	140	-3	-2	1
Mälaren/Galten	Sweden	1999-2000	15-Dec-99	26-Mar-00	102	14-Dec-99	22-Mar-00	99	-1	-4	-3
Mälaren/Galten	Sweden	2000-2001	12-Jan-01	14-Jan-01	2						
Mälaren/Ekoln	Sweden	1998-1999	11-Jan-99	1-Apr-99	80	11-Jan-99	8-Apr-99	87	0	7	7
Mälaren/Ekoln	Sweden	1999-2000	31-Dec-99	23-Apr-00	114	31-Dec-99	17-Apr-00	108	0	-6	-6
Mälaren/Ekoln	Sweden	2000-2001	10-Jan-01	14-Jan-01	4						
Pääjärvi	Finland	2000-2001	4-Jan-01	30-Apr-01	116	20-Jan-01	25-Apr-01	95	16	-5	-21
Valkea-kotinen	Finland	2002-2003		26-Apr-03		18-Oct-02	7-May-03	201		11	
Valkea-kotinen	Finland	2003-2004	10-Nov-03	21-Nov-03	28-Apr-04	159	11				
Valkea-kotinen	Finland	2004-2005	16-Nov-04	16-Nov-04	26-Apr-05	161	0				
Sparkling	Wisconsin	1999-2000	8-Dec-99	2-Apr-00	116	16-Dec-99	2-Apr-00	108	8	0	-8
Sparkling	Wisconsin	2000-2001	28-Nov-00	14-Apr-01	137	2-Dec-00	22-Apr-01	141	4	8	4
Sparkling	Wisconsin	2001-2002	13-Dec-01	24-Apr-02	132	25-Dec-01	18-Apr-02	114	12	-6	-18
Sparkling	Wisconsin	2002-2003	24-Nov-02	22-Apr-03	149	26-Nov-02	24-Apr-03	149	2	2	0
Sparkling	Wisconsin	2003-2004	21-Nov-03	20-Apr-04	151	2-Dec-03	17-Apr-04	137	11	-3	-14
Sparkling	Wisconsin	2004-2005	21-Nov-04	10-Apr-05	140	16-Dec-04	14-Apr-05	119	25	4	-21
Sparkling	Wisconsin	2005-2006	20-Nov-05	2-Dec-05	13-Apr-06	132	12				
Trout Bog	Wisconsin	2003-2004	12-Nov-03	21-Apr-04	161	8-Nov-03	20-Apr-04	164	-4	-1	3
Trout Bog	Wisconsin	2004-2005	19-Nov-04	13-Apr-05	145	23-Nov-04	14-Apr-05	142	4	1	-3
Trout Bog	Wisconsin	2005-2006	28-Nov-05	21-Nov-05	12-Apr-06	142	-7				
Ashokan Reservoir	New York	2004-2005	19-Jan-05	31-Mar-05	71	14-Jan-05	1-Apr-05	77	-5	1	6
Rondout Reservoir	New York	2004-2005	16-Jan-05	9-Apr-05	83	24-Jan-05	4-Apr-05	70	8	-5	-13
Rondout Reservoir	New York	2006-2007	14-Feb-07	27-Mar-07	41	12-Feb-07	28-Mar-07	44	-2	1	3
Rondout Reservoir	New York	2007-2008	9-Feb-08	22-Mar-08	42	2-Feb-08	31-Mar-08	58	-7	9	16
Lake Sunapee	New Hampshire	2007-2008	29-Nov-07	22-Apr-08	145		23-Apr-08	1			
Mean (all data)			20 Dec	6 Apr		23 Dec	7 Apr		2.1	1.5	-0.8
			± 8.3d	± 5.4d		± 8.3d	± 5.5d		± 2.1	± 2.1	± 3.6'
RMS Difference (all data)									7.1	6.4	10.0

Table 2. Temperature sensor and data logger information.

Site	Logger and sensor information	Temperature resolution	Upper and lower depths (m)
Lake Erken, Sweden	Campbell Scientific CR10 Thermocouple Temperature Sensors	0.05°C*	1.0, 15.0
Lake Sunapee, New Hampshire	Campbell CR10 and Apprise Technology Templine	0.1°C†	0.1, 13.0
Wisconsin Lakes	Apprise Technology. TempLine	0.1°C†	
Sparkling			0.01, 18.0
Trout Bog			0.01, 7.0
New York City Reservoirs	Vemco Minilog 12 bit self-contained temperature logger	0.015°C†	
Ashokan			0.5, 48.0
Rondout			3.0, 43.0
Finland Lakes	Vemco Minilog 8 bit self-contained temperature logger	0.2°C†	
Pääjärvi			0.2, 40.0
Valkea-kotinen			0.5, 4.5
Lake Mälaren Basins, Sweden	Onset Stow Away, 8 bit self-contained temperature logger	0.2°C†	
Ekoln			1.0, 28.0
Galten			1.0, 8.75

*Based on actual measurements—includes noise resulting from a long cable length to 15 m sensor

†Manufacturer specifications

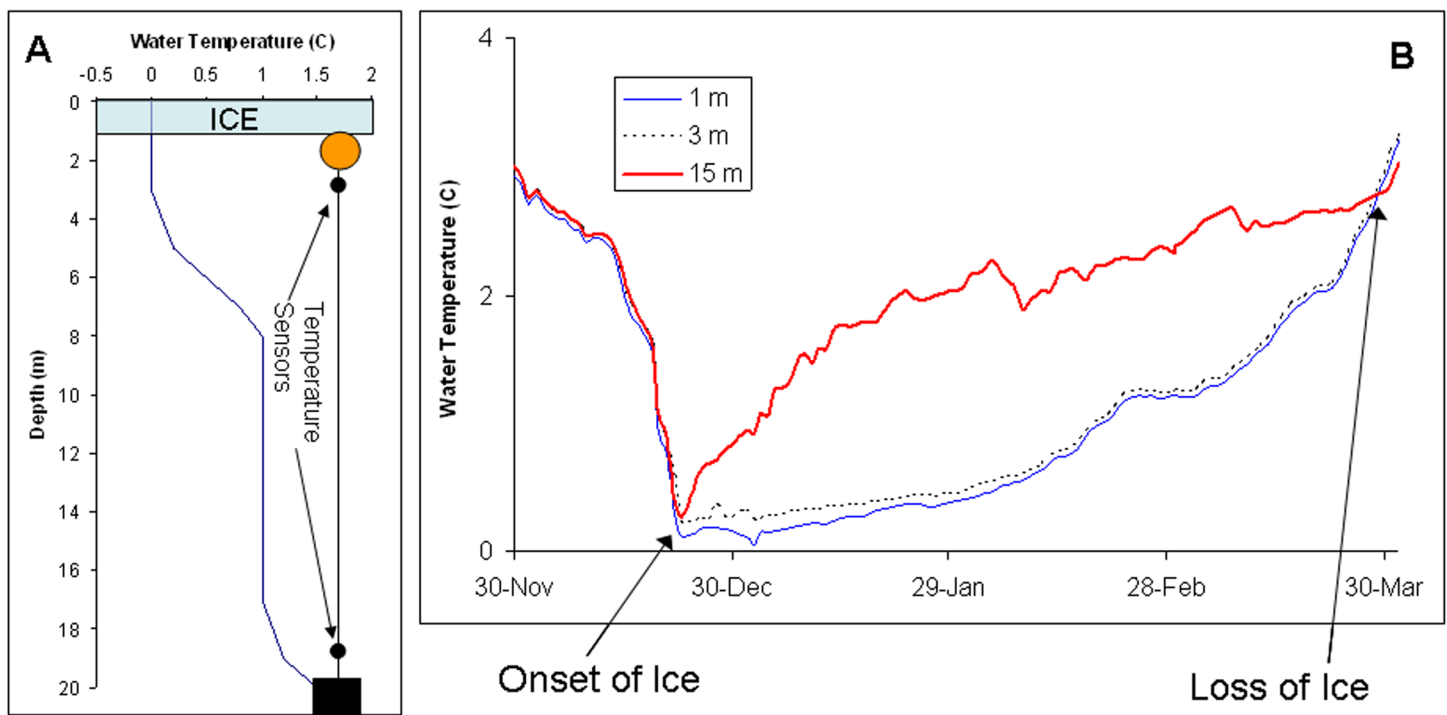


Fig. 1. (A) Illustration of mooring of temperature sensors to detect the presence and absence of ice cover. (B) Temperature recordings from sensors moored over the winter of 2001–2002 in Lake Erken, Sweden.

clear, and from temperature time-series such as those illustrated in Fig. 1B, it is possible to estimate the timing and duration of ice cover by simple visual inspection. However, to maintain the greatest possible consistency when comparing different time periods and different sites, we used a simple algorithm to define the presence of ice cover. In most cases,

lakes were classified as ice-covered any time the temperature difference between the bottom and top temperature sensors was greater than 0.1°C. The top sensor used in these calculations was always the shallowest deployed and varied in depth from 0.01–3.0 m at different sites (Table 2). This method can detect ephemeral ice formation when ice forms for relatively

short periods of time (i.e., days-weeks), or more permanent ice cover that forms for a large portion of the winter (i.e., weeks-months), and which is characteristic of all of the lakes in Table 1. Inverse stratification also can occur briefly without the development of ice. This is normally a short-term phenomenon (hours-days) that could give a false indication of ephemeral ice cover. Permanent ice cover was considered to occur over the longest continuous period during any winter when the temperature difference exceeded the 0.1°C threshold. The purpose of separating permanent ice cover from ephemeral ice cover was to allow comparisons with the available observer-based estimates, which record continuous ice cover as a single set of ice-on and ice-off dates. For lakes with 8-bit loggers, which have a temperature resolution of 0.2°C (Table 2), the same methodology was used, but ice-cover was considered to be present when the temperature difference exceeded 0.4°C rather than 0.1°C. Whereas the higher resolution temperature measurements are preferable, tests using both thresholds with data from Lake Erken found that, on average, the 0.4°C threshold resulted in the onset of ice cover being estimated 4 d later and the loss of ice cover being estimated 3 d earlier, showing that the lower resolution data could produce meaningful but less precise estimates.

Independent estimates of the calendar dates of ice-on and ice-off were obtained by visual observation at all of the sites listed in Table 1. The exact protocol for making such observations varied from lake to lake, often depending on the existence of a regular lake sampling program (the New York City Reservoirs and Wisconsin lakes), on the proximity of the lake to a field station/research lab (Wisconsin Lakes, Lake Erken, and Lake Pääjärvi), or on interested local observers (Lake Sunapee, Lake Mälaren). Factors such as the frequency of observation and the perception of what constitutes ice cover (i.e., partial as opposed to complete freeze over) adds uncertainty to the data used to verify our temperature-based calculations of the timing of ice-on and ice-off. There are errors in both temperature-derived and observer-based estimates of ice cover, and there are no clear trends in Table 1 suggesting one estimate is more accurate than the other. For example, one of the largest differences in Table 1 is for Lake Pääjärvi, the site of a university field station where visual observations are frequently made, whereas relatively small differences were obtained for Lake Mälaren where the lower resolution temperature sensors were used. Consequently, when comparing these estimates, we refer to differences between them rather than an error in either of the methods.

To provide a quantitative index of the difference between observer and temperature based estimates of ice phenology, mean values of temperature based and observation based estimates of the onset loss and duration of ice cover are given in Table 1. The mean, as well as the root mean square (RMS) of the differences between yearly estimates of ice-on, ice-off and ice cover duration, are also given in the same table. In the case of Lake Erken, we also compare the trend in ice cover derived

from both visual observation and temperature measurements with local variations in air temperature measured at the lake.

Assessment and discussion

The data in Fig. 1B illustrate how ice cover can be detected by placing two water temperature sensors in a lake as described above. Ice-on is characterized by a separation of the water temperatures, as the lake surface cools to approach 0°C and the bottom temperature gradually increases as a result of sediment heating. Loss of ice cover leads to a breakdown of this temperature gradient and a return to isothermal conditions. This method is hardly novel; various studies have adopted a similar approach, making the tacit or explicit assumption that the behavior of water temperatures measured using single or multiple thermistors are strongly linked to the timing of ice-on and ice-off (Schmidt et al. 2004; Thompson et al. 2005; Šporka et al. 2006). We are not, however, aware of a systematic comparison of temperature-based and observer-based ice phenology data as presented here.

The timing of ice-on, timing of ice-off, and the duration of ice cover were calculated for all 10 sites listed in Table 1, for all years for which both observer-based ice phenology estimates were available and temperature-based ice phenology estimates could be calculated. The observer-based and temperature-based ice phenology estimates correspond well (Fig. 2), although in some cases, there were relatively large positive or negative residuals between the two estimates (Table 1). These tended to cancel out so that over the 43 cases examined the average observation-based and temperature-based estimate of the onset and loss of ice cover agreed within 1-2 d. The RMS difference between the two estimates ranged from 6–10 d, and a linear regression between the two estimates yielded a gradient that was not statistically different ($P < 0.01$) from a 1:1 relationship (Fig. 2).

For lakes where the upper sensor was moored below the ice (Table 2), the relationship describing the timing of ice-off showed several cases where there were relatively large positive differences (Table 1), suggesting a bias that would lead to the temperature-based estimates indicating an earlier ice-off date than the observer-based estimates. Estimates of the duration of ice cover encompass discrepancies associated with both ice-on and ice-off, and as a result show a somewhat greater RMS difference than either of these (Table 1).

One possible explanation for the apparent bias toward early estimates of the timing of ice-off exhibited by the proposed temperature method can be offered based on the temperature time-series of three sensors in Lake Sunapee (Fig. 3), where the uppermost sensor was allowed to freeze into the ice. From these data, it is apparent that even though the lake became isothermal between 0.5 m and the lake bottom on 7 April 2008 (an indicator similar to that used at Lake Erken for the occurrence of ice-off), inverse stratification was still detectable between 0.1 and 0.5 m. It took an additional 15 d for this stratification just below the decaying ice cover to disappear on

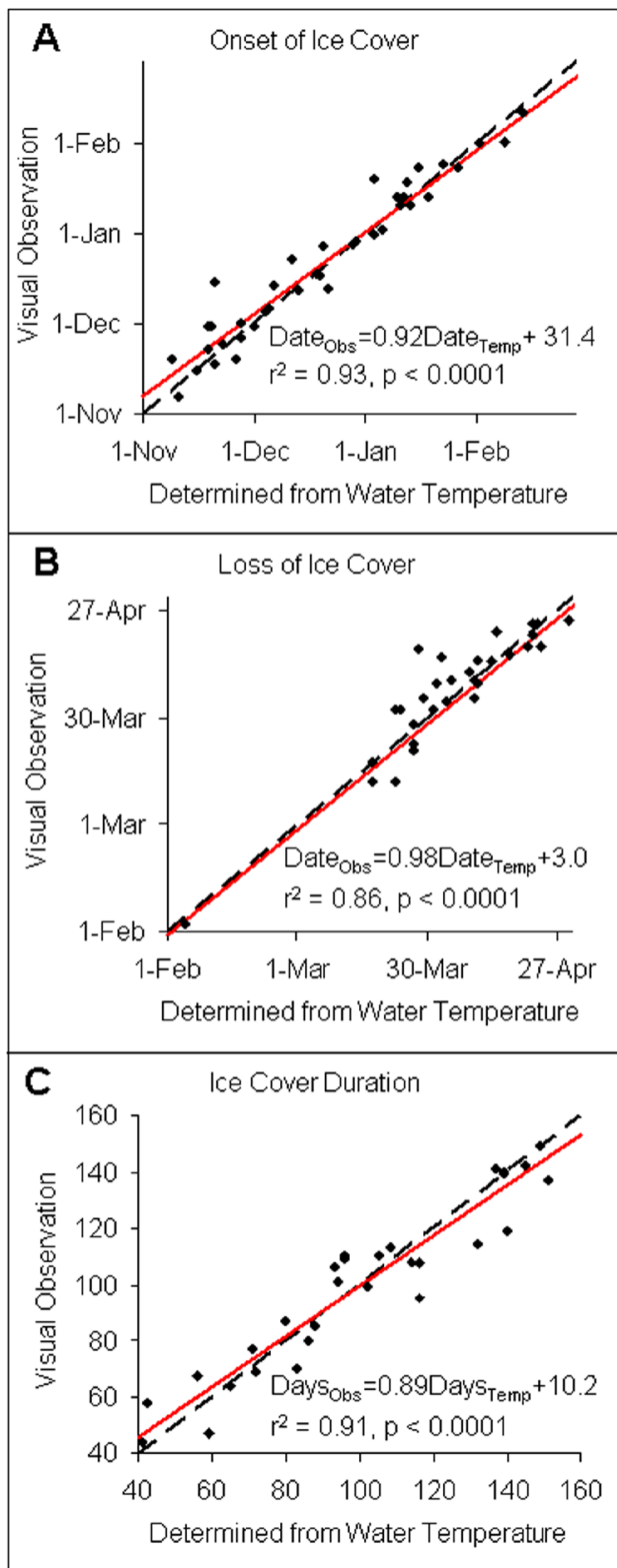


Fig. 2. Comparison between temperature-based and observer-based ice phenology estimates. (A) Date of ice-on. (B) Date of ice-off. (C) Duration of ice cover (days). Dashed black line shows the 1:1 relationship and red line shows linear regression relationships. In all cases the slope of the regression was not significantly different from 1 (*t*-test; $P < 0.01$).

22 April 2008, and the ice-off date estimated using the 0.1 m temperature sensor was within 1 d of the observed ice-off date (Table 1). Estimates of land snow cover in the vicinity of Lake Sunapee (<http://www.nohrsc.noaa.gov>) suggest that snow depth ranged between trace levels and 5 cm on 4 April 2008, and that the area was completely free of snow by 10–11 April 2008. It has been previously documented (Kelley 1997) that in the absence of snow, solar radiation passing through the ice will lead to warming and convective mixing below the ice. This is apparently what happened in Lake Sunapee (Fig. 3). As the water temperature at 0.1 m increased to above 0°C, only the upper 0.5 m of the water column remained inversely stratified. The remaining water from 0.5m–13 m warmed over time and remained isothermal, suggesting convective mixing. The period when the lake was isothermal in all but the upper most 0.5 m is shown in Fig. 3A, and detailed meteorological data from this time are shown in Fig. 3B–C. During this time, it was unusually sunny and calm. Solar radiation levels were often near the maximum that could be expected, and the air temperature was well above freezing. Wind levels during this period were relatively low, which allowed the ice cover to decay slowly.

In addition to Lake Sunapee, there are nine additional data sets in Table 1 that contain data from both a shallow (0.01–0.2 m) sensor and a sensor at 1 m depth. The differences in the timing of ice-on and ice-off as estimated using the two different surface sensor depths are shown in Fig. 4. These data show that estimation of the timing of ice-on is not affected by the depth of the upper sensor, and further suggest that the timing of ice-off can at times be underestimated using a sensor at 1 m depth. For the data in Fig. 4, the date of ice-off would be underestimated by more than a week in 3 of 10 cases.

The underestimation of the date of ice-off does not always occur as shown by Fig. 4, presumably since ice-off, especially in large lakes, often occurs during windy conditions that lead to more rapid break-up and vigorous mixing. There are many cases in Table 1 where the date of ice-off closely matches visual observations, even though a shallow surface sensor was not used. However, the phenomenon illustrated by Figs. 3 and 4 can explain the apparent bias toward earlier ice-off dates in the temperature-based estimates shown in Fig. 2B. For this reason, we recommend that, whenever possible, a sensor be deployed at a shallow depth so that it will be frozen into the ice. For all lakes for which 0.01–0.2 m data were available (Table 2), this shallow sensor was used to calculate the temperature-based ice phenology estimates in Table 1. Biases, such as those illustrated in Fig. 4, therefore, only exist in Table 1 for cases where the upper sensor was at a deeper depth (0.5–3.0 m).

A second source of uncertainty in both observational and temperature-based estimates of ice cover is related to the fact that lakes (particularly large lakes) do not always completely freeze over or become ice free during a short time interval. In some cases, the onset or loss of ice may occur over a period of

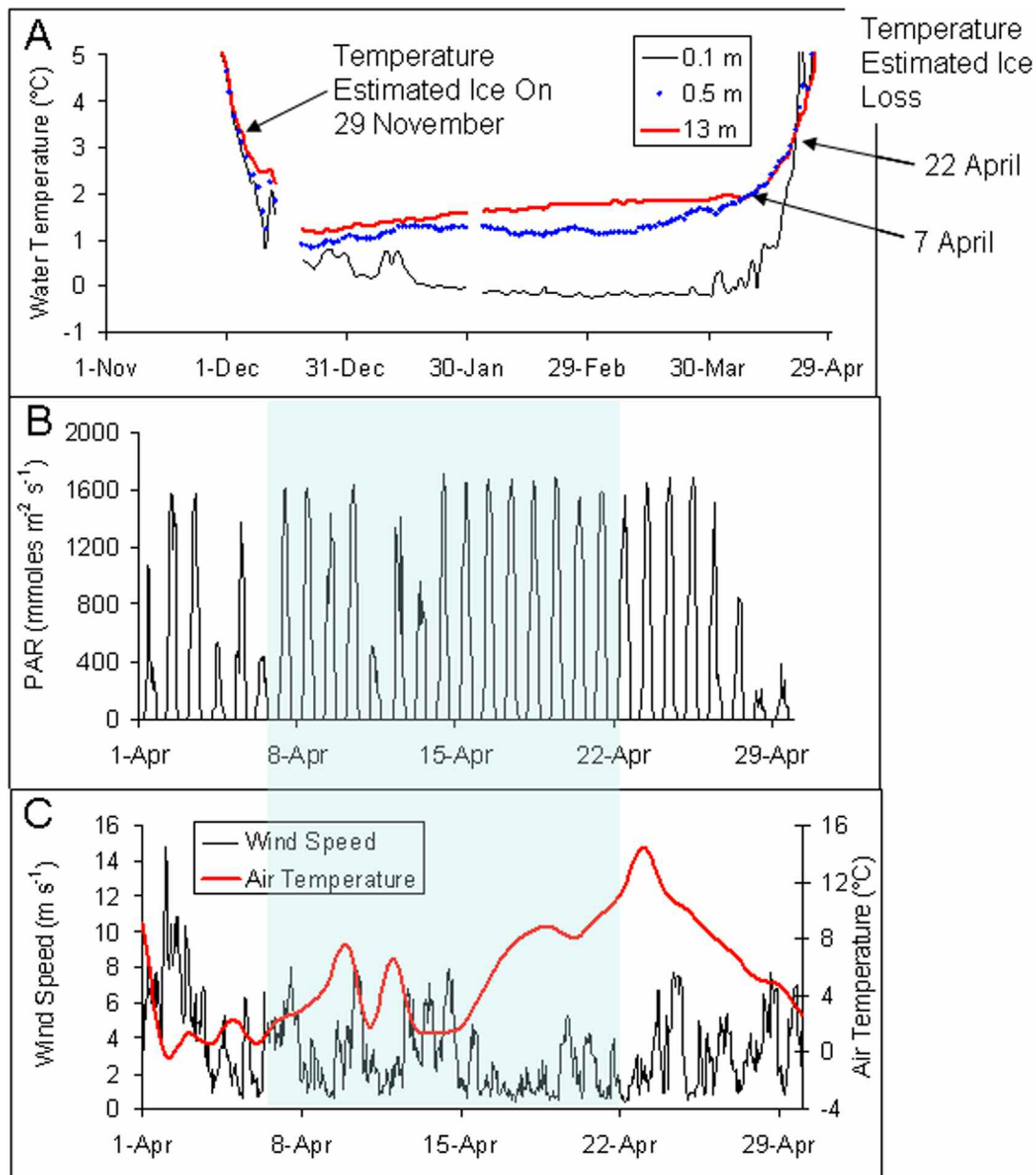


Fig. 3. (A) Example of under-ice temperature measurements made in Lake Sunapee, New Hampshire, from 2007 Nov to 2008 Apr. Data are shown from both a shallow surface sensor that froze into the ice (black solid line) and a sensor moored just below the ice cover (dashed blue line). (B) Incoming photosynthetically active radiation (PAR, hourly). (C) Wind speed (hourly) and air temperature (daily means) measured during April 2008. The shaded portions of B and C correspond to the 7 Apr 2008–22 Apr 2008 period shown in A.

a week or more, adding uncertainty to observer-based estimates because there may be differences in the perception of what constitutes “complete” ice cover, or in the case of temperature-based estimates, uncertainty may result from the placement of the sensors relative to the location of ice and open water. Such uncertainty must account for some of the variations between temperature- and observer-based estimates of ice cover in Table 1. To reduce measurement uncertainty in large lakes, or lakes that are known to freeze unevenly, we would suggest deploying multiple measurement buoys.

Utility of temperature-based estimates of ice cover

Verification of the temperature-based ice phenology estimates is difficult because the data used for comparison are based on human observations, which in themselves may be in error because of differences in perception, or more likely, differences in the frequency of measurement and availability of dedicated observers. Our results (Fig. 2) show that the temperature-based estimates are comparable with observer-based estimates, although at times there can be discrepancies between the two. It would not be appropriate to call such discrepancies

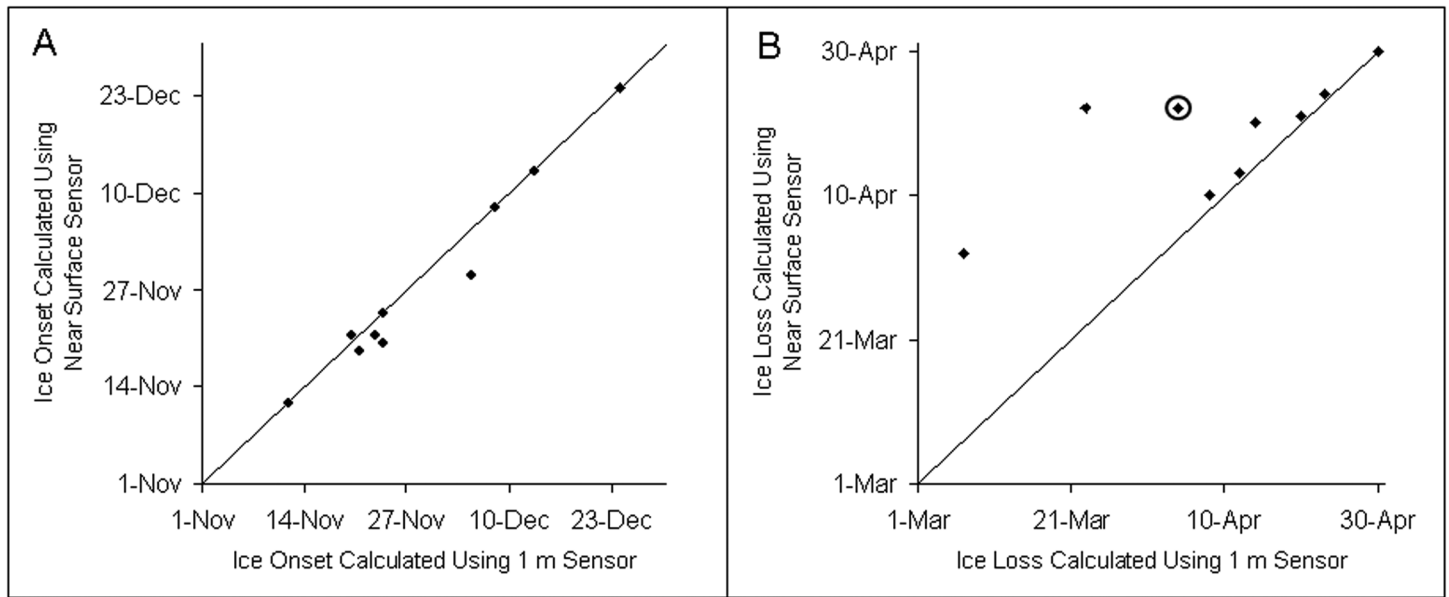


Fig. 4. Estimation of the onset (A) and loss (B) of ice cover calculated using the proposed temperature method, but with near surface versus 1-m surface sensor. The line shows the 1:1 correspondence between estimates; the circled point in (B) is Lake Sunapee.

errors in either measurement technique, because neither temperature-based nor observer-based estimates can be considered to give true measures of the timing of ice-on and ice-off, as both are subject to error.

The value of the automated temperature-based estimates can also be judged by their ability to show the same long-term trends in ice phenology that have already been shown to exist in observer-based estimates. If measurements based solely on water temperature are able to produce the same trend as data collected by more labor-intensive visual observations, this would clearly indicate that the proposed temperature-based method has practical use. To test this assumption, we made use of data collected from Lake Erken and examine trends in duration of ice cover and its relationship to measurements of air temperature made at the same site over the time period when both temperature-based and observer-based estimates of ice duration were available. The relationship between ice cover duration and cumulative negative degree days (Fig. 5) is well described using either temperature-based or observer-based estimates of ice cover. Analysis of covariance found that the linear trend lines associated with the two data sets could not be statistically distinguished from one another ($P \sim 0.5$). This example clearly verifies the value of the temperature-based estimates of ice cover duration, since estimation of ice cover duration by either method would produce essentially the same trend with air temperature.

Comments and recommendations

A simple method to automatically determine the timing of ice-on, the timing of ice-off, and the duration of lake ice cover is described that makes use of water temperature mea-

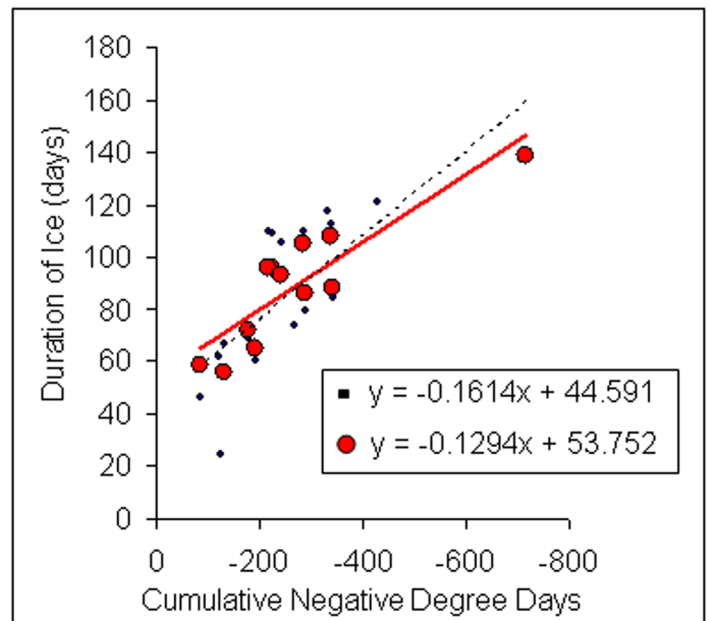


Fig. 5. Relationship between duration of ice cover and cumulative negative degree days during the winter measured at Lake Erken, Sweden. Ice cover statistics are either derived from observations (small black points) or temperature measurements (large red points). The regression line derived from observation-based ice duration is shown as a dashed black line, while the regression line derived from temperature-based ice duration is shown as a solid red line.

surements. The temperature-based estimates were compared with observation-based estimates for 43 winter seasons using data from 10 lakes and reservoirs. RMS differences between the

two estimates calculated over the entire data set were 7.1 d for the timing of ice-on, 6.4 d for the timing of ice-off, and 10.0 d for the duration of ice cover. Compared with observer-based estimates, temperature-based estimates of the date of ice-off can at times show a bias toward earlier dates. This is likely a consequence of convective mixing under the decaying ice cover, and the bias can be eliminated by using a shallow sensor that freezes into the ice. Ice phenology estimates made by the proposed temperature based method show similar differences to observations as estimates based on satellite remote sensing (Wynne et al. 1996), however many of the lakes studied here would be too small for measurement by remote sensing.

The proposed method could be used in regional studies of large numbers of lakes to better document temporal and spatial changes in ice phenology. This would lead to a better understanding of the factors that influence variations in lake ice cover, and would allow long term trends in lake ice cover to be examined in the context of more robust estimates of local and regional variability.

References

- Adrian, R., N. Walz, T. Hintze, S. Hoe.g., and R. Rusche. 1999. Effects of ice duration on plankton succession during spring in a shallow polymictic lake. *Freshw. Biol.* 41:621-632 [doi:10.1046/j.1365-2427.1999.00411.x].
- Austin, J. A., and S. M. Colman. 2007. Lake Superior summer water temperatures are increasing more rapidly than regional air temperatures: A positive ice-albedo feedback. *Geophys. Res. Lett.* 34:L06604 [doi:10.1029/2006GL029021].
- Austin, J., and S. Colman. 2008. A century of temperature variability in Lake Superior. *Limnol. Oceanogr.* 53:2724-2730 [doi:10.4319/lo.2008.53.6.2724].
- Blenckner, T. 2005. A conceptual model of climate-related effects on lake ecosystems. *Hydrobiologia* 533:1-14 [doi:10.1007/s10750-004-1463-4].
- Duguay, C. R., T. D. Prowse, B. R. Bonsal, R. D. Brown, M. P. Lacroix, and P. Menard. 2006. Recent trends in Canadian lake ice cover. *Hydrol. Proc.* 20:781-801 [doi:10.1002/hyp.6131].
- Fang, X., and H. G. Stefan. 1997. Simulated climate change effects on dissolved oxygen characteristics in ice-covered lakes. *Ecol. Model.* 103:209-229 [doi:10.1016/S0304-3800(97)00086-0].
- and ———. 1998. Potential climate warming effects on ice covers of small lakes in the contiguous U.S. *Cold Reg. Sci. Technol.* 27:119-140 [doi:10.1016/S0165-232X(97)00027-X].
- and ———. 1999. Projections of climate change effects on water temperature characteristics of small lakes in the contiguous U.S. *Clim. Change* 42:377-412 [doi:10.1023/A:1005431523281].
- Gerten, D., and R. Adrian. 2001. Differences in the persistency of the North Atlantic Oscillation signal among lakes. *Limnol. Oceanogr.* 46:448-455 [doi:10.4319/lo.2001.46.2.0448].
- Hodgkins, G. A., I. C. James, and T. G. Huntington. 2002. Historical changes in lake ice-out dates as indicators of climate change in New England, 1850-2000. *Int. J. Climatol.* 22:1819-1827 [doi:10.1002/joc.857].
- Jensen, O. P., B. J. Benson, J. J. Magnuson, V. M. Card, M. N. Futter, P. A. Soranno, and K. M. Stewart. 2007. Spatial analysis of ice phenology trends across the Laurentian Great Lakes region during a recent warming period. *Limnol. Oceanogr.* 52:2013-2026 [doi:10.4319/lo.2007.52.5.2013].
- Johnson, S. L., and H. G. Stefan. 2006. Indicators of climate warming in Minnesota: Lake ICE covers and snowmelt runoff. *Clim. Change.* 75:421-453 [doi:10.1007/s10584-006-0356-0].
- Kelley, D. E. 1997. Convection in ice-covered lakes: effects on algal suspension. *J. Plankton Res.* 19:1859-1880 [doi:10.1093/plankt/19.12.1859].
- Korhonen, J. 2006. Long-term changes in lake ice cover in Finland. *Nord. Hydrol.* 37:347-363 [doi:10.2166/nh.2006.019].
- Latifovic, R., and D. Pouliot. 2007. Analysis of climate change impacts on lake ice phenology in Canada using the historical satellite data record. *Remote Sens. Environ.* 106:492-507 [doi:10.1016/j.rse.2006.09.015].
- Livingstone, D. M. 1993. Temporal structure in the deep-water temperature of four Swiss lakes: a short-term climatic change indicator? *Verh. Internat. Verein. Limnol.* 25:75-81.
- . 1997. Break-up dates of alpine lakes as proxy data for local and regional mean surface air temperatures. *Clim. Change* 37:407-439 [doi:10.1023/A:1005371925924].
- , and others. 2000. Historical trends in lake and river ice cover in the Northern Hemisphere. *Science* 289:1743-1746 [doi:10.1126/science.289.5485.1743].
- Palecki, M. A., and R. G. Barry. 1986. Freeze-up and break-up of lakes as an index of temperature changes during the transition seasons: A case study for Finland. *J. Clim. Appl. Meteorol.* 25:893-902 [doi:10.1175/1520-0450(1986)025<0893:FUABUO>2.0.CO;2].
- Pettersson, K. 1990. The spring development of phytoplankton in Lake Erken: Species composition, biomass, primary production and nutrient conditions— A review. *Hydrobiologia* 191:9-14 [doi:10.1007/BF00026033].
- Phillips, K. A., and M. W. Fawley. 2002. Winter phytoplankton blooms under ice associated with elevated oxygen levels. *J. Phycol.* 38:1068-1073 [doi:10.1046/j.1529-8817.2002.01044.x].
- Robertson, D. M., R. A. Ragotzkie, and J. J. Magnuson. 1992. Lake ice records used to detect historical and future climatic changes. *Clim. Change* 21:407-427 [doi:10.1007/BF00141379].
- Schmidt, R., C. Kamenik, H. Lange-Bertalot, and R. Klee. 2004. *Fragilaria* and *Staurosira* (Bacillariophyceae) from sediment surfaces of 40 lakes in the Austrian Alps in relation to environmental variables, and their potential for palaeoclimatology. *J. Limnol.* 63:171-189.
- Skinner, W. R. 1993. Lake ice conditions as a cryospheric indi-

- cator for detecting climate variability in Canada, p. 204–240. In R. G. Barry, B. E. Goodison, and E. F. Ledrew [eds.], *Snow Watch 92—detection strategies for snow and ice*. Glaciological data rep. GD-25, World Data Center A.
- _porka, F., D. M. Livingstone, E. Stuchlík, J. Turek, and J. Galas. 2006. Water temperatures and ice cover in lakes of the Tatra Mountains. *Biologia* 61/Suppl. 18:77-90.
- Stefan, H. G., X. Fang, and M. Hondzo. 1998. Simulated climate change effects on year-round water temperatures in temperate zone lakes. *Clim. Change* 40:547-576 [doi:10.1023/A:1005371600527].
- Straile, D., D. M. Livingstone, G. A. Weyhenmeyer, and D. G. George. 2003. The response of freshwater ecosystems to climate variability associated with the North Atlantic Oscillation, pp. 263-279. In J. W. Hurrell, Y. Kushnir, G. Ottersen, and M. Visbeck [eds.], *The North Atlantic Oscillation: Climate significance and environmental impact*. Amer. Geophys. Union, Geophys. Monogr. Ser. Vol. 134.
- Thompson, R., C. Kamenik, and R. Schmidt. 2005. Ultra-sensitive Alpine lakes and climate change. *J. Limnol.* 64:139-152.
- Weyhenmeyer, G. A., T. Blenckner, and K. Pettersson. 1999. Changes of the Plankton Spring Outburst Related to the North Atlantic Oscillation. *Limnol. Oceanogr.* 44:1788-1792 [doi:10.4319/lo.1999.44.7.1788].
- Wiedner, C., and B. Nixdorf. 1998. Success of chrysophytes, cryptophytes and dinoflagellates over blue-greens (cyanobacteria) during an extreme winter (1995/96) in eutrophic shallow lakes. *Hydrobiologia* 369-370:229-235 [doi:10.1023/A:1017054011389].
- Williams, G., K. L. Layman, and H. G. Stefan. 2004. Dependence of lake ice covers on climatic, geographic and bathymetric variables. *Cold Reg. Sci. Technol.* 40:145-164 [doi:10.1016/j.coldregions.2004.06.010].
- Wynne, R. H., J. J. Magnuson, M. K. Clayton, T. M. Lillesand, and D. C. Rodman. 1996. Determinants of temporal coherence in the satellite-derived 1987-1994 ice breakup dates of lakes on the Laurentian Shield. *Limnol. Oceanogr.* 41:832-838 [doi:10.4319/lo.1996.41.5.0832].
- , T. M. Lillesand, M. K. Clayton, and J. J. Magnuson. 1998. Satellite monitoring of lake-ice breakup on the Laurentian Shield (1980-1994). *Photogramm. Eng. Remote Sensing* 64:607-617.

Submitted 29 April 2010

Revised 16 November 2010

Accepted 7 December 2010

Application of SWAT model to assess snowpack development and streamflow in the Cannonsville watershed, New York, USA

Soni M. Pradhanang,^{1*} Aavudai Anandhi,¹ Rajith Mukundan,¹ Mark S. Zion,²
Donald C. Pierson,² Eliot M. Schneiderman,² Adao Matonse¹ and Allan Frei^{1,3}

¹ Institute for Sustainable Cities, City University of New York, New York

² New York City Department of Environmental Protection, Kingston, New York

³ Department of Geography, Hunter College, City University of New York, New York

Abstract:

Snow is an important component of the water resources of New York State and the watersheds and reservoirs of New York City (NYC) water supply. In many of the NYC water supply watersheds the hydrologic regimes of high-elevation headwaters are linked to streamflow and channel processes in low-elevation stream reaches that serve as inputs to water supply reservoirs. To better simulate this linkage there is a need to understand spatial variations in snowpack and snowmelt. Snowmelt hydrology is an important component of the Soil and Water Assessment Tool (SWAT) model in watersheds where spring runoff is strongly affected by melting snow. This study compares model simulated snowpack and snowmelt at different elevation bands with snow survey data available for the Cannonsville reservoir watershed. Simulations examine the effects of parameterising the SWAT snowmelt sub-model using 1, 3, and 5 elevation bands by comparison with measured snow and streamflow. Comparison between measured and simulated snowpack produced correlation coefficients ranging from 0.35 to 0.85. Simulations of both daily and seasonal streamflow, improved when using 3 elevation bands with r^2 of 0.73 and E_{NS} of 0.72. Streamflow simulations showed slightly lower model performance when basin elevation was assumed to be equal to snow survey site elevation, due to the snow survey sites being somewhat biased toward lower elevations. The effect of climate change was also evaluated and showed that under higher air temperatures in future climate change scenarios, SWAT indicated more precipitation falling as rain, increased and earlier snowmelt, and a reduced snowpack leading to a change in the pattern of streamflow, particularly during winter and early spring. Copyright © 2011 John Wiley & Sons, Ltd.

KEY WORDS elevation; snowpack; snowmelt; streamflow; SWAT; climate change

Received 15 July 2010; Accepted 9 May 2011

INTRODUCTION

Snow is an important component of the hydrologic cycle particularly for land areas poleward of about 40° latitude (Adam *et al.*, 2009). Snowmelt is a significant surface water input of importance to many aspects of hydrology including water supply, erosion and flood control (Tarboton *et al.*, 1995). Hence in these regions, knowledge of the amount of snowfall and snow accumulation on the ground (snow cover), as well as their spatial distribution is essential for effective planning, management, and adaptation of water resources to climate change.

The most important snow data that snow hydrologists use is the snowpack snow water equivalent (SWE) (Dingman, 1994) and snowmelt. The SWE is defined as a mass of water contained in the snowpack and is expressed in units identical to precipitation (Paul *et al.*, 1994). The SWE is the measure of snow used in snow runoff analysis to determine the quantity and distribution of snow and it is the primary determinant governing the magnitude of

the snowmelt runoff volume. In a basin during the winter accumulation period, SWE responds, either directly or indirectly, to a variety of meteorological and topographical interactions that influences snow accumulation and distribution. The meteorological factors include air temperature, wind, precipitable water, atmospheric circulation patterns, frontal activity, lapse rate, and stability of the air mass. Topographical factors include elevation, slope, aspect, exposure, and vegetation cover (USACE, 1991).

The properties of fallen snowpack change continuously as a function of energy fluxes, wind, moisture, water vapour, and atmospheric pressure. The processes involved in snowpack development and snowmelt have been widely described (Dingman 1994; Tarboton *et al.*, 1995; Tarboton and Luce, 1996; USACE, 1991; You *et al.*, 2004). Snowmelt is modelled with different approaches from simple regression methods and approaches based only on temperature measurements to physics-based models involving all processes (Ferguson, 1999), or based on an energy balance (Walter *et al.*, 2005; Marks *et al.*, 1999). Owing to simplicity and ease of use, temperature index-based empirical models are

* Correspondence to: Soni M. Pradhanang, Institute of Sustainable Cities, City University of New York, 71 Smith Ave, Kingston, NY 12401, USA.
E-mail: spradh@hunter.cuny.edu

frequently used to estimate snowmelt compared to complex, data intensive energy budget snowmelt models (Zhang *et al.*, 2008).

The spatial variation of snow accumulation and melt processes are high in river basins which have high elevation differences, low temperatures, large areas, and complex topography, (Debele *et al.*, 2009; Zhang *et al.*, 2008). In such regions, there is a need to model these processes in a continuous and distributed way. Correctly modelling snowmelt in a hydrologic model is especially important because incorrectly simulated snowmelt may result in inaccurate predictions of the timing and magnitude of streamflow. (Frankenberger *et al.*, 1999; Fontaine *et al.*, 2002).

The most common approach to achieve distributed snowmelt modelling is to subdivide the basin into zones and/or bands based upon elevation, allowing the model to discretize the snowmelt process based on watershed topography (Rango and Martinec, 1995; Hartman *et al.*, 1999). In order to use the elevation band algorithm, for each sub-basin, the average elevation of each band and the percentage of the sub-basin area within that band are required (Fontaine *et al.*, 2002). For each elevation band, precipitation, snow, soil moisture, etc. are simulated independently; then moisture output from each band is totaled to obtain input into the hydrologic model routines dealing with soil moisture and stream runoff. The snow accumulation, sublimation and melt computed within each elevation band are weight-averaged sub-basinwise (Neitsch *et al.*, 2005). Snowmelt estimation based on the elevation band approach assumes that snowmelt depth in all sub-basins within the same elevation band is constant. While elevation is a dominant factor influencing snow processes, there are other factors that affect snowmelt, such as, land use/land cover, aspect, and slope (Morid *et al.*, 2002).

This study examined the accuracy of the SWAT 2005 model (Neitsch *et al.*, 2005) simulating snowpack SWE and snowmelt influenced stream flow in the Cannonsville watershed, which is part of the NYC water supply. SWAT2005, which uses a simple temperature index method to simulate snow, has been previously used with reasonable success to account for changes in the snowpack by other simple snow models (USACE, 1991). The objectives of this study were:

1. To evaluate the performance of SWAT model's temperature index-based snowmelt algorithm in simulating snowpack. We compared the snowpack output from SWAT 2005 model to the snow survey data collected by the New York City Department of Environmental Protection (NYCEP).
2. To evaluate model performance in predicting daily streamflow using three different distributions of elevation bands: snow survey site elevations, and the SWAT-defaults of 3 and 5 elevation bands.
3. To assess changes in annual snowfall and snowmelt as a result of change in climate using four future climate scenarios.

SITE DESCRIPTION

The Cannonsville watershed is one of New York City's largest drinking water reservoirs and is located in Delaware County in the Catskill region of New York (Figure 1). The major land uses in the 1178 km² Cannonsville watershed are forests (59% of the land area), pasture (26%) and succession farmland (10%). Mean annual precipitation at the Walton, NY climate station is about 1100 mm/yr, of which approximately one-third falls as snow. The elevation of the watershed ranges from approximately 300 m above mean sea level in the lowland areas to approximately 1100 m in the uplands, while the average land-surface slope is 19%. The development of snowpack in this region is variable. Snow accumulation can begin as early as November and snowpack can persist until late April. However, a continuous and progressive increase in the snowpack over the winter is not common. Snowpack SWE varies throughout the winter as a consequence of intermittent melt and rain on snow events. By March–April the snowpack typically begins to ripen and meltwater is released to stream resulting in the highest discharge of a year.

METHODS AND DATA

The SWAT 2005 model uses a simple snowmelt algorithm that requires readily available daily measurements of temperature and precipitation as inputs. The model allows the sub-basins to be divided into a maximum of ten elevation bands to account for elevation gradients and, therefore, spatial differences in snow accumulation and melt (Wang and Melesse, 2005). In SWAT, a watershed is divided into a number of sub-basins for modelling purposes. Within sub-basins, Hydrological Response Units (HRU) are further delineated, based on land use, soil attributes, and slope (Neitsch *et al.*, 2005). The proper inclusion and representation of available watershed specific spatial data is crucial in defining representative HRUs. Calibration efforts (i.e. the adjustment of model performance by optimisation of parameters) for streamflow focused on improving model predictions, by comparing to measurements at the stream gauging station at Walton, NY (Figure 1).

Daily precipitation, minimum and maximum temperature data were obtained from cooperative stations recognized by the National Climate Data Center and obtained from the Northeast Regional Climate Center. A digital elevation map (DEM), soil data from detailed State Soil Survey Geographic Database (SSURGO) and land use coverage (National Land Use Land Cover 2001) were input to ArcSWAT (Neitsch *et al.*, 2005) in order to generate SWAT 2005 model inputs. A total 19 sub-basins were (Figure 1) delineated in ArcSWAT using 10 m DEM for Cannonsville watershed. Model simulations were run for 12 years (1989–2000) with the first 2 years used for initialisation in order to assure that model state variables have stabilized (Kirchner, 2009).

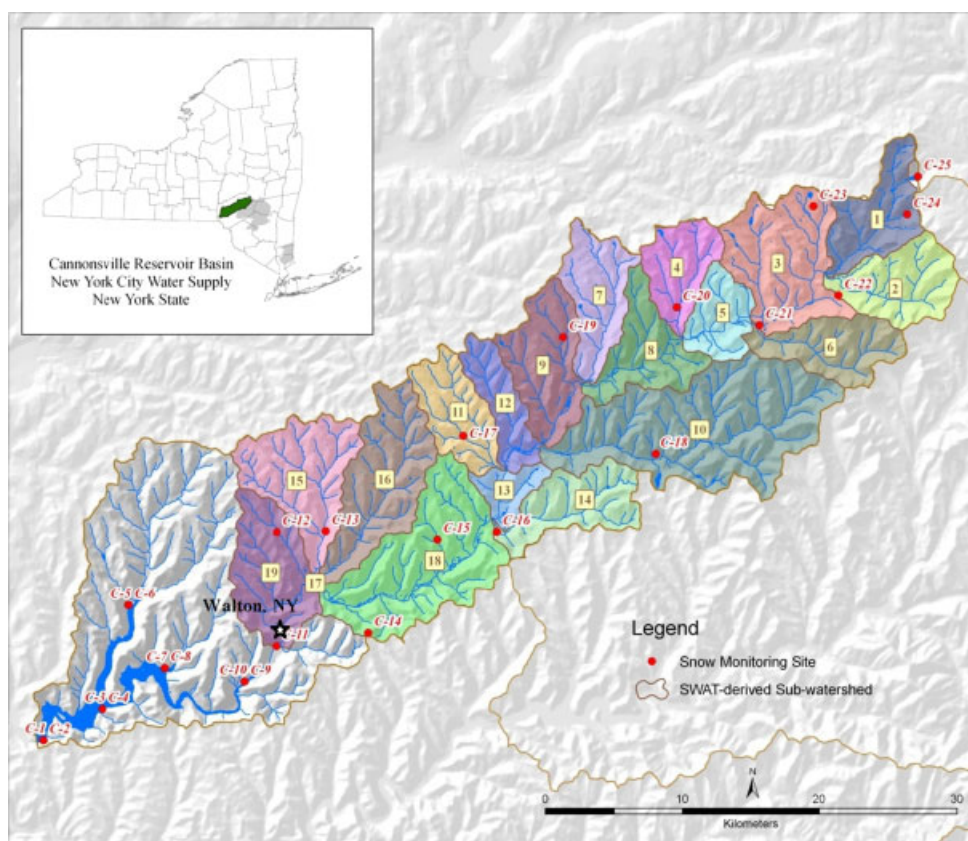


Figure 1. Cannonsville watershed and snow survey sites

Table I. Calibration parameters and their best parameter ranges for SWAT model simulations

SWAT input variables	Description	Best parameter estimate				SWAT default
		Mean elevation	Snow survey elevation	3Bands	5Bands	
SFTMP	Snowfall temperature [°C]	0.011	0.01	0.01	0.033	1.0
SMTMP	Snow melt base temperature [°C]	1.005	1.068	1.00	1.122	0.5
SMFMX	Melt factor for snow on June 21 [mm H ₂ O/°C-day]	1.697	1.37	1.01	1.74	4.5
TIMP	Snow pack temperature lag factor	0.477	0.68	0.370	0.406	1.0
PLAPS	Precipitation lapse rate [mm/km]	37.780	30.080	12.11	20.03	0.0
TLAPS	Temperature lapse rate [°C/km]	6.860	6.80	6.77	7.0	0.0
SNO_SUB	Initial snow water content [mm]	5.813	6.90	5.03	5.5	0.0
SURLAG	Surface runoff lag time [days]	0.765	1.73	0.347	0.340	4.0
ALPHA_BF	Baseflow alpha factor [days]	0.037	0.120	0.05	0.062	0.048
GW_DELAY	Groundwater delay [days]	0.397	0.011	0.354	0.01	31
GWQMN	Threshold depth of water in the shallow aquifer required for return flow to occur [mm]	0.01	3.591	0.272	2.48	0.0
REVAPMN	Threshold depth of water in the shallow aquifer for 'revap' to occur [mm]	0.017	0.011	0.563	0.711	1.0
CN2	Initial SCS CN II value	0.01 ^a	0.01 ^a	0.01 ^a	0.01 ^a	—
ESCO	soil evaporation compensation factor	0.17	0.01	0.012	0.025	0.95
EPCO	plant water uptake compensation factor	0.815	0.86	0.986	0.901	1.0
CH_N2	Manning's <i>n</i> value for main channel	0.031	0.040	0.033	0.039	0.014

^a Parameters that were used as multiplicative factors.

Parameters in SWAT that control the snowpack formation and snowmelt were adjusted to create a better match between observed streamflow data and spring runoff. The parameters that were adjusted include a number of factors

(Table I) that account for snow pack characteristics snow accumulation, snowmelt and sublimation. Other streamflow parameters such as Manning's *n* value for main channel (Ch_N2), initial Soil Conservation Service (SCS)

curve number II (CN2), baseflow alpha factor (Alpha-bf), and snowpack temperature lag factor (TIMP), the parameters surface runoff lag time (SURLAG), threshold depth of water in the shallow aquifer required for return flow to occur (GWQMN), threshold depth of water in the shallow aquifer for reevaporation to occur (REVAPMN), soil evaporation compensation factor (ESCO) and other groundwater, channel and basin related parameters were also adjusted.

Four configurations of elevation band were applied and tested at the sub-basin level. (1) SWAT default, i.e. average elevation of sub-basin (0Band); (2) A single band with snow survey site elevation used as average elevation of sub-basin (1Band); (3) Three equal area elevation bands (3Bands); and (4) Five equal area elevation bands (5Bands). The SWAT 2005 model was calibrated for streamflow from 1991–2000 and was verified for 2004–2008 years. The simulation results were compared with the corresponding observed values at daily, monthly and seasonal (winter–spring) time steps. Model performance on daily streamflow was evaluated using time series plots model performance statistics. The coefficient of determination (r^2), the Nash-Suttcliffe coefficients (E_{NS}) (Nash and Suttcliffe, 1970) and the root mean squared error (RMSE) were used to assess the ability of the model to replicate temporal trends (daily and monthly) in measured stream flow data. Streamflow simulations were based on different configurations of elevation data which are used by the snowmelt sub-model. The measured snowpack data from each snow survey site were compared to model simulated snowpack at each sub-basin when the elevation of the basin was set equal to the elevation of the snow survey site (i.e. 1Band method described above) This comparison was made for the 2004–2008 period using correlation coefficients.

SNOWMELT ALGORITHM IN SWAT

The snowmelt algorithm in SWAT consists of simple temperature index method. The major climate data needed for this purpose are maximum and minimum temperature and precipitation. When the mean daily air temperature is less than the snowfall temperature (SFTMP), the precipitation is classified as snow and the liquid water equivalent of the snow precipitation is added to the snowpack. The snowpack increases with additional snowfall, but decreases as snowmelt or sublimation occurs. The mass balance for the snowpack is computed as:

$$SNO_i = SNO_{i-1} + R_{sfi} - E_{subi} - SNO_{mli} \quad (1)$$

where SNO_i and SNO_{i-1} are the water equivalents of the snowpack on the current day (i) and previous day ($i - 1$), respectively, R_{sfi} is the water equivalent of the snow precipitation on day i , E_{subi} is the water equivalent of the snow sublimation on day i , and SNO_{mli} is the water equivalent of the snowmelt on day i . Snowmelt is calculated as a linear function of the difference between the average snowpack maximum air temperature and the

base, or threshold, temperature for snowmelt (Neitsch *et al.*, 2005). Sublimation from the snow surface is computed as the function of potential evapotranspiration. A temperature lag factor accounts for thermal characteristics of the snow pack that have influence on the snow pack density, snow pack depth, exposure. As this factor approaches 1.0, the mean air temperature on the current day exerts an increasingly greater influence on the snow pack temperature, and the snow pack temperature from the previous day become less influential (Neitsch *et al.*, 2005). Details about calculations are in SWAT 2005 theoretical documentation (Neitsch *et al.*, 2005).

In SWAT, sub-basin temperatures and precipitation are adjusted for each elevation band in a sub-basin as a function of the lapse rate and the difference between elevation of the meteorological gaging station providing input to the model and the average elevation specified for the band (Neitsch *et al.*, 2005). In this study, 3 and 5 elevation bands (with equal area) were established for each sub-basin, and the average elevation of each band and the percentage of the sub-basin area within that band are required (Fontaine *et al.*, 2002). Temperature and precipitation are calculated for each band as a function of the respective lapse rate and the difference between the gage elevation and the average elevation specified for the band using following equations:

$$T_B = T + (Z_B - Z) \cdot \frac{dT}{dZ} \quad (2)$$

$$P_B = P + (Z_B - Z) \cdot \frac{dP}{dZ} \quad (3)$$

where T_B , is the elevation band mean temperature ($^{\circ}C$), T , is the temperature measured at the weather station ($^{\circ}C$), Z_B is the midpoint elevation of the band (m), Z is the weather station's elevation (m), P_B is the mean precipitation of the band (mm), P is the precipitation measured at the weather station (mm), dP/dZ is the precipitation lapse rate (mm/km), and dT/dZ is the temperature lapse rate ($^{\circ}C/km$). To account for the orographic effects

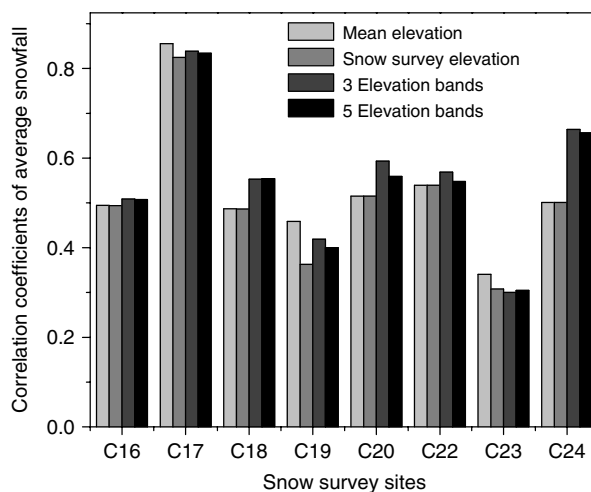


Figure 2. Correlation coefficients of mean SWE for snow survey sites and corresponding hydrologic response units

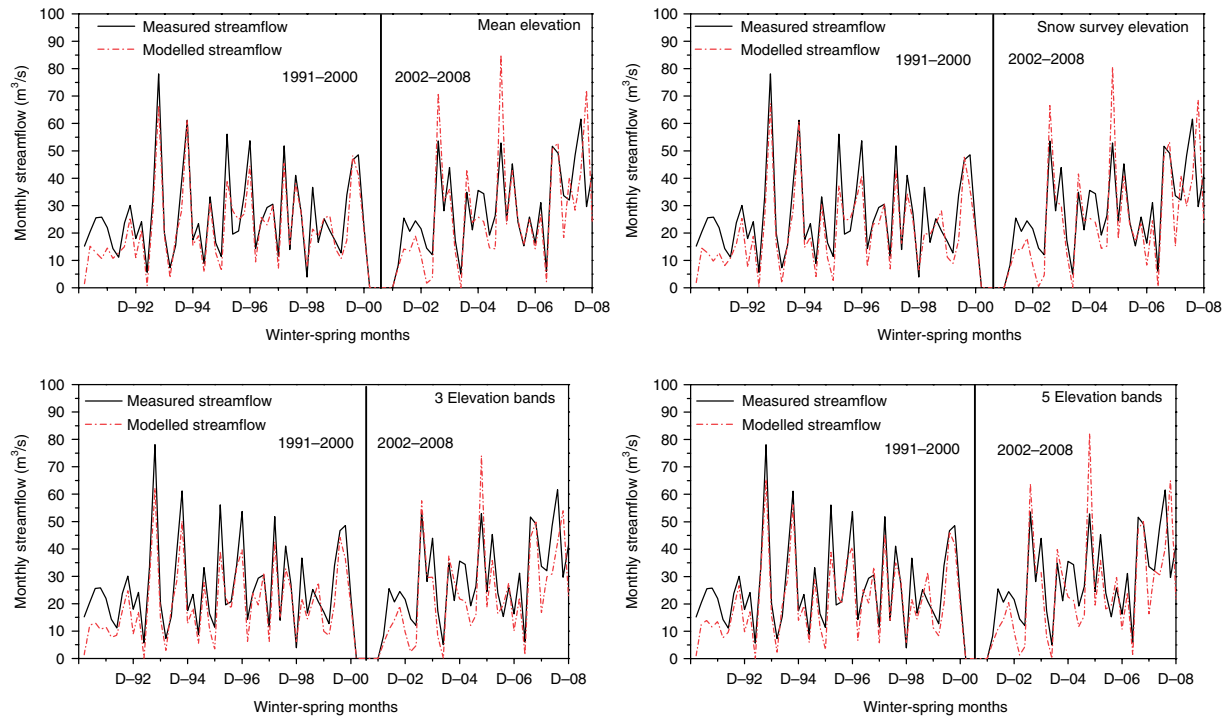


Figure 3. Winter–Spring Monthly (December–April) stream hydrograph for 1991–2000 (calibration year) and 2002–2008 study period for Cannonsville Watershed. a) SWAT-simulated and measured streamflow for simulation using mean elevation and snow survey elevation (top left and right); b) SWAT-simulated and measured streamflow for simulation using three and five elevation bands (bottom left and right)

on precipitation and temperature (and thus evapotranspiration and snow processes), algorithms for elevation bands and lapse rates were used. A temperature lapse rate of $6^{\circ}\text{C}/\text{km}$ (Gershmehl *et al.*, 1988) was initially used in the simulations, and this value was later adjusted by model calibration (Table I).

SNOW SURVEY AND METEOROLOGICAL DATA

Snowpack data were obtained from New York City Department of Environmental Protection (NYCDEP) between 2004 through 2008 from the Cannonsville watershed. The NYCDEP conducts snow surveys to measure snow depth and SWE, every two weeks from January 15 through mid April (personal communication, Jim Porter, NYCDEP). Eight snow survey sites with data through

2008 were used for this study (Figure 1). Snow data are collected using snow tubes, either Adirondack or Mt. Rose. In this method, the tube is pushed into the snow and extracted with an intact snow core, then weighed on a scale calibrated in inches of water. An initial volume of SWE is determined on the first survey date. As the snow season progresses, changes in the snowpack measured by subsequent surveys area attributed to snowmelt and accumulation.

CLIMATE SCENARIOS

The potential effect of climate change on snowfall and snowmelt was evaluated using four climate scenarios, i.e. GFDL A2, GFDL B1, IPSL A2 and IPSL B1 (Table III),

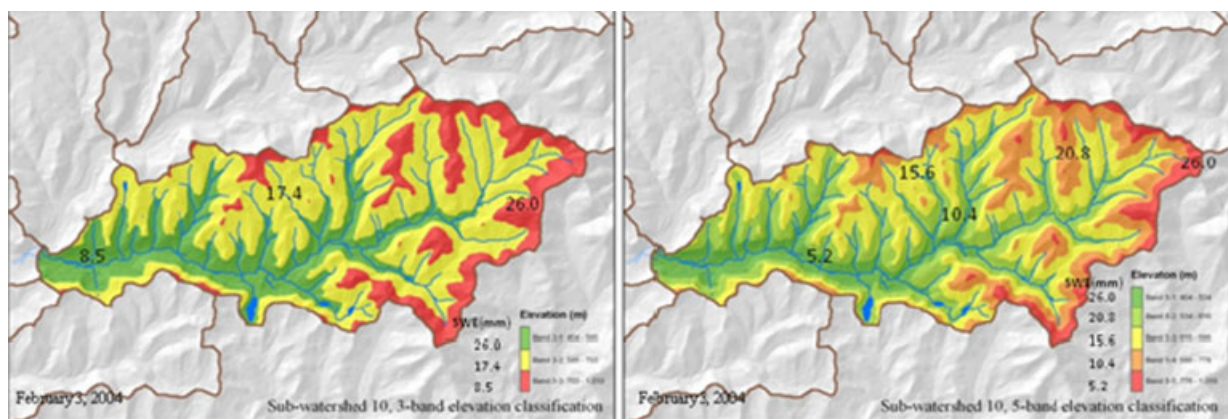


Figure 4. Snow water equivalent distribution for 3- and 5-elevation bands for sub-basin 10 simulated by SWAT model

Table II. Model performance of daily streamflow using different elevation bands (1991–2000). (Values in parentheses represent statistics for the period 2004–2008)

Period	Statistics	Snow survey elevation	SWAT mean elevation	3-elevation Bands	5-elevation Bands
Daily streamflow	Nash and Sutcliffe's Efficiency (E_{NS})	0.72 (0.50)	0.72 (0.47)	0.73 (0.46)	0.73 (0.56)
	Coefficient of Determination (r^2)	0.73 (0.55)	0.72 (0.53)	0.74 (0.61)	0.74 (0.59)
	Root Mean Squared Error (RMSE)	13.53 (20.88)	13.62 (21.52)	13.19 (18.77)	13.21 (19.66)
Winter-spring streamflow	Nash and Sutcliffe's Efficiency (E_{NS})	0.71 (0.41)	0.71 (0.39)	0.72 (0.55)	0.72 (0.47)
	Coefficient of Determination (r^2)	0.73 (0.55)	0.74 (0.54)	0.76 (0.63)	0.75 (0.60)
	Root Mean Squared Error (RMSE)	17.08 (24.55)	17.15 (25.94)	16.71 (21.46)	16.79 (23.26)
Monthly streamflow	Nash and Sutcliffe's Efficiency (E_{NS})	0.80 (0.54)	0.82 (0.58)	0.80 (0.64)	0.82 (0.57)
	Coefficient of Determination (r^2)	0.82 (0.63)	0.82 (0.64)	0.83 (0.67)	0.83 (0.63)
	Root Mean Squared Error (RMSE)	6.29 (9.89)	6.72 (9.56)	6.62 (8.76)	6.29 (9.57)

which represent a wide range of future emission scenarios and climate conditions, during the 2081–2100 future period. Climate scenarios were downscaled using change factor methodology (Anandhi *et al.*, 2010). Monthly change factors (CFs) were calculated from the difference between baseline (20C3M) and future GCM data. For temperature parameters additive factors were calculated and for all other parameters multiplicative factors were calculated. These monthly CFs were used to change local meteorological data to represent the future climate conditions associated with a given GCM, emission scenario.

RESULTS

Snowpack distribution and snowmelt comparison

The snow and hydrology parameters, default values and best parameter estimates from calibration are presented in Table I. Snow-related parameters were used in calibration to effectively simulate snow processes and hydrology. The melt factor for snow for summer solstice (SMFMX) was varied from 1.0 to 1.7 mm H₂O/°C-day based on the work of Huber and Dickinson (1988) and Westerstorm (1984). The temperature lag factor ranged from 0.3 to 0.68. This range, which produced the best fit to observed data, is close to the findings of Fontaine *et al.*, (2002) who observed values of the lag factor ranging from 0.0 to 0.5 for areas characterized by deep snowpack.

Comparison between simulated snowpack using and measured NYDCEP snow survey data showed highly variable results. The inaccuracies of model predicted snowpack depended upon the spatial and temporal scales of comparison. Snowpack data from the eight snow survey sites were compared with modelled data. Correlation coefficients ranging from 0.35 to 0.85 were obtained

when comparing the mean monthly snowpack data from 2004 to 2008 (Figure 2). The sub-basins with higher elevation had better prediction of snow as shown by the correlation coefficients (Figure 2). Snow survey sites C-17 (sub-basin 10), C-20 (sub-basin 4), C-22 (sub-basin 13) and C-24 (sub-basin 1) had average elevation greater than 500 m. The land use for C-17 and C-24 were forested, while C-22 and C-24 were classified as agriculture and low-intensity residential land use.

Spatial variations in the snowpack were better represented using three elevation bands compared to 1 and 5 bands, and this led to slight improvements in the correlation coefficients calculated between simulated and measured snowpack (Figure 2). In addition, winter-spring streamflow predictions were also slightly improved when using three elevation bands (Table II), although the differences with five elevation bands results were not substantial. The distribution of modelled snowpack for each sub-basin varied for each month. The simulated snow distribution map for the 3 and 5 elevation band configurations of sub-basin 10 is presented in Figure 3 as an example.

Among all sub-basins, the variations in snowmelt predicted using different elevation configurations (Figure 5) showed least variation in February and December. However, there was large scatter for the month of April. The mean snowmelt for the SWAT default simulation (0 Band Figure 5) was often high relative to simulations using elevation bands. The SWAT default elevation takes into account only the average for each sub-basin therefore, the model might misrepresent elevation dependent snow processes, and lead to an over prediction of snowmelt. For April, differences in snowmelt predicted using different elevation configurations increased greatly. The simulated variability in snowpack distribution within the sub-basins increased during April as a result of greater variations in

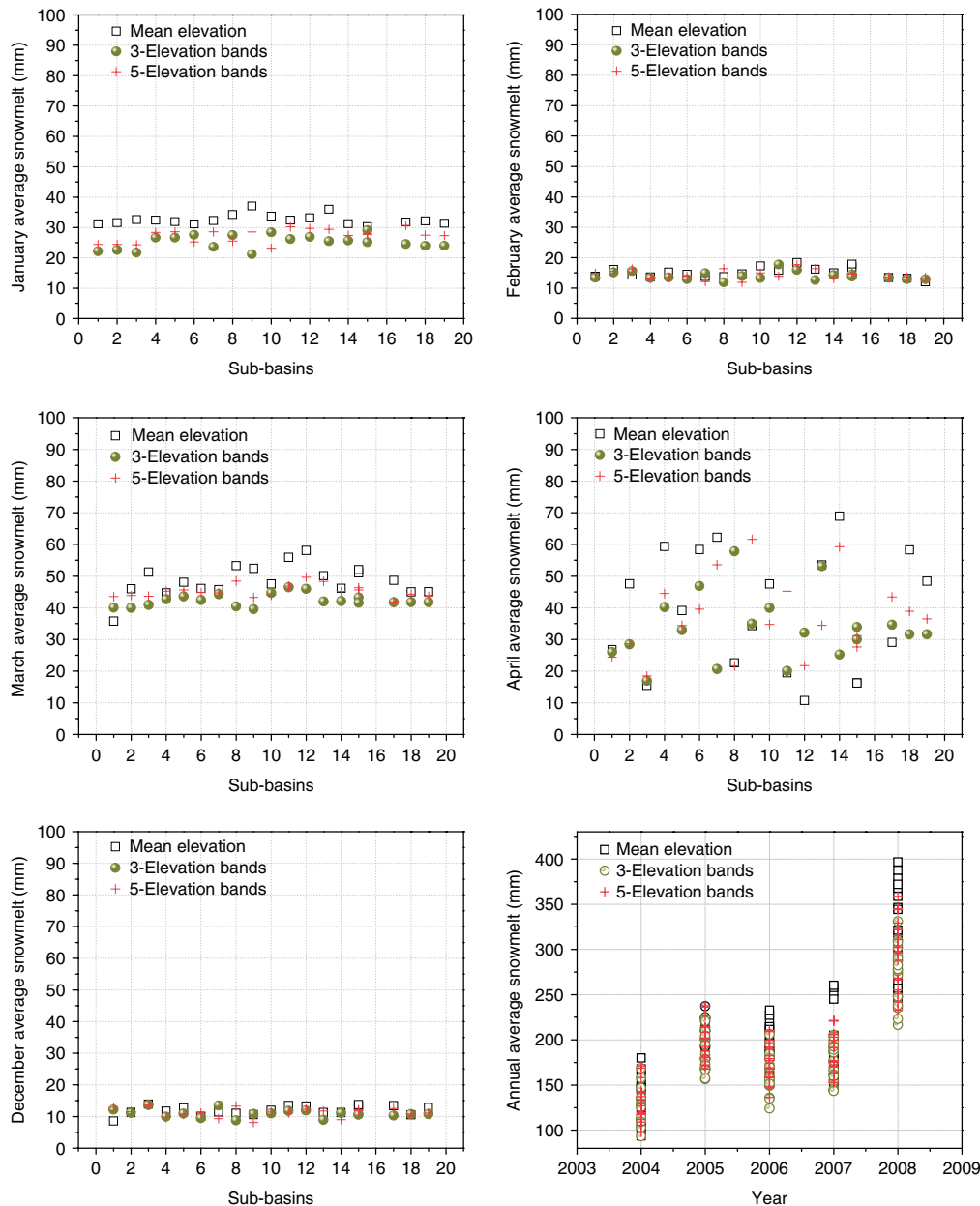


Figure 5. Scatterplots showing spatial distribution of snowmelt at monthly and annual scale. The simulated variability in snowpack distribution within the sub-basins increased during April as a result of greater variations in sub-basin melt showing a large scatter in snowmelt

sub-basin melt. This suggests that use of more elevation bands may more accurately simulate melt when snowpack reaches its seasonal low and the extent of snow cover becomes more spatially variable. Annual snowmelt showed a trend of increasing snowmelt and variability in the calculation of snowmelt between 2004 and 2008 (Figure 5).

Total snowpack and snow melt were also compared at the scale of entire Cannonsville watershed. Snowpack and snowmelt were higher for the SWAT-default simulation, whereas sublimation decreased for the simulations that used lower number of elevation bands (Table III). The snowpack within the study watershed mainly accumulated as a result of the snowfall throughout the winter and in early spring; over this period, only a small amount of the snowpack was lost to sublimation (Table III).

DAILY STREAMFLOW COMPARISON

Regardless of the simulation techniques used during the snowmelt, an essential modelling practice for streamflow simulation is to make use of field observations to verify model output, and by doing so gain some insight into the accuracy of the model's state variables. The model's computation of snowmelt was therefore, also checked by comparing computed discharge against streamflow observations. Here we considered the impacts of different snow and hydrology related parameterisation on estimates of stream discharge. The best estimate values for parameters used in calibration (Table I) show that many parameter values are similar for all model elevation band configurations used in this study; however, there are slight differences in the estimated values for some basin- and

Table III. SWAT simulated snowfall and snowmelt (mm) annual averages for 2004–2008 periods and 2 climate scenarios using 2 GCMs

Model runs	Climate data	SWAT-mean elevation			SWAT-snow survey elevation			3Bands			5Bands		
		SWE ^a	Snow _{mit} ^b	E _{sub} ^c	SWE ^a	Snow _{mit} ^b	E _{sub} ^c	SWE ^a	Snow _{mit} ^b	E _{sub} ^c	SWE ^a	Snow _{mit} ^b	E _{sub} ^c
SWAT simulations 2004–2008	Present conditions	322.12	307.94	5.14	320.67	306.92	5.57	287.50	266.81	12.07	304.81	283.02	12.67
SWAT simulations Future time slice of climate scenarios 2081–2100	GFDL_A2	157.74	155.01	2.70	155.39	152.84	2.52	141.28	135.10	6.15	149.75	142.51	7.19
	GFDL_B1	98.72	97.37	1.33	97.38	96.14	1.22	87.56	84.34	3.21	93.32	89.18	4.12
	IPSL_A2	117.90	116.21	1.67	116.81	115.22	1.57	85.27	80.79	4.09	112.45	107.28	5.16
	IPSL_B1	59.43	59.79	0.67	58.24	57.70	0.53	52.35	50.91	1.45	56.34	54.11	2.24

^a SWE: Snow Water Equivalent in mm (Snowpack represented as SWE).

^b Snow_{mit}: Snowmelt in mm.

^c E_{sub}: Sublimation in mm.

groundwater-related parameters. Since the additions of elevation bands make sub-basins more discrete in the representation of topography, it is to be expected that model parameter values representing processes affected by topography will vary between model configurations. The surface runoff lag time (SURLAG) was relatively high for the 1Band SWAT model. This allows surface runoff to have a lag of 1.7 days before reaching the channel. Since, the proxy elevation used for this band was from the snow survey site; this elevation may have misrepresented the topography resulting in higher SURLAG compared to other configuration of elevation bands. The surface runoff to the main channel delays with decrease in SURLAG values (Table I for 3 and 5 elevation bands), resulting in more accurate daily prediction of streamflow (White *et al.*, 2009). The threshold depth of shallow water for reevaporation to occur (REVAPMN) varied for each configuration of SWAT elevation bands. The minimum depth of water in soil for return flow to occur (GWQMN) value ranged from 0.01 to 3.591 mm of H₂O. The shallow aquifer contributes baseflow to the main reach within the sub-basin. Groundwater flow is allowed only if the depth of water in a shallow aquifer is equal to or greater than GWQMN parameter value (Neitsch *et al.*, 2005). The increase in number of bands used may have contributed to better representation of water table and shallow aquifers in the sub-basin.

Model performance during calibration period showed r^2 of 0.72, NSE of 0.72 and RMSE of 13.62 for daily streamflow when using SWAT default elevation for each sub-basin, i.e. average elevation of the sub-basin. Similarly, during the verification, the daily streamflow predictions were acceptable with performance statistics of (r^2 : 0.53; NSE: 0.47 and RMSE: 20.88) for default SWAT runs (Figure 3). The performance statistics was slightly better when elevation bands were used (Table II). The r^2 and NSE values were somewhat higher for the 3-elevation band SWAT simulation, but showed slight additional improvements with the 5-band simulation (Table II). The SWAT default elevation takes into account average elevation for each sub-basin; therefore elevation variability might not be completely represented. However given the relatively large number of sub-basins (Figure 1), a relatively large elevation range is covered at the scale of the entire watershed. The further division of each sub-basin into 3 or 5 elevation bands while undoubtedly providing more accurate estimates of snow accumulation (Figure 4) and melt, lead to only slightly improved streamflow and winter-spring streamflow prediction at daily time steps. The computation time for the SWAT simulations almost doubled when going from the default to 3-band simulations, making runs slower and time consuming. Since, the elevation difference within this watershed is not extremely large, using more than a 3-elevation band did not produce better streamflow predictions. The streamflow simulations for the SWAT model using sub-basin elevations corresponding to the snow survey sites showed slightly lower model performance. This is a result of the snow survey sites being biased towards sites at lower

elevations. Based on these results (Table II) it can be concluded that choice of snow elevation band configuration greater than three elevation band had little effect on SWAT 2005 simulation of streamflow in Cannonsville Watershed.

FUTURE CLIMATE SIMULATIONS

Future climate scenarios used here suggested increases in, both future temperature and precipitation (Matonse *et al.*, 2011). The SWAT simulation driven using these climate scenarios showed that future snowmelt and snowpack is expected to substantially decrease. The projected differences are not however, influenced by the use of 3 elevation band or 5 elevation band simulations (Table III). The SWE and snowmelt decreased for present condition (2004–2008) simulations ranged from 287.50 to 322.12 mm and 266.81 to 307.94 mm for different elevation bands. The climate change scenarios for a future time slice of 2081–2100 showed decrease in both SWE and snowmelt (Table III) as the climate warms, despite increasing precipitation, for two reasons. It is very likely that due to increased temperature, more precipitation will fall as rain, and that less snowpack will be developed, which in turn will result in less meltwater. The change in temperature and precipitation pattern can also affect the timing of snowpack development and occurrence of snowmelt. The snowpack may develop later and melt earlier, as a result, peak streamflow will very likely come earlier in the spring, and summer flows may be reduced. Potential impacts of these changes include an increased stream discharge in winter and early spring (Zion *et al.*, 2011), a reduced possibility of large snowmelt peaks later in the spring, and lower summer flows. With increasing temperature and changes in precipitation pattern, the amount of precipitation falling as snow and snow melt will be greatly affected (Burns *et al.*, 2007).

CONCLUSIONS

Accurate representation of variations in elevation plays an important role in snowpack and streamflow simulations, since snow generally melts, first at lower elevations, and then higher elevations. This can result in a shift in melting to higher elevations as the season progresses (USACE, 1991; Debele *et al.*, 2009). Any precipitation falling during the melt season will encounter a variety of potential situations: it can fall as fresh snow at higher elevations, as rain on snow at lower elevations, and as rain on bare ground (with reduced soil moisture) at low elevations. As a consequence of the dependence of snow processes on elevation, model simulations accounting for variations in elevation are expected to provide more accurate results. Our simulations with the SWAT 2005 model confirm this.

Snow survey data for 2004 through 2008 compared satisfactorily (correlation coefficient ranging from 0.35

to 0.85) with the snowpack that was simulated by the SWAT model. Simulations of streamflow were improved when using three elevation bands in each watershed sub-basin. The NSE of 0.73 and r^2 of 0.74 for daily streamflow were obtained for 3 elevation bands simulations. However, using more than three equally distributed elevation bands in each sub-basin led to little improvement in streamflow simulations, and since it can be computationally time consuming when the number of bands are increased we did not find any advantages to using a model configuration containing more than three elevation bands. Streamflow simulations showed slightly lower model performance using a basin elevation based on snow survey elevation, due to the snow survey sites being somewhat biased toward lower elevations and not representing the watershed elevation appropriately. In relations to water quality, it should also be stressed that the processes impacting water quality are simulated at the scale of the multiple HRUs present in each sub-basin. Spatial variations in snow melt can, therefore, influence relative contribution of each HRU to the water quality component of the SWAT model simulations, and as a result spatial variations in snowmelt can have a greater influence on water quality than water quantity, and water quality simulations may be more strongly impacted by the elevation band configuration used in the SWAT model.

Under higher air temperature in future climate change scenarios, SWAT indicate more precipitation falling as rain and reduced snowpack leading to a change in streamflow pattern particularly during winter and early spring.

Data used for conceptual modelling in snow hydrology contains many uncertainties associated with model assumptions as well as in the monitored snow. Some factors involved are as follows:

1. Snow data sampling is not consistent over a period of record. The number of sites available for comparison declined over time.
2. Snow data often have relatively short periods of record compared with precipitation data.
3. Precipitation and snow monitoring is more difficult in higher-elevation areas. The high-elevation areas receive more snow and, therefore, snow survey sites and data from under-represented high-elevation areas are important for study of snow hydrology.
4. Orographic effects, aspects, slope, different land use, and land cover have an effect on snow development and melt processes. Such processes are, however, not well represented in the simple temperature-index method.

Despite the above uncertainties, we found that the simple snowmelt model in SWAT 2005 can be effectively used for snowpack and streamflow modelling in the Cannonsville watershed.

ACKNOWLEDGEMENTS

The authors would like to thank James Porter, Watershed Monitoring and Operation Support at New York City Environmental Protection for providing snow survey data for this research. The GIS support from David G. Lounsbury and data support from Don Kent is also acknowledged.

REFERENCES

- Adam JC, Hamlet AF, Lettenmaier DP. 2009. Implications of global climate change for snowmelt hydrology in the twenty-first century. *Hydrological Processes* **23**: 962–972.
- Anandhi A, Frei A, Pierson DC, Schneiderman EM, Zion MS, Lounsbury D, Matonse AM. 2010. Examination of change factor methodologies for climate change impact assessment. *Water Resource Research* **47**: W03501, DOI:10.1029/2010WRR009104.
- Burns D, Klaus J, McHale MR. 2007. Recent climate trends and implications for water resources in the Catskill Mountain Region, New York, USA. *Journal of Hydrology* **336**: 155–170.
- Debele B, Srinivasan R, Gosain AK. 2009. Comparison of process based and temperature-index snowmelt modeling in SWAT. *Water Resource Management* **24**(6): 1573–1650.
- Dingman SL. 1994. *Physical Hydrology*. Macmillan: New York; p. 575.
- Ferguson RI. 1999. Snowmelt runoff models. *Progress in Physical Geography* **23**(2): 205–227.
- Fontaine T, Cruickshank T, Arnold J, Hotchkiss R. 2002. Development of a snowfall–snowmelt routine for mountainous terrain for the soil water assessment tool (SWAT). *Journal of Hydrology* **262**(1): 209–223.
- Frankenberger JR, Brooks SE, Walter MT, Walter MF, Steenhuis TS. 1999. A GIS-based variable source area hydrology model. *Hydrological Processes* **13**: 805–822.
- Gershmehl P, Kammrath W, Gross H. 1988. *Physical Geography*. Saunders College: Philadelphia, PA; p. 415.
- Hartman MD, Baron JS, Lamners RB, Cline DW, Band LE, Liston GE, Tague C. 1999. Simulations of snow distribution and hydrology in a mountain basin. *Water Resource Research* **35**(5): 1587–1603.
- Huber WC, Dickinson RE. 1988. Storm water management model, Version 4, User's manual. EPA/600/3-88/001, U.S. EPA, Athens, GA.
- Kirchner JW. 2009. Catchments as simple dynamical systems: Catchment characterization, rainfall-runoff modeling, and doing hydrology backward. *Water Resource Research* **45**: W02429, DOI:10.1029/2008WR006912.
- Marks D, Domingo J, Susong D, Link T, Garen D. 1999. A spatially distributed energy balance snowmelt model for application in mountain basins. *Hydrological Processes* **13**: 1935–1959.
- Matonse A, Pierson D, Frei A, Zion M, Schneiderman E, Aavudai A, Mukundan R, Pradhanang SM. 2011. Effects of changes in snow and timing of runoff on NYC water supply. *Hydrological Processes* DOI:10.1002/hyp.8121.
- Morid S, Goshain AK, Keshari AK. 2002. Comparison of temperature based and statistical approaches for estimation of solar radiation. *Journal of Nordic Hydrology* **33**: 291–301.
- Nash JE, Sutcliffe JV. 1970. River flow forecasting through conceptual models, part i. A discussion of principles. *Journal of Hydrology* **10**: 282–290.
- Neitsch SL, Arnold JG, Kiniry JR, Srinivasan R, Williams JR. 2005. Soil and water assessment tool: Theoretical documentation. Blackland Research Center, Texas Agricultural Experiment Station, Temple, TX. Version 2005.
- Paul PR, Rao LVR, Sankar ES. 1994. Estimation of basin snow water equivalent (SWE) using accumulation and depletion patterns of snowcover from optical satellite data. *GIS Development*. URL: <http://www.gisdevelopment.net/aars/acrs/1994/ts2/ts2005.asp> Accessed 11 July, 2010.
- Rango A, Matrinec J. 1995. Revisiting the degree-day method for snowmelt computations. *Water Resource Bulletin* **31**(4): 657–669.
- Tarboton DG, Chowdhury TG, Jackson TH. 1995. A Spatially Distributed Energy Balance Snowmelt Model. In *Proceedings of a Boulder Symposium*, Tonnessen KA, Williams MW, Tranter M (eds), July 3–14, IAHS Publ. no. 228, pp. 141–155.
- Tarboton DG, Luce CH. 1996. Utah energy balance snow accumulation and melt model (UEB), computer model technical description and users' guide. Utah Water Research Laboratory and USDA Forest Service Intermountain Research Station (<http://www.engineering.usu.edu/dtarb/>).<http://citeseer.ist.psu.edu/tarboton96utah.html>
- U.S. Army Corps of Engineers. 1991. Engineering and Design: Runoff from snowmelt. Engineer Manual 1110-2-1406. Department of Army. Washington DC.
- Walter MT, Brooks ES, McCool DK, King LG, Molnau M, Boll J. 1996. Process-based snowmelt modeling: does it require more input data than temperature-index modeling? *Journal of Hydrology* **300**(1): 65–75.
- Wang X, Melesse AM. 2005. Evaluation of the SWAT model's snowmelt hydrology in northwestern Minnesota Watershed. *Transactions of the ASAE* **48**(4): 1–18.
- Westerstöröm G. 1984. Snowmelt runoff from Porsön residential area, Luleå Sweden in Proc. of the 3rd Int. Conf. on Urban Storm Drainage, Gothenburg, Sweden. pp. 315–323.
- White ED, Feyereisen GW, Veith TL, Bosch DD. 2009. Improving daily water yield estimates in the little river watershed: SWAT adjustments. *Transactions of the ASABE* **52**(1): 69–79.
- You J, Tarboton DG, Luce C H. 2004. Modeling the snow surface temperature in an energy balance snowmelt model. Lincoln, Nebraska, 68583.
- Zhang X, Srinivasan R, Debele B, Hao F. 2008. Runoff simulation of the headwaters of the Yellow River using the SWAT model with three snowmelt algorithms. *Journal of the American Water Resources Association* **44**(1): 48–61.
- Zion MS, Pradhanang SM, Pierson DC, Aavudai A, Lounsbury DG, Matonse A, Schneiderman E. 2011. Investigation and Modeling of Winter Streamflow Timing and Magnitude under Changing Climate Conditions for the Catskill Mountain Region, New York, USA. *Hydrological Processes* (In Press).



A SATURATION EXCESS EROSION MODEL

Seifu A. Tilahun^{1,2}, Rajith Mukundan^{3,4}, Bezawit A. Demisse⁵, Christian Guzman¹, Birara C. Tarakegn⁴, Tegenu A. Engda^{5,6}, Zachary M. Easton^{1,7}, Amy S Collick^{1,2}, Assefa D. Zegeye^{5,8}, Elliot M. Schneiderman⁴, J.-Yves Parlange¹, Tammo S. Steenhuis^{1,2}

ISELE Paper Number 11061

Presented at the

International Symposium on Erosion and Landscape Evolution

Hilton Anchorage Hotel, Anchorage, Alaska

September 18-21, 2011

A Specialty Conference of the

American Society of Agricultural and Biological Engineers

Held in conjunction with the Annual Meeting of the

Association of Environmental & Engineering Geologists

September 19-24, 2011

¹ Department of Biological Engineering, Cornell University, Ithaca NY 14853, USA

² School of Civil and Water resources Engineering, Bahir Dar University, Bahir Dar, Ethiopia

³ CUNY Institute for Sustainable Cities Hunter College, City University of New York, New York USA

⁴ New York City Department of Environmental Protection, Kingston NY USA

⁵ Cornell Master Program in Integrated Watershed Management and Water Supply, Bahir Dar, Ethiopia

⁶ Department of Renewable Resources, University of Wyoming, Laramie

⁷ Department of Biological Systems Engineering, Virginia Tech

⁸ Amhara Regional State Agricultural Research Institute, Addet, Ethiopia

A SATURATION EXCESS EROSION MODEL

Seifu A. Tilahun^{1,2}, Rajith Mukundan^{3,4}, Bezawit A. Demisse⁵, Christian Guzman¹, Birara C. Tarakegn⁴, Tegenu A. Engda^{5,6}, Zachary M. Easton^{1,7}, Amy S Collick^{1,2}, Assefa D. Zegeye^{5,8}, Elliot M. Schneiderman⁴, J.-Yves Parlange¹, Tammo S. Steenhuis^{1,2}

ABSTRACT

Scaling up sediment transport has been problematic because most sediment loss models (e.g., the Universal Soil Loss Equation) are developed using data from small plots where runoff is generated by infiltration excess. However, in most watersheds, runoff is produced by saturation excess processes. Therefore, scaling up requires a hydrology model that accurately predicts the location and extent of runoff source areas. These runoff predictions can then be used for simulating sediment concentrations. We base sediment predictions on a simple, well-tested distributed saturation excess hydrology model, which calculates surface runoff, interflow, and baseflow. Surface runoff originates from bottom lands that become saturated during the rainy season or from severely degraded lands with little or no storage capacity. Baseflow and interflow are generated from the remaining parts of the landscape. Interflow comes from the shallow soils over an impermeable surface and base flow results from percolation below the impervious layer. To obtain the sediment concentrations, we assume that during surface runoff, there is a linear relationship between runoff velocity and sediment concentration, but baseflow and interflow are sediment free. Thus only the runoff component of stream discharge is involved in active erosive work compared to baseflow and interflow that contribute minimally to watershed sediment yield. To show the general applicability of the Saturation Excess Erosion Model (SEEModel), the model was tested for watersheds located 10,000 km apart, in the United States and in Ethiopia. In the Ethiopia highlands, we simulated the 113 ha Anjeni watershed, the 400 ha Enkulal watershed and the 180,000 km² the Blue Nile basin. In the Catskill Mountains in New York State, the sediment concentrations were simulated in the upper 493 km² Esopus Creek watershed. Daily discharge and sediment concentration were well simulated over the range of scales with comparable parameter sets. The Nash Sutcliffe values for the daily stream discharge were greater than 0.80 and the daily sediment concentrations had Nash Sutcliffe values of 0.65 using only two calibrated sediment parameters and the subsurface and surface runoff discharges calculated by the hydrology model. The model results suggest that correctly predicting both amount of surface runoff and subsurface flow is an important step in simulating the sediment concentrations.

KEYWORDS. Variable source areas. partial area hydrology, sediment, monsoon climates, USLE

¹ Department of Biological Engineering, Cornell University, Ithaca NY 14853, USA

² School of Civil and Water resources Engineering, Bahir Dar University, Bahir Dar, Ethiopia

³ CUNY Institute for Sustainable Cities Hunter College, City University of New York, New York USA

⁴ New York City Department of Environmental Protection, Kingston NY USA

⁵ Cornell Master Program in Integrated Watershed Management and Water Supply, Bahir Dar, Ethiopia

⁶ Department of Renewable Resources, University of Wyoming, Laramie

⁷ Department of Biological Systems Engineering, Virginia Tech

⁸ Amhara Regional State Agricultural Research Institute, Addet, Ethiopia

Introduction

The success of soil and water conservation practices depend on the understanding of the processes involved in the generation and transport of sediment (Ciesiolka et al, 1995). Many models use the Universal Soil Loss Equation for predicting sediment loads, which assumes that rainfall intensity is one of the main driving forces for causing erosion. Although this might be a reasonable assumption for areas with limited infiltration capacity and/or extremely high intensity storms, it is not applicable for humid climates, where soils are well structured and rainfall intensities are usually less than the infiltration capacity of the soil. In these areas runoff is generated from saturated areas of the landscape and the amount of runoff is a function of the precipitation depth and available soil storage. The objective of this research is to develop an alternative to the USLE for humid monsoonal climates and test if this method also applies to humid temperate climates.

SATURATED EXCESS EROSION MODEL(SEEMODEL) DEVELOPMENT

In this section, the amount of erosion is predicted as a function of the (daily) amounts of surface runoff, interflow, and baseflow. These fluxes are obtained from a relatively simple hydrology model (Steenhuis et al. 2009; Tesemma et al. 2011). In this simple model, the watershed is divided into three zones: two surface runoff zones consisting of areas, one that becomes saturated during the wet monsoon period and the other the degraded hillsides. The remaining hillsides are the third zone where the rainwater infiltrates and becomes either interflow (zero order reservoir) or base flow (first order reservoir) depending on its path to the stream. A daily water balance is kept for each of the zones using the Thornthwaite Mather procedure where actual evaporation has a linear relationship with the available water storage in the root zone. At maximum storage, S_{max} , actual evaporation is equal to the potential evaporation (Steenhuis and van der Molen, 1986). More information about the hydrology model can be found in Steenhuis et al (2009) and Tesemma et al (2011). Erosion originates from the runoff producing zones. Erosion is negligible from the non-degraded hillsides because almost all water infiltrates before it would reach the stream.

In calculating the erosion from runoff producing area, we are assuming that rate of erosion depends on the stream power (Ω) per unit area.. The maximum concentration of sediment that a stream can carry (called the transport limiting capacity C_t (g/L)) can be derived from the stream power function as shown by Hairshine and Rose (1992); Siepel et al. (2002); Ciesiolka et al. (1995) and Yu et al. (1997)

$$: \quad C_t = a_t q_r^n \quad 1$$

Where q_r (mm/day) is the runoff rate per unit area from each runoff producing region, a_t ($\text{g L mm}^{-n} \text{day}^n$) is a variable derived from the stream power. The variable a_t is a function of the slope, Manning's roughness coefficient, slope length, and the effective depositability (Yu et al 1997). As water depth increases a_t essentially becomes independent of the runoff rate per unit area and can be taken as a constant (Yu et al, 1997). The exponential, n , that takes a value of 0.4 assuming both a wide channel and a linear relationship between sediment concentration and velocity (Ciesiolka et al 1995 and Yu et al 1997). In this paper where the smallest watershed considered is 113 ha, the water in the channel is sufficiently deep so that a_t is constant.

For erosion of cohesive soils, the sediment concentration will not always reach the transport limit. Only in cases where, for example, the rills are formed in newly plowed soils, the transport capacity will be met. Tebebu et al (2010) found that once the rill network has been fully established, no further erosion will take place and the sediment source becomes limited and, the concentration, C , will fall below the transport limit. For the cases when the sediment concentration becomes lower than the

transport limit, C_t , Ciesiolka et al. (1995) found based on the work of Hairsine and Rose that the sediment concentration will not decline below the “source limit”, C_s (g/L):

$$C_s = a_s q_r^n \quad 2$$

where a_s is the source limit and is assumed to be independent on the flow rate for a particular watershed (as compared to plots). Introducing a new variable, H , defined as the fraction of the runoff producing area with active rill formation, the concentration of sediment from the runoff producing area can then be written as:

$$C_r = [C_s + H(C_t - C_s)] \quad 3$$

Combining Eq. 3 with Eqs. 1 and 2, the concentration from the runoff producing area becomes

$$C_r = [a_s + H(a_t - a_s)] q_r^n \quad 4$$

Finally, in the calculation of the daily concentration, baseflow and interflow play an important role. In a monsoon climate, baseflow can be at the end of the rainy season a significant portion of the total flow. Thus, in the last part of the rainy season the subsurface flow dilutes the peak storm sediment concentration from the runoff producing zones when simulated on a daily basis. It is therefore important to incorporate the contribution of baseflow in the prediction of sediment concentration.

Next we will calculate the concentration of the sediment yield in the stream. Since the interflow and baseflow are sediment free the sediment load per unit watershed area, Y ($\text{g m}^{-2}\text{day}^{-1}$), can be obtained by multiplying C_r in Eq. 4 by the relative area and the flux per unit area, e.g.,

$$Y = A_1 q_{r_1} [a_{s_1} + H(a_{t_1} - a_{s_1})] q_{r_1}^n + A_2 q_{r_2} [a_{s_2} + H(a_{t_2} - a_{s_2})] q_{r_2}^n \quad 5$$

where q_{r_1} and q_{r_2} are the runoff rates expressed in depths units for contributing area A_1 (fractional saturated area) and A_2 (fractional degraded area), respectively. Assuming that the saturated and the degraded zones have the same values for transport and source limiting capacities, the concentration of sediment in the stream can be obtained by dividing the load Y (Eq. 5) by the total watershed discharge

$$C = \frac{(A_1 q_{r_1}^{n+1} + A_2 q_{r_2}^{n+1}) [a_s + H(a_t - a_s)]}{A_1 q_{r_1} + A_2 q_{r_2} + A_3 (q_b + q_i)} \quad 6$$

Where q_b (mm/day) is the base flow and q_i (mm/day) is the interflow per unit area of the non-degraded hillside, A_3 where the water is being recharged to the subsurface (baseflow) reservoir.

These equations are only as good as the experimental data. Therefore Eq. 6 is tested in three watersheds in the Ethiopian highlands and one in New York State, The areas range from 113 ha (Anjeni, Ethiopia) to 180,000 km^2 (entire the Blue Nile Basin in Ethiopia). The other watersheds are Enkulal (400 ha) in Ethiopia and Esopus Creek (493 km^2) in New York state.

Watershed descriptions

The Anjeni watershed covers an area of 113 ha with elevations ranging between 2405 and 2507m and is cropped. It is located in the sub-humid northwestern part of Ethiopia near Debre Markos 370 km NW of Addis Ababa. The mean annual rainfall is 1690 mm, which lasts from the middle of May to the middle of October. There is a large active gully in the upper part of the watershed. Both discharge and sediment concentrations were measured during storm events. Daily average discharge and sediment concentrations were calculated. Rainfall, potential evaporation, stream discharge and sediment concentrations were collected from 1988 to 1997. In 1990 soil and water conservation practices were installed resulting in a decrease in soil loss for two years. Periods in which there is incomplete data) were excluded. The model was calibrated for the years 1988 and 1990 for discharge, and was

validated for the years 1989, 1991-1993 and 1997. Only three years were available for sediment concentration: The year 1990 was used for calibration and 1992 and 1993 for validation.

The Enkulal catchment is a small tributary of Gumara watershed, located approximately 80 km northeast of Bahir Dar. Enkulal watershed covers an area of 400 ha. Elevation ranges from 2306 to 2528 m. The average annual rainfall is 1577 mm. Most of the rainfall is concentrated from June to September. More than three quarter of the watershed is in low yielding oxen-plowed agriculture. Discharge and sediment concentration data were available twice a day at 6 a.m. and 6 p.m. for the year 2010. Especially at the end of the rainy season many storms occurred at night and the peak flows were not recorded. The rivers in the watershed are stable and in the lower part run over bedrock

The last watershed modeled in Ethiopia is the entire Blue Nile Basin in Ethiopia. It is 180,000 km² and encompasses the Anjeni and the Enkulal watersheds. It is said that the source of the Blue Nile is a spring located about 100 km south of Lake Tana at an elevation of 2,900 m. This spring is the beginning of the Gilgil Abbay, which flows into Lake Tana. After Lake Tana the Nile flows through a 1 km deep gorge to the Sudanese border mostly over bedrock. The Blue Nile leaves the highlands near the western border of Ethiopia, and enters the Sudan at an elevation of 490 m. The annual rainfall varies from less than 1000 mm near the Sudanese border to over 1800 mm in the highlands south of Lake Tana. Three years of discharge and sediment data were available at the Sudanese border (1997, 2003 and 2004). The year 1997 was used for calibration and 2003 and 2004 for validation. Tesemma et al (2010) found that the degraded soils had increased by 10% during a 25 year time span. For that reason the degraded hillslope was increased by 3% from 1997 to 2003 and 2004.

The final watershed is The Esopus Creek watershed located in the Catskill region of New York State drains 493 km² and is dominated by forests, which occupy more than 90 % of the watershed area. The elevation of the watershed ranges from 194 m near the watershed outlet at Coldbrook to 1275 m at the headwaters. Widespread stream channel erosion of glacial clay deposits has been identified as the primary cause of high levels of turbidity. For the Esopus Creek watershed, measured daily stream discharge from the USGS gauging station at the watershed outlet near Coldbrook was used. Turbidity measurements were taken at intervals between 15 min and 1 hr using a YSI water quality sonde from which flow-weighted average daily values were calculated. The measured stream discharge was separated into base flow and surface runoff components using a base flow filter program (Arnold and Allen, 1999). The values for surface runoff region (A1 and A2) and hillside recharge region (A3) were derived as the long-term (1931-2011) mean proportions of runoff and base flow to total stream flow. Observed daily turbidity and daily stream discharge from the March 2003 to March 2004 period were used for calibration of the sediment of the SEEModel and a power function and data from March 2007-2008 period were employed for validation. The Esopus Creek is at times fed by a diversion tunnel operated from the nearby Schoharie reservoir that contributes to stream discharge. Therefore all calculations were confined to days when the tunnel contribution of stream discharge was insignificant.

Results

The model calibration over a wide range of scales has some remarkable similarities (Table 1). Especially the fraction of surface runoff zones in the three watersheds, which is between 0.3 to 0.4. Only in the Anjeni watershed the surface runoff area is equal to 15% of the watershed. The size of permeable hillside increases with watershed size. The small watersheds are located in the top of the watershed and some of the subsurface water passes under the gaging station and provides water for springs below. The hillside area is especially small for the Enkulal watershed, which is in accordance with the data from piezometers readings that indicated that the top part of the watershed contributed mainly to baseflow. The maximum storage of water in the root zone varies among the watersheds. However, the model is relatively insensitive to the S_{max} values since it only affects the amount of

surface runoff in the beginning of the rainfall season. Variations in these values between watersheds are therefore not significant with the exception of the maximum storage for the hillside and saturated area of the whole Blue Nile Basin that is larger.

Table 1: Calibrated model parameters and model efficiencies for the four watersheds

Component	Description	parameters	Unit	Calibrated Values			
				Anjeni	Enkualal	Blue Nile	Esopus
Hydrology	Saturated area	Area A_1	fraction	0	0.1	0.2	-
		S_{max} in A_1	mm	-	50	200	-
	Degraded area	Area A_2	fraction	0.15	0.2	0.2	0.32
		S_{max} in A_2	mm	10	10	25	-
	Hillside	Area A_3	fraction	0.5	0.3	0.6	0.68
		S_{max} in A_3	mm	100	50	250	-
	Subsurface	$t_{1/2}$	days	70	120	80	-
		τ^*	days	10	100	200	-
Sediment transport limit		a_t	see text	4.5	17	6.9	-
Sediment Source limit		a_s	see text	3	5	4	0.63
Nash Sutcliffe Efficiencies	Time step		days	1	7	10	1
	Hydrology	calibration	none	0.84	0.75	0.95	-
		validation	none	0.80		0.92	-
	Erosion	calibration	none	0.70	0.76	0.86	0.63
		validation	none	0.75		0.72	0.66

There are two parameters that determine the subsurface flow: Interflow and baseflow. While the baseflow contribution to streamflow decreases slowly depending on the amount of water in the aquifer, the interflow remains constant for a particular storm and stops after a time, t^* . As expected t^* increases with watershed size, because more deep flow paths are intercepted by the river. The larger than expected t^* for the Enkualal watershed is likely a consequence of missing most of the peak flows especially later in the rainy season (due to the sample collection timing). The half-life, $t_{1/2}$, for the aquifer system is almost independent of watershed size, indicating that there is not a large aquifer. With the Nile flowing over bedrock this should not be a surprise. Finally, the hydrology model could not be fitted very well to the Esopus Creek watershed discharge data, because in a temperate climate the snowmelt requires another subroutine and with the large height differences in the watershed, the snowmelt is spatial variable. The proportion of surface runoff zone and permeable hillsides were derived statistically from the discharge data. The simple SEEM model was able to simulate the discharge pattern quite well in the watersheds.

The Nash Sutcliffe efficiencies in Table 1 for validation for the daily discharge data in the Anjeni watershed was 0.80 (Table 1) and for the 10-day average discharge in the entire Blue Nile in Ethiopia was 0.92. The simple SEEM model was able to simulate the discharge pattern quite well in the watersheds. The predicted and observed discharge for 1989 validation year for the Anjeni watershed is shown in Figure 1a. In Anjeni daily the peak flows were underestimated likely because saturated areas were forming near the river for the high flows and they were not included in the model. The data

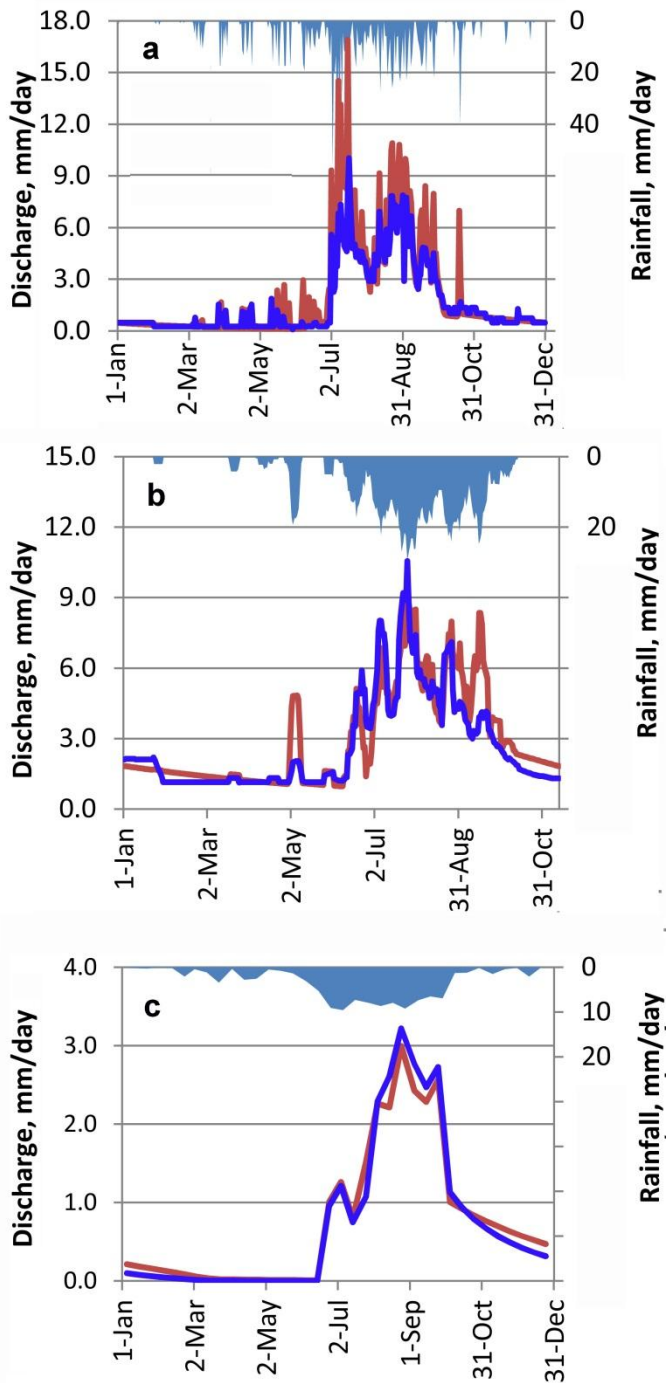


Figure 1. Predicted (red line) and observed (blue line) discharge data for a) Anjeni validation for daily discharge in 1989; b) Enkual calibration running weekly average discharge in 2010; c) Validation for the Blue Nile at the Ethiopian-Sudan border in 2003.

concentration, a_t , for Anjeni and the Blue Nile, are surprisingly similar (Table 1). The transport limiting capacity, a_r , for Enkual watershed is the

greater than the other two watersheds. Both the for the Enkual watershed was only collected in 2010 and weekly running averaged discharge in 2010 is compared in Figure 1b. The fit is not great and is partly caused by the uncertainty of the peak flows. The Blue Nile validation is shown for the year 2003 in Figure 1c. The NSE values were improved over the Collick et al. (2009) spreadsheet model and comparable to the SWAT-WB model in Easton et al (2010) for Anjeni and the entire Ethiopian Blue Nile basin. The good fit of the hydrology model is a consequence that the model recognizes that before the watershed discharge can respond to precipitation after the dry season, the soils need to be filled to field capacity or saturation.

In simulating the sediment losses, we first define the form of the function of H , indicating the fraction of plowed land with active gully formation. Tebebu et al (2010) and Zegeye et al. (2011), found that the erosion is the greatest just after plowing and stopped after rills were formed in the field. Cultivation begins after the first rainfall and then continues for approximately a three to four week period. Therefore, in the model we assume that the concentration from the runoff areas is at the transport limit (i.e., $H=1$) for the first four weeks after the first rainfall event. Then for another month a few more fields are being prepared and the H decreases from 1 to zero. Around August 1 the sediment concentration from the runoff areas is at the source limit except for the Esopus Creek watershed where the sediment remains at its transport limit due to the unstable banks.

The sediment concentration shown in Figure 2 are calculated according to Eq 6 by using the H values as specified above and the discharges predicted by the hydrology model. The value for n was 0.4 as it theoretically should be for a wide field (Tilahun et al, 2010). The coefficients a_t and a_s in Table 1 were calibrated for first year of data and then validated with the remaining years of data. The observed and predicted values for the validation of two watershed with multiple years of data fit well (Table 1; Figures 2a and 2c. The transport limiting concentration, a_t , for Anjeni and the Blue Nile, are surprisingly similar (Table 1). The transport limiting capacity, a_r , for Enkual watershed is the

slopes are steeper and the soils in this watershed are sandier than in the Anjeni watershed and the Blue Nile Basin. The source limits for all three watersheds spanning a range of scales in Ethiopia are similar.

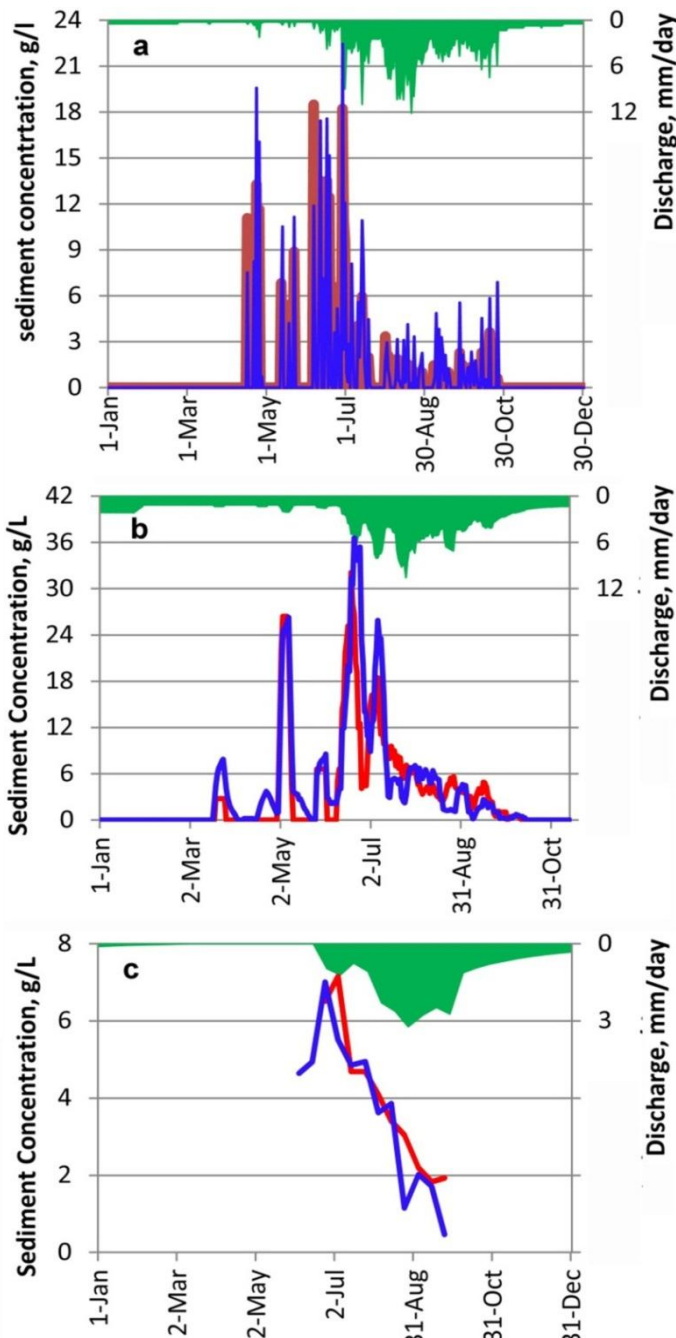


Figure 2: Predicted (red line) and observed (blue line) sediment concentration for a) Anjeni validation for daily concentrations in 1992; b) Enkulal calibration running weekly average concentrations in 2010; c) Validation for the Blue Nile at the Ethiopian-Sudan border in 2003. Discharge expressed in mm/day is the solid green area chart hanging from the top of figure

For the Esopus Creek we could not use the model employed for Ethiopia because of the inability to simulate snow melt accurately. Therefore, based on the long-term statistical analysis the average area contributing to base and interflow (A_3 in Eq 6) was found to be 0.68 and therefore ($A_1 + A_2$) was 0.32. The H value was kept constant at 0. We left the exponential term $n=0.4$ and calibrated the value of the transport limiting capacity, a_s as 0.63 (Figure 3). This was much lower than in the Nile basin, likely because the watershed was completely forested. The Nash Sutcliffe efficiency was 0.61 for calibration. A simple power function rating curve (using two calibration parameters using data from the same period had as expected a better NS efficiency of 0.83. However, during the validation period the one parameter model (Eq 6) performed better (NS efficiency of 0.66) than the rating curve (NS efficiency of 0.40). Unlike the rating curve the SEEModel was able to capture the variability in stream discharge- turbidity relationship to a certain extent (Figure 3).

CONCLUSIONS

Sediment concentrations in the stream were monitored in four watersheds. The SEEModel was developed by assuming that the concentration in the stream was the transport limiting capacity at the time the fields were plowed and then became equal the source limit once the rill network in the field were fully developed. The Nash Sutcliffe efficiencies are remarkably good for such a simple model over such a wide range of scales and better than most values reported in the literature for the Blue Nile Basin. Although the hydrology model could not be used in temperate climate where most runoff is produced during snowmelt, the sediment relationships seemed to apply as we

REFERENCES

Arnold, J. G. and P. M. Allen. 1999. Methods for estimating baseflow and groundwater recharge from streamflow. Journal of the American Water Resources Association 35(2): 411-424

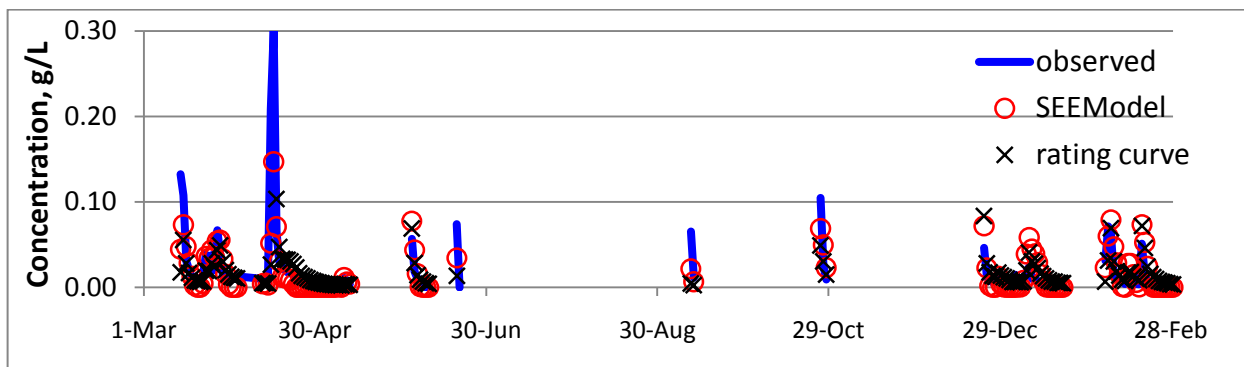


Figure 3: Esopus creek watershed 2007-2008 validation

Ciesiolka, C. A. A., Coughlan, K. J., Rose, C. W., Escalante, M. C., Hashim, G. M., Paningbatan Jr., E. P., and Sombatpanit, S. 1995. Methodology for a multi-country study of soil erosion management, *Soil Technol.*, 8, 179–192.

Collick, A. S., Easton, Z. M., Ashagrie, T., Biruk, B., Tilahun, S., Adgo, E., Awulachew, S. B., Zeleke, G., and Steenhuis, T. S. 2009. A simple semidistributed water balance model for the Ethiopian Highlands, *Hydrol. Process.*, 23, 3718–3727.

Easton, Z. M., Fuka, D. R., White, E. D., Collick, A. S., Biruk B., Ashagrie, T., McCartney, M., Awulachew, S. B., Ahmed, A. A., and Steenhuis, T. S. 2010. A multi basin SWAT model analysis of runoff and sedimentation in the Blue Nile, Ethiopia, *Hydrol. Earth Syst. Sci.*, 14, 1827–1841, doi:10.5194/hess-14-1827-2010.

Hairsine, P. B. and Rose, C. W. 1992. Modeling water erosion due to overland flow using physical principles 2. Rill flow, *Water Resour. Res.*, 28(1), 245–250.

Siepel, A. C., Steenhuis, T. S., Rose, C. W., Parlunge, J.-Y., and McIsaac, G. F. 2002. A simplified hillslope erosion model with vegetation elements for practical applications, *J. Hydrol.*, 258, 111–121.

Steenhuis, T. S. and van der Molen, W. H.: The Thornthwaite-Mather procedure as a simple engineering method to predict recharge, *J. Hydrol.*, 84(3–4), 221–229, 1986.

Steenhuis, T. S., Collick, A. S., Easton, Z. M., Leggesse, E. S., Bayabil, H. K., White, E. D., Awulachew, S. B., Adgo, E., and Ahmed, A. A. 2009. Predicting discharge and erosion for the Abay (Blue Nile) with a simple model, *Hydrol. Process.*, 23, 3728–3737.

Tebebu, T.Y., Abiy, A.Z., Zegeye A.D Dahlke H.E, Easton Z.M, Tilahun S.A., Collick A.S. Kidnau S, Moges S., Dadgari, F. and T. S. Steenhuis. 2010. Surface and subsurface flow effect on permanent gully formation and upland erosion near Lake Tana Ethiopia. *HESS* 14: 2207-2217.

Tesemma, Z. K., Mohamed, Y. A., and Steenhuis, T. S. 2010. Trends in rainfall and runoff in the Blue Nile Basin: 1964–2003, *Hydrol. Process.*, 24(25), 3747–3758, doi:10.1002/hyp.7893.

Tilahun, S.A., Engda, T.A., Legesse, E.S., Guzman, C.D. Zegeye, A.D. Collick, A.S., Rimmer, A. and Steenhuis, T.S. 2010. An efficient semi-distributed hillslope erosion model: The Anjeni in the sub humid Ethiopian highlands., *HESSD* 8: 2207-2233

Yu, B., Rose, C. W., Ciesiolka, B. C. A. A., Coughlan, K. J., and Fentie, B. 1997. Toward a framework for runoff and soil loss prediction using GUEST technology, *Aust. J. Soil Res.*, 35, 1191-1212..

Zegeye, A.D., Steenhuis, T.S., Blake, R.W. Kidnau, S. Collick A.S. and Dadgari, F. 2011. Assessment of Upland Erosion Processes and Farmer Perception of Land Conservation in Debre-Mewi Watershed, near Lake Tana, Ethiopia. *Ecorhydrologica*. In Press.

Investigation and Modeling of winter streamflow timing and magnitude under changing climate conditions for the Catskill Mountain region, New York, USA

Mark S. Zion,^{1*} Soni M. Pradhanang,² Donald C. Pierson,¹ Aavudai Anandhi,²
David G. Lounsbury,¹ Adao H. Matonse² and Elliot M. Schneiderman¹

¹ Bureau of Water Supply, New York City Department of Environmental Protection, Kingston, New York

² Institute for Sustainable Cities, Hunter College, City University of New York, New York City

Abstract:

Snowfall is an important part of the yearly water balance for the Catskill Mountains in New York State, the location of water supply reservoirs for New York City. Recent studies have shown that the effects of climate change on the hydrology of the Catskills will most likely create (1) a decrease in the proportion of precipitation falling as snow, (2) a shift in the timing of snowmelt that will cause snowmelt-supplemented streamflow events to occur earlier in the fall and winter, and (3) a decrease in the magnitude of traditionally high April streamflow. The shift in timing of snowmelt-influenced streamflow events is measured by the winter-early spring centre of volume (WSCV), defined as the Julian Day on which half the total streamflow volume from January to May occurs. Studies of streamflow, precipitation, and temperature trends in the last 50 years have shown that the WSCV is already earlier by about 5–10 days. This study investigates the use of watershed-scale snowpack and snowmelt algorithms that are incorporated in two existing watershed water quality models, Generalized Watershed Loading Functions-Variable Source Area (GWLf-VSA) and Soil and Water Assessment Tool (SWAT), to capture the potential effects of climate change on the timing and magnitude of streamflow during the late fall, winter, and early spring for the Catskill Mountain region. The GWLf-VSA model reasonably simulated the recent shifts in the winter streamflow timing, with simulations over the previous 50-year period yielding shifts in WSCV of 2–15 days. The SWAT model yielded similar results as the GWLf-VSA simulations. Scenarios of potential climate change 100 years in the future showed a similar shift in direction of timing winter streamflow, but at a larger magnitude than observed to date with WSCV occurring 15–20 days earlier. Copyright © 2011 John Wiley & Sons, Ltd.

KEY WORDS streamflow timing; trend analysis; watershed modelling; climate change; Catskill Mountains

Received 30 July 2010; Accepted 17 May 2011

INTRODUCTION

Current predictions of climate change in the northeastern United States (US) suggest increased temperatures over the next century, including winter increases ranging from 3 to 7 °C (Frumhoff *et al.*, 2007). Increased winter temperatures in northern latitudes and mountainous areas can have a profound effect on the accumulation of snow, the timing of snowmelt and, in turn, the magnitude and timing of winter and spring streamflow. Changes in the timing of winter streamflow can have many implications for the management of water supplies, flood control, and water quality.

A number of studies have shown that temperatures in the northeastern US have risen in the last 50 years (Trombulak and Wolfson, 2004; Burns *et al.*, 2007). These temperature increases have already created a shift in the winter streamflow patterns, with a movement of the traditional high spring runoff period due to snowmelt to earlier in the year (Zhang *et al.*, 2001; Hodgkins *et al.*,

2003; Burns *et al.*, 2007; Hodgkins and Dudley, 2006; Burn, 2008). This phenomenon of shifting streamflow is more pronounced in northern and more mountainous catchments due to the greater influence of snow processes in these areas. (Hodgkins *et al.*, 2003; Hodgkins and Dudley, 2006; Burns *et al.*, 2007).

The Catskill Mountain region of New York State supplies water for 9 million residents of New York City (NYC) and surrounding areas. Winter precipitation (December–April) accounts for approximately 40% of the total yearly precipitation. Streamflow during the winter and early spring (January–May) which is highly dependent on the December–April precipitation accounts for about 60% of the total annual flow, based on long-term stream gage records (USGS, 2009). Much of winter precipitation currently falls as snow, creating a snowpack that is an important component of water storage during the winter, and is a source of streamflow in early spring.

In order to evaluate and plan for the potential impacts of climate change on the NYC Water Supply, the New York City Department of Environmental Protection (NYCDEP) has undertaken a Climate Change Integrated Modeling Project (CCIMP) to investigate the potential

*Correspondence to: Mark S. Zion, Bureau of Water Supply, NYC Department of Environmental Protection, 71 Smith Ave, Kingston, NY 12401, USA. E-mail: mzion@dep.nyc.gov

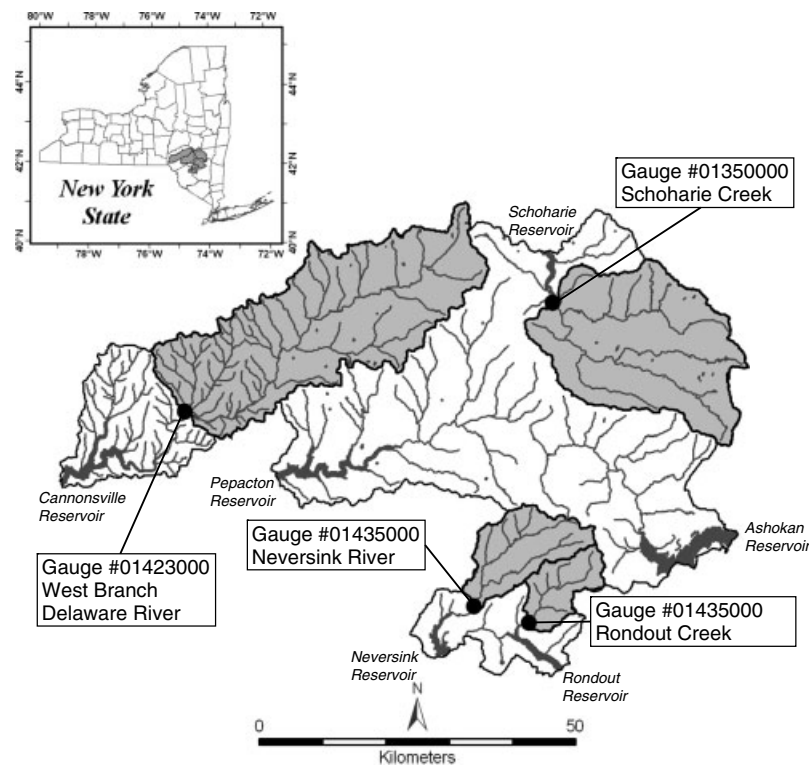


Figure 1. Location of study watersheds (shaded) corresponding USGS gauges within Catskill Mountain region. The full area depicts the boundaries of the West of Hudson watersheds and reservoirs of the NYC water supply system

effects of climate change on the quantity and quality of the water supply (NYCDEP, 2008). Preliminary modelling efforts undertaken by this project have consistently shown a major shift in the timing of winter streamflow (NYCDEP, 2009). This shift in the streamflow has some potential effects on the patterns of the system's overall storage, with reservoirs filling earlier in the spring (Matonse *et al.*, 2010) and on the timing and magnitude of nutrient and sediment loads to the reservoirs (NYCDEP, 2009).

As part of the CCIMP, existing watershed water quality models are being utilized to develop flows and constituent loads to the reservoir system. The models used within this program include the Generalized Watershed Loading Functions-Variable Source Area version (GWLf-VSA) (Haith and Shoemaker, 1987; Schneiderman *et al.*, 2002; Schneiderman *et al.*, 2007) and the Soil Water Assessment Tool (SWAT) (Neitsch *et al.*, 2005), since these models incorporate the necessary water quality algorithms for CCIMP analyses.

Hydrological modelling of snow processes can span a wide range of spatial and temporal scales, and the algorithms can also span a wide range of complexity from methods based only on temperature (e.g. GWLf-VSA, SWAT), to physically based, data-intensive energy balance approaches (Walter *et al.*, 2005; Ferguson 1999; Marks *et al.* 1999). The models used in this study generally use the more simple temperature index approaches. Zhang *et al.* (2008) compared the use of an energy balance algorithm *versus* the default temperature index algorithm in SWAT and found that the temperature index

method when combined with the multiple elevation bands performed well for simulating monthly streamflow in the headwaters of the Yellow River in China which has a significantly greater range in elevation than the Catskill region. As the GWLf-VSA and SWAT models are being used as part of the CCIMP, one goal of this study is to ascertain if the temperature index approaches embedded in these models are sufficient to simulate potential shifts in streamflow due to rising winter temperatures.

This study consists of three parts: (1) quantify trends for 1952–2008 in winter and early spring streamflow timing for the Catskill Mountain region; (2) investigate the ability of GWLf-VSA and SWAT models to capture any streamflow trends found in part 1; and (3) compare model estimates of streamflow in the context of potential future climate change.

METHODS AND DATA

Study area

Four watersheds with long-term historical streamflow measurements within the Catskill Mountain region of New York State are used for this study (Figure 1). These four streams are also major tributaries to four separate water supply reservoirs for NYC. Each of the watersheds contains a streamflow gauge operated by the United States Geologic Survey (USGS). Table I lists the important features of each of the watersheds. Generally, the watersheds are largely forested. There is some agriculture, mainly dairy, within the West Branch Delaware River (WBDR) watershed and, to a lesser

Table I. Land use, drainage areas and other facts regarding study watersheds

Watershed	USGS gauge no.	Station lat–lon	Watershed area (km ²)	Elevation range and (mean) (m)	Land use % ^a		
					forest/agri-undeveloped	cultural developed	
West Branch Delaware River at Walton	01423000	N 42° 09'58", W 75° 08'25"	859.25	370–1020 (590)	82	14	3
Schoharie Creek at Prattsville	01350000	N 42° 19'10", W 74° 26'13"	612.50	360–1230 (650)	94	3	3
Neversink River near Claryville	01435000	N 41° 53'24", W 74° 35'25"	172.48	470–1260 (770)	99	<1	1
Rondout Creek near Lowes Corners	01365000	N 41° 51'59", W 74° 29'15"	99.49	270–1270 (630)	98	1	1

^a Land use percentages derived from LandSat imagery from 2001. (NYCDEP, 2006a).

extent, within the Schoharie Creek basin. Additionally the WBDR and Schoharie watersheds contain a number of small hamlets. The Rondout and Neversink watersheds contain little or no agriculture and only some scattered development. The elevation ranges from about 270 to 1270 m, with the higher elevations more dominant in the Rondout and Neversink watersheds. There has been little change in land development over the last 50 years, except for a slight decline in active agricultural activity in the WBDR basin. None of these watersheds contains any water diversions, transfers, or flow regulation that significantly affect the inter- or intra-annual variability of the streamflow.

Streamflow data

The streamflow data for the 4 watersheds are investigated over a 57-year period for water years 1952–2008. Figure 2 shows the average monthly streamflow for each of the study gauges for the study period. Flow tends to peak in March and April, a period of spring snowmelt and low potential evapotranspiration. The extent of the spring peak is magnified in the more mountainous basins (Neversink and Rondout) as the influence of snow on streamflow is much stronger in these watersheds than in the other two basins. Minimum flows occur during the summer months when canopy interception and evapotranspiration are greatest. Snow water equivalent (SWE) data are collected by NYCDEP at various sites throughout these watersheds on various dates throughout the January–April period. Figure 3 displays boxplots of all SWE measurements collected by NYCDEP during winters of 2004–2008, the period for which data are available. The snowpack tends to peak during March and is typically melted away by the end of April. Again, the Rondout and Neversink watersheds have higher SWE measurements, especially during March, illustrating the greater influence of snow in these watersheds.

To analyse the effects of shifts in snowpack development and melting two statistics are used throughout this study: (1) total winter–early spring flow volume; and (2) the winter–early spring centre of volume (WSCV) (Hodgkins *et al.*, 2003). In this study, the total

winter–early spring flow is defined as the total volume of water in the streamflow for the months of January through May. This period is consistent with that used by Hodgkins *et al.* (2003) in a similar study of streamflow timing in New England and represents the time when the streamflow is most influenced by snow processes in the Catskill Region. In most years, the snowpack in the Catskill Region is completely melted by early May. The WSCV is the Julian Day by which 50% of the total winter–early spring flow volume has passed the flow gauge (Hodgkins *et al.*, 2003). Court (1962) suggested that this type of half-flow date is more representative of shifts in the mass of streamflow as opposed to a seasonal maximum flow which may be more dependent on the finer details of an individual year's meteorology.

Trend analyses

To test the trends in the streamflow time series, the Mann-Kendall test is used (Mann, 1945; Kendall, 1975). This nonparametric test is applicable for monotonic increasing or decreasing trends, detects either linear or nonlinear trends and accounts for outliers. This test has been widely used to test trends in hydrologic time series (Zhang *et al.*, 2001; Burn and Hag Elnur, 2002; Hodgkins *et al.*, 2003; Hodgkins and Dudley, 2006; Burns *et al.*, 2007; Dery *et al.*, 2009). The results of the Mann-Kendall test were evaluated at a significance level of $p < 0.1$. To calculate the slope of the trend, the Sen method (Sen, 1968) was used. The Sen slope is computed as the median of all possible pair-wise slopes for the data. None of the trend analyses in this study exhibited any statistically significant serial correlation.

Modelling analyses

The watershed hydrology and water quality models tested within this study include the GWLF-VSA (Haith and Shoemaker, 1987; Schneiderman *et al.*, 2002; Schneiderman *et al.*, 2007) and the SWAT 2005 (Neitsch *et al.*, 2005). These models have been used in the past for analysing the potential effects of land use and agricultural practices on water quality in the Catskill region (Gitau *et al.*, 2004; NYCDEP, 2006b; Easton *et al.*, 2008; Rao

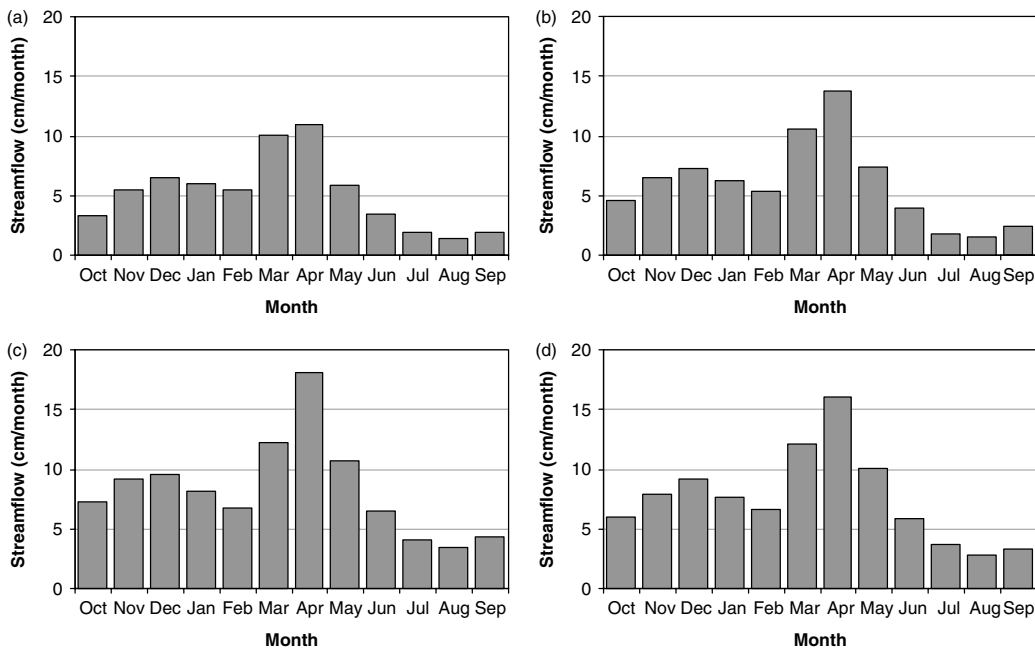


Figure 2. Monthly average streamflows for the study period (water years 1952–2008) as measured at USGS gauges for (a) WBDR, (b) Schoharie Creek, (c) Rondout Creek, and (d) Neversink River. All flow values are in cm/month representing the total monthly flow volume divided by the watershed area

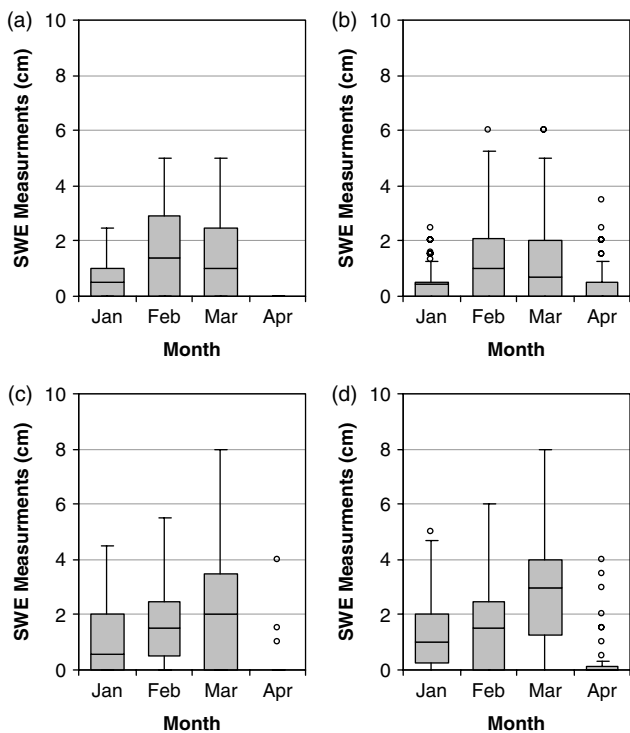


Figure 3. Boxplots of SWE measurements during 2004–2008 at various sites within (a) WBDR, (b) Schoharie Creek, (c) Rondout Creek, and (d) Neversink River watersheds. Boxes show range of 25th–75th percentile, whiskers show extent of data up to maximum 1.5 times interquartile range. Outliers represent data values beyond the maximum whisker extent

et al., 2009). The GWLF-VSA model has been applied in most of the NYC reservoir watersheds, while application of the SWAT model has occurred largely in the WBDR watershed where this model’s agricultural water quality algorithms are most applicable. Given their past history

of use in the study area, these models are potential candidates for use in studies of climate change. Since one goal of this study is to better understand the differences in the winter and spring streamflows that are simulated by these two models, both models were used to simulate streamflow in the WBDR watershed. To further understand the patterns in the winter spring streamflow shifts, the GWLF-VSA model was also used for simulations in the other three study watersheds. The models were applied for the period 1952–2008 to understand if the models adequately translated the underlying forcing data into the winter streamflow timing shifts observed in the measured data.

The GWLF-VSA watershed loading model is a lumped-parameter continuous simulation model that simulates daily streamflow, nutrients, and sediment loads from non-point and point sources. Model forcing inputs include daily minimum and maximum air temperatures, precipitation, incoming solar radiation, and daily average relative humidity. The original GWLF (Haith and Shoemaker, 1987) treats the watershed as a system of different land areas (Hydrologic Response Units or HRUs) that produce surface runoff, and a single groundwater reservoir that supplies baseflow. GWLF-VSA incorporates a saturation-excess runoff on variable source areas, which is considered the primary runoff-generation mechanism in Catskill watersheds (Walter et al., 2003). The GWLF-VSA model simulates runoff volumes using the SCS Curve Number Method, as in the original GWLF model, but spatially distributes the runoff response according to a soil wetness index, based on the TOPMODEL soil-topographic index (Schneiderman et al., 2007). The spatial distribution of runoff by soil wetness index provides a more realistic identification of runoff generating areas

in the NYC watersheds, with important consequences for simulation of pollutants that are typically transported by runoff.

The snowmelt algorithm in GWLF-VSA follows a temperature degree-day-based methodology, with the daily updating of a single watershed-wide snowpack:

$$SNO_d = SNO_{d-1} + P_{snowd} - M_d \quad (1)$$

where SNO_d is the snowpack for day d , SNO_{d-1} is the snowpack for day $d-1$, P_{snowd} is the snowfall for day d and M_d is snowmelt for day d . The daily input precipitation falls as snow when the average daily temperature (T_{avg}) is less than 0°C . The average daily temperature is defined as:

$$T_{avg} = \frac{T_{min} + T_{max}}{2} \quad (2)$$

where T_{min} is the minimum daily air temperature and T_{max} is the maximum daily air temperature. When the T_{avg} exceeds 0°C , melt of the snowpack proceeds as:

$$M_d = b_{melt} \cdot (T_{avg} - 0^\circ\text{C}) \quad (3)$$

where b_{melt} is a calibrated constant melt coefficient. The snowmelt is added to any precipitation that falls as rain ($T_{avg} > 0^\circ\text{C}$), and this total is considered available to be partitioned between direct runoff and infiltration. Direct runoff is added to streamflow with a short first-order delay function to incorporate routing, while infiltrated water is stored in the groundwater zone and can be available for either evapotranspiration or slowly released as baseflow.

The SWAT model is also a continuous simulation watershed water quality model and is significantly more complex than the lumped GWLF-VSA model. The model splits the watershed into sub-basins, with each sub-basin including HRUs defined by unique land use and soil combinations. Model forcing inputs include daily minimum and maximum air temperatures and precipitation for each sub-basin. Direct runoff, evapotranspiration and infiltration are calculated for each HRU and summed for the sub-basin. Sub-basin flows are routed through a stream network using a variable storage routing scheme. Infiltrated water is available for evapotranspiration or stored in a single sub-basin groundwater reservoir for slow release as baseflow.

The SWAT snowmelt algorithm (as described in Neitsch *et al.* (2005)) uses a temperature degree-day methodology to calculate a daily snowpack for each sub-basin. The snowpack in each sub-basin can be further divided into a maximum of ten elevation bands. For this study, the model was run twice: once with a single elevation band (SWAT-1Band), and a second time with three equal area elevation bands (SWAT-3Band) for each sub-basin. The input sub-basin temperatures are adjusted for each elevation band based on a calibrated lapse rate. For each elevation band within each sub-basin the daily snowpack is calculated by:

$$SNO_d = SNO_{d-1} + P_{snowd} - M_d - E_{subd} \quad (4)$$

where E_{subd} is the daily sublimation which is computed as the function of potential evapotranspiration. The daily input precipitation falls as snow when the minimum daily temperature is less than 1°C for this application). Melt of the snowpack proceeds as:

$$M_d = b_{melt} \cdot sno_{cov} \left(\frac{T_{avg} + T_{max}}{2} - T_{melt} \right) \quad (5)$$

where b_{melt} is a calibrated melt coefficient, T_{melt} is a melt temperature parameter set to 0.5°C for this application, and sno_{cov} is the fraction of the sub-basin with snow cover and was set to 1 when the SWE of the snowpack is greater than 1 mm and is set to 0 when the SWE was 0.

Model input data

Both the GWLF-VSA and SWAT models require daily forcing data, including temperature and precipitation. In addition the GWLF-VSA model uses input solar radiation data as part of a Priestley-Taylor evapotranspiration calculation. SWAT performs a similar calculation, but estimates the necessary solar radiation based on empirical relationships to daily temperature values. In addition to the daily forcing data, both models require information about the soils, land use/land cover and topographic information.

The required daily precipitation and daily minimum and maximum temperature data were from cooperator stations recognized by the National Climate Data Center and were obtained from the Northeast Regional Climate Center. For GWLF-VSA, the daily precipitation station data is averaged for the entire basin using a Thiessen polygon method (Burrough, 1987). Any potential biases of model input precipitation due to spatial averaging over mountainous terrain were corrected with a constant multiplicative factor calibrated to the long-term water balance for input model precipitation.

A basin-wide estimate of daily minimum and maximum temperatures was calculated based on an inverse distance weighting to four cooperator stations (Cooperstown, Liberty, Slide Mountain, and Walton) and an environmental lapse rate of $6^\circ\text{C} \cdot \text{km}^{-1}$ was applied to adjust for the difference in station elevation versus basin average elevation. The lapse rate was derived based on the average difference in temperature and the elevation difference between the four measurement stations used in this study. For SWAT a 5-km grid of both air temperature and precipitation data were derived from the cooperator station data using an inverse distance squared weighting scheme and again correcting temperature based on the same environmental lapse rate. The values for the closest grid point to each sub-basin were used as inputs to the SWAT model. Solar radiation data for GWLF-VSA was derived as the average of airport stations at Albany and Binghamton as supplied from the Northeast Regional Climate Center.

Land cover and land use (LC/LU) data for model input was derived from a combination of sources including a

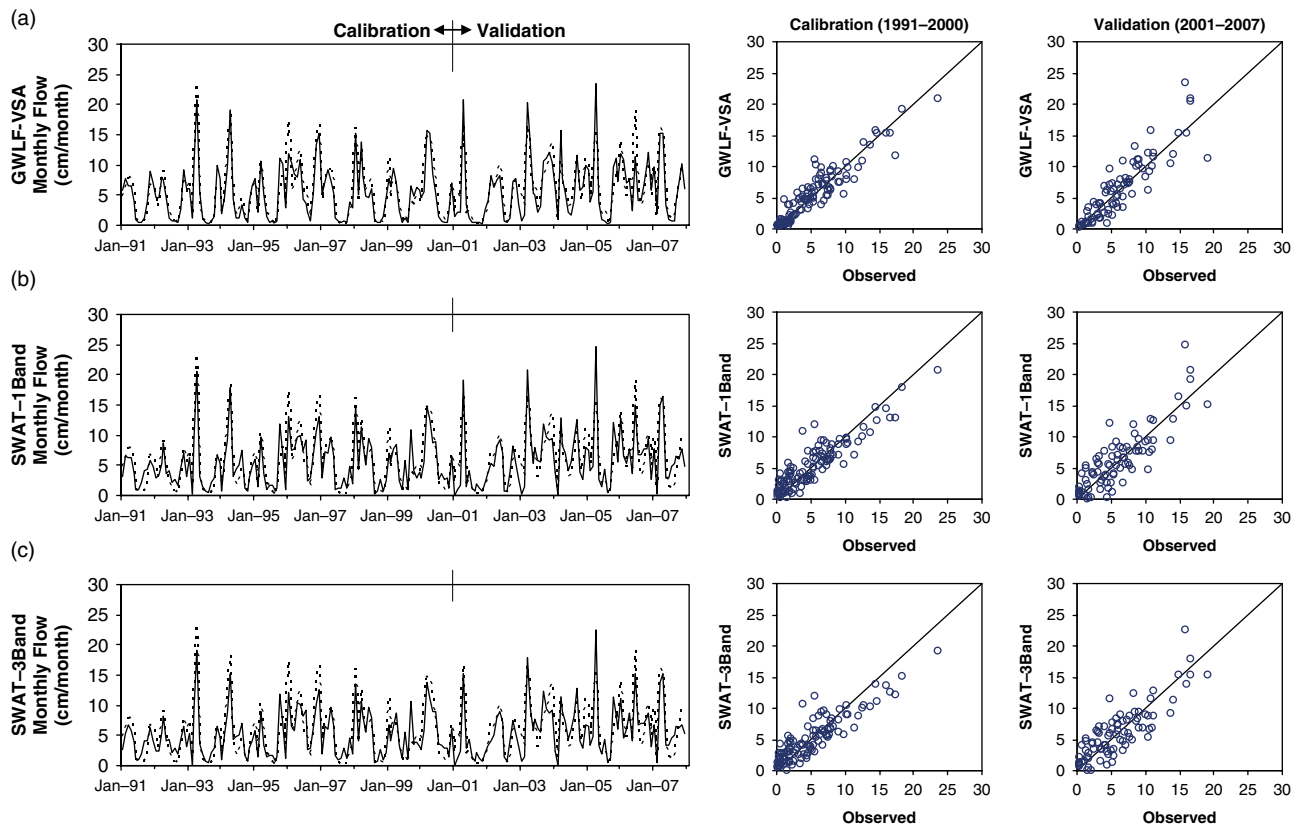


Figure 4. Calibration (1991–2000) and validation (2001–2008) results for monthly streamflow for the WBDR watershed using the (a) GWLF-VSA, (b) SWAT-1Band, and (c) SWAT-3Band watershed models. All flow values are in cm/month representing the total monthly flow volume divided by the watershed area. The panels on the left show a time series of simulated (solid lines) and observed (dotted lines) monthly streamflow. The scatterplots show the modelled (y -axis) monthly flows versus the observed (x -axis) monthly flows for calibration and validation periods. The lines on the scatterplots show the 1:1 relationship

supervised LC/LU classification derived from 2001 Land-Sat imagery, information from the New York City Watershed Agricultural Program to refine total agricultural areas, and New York State Department of Transportation GIS road data (NYCDEP, 2006a). Sixteen land use classes are distinguished in the model classification—deciduous forest, coniferous forest, mixed forest, brushland, non-agricultural grass, cropland, permanent hayland, pasture, barnyard, rural roads, residential pervious and impervious, commercial/industrial pervious and impervious, wetland, and water. Soils data, including available water capacity, saturated hydraulic conductivity and soil depth are derived from the digital Soil Survey Geographic (SSURGO) Database (NRCS, 2005). Soils-topographic index values used in the GWLF-VSA model (Beven and Kirkby, 1979; Schneiderman *et al.*, 2007) were derived from the soils data and a 10-m digital elevation model (USGS, 1998).

Model calibration

Both the GWLF-VSA and the SWAT models were calibrated for the watersheds of application for the period of 1991–2000. For GWLF-VSA, the calibration optimized total streamflow and also the partitioning of streamflow into direct runoff and baseflow for all events during the calibration period. For purposes of calibration, an event period is defined to begin on the first day

of a rise in the hydrograph over a threshold value and continues until the beginning of the next event period. In this way, an event period includes both the storm period with elevated flow and the inter-storm period following the storm flow. There are seven calibrated parameters for the hydrology portion of the GWLF-VSA model: a precipitation factor to calibrate long-term water balance; two water storage parameters partitioning of rain and melt into direct runoff and baseflow; two recession coefficients and a soil drainage coefficient controlling timing of direct runoff and baseflow at the watershed outlet; and the melt coefficient, b_{melt} (Equation (3)), which controls the rate at which the snowpack melts. Figure 4(a) shows the results for monthly streamflow for the calibration period (1991–2000) and for a validation period from 2001 to 2008 for the WBDR watershed. Table II lists the model performance statistics including the percent bias (the average difference in simulated minus observed values for the comparison period divided by the average observed value in terms of percent), the Nash-Sutcliffe coefficients (Nash and Sutcliffe, 1970) and the RMSE expressed as percent. All four watershed simulated with GWLF-VSA show consistently good results for monthly streamflow with validation Nash Sutcliffe coefficients above 0.76 and average percent errors ranging from -3.4 to $+3.4\%$.

Table II. Summary of GWLF-VSA and SWAT calibration and validation results for monthly streamflow. Calibration period is for 1991–2000, and validation period is for 2001–2008. Average monthly streamflow in cm/month representing the total monthly flow volume divided by the watershed area

Watershed	Model	Calibration results (1991–2000)					Validation Results (2001–2008)				
		Observed average (cm/month)	Simulated average (cm/month)	% Bias	Nash-Sutcliffe efficiency	RMSE	Observed average (cm/month)	Simulated average (cm/month)	% Bias	Nash-Sutcliffe efficiency	RMSE
West Branch Delaware River at Walton	GWLF-VSA	5.09	5.09	0.02	0.887	1.54	6.07	6.11	0.63	0.762	2.23
West Branch Delaware River at Walton	SWAT-1Band	5.09	5.14	1.06	0.826	1.90	6.07	6.20	2.12	0.693	2.53
West Branch Delaware River at Walton	SWAT-3Band	5.09	4.99	-1.98	0.798	2.05	6.07	6.02	-0.74	0.712	2.45
Schoharie Creek at Prattsville	GWLF-VSA	5.90	5.90	-0.04	0.800	2.54	7.01	7.24	3.36	0.776	2.85
Neversink River near Claryville	GWLF-VSA	8.50	8.49	-0.06	0.818	2.76	9.37	9.28	-0.93	0.827	2.71
Rondout Creek near Lowes Corners	GWLF-VSA	7.64	7.63	-0.11	0.789	2.66	8.66	8.36	-3.39	0.836	2.55

The SWAT model was calibrated for daily streamflow for the WBDR watershed for the 1991–2000 calibration period as described in Pradhanang *et al.* (2010). Sixteen model parameters are calibrated which control all aspects of streamflow simulation including the base-flow recession, the partitioning of rainfall and snowmelt into direct runoff and infiltration, streamflow routing, and the rates of snowpack development and depletion. Figures 4(b) and (c) show the time series and scatterplots of SWAT-1Band and SWAT-3Band monthly streamflow results for the calibration and validation periods. Table II lists the model performance statistics for the monthly streamflow results. Overall model results are good with validation period Nash-Sutcliffe coefficients above 0.69 and average percent errors ranging from -0.7 to +2.1%.

Climate change analysis inputs

To place the results of the trends into the context of potential climate change, the models for WBDR were further run with input precipitation and temperature forcing scenarios based on Global Climate Model (GCM) simulations of future climate.

The future climate forcing scenarios are defined by the combination of the GCM, an emission scenario based on the projected greenhouse gas emissions, and a time slice which defines the time period over which the prediction applies. Precipitation and average temperatures at the land surface were obtained from GCM simulations archived in the World Climate Research Programme's Coupled Model Intercomparison Project phase 3 (Meehl *et al.*, 2007) multi-model dataset. The GCM results from the region surrounding the study region are extracted and interpolated to a common 2.5° grid using bilinear interpolation. Two GCMs were used for this study, GFDL 2.0 (Geophysical Fluid Dynamics Laboratory) and IPSL (Institut Pierre Simon Laplace), as both of these GCMs showed good results using the winter precipitation and temperature forcings to simulate snowpack using current conditions (Anandhi *et al.*, 2010). The emission scenarios used include the A2 and B1 scenarios (Nakicenovic *et al.*, 2000). These two scenarios represent opposite ends of the spectrum of possible greenhouse gas emissions with A2 representing a greater greenhouse gas emissions and B1 representing lesser emissions. To represent the future climate the GCM results for the 2080–2100 time slice are used. In total, four future climate forcing scenarios (2 GCMs × 2 emission scenarios × 1 time slice) are generated.

To interpret the GCM results into precipitation and temperature scenarios appropriate for hydrologic model input, a monthly change factor method (also referred as delta change factor methodology) (Anandhi *et al.*, 2011) was used to downscale the GCM results and generate the four future climate forcing scenarios. The change factor method for temperature utilizes the difference between the results of a GCM simulation for a future time slice and the similar simulation made with the same GCM model of the current climate (1960–2000).

This difference is averaged for each month of the GCM simulation, producing one average change factor for each month (12 values). These average monthly change factors represent the monthly difference in temperature between the two time periods (future minus current) as simulated by a given GCM for an individual future climate scenario. The monthly change factors are then added to the long-term (1952–2008) historically observed temperature time series used as hydrologic model input to produce a future climate scenario. The advantage of this method is that hydrologic model results between future scenarios and current climate can be easily derived and compared.

A similar procedure is followed for producing future climate precipitation input scenarios for hydrologic model simulations, except that instead of the difference in monthly average values between GCM simulation of future and current climate, a ratio of future GCM simulated average monthly precipitation to current climate GCM simulated results (future simulation precipitation divided by current climate simulated precipitation) is used to derive the monthly change factors. These monthly change factors are then multiplied by the long-term precipitation inputs to the hydrologic model to produce a set future climate scenario precipitation inputs for the hydrologic model.

Figure 5 shows the range of average monthly temperatures and precipitation for the four future climate forcing scenarios as compared to the baseline historical values. For temperature, there is a consistent increase of about 2–8 °C throughout the year. For precipitation, the difference relative to present conditions varies widely across

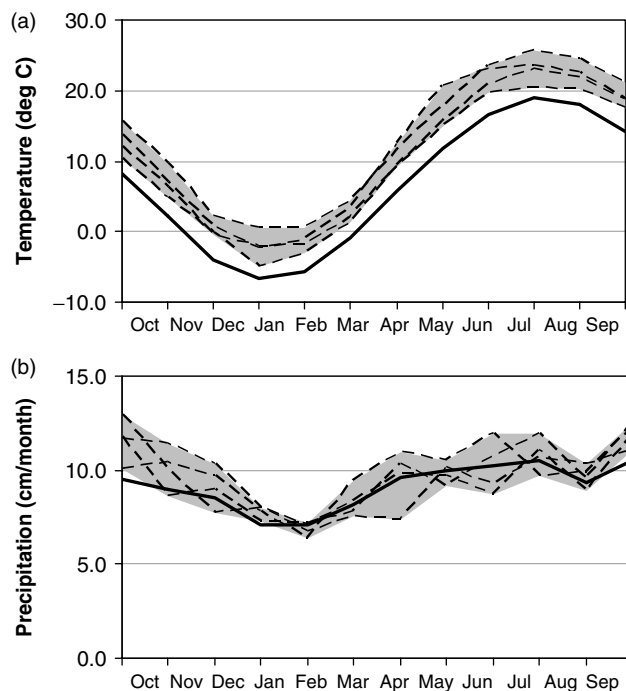


Figure 5. Range of climate change forcing scenarios for (a) temperature, and (b) precipitation shown on a monthly basis for the WBDR watershed. The solid line represents the monthly average current observed conditions (1952–2008), and the dotted lines display the four climate change forcing scenarios with the range of the future scenarios shaded

the scenarios with both increases and decreases in precipitation during most months. The range of change for all months is -2.3 to $+3.4$ cm per month. September and October are notable exceptions, when all four scenarios predict increases in average precipitation ranging from $+0.6$ to $+3.4$ cm per month. This wide range of results for potential future climate precipitation is consistent with the highly uncertain nature of GCM precipitation predictions (IPCC, 2007).

RESULTS AND DISCUSSION

Trends in winter–spring streamflow

An understanding of the streamflow trends that have occurred over the last 50 years is the first step in this study. Burns, *et al.* (2007) found that there were fairly significant trends of increasing temperature (0.5 – 2.0 °C/50 years) and increasing precipitation (8 – 26 cm/50 years) over the last 50 years at about half of the sampling stations in the region. The increased temperature, especially in the winter generally shifted the timing of the spring runoff period about 1–2 weeks earlier in the year. The streamflow shift was more pronounced in the more mountainous catchments of the study (Burns, *et al.*, 2007).

This study investigates four of the same watersheds as in Burns *et al.* (2007), and analyses these basins for a slightly longer time period through 2008. The update of the analysis is performed to allow for consistency with the modelling portion of this study and to include more recently available data. Figure 6 shows the winter early spring flow volume for 1952–2008 for each of the study streamflow gauges along with the trends and the Sen slope for each of the time series. Although the slopes of the trend lines are slightly positive, the Mann-Kendall significance p -values are much greater than 0.1 suggesting that the trends in increasing temperature and precipitation are not having a significant effect on the total winter streamflow.

In order to investigate potential changes in the timing of the winter–spring streamflow, the WSCV is used as an indicator. Figure 7 shows the WSCV for 1952–2008 for each of the study watersheds. In this case, the Sen slopes of the trend lines show a fairly high negative slope, indicating a shift in the WSCV day ranging from 5.6 to 10 days earlier over a 50-year period (Table III). This trend is statistically significant ($p < 0.10$) in two cases, the Rondout and Neversink watersheds and not statistically significant in the Schoharie and WBDR watersheds. This result is consistent with the findings of Burns, *et al.* (2007) as the Rondout and Neversink watersheds are more mountainous and contain the highest elevations in the Catskill Region where the winter temperature increases have been greatest.

The shift in winter streamflow is further illustrated in Figure 8 which shows boxplots of annual fraction of the winter–spring flow that occurs in each month. The white boxes show the fractions of winter–spring flow during

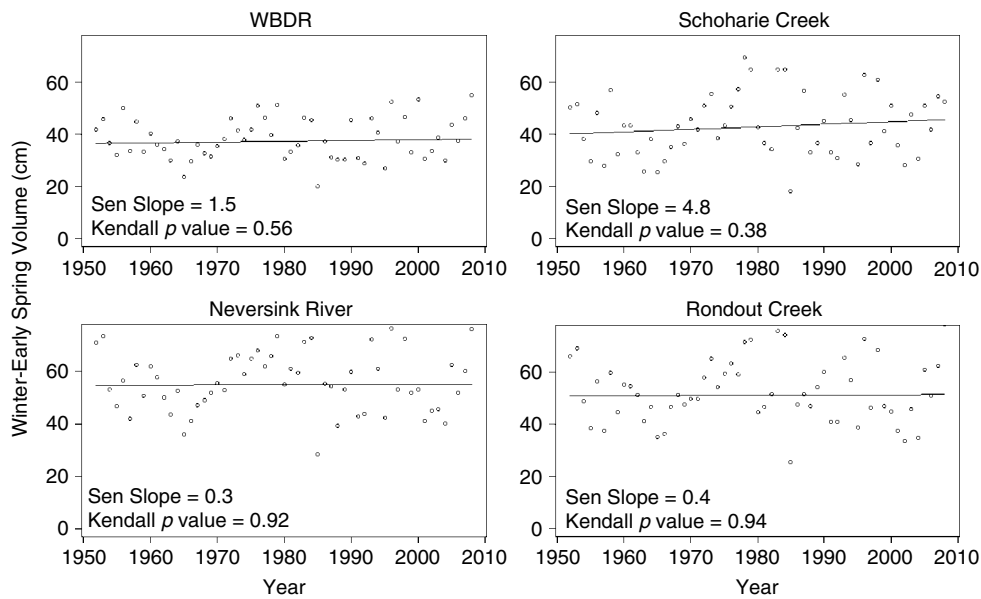


Figure 6. Annual time series of winter–early spring streamflow volume in unit depth (volume divided by watershed area). Sen slopes are in cm per 50 years

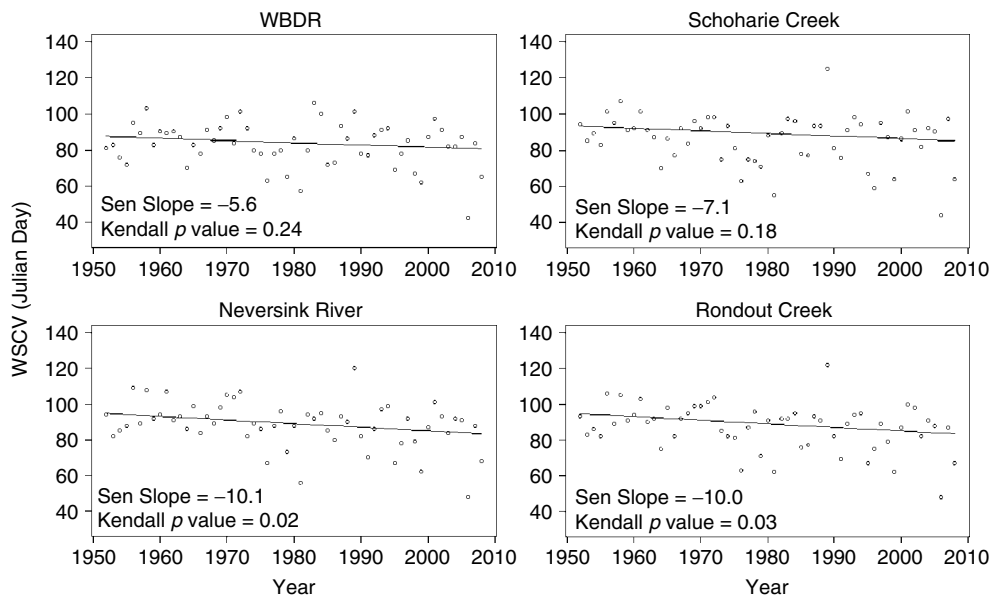


Figure 7. Plot of WSCV in Julian Day for each study watershed. Points show annual WSCV. Sen Slopes are in days per 50 years

each month in the years 1952–1966 and the grey boxes show the same values for the years 1994–2008. These two 15-year periods were chosen since they were long enough to represent some inter-annual variability and short enough to allow for a 28-year time gap between the two periods so that changes in the WSCV could materialize.

For Rondout and Neversink watersheds, about 35–45% of the winter–spring flow occurred in April for a majority of the years in the earlier 15-year period, while in the later 15-year period only about 20–30% of the winter–spring flow occurred in April. The fraction of winter–spring flow in April seems to shift somewhat to January. This shift is most likely due to the increased temperatures during the winter creating a combination

of more precipitation falling as rain during the winter and more melt of the snowpack prior to the traditional late March–April snowmelt period. These boxplots also illustrate the much stronger response to the temperature changes in the higher elevation watersheds (Rondout and Neversink) *versus* the other two study watersheds.

Modelling of streamflow trends

The GWLF-VSA model was run for each of the study watersheds for the period of 1952–2008 to further ascertain how well the model could simulate trends in the changing in timing of winter streamflow. Figure 9 shows the time series of the yearly modelled and observed WSCV for each of the study watersheds and Table III summarizes the Sen slope for the trend in WSCV. For

Table III. Summary of results for Sen slope of trend in WSCV for observed streamflow (data) and for GWLF-VSA, SWAT-1Band and SWAT-3Band model applications

Watershed	Sen Slope of trend in WSCV (days/50 years)			
	Data	GWLF-VSA	SWAT-1Band	SWAT-3Band
West Branch Delaware River at Walton	-5.6	-1.8	-4.1	-4.4
Schoharie Creek at Prattsville	-7.1	-6.7	N/A	N/A
Neversink River near Claryville	-10.1	-15.0	N/A	N/A
Rondout Creek near Lowes Corners	-10.0	-12.5	N/A	N/A

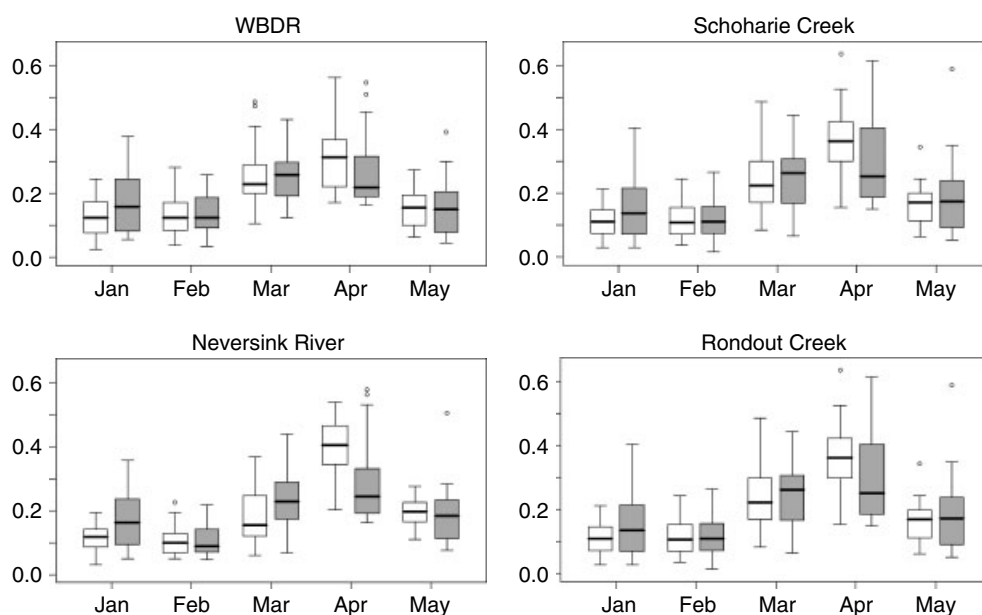


Figure 8. Boxplot of fraction of winter-early spring flow volume occurring in each month. The white boxes include data for years 1952-1966, and the grey boxes are for years 1994-2008. Boxes show range of 25th-75th percentile, whiskers show extent of data up to maximum 1.5 times interquartile range. Outliers represent data values beyond the maximum whisker extent

all the basins, if the trend in the data was strong, then the model also simulated a similarly strong trend. In cases where the trend in the data was not particularly strong, the model also indicated a weak trend. The data from the Rondout and the Neversink watersheds showed some of the strongest and most significant trends leading to an earlier WSCV, with the WSCV moving back at a rate of approximately -10 days per 50 years. The models also showed statistically significant trends ($p < 0.10$) in these two watersheds, with slopes that showed a slightly higher rate of reduction (-12 to 15 days per 50 years) than the observed values. For the Schoharie watershed the trend in the model was almost exactly the same as that for the data (a reduction of about -7 days per 50 years) even though the p -values associated with both trend lines indicated that they were not statistically significant. Finally for WBDR, where the observed slope of the trend is the least and the trend test is least significant, the model slope of the trend was somewhat less than that of the data (-1.8 days per 50 years for the model *versus* -5.6 days per 50 years for the data) and the p -value also indicates statistical non-significance for the trend.

The SWAT model, using both a single elevation band and three elevation bands, was also run for the WBDR

watershed to test if the less significant trend in this basin is able to be better simulated using the slightly more complex snow processes included in this model. Figure 10 shows the results of the SWAT model for the simulated WSCV trends *versus* the observed trends. Both SWAT model tests produced trend results similar to the GWLF-VSA runs. The model based trends were slightly underestimated when compared to the -5.6 days per 50-years shift estimated from the measured data. The SWAT-1Band model produced a shift in WSCV of -4.1 days per 50 years, and the SWAT-3Band model produced a shift of -4.4 days per 50 years. For the WBDR basin, where WSCV trends are not strong or statistically significant in the data, model simulations yielded similar results for the shift in WSCV when using either GWLF-VSA or SWAT model applications.

Overall, the GWLF-VSA model captured the shift in timing of the winter streamflow well, especially for the basins with the strongest and most significant trends. For the WBDR basin, where the trends are not strong or significant in the data, similar results were simulated for the shift in WSCV in both the GWLF-VSA and the two SWAT models.

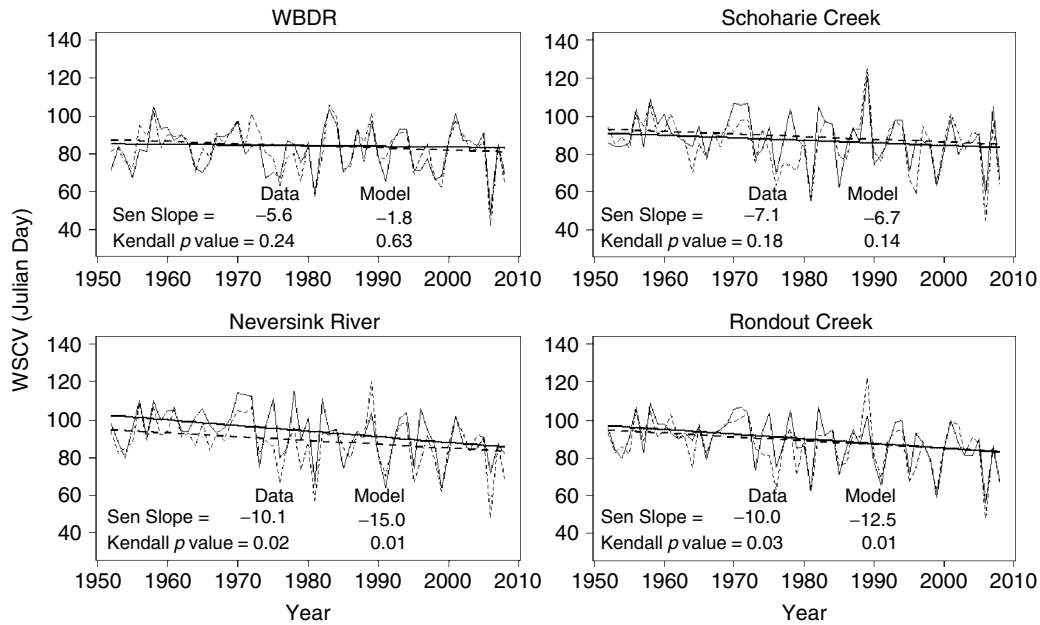


Figure 9. Plot of the annual WSCV and the corresponding Sen Slope in Julian Day for each study watershed for data (dashed lines) and for the GWLF-VSA model simulation (solid lines). Sen Slopes are in days per 50 years

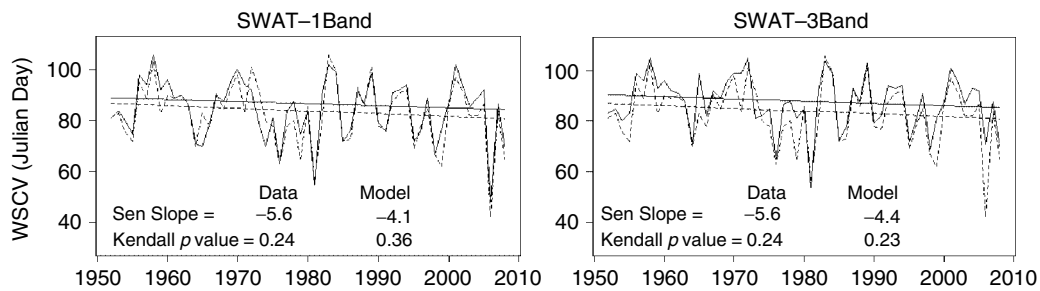


Figure 10. Plot of the annual WSCV and the corresponding Sen Slope in Julian Day for WDBR watershed for data (dashed lines) and for the SWAT model simulations (solid lines). Sen Slopes are in days per 50 years

Climate change and streamflow

The climate change scenarios are modelled in the WDBR watershed to compare the already occurring shift in winter streamflow to the changes projected to occur under future climate conditions. It is important to note that these results are obtained with a limited number of climate change scenarios, and therefore, only give a sampling of potential climate change impacts and do not encompass the full range potential outcomes. In addition, the changes in temperature and snowmelt timing may have considerable impacts on the land cover and canopy dynamics within the watersheds, providing further feedback on streamflow which is not included in this analysis.

Figure 11 shows the monthly average streamflow for the current conditions and the range of streamflows for the four climate change scenarios using the GWLF-VSA, SWAT-1Band and SWAT-3Band models. Each of the models consistently indicates a shift in streamflow timing from the spring to the early winter, with the traditional April peak decreasing and the flows during the early winter increasing. This is consistent with the direction of shifts observed in the most recent data (Figure 8). As expected the magnitude of the shift is much greater in

the climate change runs, as the climate change scenario temperature shifts are much greater than any observed to date. Future work in this area could include a more detailed investigation of climate change on the extreme precipitation events that impact the magnitude of the peak spring streamflow. This issue depends greatly on the prediction of future extreme precipitation which is not well represented in current GCMs primarily due to the large spatial resolution used within these climate prediction models (Wehner, *et al.*, 2010).

Although not the major focus of this study, one area of difference between the future simulations made with the three different models occurs during the summer, with flows decreasing more in the SWAT runs than in the GWLF-VSA runs. This could point to differences in how the climate changed forcings affect the evapotranspiration calculations within each model. Differences in changes in summer evapotranspiration rates could be an important factor in further studies of climate change effects on summer streamflow. As evapotranspiration occurs at a much slower rate during the winter, any differences in evapotranspiration should have little effect on the winter streamflows.

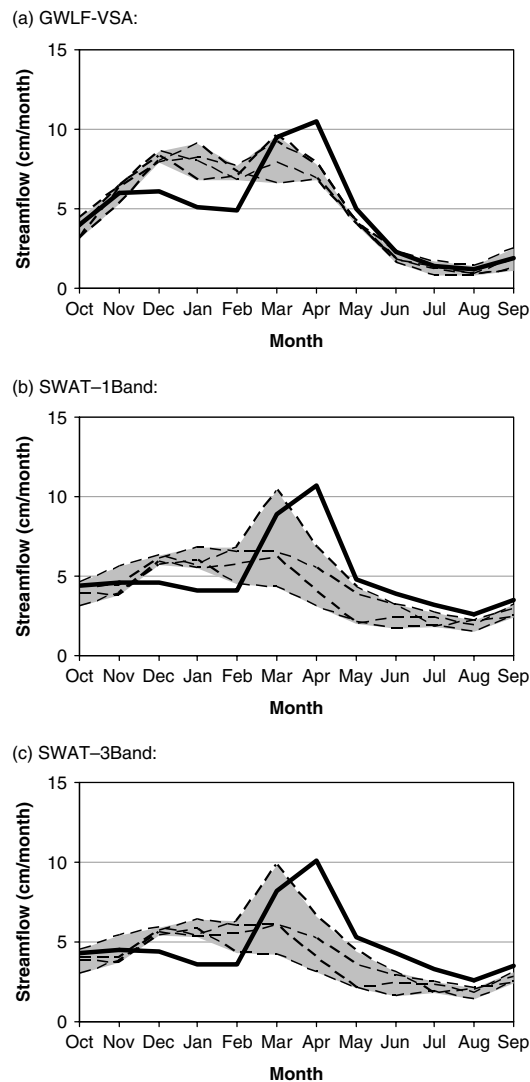


Figure 11. Monthly average streamflow results for climate change simulations in WBDR watershed using (a) GWLF-VSA, (b) SWAT-1Band, and (c) SWAT-3Band models. Solid line shows the mean monthly streamflow from the baseline simulation (1960–2000) and the shaded area shows the range in the mean monthly streamflow simulated for the four climate change scenarios (2080–2100)

Figure 12 further illustrates the result for the winter–early spring flow volume and the WSCV. The climate change runs show little change from the current conditions for total winter–early spring volume. In the future climate scenarios the WSCV seems to shift consistently in all the models with the median WSCV shifting about 15–20 days earlier from mid-March to late February. This result is fairly consistent between the three models. The predicted shift is also reasonably consistent with the current trend for this watershed (Figure 7), of about 5–6 days per 50 years.

CONCLUSIONS

In recent years, the traditionally strong April snowmelt influenced streamflow peak has lessened in the Catskill Mountain region with a greater proportion of flow now occurring during the earlier winter months, as illustrated

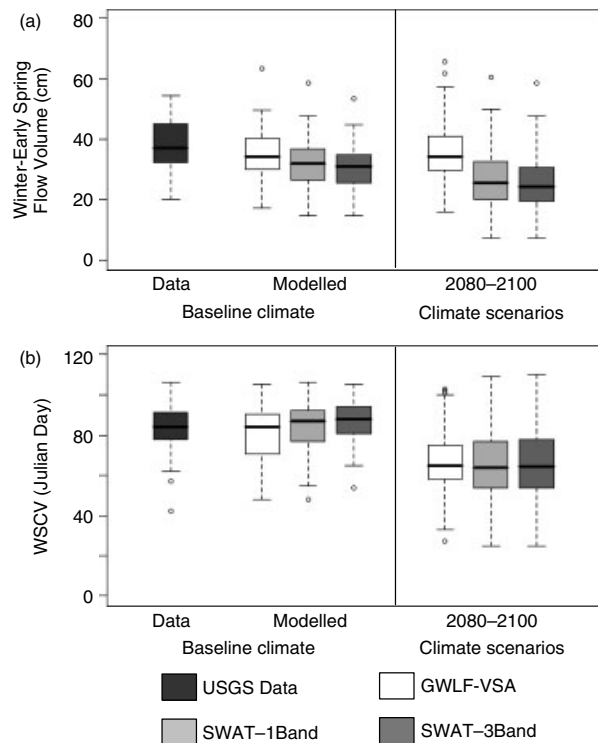


Figure 12. Boxplots showing range of WBDR baseline and future climate scenarios obtained from data and different watershed model simulations for (a) winter–early spring flow volume in unit depth (flow volume/watershed area), and (b) WSCV in Julian Day. Boxes show range of 25th–75th percentile; whiskers show extent of data up to maximum 1.5 times interquartile range. Outliers represent data values beyond the maximum whisker extent

by the shift in WSCV to earlier in the year. This phenomenon, which has been shown in other studies (e.g. Hodgkins *et al.*, 2003; Burns *et al.*, 2007), is most likely due to increased temperatures creating earlier snowmelt and more winter precipitation falling as rain instead of snow. This streamflow timing shift seems to be strongest in the more mountainous catchments of the region. A test of the GWLF-VSA has shown that a relatively simple temperature index method for predicting snow accumulation and melt is able to capture this seasonal shift in streamflow. Tests of the SWAT model, using either a single elevation band or three elevation bands in each simulated sub-basin, yielded similar results to GWLF-VSA in detecting the streamflow timing trends. Finally, a preliminary investigation of potential climate change using both the GWLF-VSA and the SWAT models yield a significant 15–20 day earlier WSCV for a scenario 100 years into the future. Some potential impacts of this shift in streamflow timing include changes in the timing of water supply reservoir filling and spills (Matonse *et al.*, 2010), and changes in the timing of sediment and nutrient delivery to reservoirs impacting reservoir water quality.

ACKNOWLEDGEMENTS

The authors thank New York City Department of Environmental Protection which provided funding for the research that lead to this manuscript. We acknowledge the

modeling groups, the Program for Climate Model Diagnosis and Intercomparison (PCMDI) and the WCRP's Working Group on Coupled Modelling (WGCM) for their roles in making available the WCRP CMIP3 multi-model dataset. Support of this dataset is provided by the Office of Science, U.S. Department of Energy.

REFERENCES

- Anandhi A, Frei A, Pierson DC, Schneiderman EM, Zion MS, Lounsbury D, Matonse AH. 2011. Examination of change factor methodologies for climate change impact assessment. *Water Resources Research* **47**: W03501.
- Anandhi A, Pradhanang S, Zion M, Pierson D, Frei A, Schneiderman E, Mukundan R, Matonse A. 2010. AR4 climate model performance in simulating snow water equivalent over Catskill Mountain watersheds, New York, USA. *Proceedings of the 67th Annual Eastern Snow Conference*, Hancock, MA, June 8–10, 2010.
- Beven KJ, Kirkby MJ. 1979. A physically-based, variable contributing area model of basin hydrology. *Hydrological Science Bulletin* **24**: 43–69.
- Burn DH. 2008. Climatic influences on streamflow timing in the headwaters of the Mackenzie River Basin. *Journal of Hydrology* **352**: 225–238.
- Burn DH, Hag Elnur MA. 2002. Detection of hydrologic trends and variability. *Journal of Hydrology* **255**: 107–122.
- Burns DA, Klaus J, McHale MR. 2007. Recent climate trends and implications for water resources in the Catskill Mountain region, New York, USA. *Journal of Hydrology* **336**: 155–170.
- Burrough PA. 1987. *Principles of Geographical Information Systems for Land Resources Assessment*. Clarendon Press: Oxford, England; p. 186.
- Court A. 1962. Measures of streamflow timing. *Journal of Geophysical Research* **67**(11): 4335–4339.
- Dery SJ, Stahl K, Moore RD, Whitfield PH, Menounos B, Burford JE. 2009. Detection of runoff timing changes in pluvial, nival and glacial rivers of western Canada. *Water Resources Research* **45**: W04426.
- Easton ZM, Walter MT, Steenhuis TS. 2008. Combined monitoring and modeling indicate the most effective agricultural best management practices. *Journal of Environmental Quality* **37**: 1798–1809.
- Ferguson RI. 1999. Snowmelt runoff models. *Progress in Physical Geography* **23**(2): 205–227.
- Frumhoff PC, McCarthy JJ, Melillo JM, Moser SC, Wuebbles DJ. 2007. *Confronting Climate Change in the U.S. Northeast: Science, Impacts, and Solutions*. Synthesis report of the Northeast Climate Impacts Assessment (NECIA). Union of Concerned Scientists (UCS): Cambridge, MA.
- Gitau MW, Veith TL, Gburek WJ. 2004. Farm-Level optimization of BMP placement for cost-effective pollution reduction. *Transactions of the ASABE* **47**(6): 1923–1931.
- Haith DA, Shoemaker LL. 1987. Generalized watershed loading functions for stream flow nutrients. *Water Resources Bulletin* **23**(3): 471–478.
- Hodgkins GA, Dudley RW, Huntington TG. 2003. Changes in the timing of high river flows in New England over the 20th Century. *Journal of Hydrology* **278**: 244–252.
- Hodgkins GA, Dudley RW. 2006. Changes in the timing of winter-spring streamflows in eastern North America. *Geophysical Research Letters* **33**: L06402.
- IPCC. 2007. *Climate Change 2007: The Physical Science Basis. Contribution of Working Group I to the Fourth Assessment Report of the Intergovernmental Panel on Climate Change*. Solomon S, Qin D, Manning M, Chen Z, Marquis M, Averyt KB, Tignor M, Miller HL (eds). Cambridge University Press: Cambridge: United Kingdom and New York, NY, USA; p. 996.
- Kendall MG. 1975. *Rank Correlation Methods*. Charles Griffin: London.
- Mann HB. 1945. Non-parametric tests against trend. *Econometrica* **13**: 245–259.
- Marks D, Domingo J, Susong D, Link T, Garen D. 1999. A spatially distributed energy balance snowmelt model for application in mountain basins. *Hydrological Processes* **13**: 1935–1959.
- Matonse A, Pierson D, Frei A, Zion M, Schneiderman E, Anandhi A, Pradhanang S, Mukundan R. 2010. Effects of changes in snow and timing of runoff on NYC water supply. *Proceedings of the 67th Annual Eastern Snow Conference*, Hancock, MA, June 8–10, 2010.
- Meehl GA, Covey C, Delworth T, Latif M, McAvaney B, Mitchell JFB, Stouffer RJ, Taylor KE. 2007. The WCRP CMIP3 multi-model dataset: A new era in climate change research. *Bulletin of the American Meteorological Society* **88**: 1383–1394.
- Nakicenovic N, Alcamo J, Davis G, de Vries B, Fenhann J, Gaffin S, Gregory K, Grübler A, Jung TY, Kram T, La Rovere EL, Michaelis L, Mori S, Morita T, Pepper W, Pitcher H, Price L, Raihi K, Roehrl A, Rogner HH, Sankovski A, Schlesinger M, Shukla P, Smith S, Swart R, van Rooijen S, Victor N, Dadi Z. 2000. *IPCC Special Report on Emissions Scenarios*. Cambridge University Press: Cambridge, UK and New York, NY, USA, p. 599.
- Nash JE, Sutcliffe JV. 1970. River flow forecasting through conceptual models, part i. A discussion of principles. *Journal of Hydrology* **10**: 282–290.
- Natural Resources Conservation Service (NRCS), United States Department of Agriculture, 2005. Soil Survey Geographic (SSURGO) Database. Available URL: <http://soildatamart.nrcs.usda.gov>.
- Neitsch SL, Arnold JG, Kiniry JR, Srinivasan R, Williams JR. 2005. *Soil and water assessment tool: Theoretical documentation, Version 2005*. Agricultural Research Service: Temple, Texas, p. 476.
- New York City Department of Environmental Protection (NYCDEP), 2006a. *Multi Tiered Water Quality Modeling Program Semi-Annual Status Report*. Valhalla, NY. January 2006.
- New York City Department of Environmental Protection (NYCDEP), 2006b. *2006 Watershed Protection Program and Assessment*. Valhalla, NY. March 2006.
- New York City Department of Environmental Protection (NYCDEP), 2008. *Climate Change Program: Assessment and Action Plan*. New York, NY. May 2008.
- New York City Department of Environmental Protection (NYCDEP), 2009. *Multi Tiered Water Quality Modeling Program Annual Status Report*. Valhalla, NY. October 2009.
- Pradhanang SM, Anandhi A, Mukundan R, Zion MS, Pierson DC, Schneiderman EM, Matonse A, Frei AP. 2010. Using SWAT model and snow survey data to assess spatial variability of snowpack in the Cannonsville watershed, New York, USA. *Proceedings of the 67th Annual Eastern Snow Conference*, Hancock, MA, June 8–10, 2010.
- Rao NS, Easton ZM, Schneiderman EM, Zion MS, Lee DR, Steenhuis TM. 2009. Modeling watershed-scale effectiveness of agricultural best management practices to reduce phosphorus loading. *Journal of Environmental Management* **90**: 1385–1395.
- Schneiderman EM, Pierson DC, Lounsbury DG, Zion MS. 2002. Modeling the Hydrochemistry of the Cannonsville Watershed with Generalized Watershed Loading Functions (GWLF). *Journal of the American Water Resources Association* **38**(5): 1323–1347.
- Schneiderman EM, Steenhuis TS, Thongs DJ, Easton ZM, Zion MS, Neal AL, Mendoza GF, Walter MT. 2007. Incorporating variable source area hydrology into the curve number based Generalized Watershed Loading Function model. *Hydrological Processes* **21**: 3420–3430.
- Sen PK. 1968. Estimates of the regression coefficient based on Kendall's tau. *Journal of the American Statistical Association* **63**: 1379–1389.
- Trombulak SC, Wolfson R. 2004. Twentieth-century climate change in New England and New York, USA. *Geophysical Research Letters* **31**: L19202.
- United States Geological Survey (USGS), 1998. Digital Elevation Models (DEM)—New York State. Available URL: <http://www.dec.ny.gov/geodata/ptk>.
- United States Geological Survey (USGS), 2009. 2009 Water Year Annual Data Report—New York State, Vol. 1: Eastern New York excluding Long Island. Available URL: <http://ny.water.usgs.gov/pubs/wdr/wdrny091/troy.listing09.pdf>.
- Walter MT, Brooks ES, McCool DK, King LG, Molnau M, Boll J. 2005. Process-based snowmelt modeling: does it require more input data than temperature-index modeling? *Journal of Hydrology* **300**: 65–75.
- Walter MT, Mehta VK, Marrone AM, Boll J, Gerard-Merchant P, Steenhuis TS, Walter MF. 2003. A simple estimation of the prevalence of Hortonian flow in New York City's watersheds. *ASCE Journal of Hydrologic Engineering* **8**(4): 214–218.
- Wehner M, Smith R, Bala G, Duffy P. 2010. The effect of horizontal resolution on simulation of very extreme us precipitation events in a global atmosphere model. *Climate Dynamics* **34**: 241–247.
- Zhang X, Harvey KD, Hogg WD, Yuzyk TR. 2001. Trends in Canadian streamflow. *Water Resources Research* **37**(4): 987–998.
- Zhang X, Srinivasan R, Debele B, Hao F. 2008. Runoff simulation of the headwaters of the Yellow River using the SWAT model with three snowmelt algorithms. *Journal of the American Water Resources Association* **44**(1): 48–61.